Novel approaches to modelling discrete particle systems

By:

Hang LI

A thesis submitted in partial fulfilment of the requirements for the degree of
Doctor of Philosophy

THE UNIVERSITY OF SHEFFIELD

Faculty of Engineering

Department of Civil and Structural Engineering

Submission Date:

December 16, 2020

Abstract

In recent years discrete element methods (DEM) have become increasingly pervasive in modelling granular soils because they provide an efficient way to investigate microscopic soil behaviours which are difficult to observe by experiments and continuum modelling methods. The most popular DEM used so far in geotechnical engineering is the distinct element method, however, it is computationally expensive to simulate large volumes of particles or complex grain geometries, especially in some specific problems such as footings and retaining walls. Resorting to other powerful numerical methods to model granular media is more workable than enhancing the computational power currently. A physics engine is an open-source computer software library to simulate rigid body interactions and has been shown to be able to successfully capture microscopic soil behaviours. It is designed to simulate rigid body interaction or collision events with high accuracy and also fast processing response. Therefore, it is a novel modelling tool as an alternative approach to conventional DEMs. Box2D is a two-dimensional physics engine which was used in this study to explore its performance in modelling benchmark biaxial tests and retaining wall problems. The thesis firstly introduces the contact models in Box2D and the random convex polygonal particle generation methods, then particle shape and packing effects on granular soil mechanical behaviours are presented which were investigated by means of both quantitative analysis and qualitative graphical interpretation methods. Model scaling and confining pressure effects on small-strain stiffness of various granular packings were studied. Besides, more practical retaining wall models were established for the purpose of analysing how the local wall friction coefficient influences the wall/backfill interface friction coefficient and the lateral earth pressure coefficients. Particle size and shape effects were also analysed on backfill strength which are ignored in continuum analyses. The original contributions of this work include: Voronoi-based random polygonal particle and packing generation techniques and graphical interpretation approaches for post-processing for use in physics engine Box2D, model scaling effects on small-strain stiffness of cohesionless granular samples as well as novel comparison between Box2D and LimitState:GEO for retaining walls, etc. This study shows Box2D is a powerful numerical modelling technique able to accurately capture granular micro to macro soil behaviours and can help better understand microscopic geomechanics and solve practical engineering problems.

Acknowledgements

Contents

Chapter 1

Introduction

1.1 Background

Numerical modelling becomes increasingly more dominant in geotechnical design, optimisation and risk assessment so far as the computer technology develops. Many numerical methods have been developed since the early 1940s for the purpose of solving civil engineering problems. The most widely used method until now is the finite element method (FEM), firstly published for the term "finite elements" by Clough (1960) who was one of the founders for this theory. The general idea is to discretise a large domain into smaller and simpler sub-domains called "finite elements" by meshing, with a finite number of nodes of which the mechanical values are solved by partial differential equation (PDE). FEM can handle problems involving very complicated geometries, such as solid mechanics, dynamics, heat transfer, fluids, and the preprocess modelling is straightforward. A large group of commercial software has been developed, such as ABAQUS, ANSYS, ADINA, MIDAS and PLAXIS. However, a larger variety of parameters depending on the constitutive model selected should be determined in the computation and many of them lack physical meaning (this problem is also associated with conventional DEMs), making it difficult for people to understand and calibrate with experimental data. In addition, the results can be very sensitive to the meshing and advance knowledge may be needed to tailor the meshes to suit a specific problem.

The material point method (MPM) used to simulate continuum material (solids, fluids and gases) behaviours and their multi-phase interactions was proposed by Sulsky et al. (1994). It is a spacial discretisation method in which a continuum body is discretised by a number of material points surrounded by meshes or grids to calculate gradients, and it is classified into a meshfree or continuum-based particle method since predefined meshes are not required to compute the interpolation functions as in FEM. Compared with FEM, one of the advantages of MPM is that it can deal with large deformation problems because no remeshing is required as the simulations continues, able to make MPM handle discontinuity problems like crack propagation. Peridynamics is one of the MPMs and has been applied to simulate soil particle crushing (Zhu and Zhao, 2019). However, MPM is more time-consuming than FEM as both material point and mesh data need to be initialised and updated in each

time step. The same as FEM, MPM results are also sensitive to mesh size and orientation.

Finite difference method (FDM) is another discretisation numerical method using finite differences to approximate derivatives. This method needs less computational costs than FEM because FDM simplifies the nonlinear partial differential equations by matrix algebra techniques, while this also causes corresponding inaccuracy especially for rapid deformation problems. FLAC (Fast Lagrangian Analysis of Continua) is one of the FDM software widely used in geotechnical engineering.

In some circumstances, where the ultimate collapse load (stability problems) is concerned, limit analysis, developed since the 1950s can be a better choice than detailed calculation of local behaviours based on complex constitutive models and dynamic responses. Generally, the goal of limit analysis is to find the optimal upper bound or lower bound solution. There are three basic conditions required to be satisfied in terms of the lower bound solution: (1) equilibrium equations, (2) stress boundary conditions, and (3) local yield criteria everywhere. The upper bound solution does not take the stress equilibriums into account, and only considers velocity or failure modes and energy dissipations, for which (a) velocity boundary conditions and (b) strain and velocity compatibility conditions should be satisfied. Limit analysis theory can only be applied to study perfectly plastic materials and the associated flow rule is hypothesised. Currently available limit analysis software includes LimitState:GEO based on discontinuity layout optimisation (DLO), and Optum GE based on finite element limit analysis.

The aforementioned numerical methods can be categorised into continuum methods as they consider an object as a homogeneous continuum. However, considering granular soils as a continuum system is not the best solution because their particulate nature (e.g. particle shape and packing) influences the mechanical response, and continuum analysis cannot capture microscale behaviours, such as local void ratio and multifracture in solids. Many time-stepping discrete element methods have been developed among which the the distinct element method proposed by Cundall (1971) is the most utilised in geotechnical engineering.

Current DEMs can be categorised into soft sphere and hard sphere methods in a rather general way (Duran, 2012). Their main difference lies in the rigid body contact algorithm in which the hard sphere model does not allow any inter-particle penetration and only one contact will be handled in each time integral. A more intensive categorisation in the contact simulator paradigms can be found in Kenny (2004). On the other hand, Sutmann (2002) divided the present developed simulation methods into stochastic and deterministic simulations. In the stochastic simulation, particle movements are along the paths towards lower energy, while the deterministic simulation is based on traditional mechanical theories. The non-smooth contact dynamics proposed by Jean (1999) and the molecular dynamics introduced by Alder and Wainwright (1959) are other two branches of DEMs. Molecular dynamics is aimed to simulate interatomic interactions, hence both repulsive and attractive forces are involved, different from others where inter-particle forces do not exist when the particles are not in contact, and the time step integral is changing depending on the next collision time. It is worth mentioning that molecular dynamics is a hard sphere method while contact dynamics lies between because finite contact durations exist although no particle deformation is allowed (O'Sullivan, 2011),

and it can be classified as the constrained-based method (Kenny, 2004). Discontinuous deformation analysis (DDA) allowing large deformations and larger displacements is another type of DEM initially developed by Shi (1992) for solving discrete particle systems by computing force-displacement equilibrium formulations based on the principle of potential energy minimisation. No inter-particle overlap or tensile contact force is allowed in DDA. The boundary constraints and collisional contacts are solved by springs and dashpots.

One common disadvantage of DEMs is lack of computational efficiency limited by current computer power. In recent years, physics engines have been proved to be able to successfully simulate granular media systems in geotechnics (e.g. Cicekci et al. (2014); Ehsan and Bezuijen (2015); He and Zheng (2020); Izadi and Bezuijen (2018); Pytlos (2015); Zhu and Zhao (2019)). Physics engines are software libraries designed to simulate rigid body interactions and generally used in digital game and film industries. From the contact method perspective, physics engines use the constraint-based methods to avoid any inter-particle penetration and this is in sharp contrast with the penalty method applied in the distinct element method while very similar with the contact dynamics. The constraint-based method relies on impulses to prevent penetration by changing relative velocities of rigid bodies in contact during a collision event, therefore, the constraint-based method is built at the velocity level. Although computation of impulses is more complicated than that of forces in a single time step, far less times steps are required to reach stability in constraint-based method, and this means physics engines have huge potential in simulation acceleration compared with conventional DEMs. Particularly, as the elastic deformation is ignored in physics engines, a single time step can be several orders of magnitude larger than that in other DEMs. Furthermore, the numerical integration method in each time step in physics engines is the semi-implicit scheme, hence the damping coefficient is not necessary for computational convergency and as a result simplifying the parameter input because this non-physical parameter will cause difficulties in modelling which is however essential in other DEMs using the explicit time integration scheme.

A variety of physics engines have been applied to granular soil modelling so far, such as Unity, Bullet Physics and PhysX. It is shown that physics engines are capable to accurately model soil and structure behaviours in modelling granular soils, arch bridges, collapse of bridges facilitated by FEM and particulate grain breakage coupled with peridynamics. In this research, open-source two-dimensional physics engine Box2D was used in modelling discrete media. A full description of Box2D and its advantages over other DEMs will be given in section 2.2.

1.2   Aims and objectives

This study is based on the hypothesis that physics engine Box2D can accurately capture granular soil behaviours (Pytlos, 2015), such as microscopic strain localisation phenomenon, macroscopic strain hardening, softening and critical state behaviours. The overall aims of this thesis are to show the capabilities of physics engine Box2D in modelling discrete particle systems and granular soil behaviours in benchmark tests and real engineering problems. One of the advantages of DEMs over FEMs is the

ability to analyse the particle characteristic effects on soil behaviours, therefore, new particle shape and packing generation technologies will be explored and used in the Box2D simulations, following the work by Pytlos (2015) who used random dodecagonal particles as granular materials in biaxial and arch bridge simulations. Graphical interpretation is important in DEM as it can help qualitatively study the skeleton evolutions during shearing within soil samples which are difficult to observe in laboratory experiments because of facility limitations. Some more graphic interpretation methods, in addition to the particle accumulated rotation and displacement diagrams built by Pytlos (2015), will be represented to help better understand local behaviours within soil samples, for example, the local void ratio and volumetric strain rate diagrams. Parametric studies are always important in simulation because some parameters can influence the final results significantly and different numerical modelling methods have different system parameters which will dominate the simulation performance. Therefore, some parametric studies will be implemented to further investigate Box2D system parameter effects on simulation results. The objectives of this thesis are set as:

1) Develop Voronoi-based particle and packing generation techniques in Box2D and study particle shape and packing effects on soil behaviours in biaxial test modelling under the help of various graphical interpretation methods.

2) Quantitatively and qualitatively investigate model scaling effects on small-strain stiffness of various packings made of cohesionless particulate soils.

3) Study retaining wall local friction effects and packing and particle size effects on lateral earth pressure coefficients in both passive and active conditions, and compare the results with theoretical continuum methods.

1.3   Overview

Chapter 2 gives a thorough literature review on the most prevailing particle generation techniques and compares different discrete element methods both in particle contact models and time integration schemes. Chapter 3 then introduces physics engine Box2D which is utilised in this research in more detail including its contact collision and detection algorithms. The Voronoi tessellation algorithm applied to create random polygonal particles and perfectly in-situ packings will be presented in Chapter 4. Three separate projects are conducted and discussed in the next three chapters. Chapter 5 studies the particle shape and packing effects on granular soil behaviours using the established biaxial model, and also carries out a series of parametric studies to investigate the influences of Box2D system and model set-up parameters on the results. The influences of model scaling ratio and confining pressure on small-strain behaviour are explored in Chapter 6. A more practical retaining wall model will be set up and the relationship between the wall local friction angle with the wall/backfill contact interface friction angle is to be discussed in Chapter 7. The particle shape and packing effects on lateral earth pressure coefficients will also be investigated, which are ignored in conventional theoretical solutions

purely considering continuum backfills. The DEM results will be compared with those obtained by theoretical solutions given by Powrie (2018) and LimitState:GEO in order to find the gap between DEM and continuum analysis. Finally, overall discussion and conclusions will be given in Chapters 8 and 9, pointing out the issues in modelling that may influence the results and further developments of the Box2D contact model to better model granular materials.

Chapter 2

Literature Review

This chapter reviews several particle generation approaches normally applied in discrete element modelling and some prevalent conventional DEM methods. Their advantages and disadvantages will also be compared with physics engine Box2D in this part. More specific research findings related to particle shape effects, small-strain stiffness of cohesionless granular soils and retaining walls will be reviewed separately at the beginning of each corresponding chapter.

2.1   Overview of up-to-date particle generation techniques

Many algorithms have been developed to date in order to create granular soil samples made of various particle shapes and packings, in order to resemble real particle shapes in DEMs while balancing reality and computational cost in the meantime. Current algorithms capable of generating random particles can be classified into two groups: dynamic approaches and constructive approaches.

Dynamic approaches are normally applied in DEMs to obtain initial deposit arrangements. One of the most common approaches is filling a number of particles into a specified domain and consolidating the sample by applying a confining pressure until a prescribed requirement is satisfied, such as a target density (e.g. Cui and O'Sullivan (2003); Hanley et al. (2014)). Another approach is to drop generated particles to fill up a container under a gravitational environment (e.g. Feng et al. (2003)).

In terms of constructive algorithms, the assemblies are created by geometrical calculations without dynamic motion. One of the constructive algorithms to create spherical particles is the lily-pond model (Häggström and Meester, 1996) in which a variety of infinitesimal points are randomly located at the beginning and expanded with a uniform speed until they contact with others. The Stienen model (Stoyan, 1998) is similar to the lily-pond model: a group of random seed points are distributed inside a domain initially followed by radius expansion to half the distance between one seed and its closest one. A similar method to the Stienen model is creating spherical particles inscribed by Voronoi cells and also at their nodes as introduced by Cui and O'Sullivan (2003). It is difficult to obtain particles obeying a desired particle size distribution using these algorithms. Bagi (1993) put forward a quasi-static dropping method to create packings of circular discs using a displacement

method and global equilibrium equations to find the stable position for each particle. Similar to the dropping method, the sedimentation method (Zhou et al., 2009) simulates the sedimentation process following a constructive approach: a number of spherical particles along the bottom of a container are created at the start and there will be one new particle in each turn created and translated downwards into the container until it contacts with an existing one, and the difference from the dynamic approach is that the newly-generated particle rolls along the contacting one to a stable position supported by two existing particles (for two-dimensional) or three existing ones (for three-dimensional) purely by geometric calculations. Both the quasi-static dropping method and the sedimentation method can create denser deposits constituted with target particle size distribution compared with the Stienen model and the lily-pond model, however they can cause anisotropy to the original deposit on the other hand, which means larger vertical stiffness. To overcome the inherent anisotropy problem caused by sedimentation processes, Bagi (2005) proposed the inwards packing method as an improvement of the closed front method presented by Feng et al. (2003) in avoiding large gaps between circumferential particles and boundaries. This approach provides a facility to fill a prescribed domain with spherical particles from the outmost zone contacting with the boundaries further into the interior layer by layer, and the created assemblies are more isotropic than those deposited by the sedimentation process and their size distribution can also be specified beforehand. All the aforementioned constructive approaches can only create spherical particle packings because geometry models between particles of complex geometries are difficult to establish. The Voronoi tessellation is an efficient and powerful constructive approach to generate random polygonal and polyhedral particles in modelling granular particles (e.g. Galindo-Torres et al. (2010); Galindo-Torres and Pedroso (2010); Mollon and Zhao (2012)) and this method will be introduced in detail in section 4.1.

There is no doubt that dynamic approaches are much easier to achieve within an environment in which particle contact detection and collision models are established, however longer execution time is required to reach stability compared with more complex constructive approaches. Constructive approaches are more versatile and can be applied in any numerical modelling technique such as limit analysis and FEM.

To model more realistic particles, Thomas and Bray (1999) used simple disc clumps in the biaxial test simulation and the anchor pullout simulation. The simulation of real particle shape in DEM has advance well beyond the use of clumps which has been used to produce "avatars" from real samples scanned using X-Ray and micro-CT methods. Matsushima and Saomoto (2002) proposed a dynamic optimisation method using disc or sphere clumps to model a 2D or 3D particle which is described by a number of nodes on its contour, determined by laser scanning or stereo-photogrammetry techniques beforehand. A controlled number of discs or spheres (primitive elements) far smaller than the modelled particle size are built at random positions firstly and then the distances between the nodes on the primitive element surfaces and the closest nodes on the particle surfaces are summed and iterated in several time steps by translating and also expanding or shrinking the primitive elements until the error index is below the specified threshold. A simple clustering method was published by Ferellec and McDowell (2008) to model complex particle shapes using disc clusters: a number of

nodes apart from each other by a set distance are specified along the surface contour of a particle, and then a series of infinitesimal discs inwardly tangential to these node surfaces are expanded along their own normal directions to the surface until they contact with the other side of the surface contour. Apart from abovementioned approaches, Bowman et al. (2001) proposed a novel technique to describe real particle shapes by using Fourier descriptor analysis which can accurately capture sand grain morphology and texture through scanning electron microscope photographs beforehand. Mollon and Zhao (2014) subsequently used the Fourier-shape-descriptor based method to generate 3D realistic particles packed and confined in cells created by Voronoi tessellation.

2.2 Discrete particle system modelling

2.2.1 Distinct element method

The distinct element method was pioneered by Cundall (1971, 1974) and initially applied to model interactions of discs and spheres. Its soft sphere contact model is appreciated by many users. The general dynamic process in the simulation and contact models will be introduced separately in this section.

Computation cycle

The whole dynamic process (Cundall and Strack, 1978, 1979) is governed by Newton's second law to track the particle motion and a prescribed contact law to compute the contact force used to compute accelerations and velocities and hence update particle positions. A rather small overlap between soft particles is allowed in the distinct element method and this can be envisaged as a small deformation produced by a collision which also contributes to the whole sample deformation. The contact force is linearly proportional to the inter-particle overlap magnitude. The velocities and accelerations are kept constant over a time step which is stipulated to be small enough so that single time step disturbances cannot propagate from a particle further to its nearest neighbour particles. The dynamic cycle for solving a contact between two particles in the normal direction is simplified into equations (2.1) to (2.5):

$$F_n = k_n \Delta n_t = k_n v \Delta t \tag{2.1}$$

$$\ddot{x}_i = F_n / m_i \quad \ddot{x}_j = -F_n / m_j \tag{2.2}$$

$$\ddot{\theta}_i = M / I_i \quad \ddot{\theta}_j = -M / \theta_j \tag{2.3}$$

$$\dot{x}_{t+\Delta t} = \dot{x}_t + \ddot{x}_t \Delta t \quad \dot{\theta}_{t+\Delta t} = \dot{\theta}_t + \ddot{\theta}_t \Delta t \tag{2.4}$$

$$\Delta n_{t+\Delta t} = \dot{x}_{i_t} \Delta t - \dot{x}_{j_t} \Delta t \tag{2.5}$$

Initially, the normal contact force F_n and the moment M will be calculated based on the existing contact overlap depth Δn_t at time step t and the normal contact stiffness k_n related to the particle

geometric and material properties (i.e. Young's modulus E, shear modulus G and Poisson's ratio ν), then followed by computations for the translational and rotational accelerations $\ddot{x}$ and $\ddot{\theta}$. The new velocities $\dot{x}_{t+\Delta t}$ and $\dot{\theta}_{t+\Delta t}$ after time step Δt can be updated and also the new relative overlap depth $\Delta n_{t+\Delta t}$.

Coulomb's friction law (2.6) is incorporated where ϕ and c are the smaller inter-particle friction angle and cohesion between two contacting particles, respectively. Dynamic friction is constant and equal to $F_{s,max}$.

$$F_{s,max} = F_n \tan \phi + c \tag{2.6}$$

Friction damping and two forms of viscous damping: contact damping and global damping which can be regarded as dashpots are involved in the computation. The contact damping is operated at the relative velocity level during a collision event and the global damping is built at the absolute velocity level. Friction damping is only considered when inter-particle sliding occurs, and on the contrary, the optional viscous damping is only allowed in the condition without sliding occurring. The normal and tangential contact damping coefficients c_n and c_t, and the global damping coefficients C and C^* related to translational and rotational velocities, with regard to stiffness k, mass m and moment of inertia I, can be established by:

$$c_n = \beta k_n \quad c_t = \beta k_s$$
$$C = \alpha m \quad C^* = \alpha I$$

The time integration method is the technique used to update mechanical parameters given the first and second derivatives with respect to time (i.e. displacements and rotations from velocities, and velocities from accelerations) in the numerical analysis (O'Sullivan, 2011). An explicit central-difference integration scheme given by equation (2.7) is adopted in the distinct element method for its comparatively easy implementation.

$$\vec{v}(t + \tfrac{\Delta t}{2}) = \vec{v}(t - \tfrac{\Delta t}{2}) + \dot{\vec{v}}(t)\Delta t$$
$$\vec{\omega}(t + \tfrac{\Delta t}{2}) = \vec{\omega}(t - \tfrac{\Delta t}{2}) + \dot{\vec{\omega}}(t)\Delta t$$
$$\vec{x}(t + \Delta t) = \vec{x}(t) + \Delta t \vec{v}(t + \tfrac{\Delta t}{2}) \tag{2.7}$$
$$\vec{\Omega}(t + \Delta t) = \vec{\Omega}(t) + \Delta t \vec{\omega}(t + \tfrac{\Delta t}{2})$$

The velocities used to update new position $\vec{x}$ and rotation $\vec{\Omega}$ at time step $t + \Delta t$ are the values at time step $t + \frac{\Delta t}{2}$, which are calculated according to the values at time steps $t - \frac{\Delta t}{2}$ and t. This second order central-difference integration form is also called the leap-frog method and its accuracy depends on Δt^2. It is required that the time step Δt must be small enough to guarantee numerical stability in the explicit integration method. As stated by Cundall and Strack (1979), the time step size Δt must be kept less than the critical time step to reach stability (Belytschko et al. (2013) regarded that the critical time step size should be multiplied by a factor between 0.8 and 0.98 to account for the non-linearity destabilizing effects). There is however no consensus upon the value of the critical time

step size. Tsuji et al. (1993) defined the critical time step Δt_{crit} as:

$$\Delta t_{crit} = \frac{\pi}{5}\sqrt{m/k}$$

in his 2D model according to the energy perspective, while Sheng et al. (2004) gave the expression as:

$$\Delta t_{crit} = \frac{\pi r_{min}}{\alpha}\sqrt{\rho}G$$

where r_{min} is the minimum radius of the spheres, ρ and G are density and shear modulus, and α is related to the Poisson's ratio. This critical time step size was also taken by Li et al. (2005) while the minimum spherical radius was replaced with the mean spherical radius. Another approach to determine critical time step size is based on eigenvalue analysis as proposed by Otsubo et al. (2017) for which an extension of Rayleigh's theorem is adopted in explicit finite element analysis:

$$\lambda_{max} \leq \lambda_{max}^e$$

where λ_{max} and λ_{max}^e are the maximum eigenvalues of the global and the element $M^{-1}K$ matrix respectively. M and K are the mass matrix and the stiffness matrix. Then the critical time step size is given by:

$$\Delta t_{crit} = \frac{2}{\omega_{max}}$$

and the maximum frequency ω_{max} is equal to $\sqrt{\lambda_{max}}$.

O'Sullivan (2011) gave some good conclusions about the key points to note on Δt_{crit} for DEM users:

1) Δt_{crit} depends on the contact stiffness: the stiffer the contact, the smaller Δt_{crit} is.

2) Δt_{crit} depends on the density: the greater the density, the larger Δt_{crit} is.

3) Δt_{crit} depends on contact numbers: the more contacts, the smaller Δt_{crit} is.

Contact force models

In the distinct element method, the modelled particles are regarded as soft bodies while deformation is allowed between particles which is modelled by inter-particle overlap (a penalty spring method) and the contact model is a combination of springs, sliders and dashpots. The contact constitutive model is defined as a force-deformation relationship. A spring model is used to represent a linear (Figure 2.1a) or non-linear elastic (Figure 2.1b) force-deformation response, a slider model (Figure 2.1c) describes the behaviour that there is no deformation until the force increases up to a yield point, and a dashpot model (Figure 2.1d) indicates the force increase is linearly proportional to the deformation rate.

As summarised by O'Sullivan (2011), there have been many linear and nonlinear elastic normal and tangential contact constitutive models established, for instance, the Hertz-Mindlin contact model

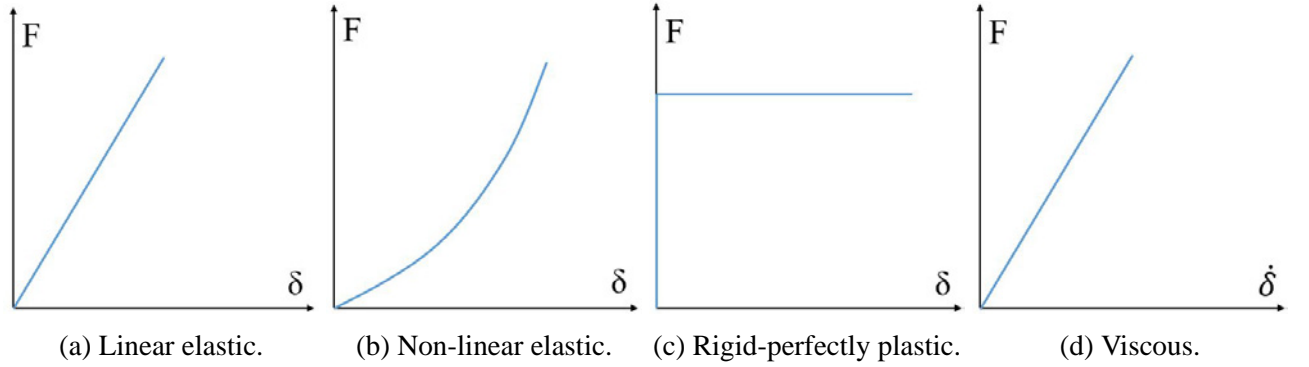|			
(a) Linear elastic.	(b) Non-linear elastic.	(c) Rigid-perfectly plastic.	(d) Viscous.

Figure 2.1: Four basic force-deformation relations in the contact constitutive model.

(Johnson and Johnson, 1987) (also called the Hertzian contact model) derived from the Mindlin-Deresiewicz tangential model (Mindlin, 1953), the Walton-Braun linear model (Walton and Braun, 1986) referred to as the hysteretic damping model in the commercial software PFC and the Thornton and Yin model (Thornton and Yin, 1991). The non-conforming Hertz-Mindlin contact model and the Mindlin-Deresiewicz tangential model define the normal stiffness k_n and the tangential stiffness k_s as equations (2.8) and (2.9), where A is contact zone radius, R_1 and R_2 are radii of two contacting bodies.

$$
\begin{aligned}
k_n &= 2EA \\
\tfrac{1}{E} &= \tfrac{1-\nu_1}{2G_1} + \tfrac{1-\nu_2}{2G_2} \\
A &= \left(\tfrac{3F_n R}{8E}\right)^{\frac{1}{3}} \\
R &= \tfrac{2R_1 R_2}{R_1 + R_2}
\end{aligned}
\tag{2.8}
$$

$$
\begin{aligned}
k_s &= 8GA\left(1 - \tfrac{F_t}{F_n \tan\phi}\right)^{\frac{1}{3}} \\
\tfrac{1}{E} &= \tfrac{1-\nu_1}{2G_1} + \tfrac{1-\nu_2}{2G_2} \\
G &= \tfrac{2-\nu_1}{G_1} + \tfrac{2-\nu_2}{G_2}
\end{aligned}
\tag{2.9}
$$

2.2.2 Contact dynamics

The non-smooth contact dynamics method was firstly introduced by Jean (1999) for short contact dynamics and the term "non-smooth" indicates discontinuities in dynamic systems such as velocity jumps produced before and after collision events. Radjai and Richefeu (2009) also gave a clear description about its intuitive features and precision issues. To understand the contact algorithm adopted in the contact dynamics, a unilateral contact will be introduced firstly. A unilateral condition must satisfy the following conditions:

- Impenetrability: inter-particle collision or any penetration across the contacting particle boundaries is not allowed in the unilateral condition.

- The Signorini condition: only repulsive contacting forces exist between particles, and attracting forces are not defined. If the contact is not active, the contact force vanishes as illustrated in Figure 2.2a, in which F_n is the normal contact force and δ_n is the normal relative distance

between particles in considering.

- Dry friction: a static friction force may exist before sliding occurs, after the dynamic friction exceeds the threshold defined by Coulomb's friction law equal to μF_n and opposite to the sliding direction as shown in Figure 2.2b, in which μ is the frictional coefficient, and F_t and u_t are the tangential frictional force and the tangential relative velocity respectively.

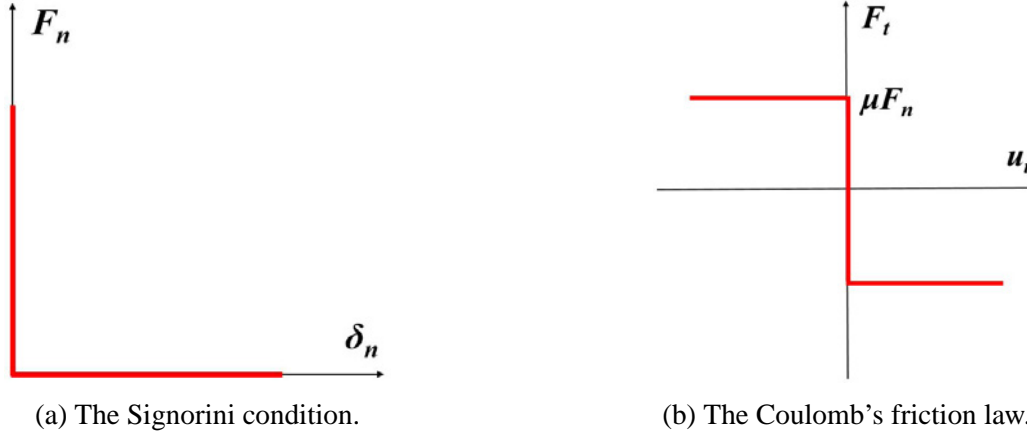(a) The Signorini condition.   (b) The Coulomb's friction law.

Figure 2.2: Unilateral contact conditions.

The contact dynamics aims to solve the unilateral contact conditions which can be established by equations (2.10) and (2.11) for the normal direction and the tangential direction respectively.

$$\begin{cases} \delta_n > 0 & \Rightarrow \quad F_n = 0 \\ \delta_n = 0 \quad \cap \quad \begin{cases} u_n > 0 & \Rightarrow \quad F_n = 0 \\ u_n = 0 & \Rightarrow \quad F_n \geq 0 \end{cases} \end{cases} \tag{2.10}$$

$$\begin{cases} u_t > 0 & \Rightarrow \quad F_t = -\mu F_n \\ u_t = 0 & \Rightarrow \quad -\mu F_n \leq F_t \leq \mu F_n \\ u_t < 0 & \Rightarrow \quad F_t = \mu F_n \end{cases} \tag{2.11}$$

When two bodies are separate by a distance δ_n in the normal direction ($\delta_n > 0$), there should not be any contact force produced ($F_n = 0$), while for potential contacting bodies ($\delta_n = 0$), there are two circumstances of which one is that the contact will vanish immediately ($u_n > 0$), and hence the contact force is zero, and the other is that the contact will persist and in this case the contact force will be generated ($F_n \geq 0$). For the contacting bodies, the contact forces are computed based on their relative velocities by impulses applied rather than the inter-penetration distance as used in the conventional distinct element method because inter-particle overlap is not allowed in the contact dynamics. The whole contact collision process calculation is very similar with that in physics engines and will be introduced in detail in section 3.1.

One of the features of the contact dynamics is its fully implicit time-stepping scheme (described by equation (2.12)).

$$\vec{v}(t + \Delta t) = \vec{v}^+$$
$$\vec{\omega}(t + \Delta t) = \vec{\omega}^+$$
$$\vec{x}(t + \Delta t) = \vec{x}(t) + \frac{\Delta t}{2}\vec{v}(t + \Delta t)$$
$$\vec{\Omega}(t + \Delta t) = \vec{\Omega}(t) + \frac{\Delta t}{2}\vec{\omega}(t + \Delta t)$$

(2.12)

The left limit "-" and right limit "+" represent the contact states at t and $t + \Delta t$ in a considered time integral, respectively. The implicit time-stepping scheme uses the right limit displacement velocity $\vec{v}^+$ and the angular velocity $\vec{\omega}^+$ as the updated velocities $\vec{v}(t + \Delta t)$ and $\vec{\omega}(t + \Delta t)$ in a time step, and the new position $\vec{x}(t + \Delta t)$ and the rotation magnitude $\vec{\Omega}(t + \Delta t)$ are computed by the updated velocities over half time step size. One of the advantages of the fully implicit method is the unconditional stability, hence no damping ratio is needed which can cause difficulties as this parameter is physically meaningless (mainly designed to dissipate energy) and difficult to measure in physical experiments. In addition, the non-smoothness characteristic gives a possibility to increase the time step size. As stated by Radjai and Richefeu (2009), the typical time step size could be of the order 10^{-4} s for a high-quality shear flow simulation in the contact dynamics, and this is by several orders magnitude larger than that in the molecular dynamics which is of the order 1 ns (10^{-9} s) (Sutmann, 2002). However, the implicit integration method is not as that straightforward as the explicit integration method to implement (Krabbenhoft, Lyamin, Huang and da Silva, 2012; Radjai and Richefeu, 2009).

The criterion to stop one iteration for a contact α is to check whether the updated contact force lies within a specific precision with regard to the previous time step:

$$\frac{\left| F_{t+1}^\alpha - F_t^\alpha \right|}{F_{t+1}^\alpha} < \epsilon_f$$

(2.13)

and the number of iterations required is found to be strongly dependent on the convergence criterion ϵ_f instead of the time step size Δt (Radjai and Richefeu, 2009), as a result, only the weak contacts will be influenced in accuracy.

2.2.3 Molecular dynamics

The molecular dynamics initially proposed by Alder and Wainwright (1957) is widely applied in chemistry and material science as it is designed to simulate interactions between atomic and molecular particles and not only repulsive contact forces but also attractive forces exist between hard sphere particles. The typical time step size and trajectory length are of order 1 ns (10^{-9} s) and 10-100 Å (1 Angstrom is 10^{-10} m) in molecular dynamics (Sutmann, 2002).

At the incipient time step, molecules i and j are given positions $\vec{r}_0$ and velocities $\vec{u}$, and their new relative positions $\vec{r}_i - \vec{r}_j$ after time step t can be represented by equation (2.14), and we can also get

the time step size t required for the next collision (repulsive or attractive) using equation (2.15).

$$(\vec{r}_i - \vec{r}_j)^2 = [(\vec{r}_{i0} - \vec{r}_{j0}) + t(\vec{u}_i - \vec{u}_j)]^2 \tag{2.14}$$

$$t = \frac{-b_{ij} \pm (b_{ij}^2 - \vec{u}_{ij}^2 C_{ij}^{(\alpha)})^{\frac{1}{2}}}{\vec{u}_{ij}^2} \tag{2.15}$$

in which

$$\vec{r}_{ij} = \vec{r}_{i0} - \vec{r}_{j0} \quad b_{ij} = \vec{r}_{ij} \cdot \vec{u}_{ij}$$
$$\vec{u}_{ij} = \vec{u}_i - \vec{u}_j \quad C_{ij}^{(\alpha)} = \vec{r}_{ij}^2 - \sigma_\alpha^2$$

From the expression for the time step size t, we know the time step size is always changing according to the motion propagation. Let $t^{(1)}$ and $t^{(2)}$ be the time periods required for repulsive and attractive collisions, respectively. The parameter $C_{ij}^{(1)}$ must be positive otherwise the molecules will overlap which is not allowed in the hard sphere model compelling the programme to stop. In contrast, $C_{ij}^{(2)}$ could be either positive or negative depending on whether two molecules move within the attractive potential. The parameter σ_α is used to specify the repulsive and attractive ranges. For brevity, the process to calculate collision time t can be summarised as below (Alder and Wainwright, 1959):

I. $b_{ij} < 0$ (molecules approaching)

   (a) $C_{ij}^{(2)} < 0$ ($\vec{r}_{ij}$ within the attractive range)

      i. $b_{ij}^2 - \vec{r}_{ij}^2 C_{ij}^{(1)} > 0$ (Repulsive collision)
      at $t^{(1)} = \frac{-b_{ij} + (b_{ij}^2 - \vec{u}_{ij}^2 C_{ij}^{(1)})^{\frac{1}{2}}}{\vec{u}_{ij}^2}$

      ii. $b_{ij}^2 - \vec{r}_{ij}^2 C_{ij}^{(1)} < 0$ (Attractive collision)
      at $t^{(2)} = \frac{-b_{ij} + (b_{ij}^2 - \vec{u}_{ij}^2 C_{ij}^{(2)})^{\frac{1}{2}}}{\vec{u}_{ij}^2}$

   (b) $C_{ij}^{(2)} > 0$ ($\vec{r}_{ij}$ outside the attractive range)

      i. $b_{ij}^2 - \vec{r}_{ij}^2 C_{ij}^{(2)} > 0$ (Attractive collision)
      at $t^{(2)} = \frac{-b_{ij} + (b_{ij}^2 - \vec{u}_{ij}^2 C_{ij}^{(2)})^{\frac{1}{2}}}{\vec{u}_{ij}^2}$

      ii. $b_{ij}^2 - \vec{r}_{ij}^2 C_{ij}^{(2)} < 0$
      No collision takes place.

II. $b_{ij} > 0$ (molecules receding)

   (a) $C_{ij}^{(2)} < 0$ ($\vec{r}_{ij}$ within the attractive range, attractive collision)
   at $t^{(2)} = \frac{-b_{ij} + (b_{ij}^2 - \vec{u}_{ij}^2 C_{ij}^{(2)})^{\frac{1}{2}}}{\vec{u}_{ij}^2}$

   (b) $C_{ij}^{(2)} > 0$ ($\vec{r}_{ij}$ outside the attractive range)
   No collision takes place.

After the collision occurs, the molecule velocity will be changed according to the conservation of momentum and energy where the interactive forces are determined based on the interatomic potentials or molecular mechanics force fields (Sutmann, 2002).

The two common explicit time integration methods adopted in molecular dynamics are the leapfrog and Verlet methods, the same as the distinct element method (Repaport, 2004).

2.2.4 Physics engines

A physics engine is an open-source computer software library originally used to develop video games and films for its capability in simulating interactions or collisions between rigid bodies. It can generally be divided into two groups: high-precision physics engines and real-time physics engines. Real-time physics engines are normally applied in video games as they are less expensive in compuational requirements, while high-precision physics engines need more computational power (high performance computers and vector processors are commonly used to accelerate the calculations and enhance efficiencies) to deal with more complex contact models.

In recent years, physics engines have been used in civil engineering to replace conventional discrete element methods to speed up simulation process. For example, Xu et al. (2013) used combined FEM and the physics engine PhysX to simulate bridge collapse process and obtained real-time visualisation for the deactivated elements that are difficult to capture in a FEM environment (Figure 2.3).

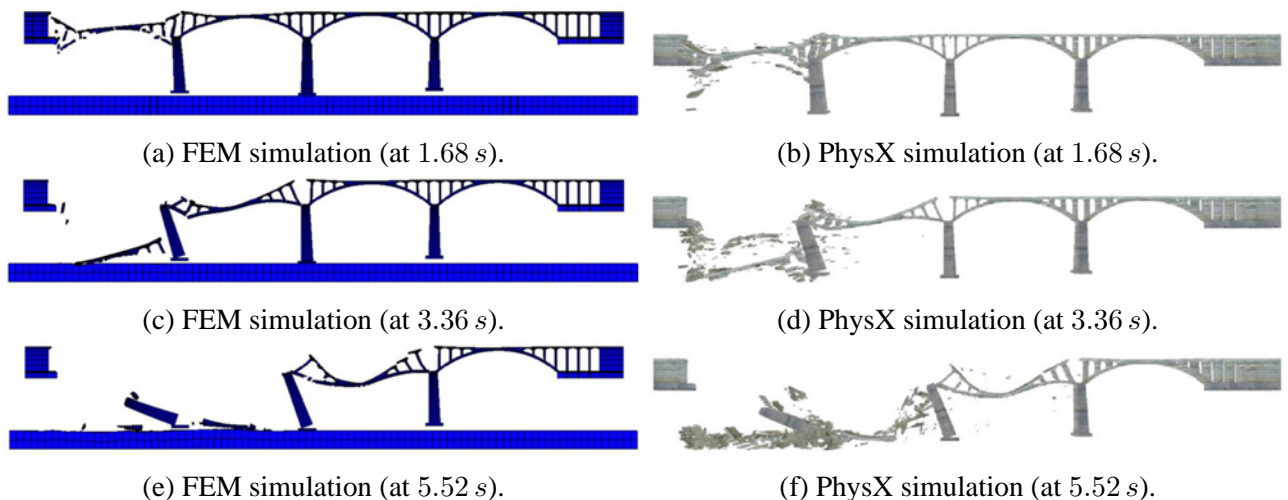|	
(a) FEM simulation (at $1.68\,s$).	(b) PhysX simulation (at $1.68\,s$).
(c) FEM simulation (at $3.36\,s$).	(d) PhysX simulation (at $3.36\,s$).
(e) FEM simulation (at $5.52\,s$).	(f) PhysX simulation (at $5.52\,s$).

Figure 2.3: Comparison of collapse process between FEM and PhysX (Xu et al., 2013).

Pytlos (2015) applied physics engine Box2D in arch bridge modelling where the weightless loading beam was velocity-controlled providing vertical stress on the backfilled frictional soil. Figure 2.4 shows particle total displacements and rotations at different loading beam vertical movements: $0.1\,m$ at which the left hinge firstly initiates, and $0.6\,m$ at which the global failure occurs. The failure load was also compared with that computed in limit analysis using software LimitState:RING and showed good agreements although small discrepancies existed due to unavoidable simulation variances (e.g. differences to define the failure mode between the two methods and small but existing model geometry differences).

To overcome the difficulties in simulating crushing particles, Zhu and Zhao (2019) resorted to

(a) Loading beam displacement: $0.1\,m$.

(b) Loading beam displacement: $0.6\,m$.

(c) Loading beam displacement: $0.1\,m$.

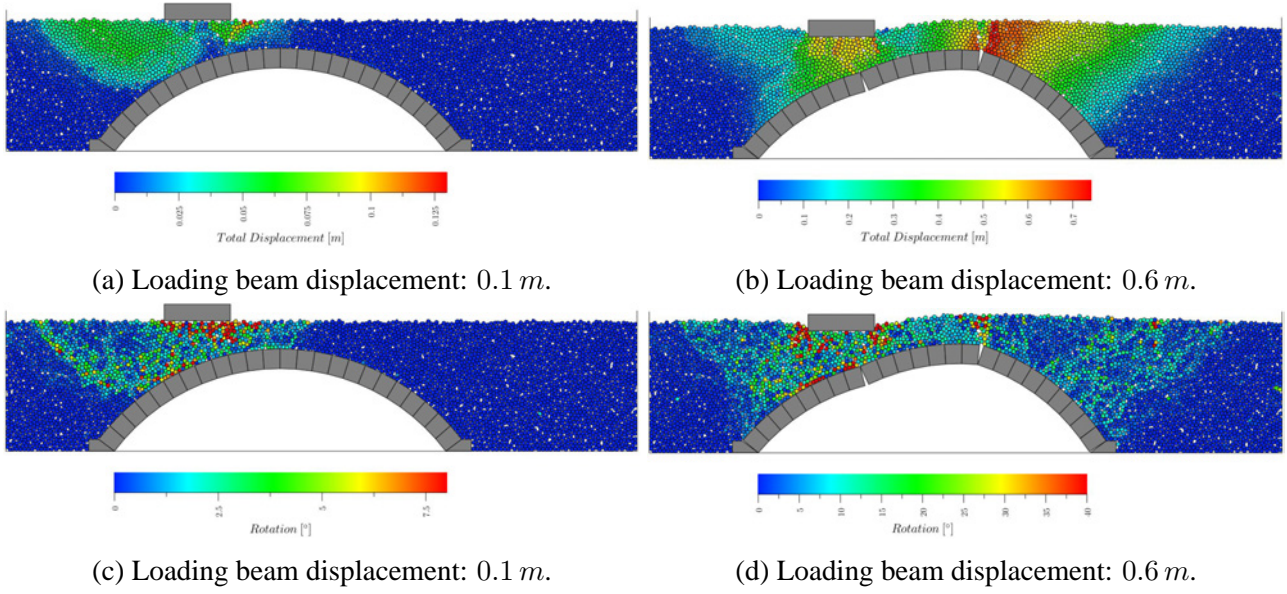(d) Loading beam displacement: $0.6\,m$.

Figure 2.4: Total particle displacements and rotations in full backfilled arch simulations (Pytlos, 2015).

peridynamics to simulate crushing behaviours and combined the Bullet physics engine to animate rigid body interactions. Figure 2.5 shows some snapshots and the number of crushing events occurring during a 1D compression test as the vertical pressure increased using this hybrid method.

Physics engines use the constraint-based method to solve contact events in which overlap between particles is not allowed during collision. The Signorini condition and Coulomb's law are both satisfied in physics engines. Contact forces only exist between contacting bodies. The time integration scheme adopted in physics engines is the semi-implicit method. The integration process is summarised by equation (2.16). The translational and rotational velocities after each time step Δt are computed based on the velocities at previous time step $\vec{v}(t)$, $\vec{\omega}(t)$ and their corresponding changes $\Delta\vec{v}$ and $\Delta\vec{\omega}$ given by impulses applied on contacting rigid bodies to avoid inter-particle penetration and sliding. The new position $\vec{x}(t+\Delta t)$ and rotation $\vec{\omega}(t+\Delta t)$ are updated using their values at previous time step and new velocities $\vec{v}(t)$ and $\vec{\omega}(t)$ during the time integral Δt. The semi-implicit integration scheme is much more stable than the explicit method which is used by most DEMs, therefore no damping coefficients are required which can complicate the simulation input parameters, and the semi-explicit method is easier to implement than the fully-implicit method adopted in the contact dynamics.

$$
\begin{aligned}
\vec{v}(t+\Delta t) &= \vec{v}(t) + \Delta\vec{v} \\
\vec{\omega}(t+\Delta t) &= \vec{\omega}(t) + \Delta\vec{\omega} \\
\vec{x}(t+\Delta t) &= \vec{x}(t) + \Delta t\,\vec{v}(t+\Delta t) \\
\vec{\Omega}(t+\Delta t) &= \vec{\Omega}(t) + \Delta t\,\vec{\omega}(t+\Delta t)
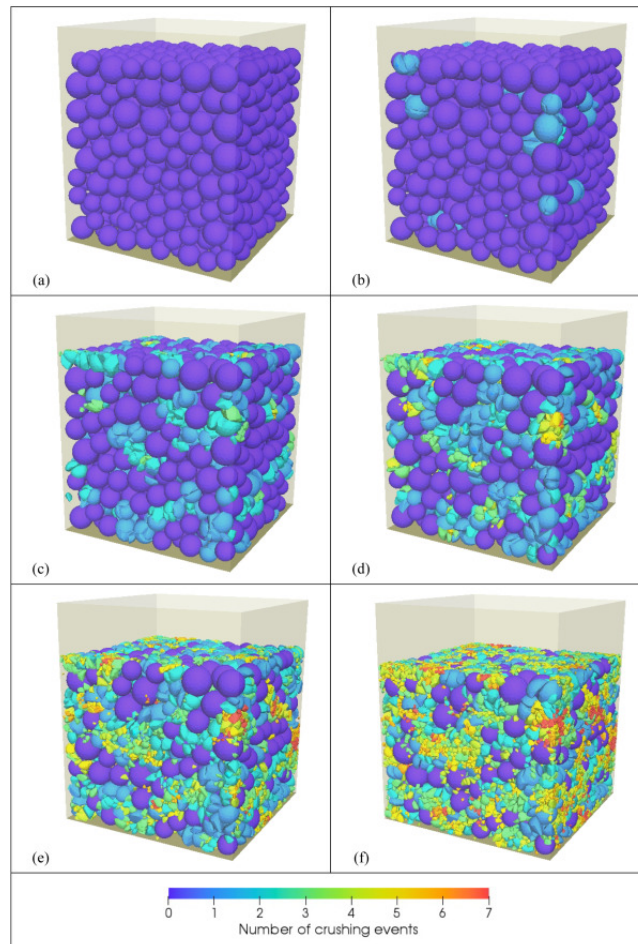\end{aligned}
\tag{2.16}
$$

Figure 2.5: Simulation of crushing particles using combined peridynamics and Bullet at various vertical pressures: (a) initial condition; (b) 5 MPa; (c) 10 MPa; (d) 15 MPa; (e) 20 MPa; (f) 30 MPa (Zhu and Zhao, 2019).

2.3 Comparison of various numerical modelling techniques

The reviewed numerical modelling techniques are to be compared as a conclusion for this section and the motivations to select the physics engine Box2D used in this study will be given. The dominant variance of different numerical modelling techniques is the contact model. As discussed previously, the distinct element method uses the penalty method in its contact model, in which small inter-particle overlap is allowed and minimised by exerting normal forces to both the particles in contact of which magnitudes are equal and proportional to the overlap depth applied to change the accelerations and velocities of the particles, hence the contact model is also an acceleration-based method. The contact model in molecular dynamics is based on the conservation of momentum and energy, however, not only repulsive contact forces exist, but also attractive forces are produced in molecular dynamics and different from the distinct element method, inter-particle overlap is not allowed. Both the contact dynamics and physics engines adopt the constraint-based method as their contact models. This type contact model does not allow any inter-penetration during a collision event and this is achieved by applying impulses on contacting bodies, directly changing the relative particle velocities rather than

accelerations by giving contact forces, hence it is a velocity-based contact model. Although the calculation in a single time step in the constraint-based method is more complex than that in the acceleration-based method, less time steps are required to reach stability, giving a significant potential to speed up the calculation process (Baraff, 1989). The constraint-based method obeys the Signorini condition, therefore attractive force does not exist in contact dynamics and physics engines.

Another main difference lies in the time integration scheme. Most DEMs prefer the explicit integration method due to its simplicity in implementation, such as the distinct element method and molecular dynamics. One of the drawbacks of this scheme is that damping coefficients are required to guarantee numerical convergency. On the other hand, because the stiffness matrix must be reformulated once a contact is activated or deactivated and both the geometry and the contact model are non-linear, the time step size should be kept quite small (O'Sullivan, 2011). Contact dynamics adopts the implicit method, ensuring unconditional stability and hence no damping coefficient is necessary. Due to the non-smoothness of the dynamics system, the sub-particle scale or the contact elastic behaviour may be neglected. Therefore the time step size can be scaled up compared with that in the explicit method. However, the implicit time integration scheme is more difficult to implement because the stiffness matrix is determined at the end of each time step after being predicted at the start and refined iteratively and numerously during a time integral. The semi-implicit time integration scheme adopted in physics engines keeps the advantage of the explicit method that the implementation is not as difficult as the fully implicit method, and the advantage of the implicit method that the stability is much easier to obtain and no damping coefficient is required which causes complexities in computation. The same as the contact dynamics, the time step size in physics engines could be amplified by several orders of magnitude compared with that in the distinct element method. The time step size is one of the most influential parameters on accuracy and efficiency in modelling, and choosing a suitable time step size can enhance the modelling performance without compromising the accuracy. The molecular dynamics method adopts a variable time step scheme that the time step size keeps changing according to a potential collision event. The typical time step sizes normally used in different numerical techniques are listed in Table 2.1. The time step size in physics engine Box2D is larger than others by several orders of magnitude, hence offering significant potential possibility to accelerate the simulation process.

Table 2.1: Comparison of typical time step size in various numerical techniques.

Numerical techniques	Typical time step size[1]
Distinct element method	10^{-6} s (Otsubo et al., 2017)
Molecular dynamics	10^{-9} s (Sutmann, 2002)
Contact dynamics	10^{-4} s (Radjai and Richefeu, 2009)
Physics engine Box2D	$1/60$ s (Catto, 2013)

[1] Only an approximate order of magnitude and varying according to different environments.

In conclusion, the advantages of physics engine Box2D over the conventional DEMs are:

1. Semi-implicit time integration scheme is adopted in Box2D which is simpler to implement than the fully implicit method used in contact dynamics and difficult-to-be-tuned damping parameters unable to be physically measured are not necessary for computational convergency as required to be defined in conventional DEMs.

2. The time step size can be larger than that in other DEMs since the sub-particle scale or the contact elastic behaviour is ignored in Box2D, and far much less time steps are required to solve the contact model during simulation, both bringing huge potential to speed up the simulation.

2.4 Discontinuity layout optimisation (DLO)

Discontinuity layout optimisation (DLO) is a numerical limit analysis developed to calculate the maximum load that a solid or structure can carry prior to collapse. It overcomes the difficulties met in traditional finite element limit analysis, e.g. being sensitive to the mesh geometry particularly in the region of stress and displacement singularities (Smith and Gilbert, 2007; Gilbert et al., 2010). DLO is entirely formulated upon slip or yield lines interconnected by distributed nodes in the domain rather than upon elements, deriving upper bound mechanism solutions. The four stages of a DLO computation process are illustrated in Figure 2.6. A block is considered to be fixed along its left and bottom boundaries and surcharged on its top surface. A number of potential slip lines are inter-linked by the generated nodes and the final failure mechanisms are determined by optimisation facilitated by linear programming techniques.

The DLO solution aims to find the minimum energy dissipation caused by applied external loads and this can be formulated as equation (2.17), subject to conditions (2.18) to (2.21):

$$min \ \lambda \boldsymbol{f}_L^T \boldsymbol{d} = -\boldsymbol{f}_D^T \boldsymbol{d} + \boldsymbol{g}^T \boldsymbol{p} \tag{2.17}$$

subject to:

$$\boldsymbol{B}\boldsymbol{d} = \boldsymbol{0} \tag{2.18}$$

$$\boldsymbol{N}\boldsymbol{p} - \boldsymbol{d} = \boldsymbol{0} \tag{2.19}$$

$$\boldsymbol{f}_L^T \boldsymbol{d} = 1 \tag{2.20}$$

$$\boldsymbol{p} \geq \boldsymbol{0} \tag{2.21}$$

in which λ is the unknown load factor multiplied on the external applied live loads $\boldsymbol{f}_L$ causing collapse, d is the displacement at the discontinuities under loads, $\boldsymbol{f}_d$ is the dead loads (e.g. self-weight), $\boldsymbol{g}$ is the dissipation coefficients equal to $\boldsymbol{cl}$ where $\boldsymbol{c}$ is the soil cohesion and $\boldsymbol{l}$ is the area of the discontinuity failure plane, $\boldsymbol{p}$ is a vector containing the plastic multipliers representing positive combinations of discontinuity slip displacements, $\boldsymbol{B}$ and $\boldsymbol{N}$ are compatibility matrix and flow matrix respectively

(a) Initial block applied by surcharge.

(b) Discretisation using nodes.

(c) Potential discontinuities interconnected by nodes.

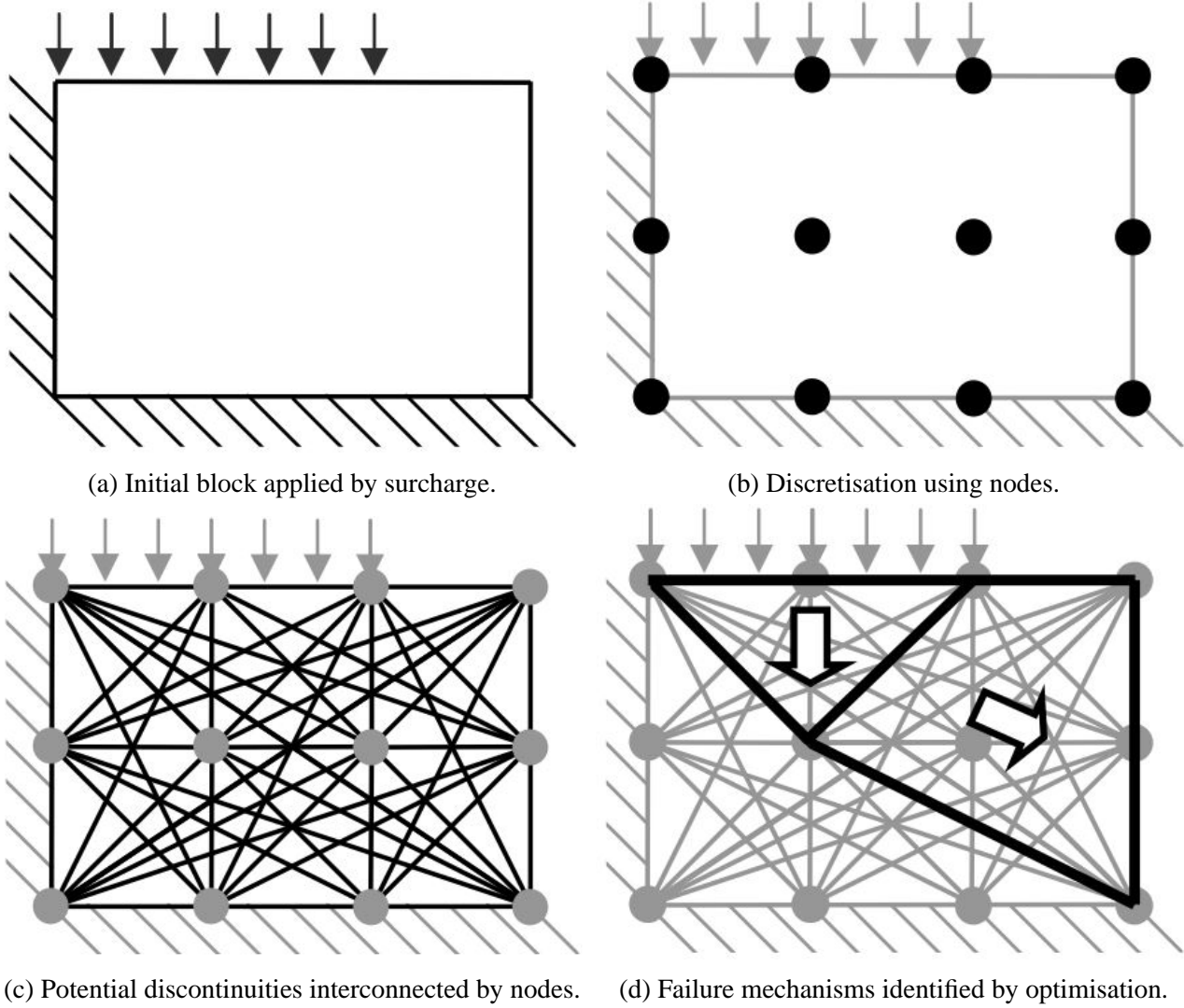(d) Failure mechanisms identified by optimisation.

Figure 2.6: DLO computation process (Gilbert et al., 2010).

and formulated as equations (2.22) and (2.23):

$$
\boldsymbol{B}_i \boldsymbol{d}_i =
\begin{bmatrix}
\cos \theta_i & -\sin \theta_i \\
\sin \theta_i & \cos \theta_i \\
-\cos \theta_i & \sin \theta_i \\
-\sin \theta_i & -\cos \theta_i
\end{bmatrix}
\begin{bmatrix}
s_i \\
n_i
\end{bmatrix}
\tag{2.22}
$$

$$
\boldsymbol{N}_i \boldsymbol{p}_i - \boldsymbol{d}_i =
\begin{bmatrix}
1 & -1 \\
\tan \phi_i & \tan \phi_i
\end{bmatrix}
\begin{bmatrix}
p_i^1 \\
p_i^2
\end{bmatrix}
-
\begin{bmatrix}
s_i \\
n_i
\end{bmatrix}
= 0
\tag{2.23}
$$

where θ_i is the inclined angle between discontinuity i and x-axis, s_i and n_i are the relative shear and normal displacements at discontinuity i correlated by $n_i = s_i \tan \phi_i$, and ϕ is the angle of friction. The Mohr-Coulomb failure envelope is applied to describe the local plastic flow constraint in equation (2.23).

After set-up of the compatibility matrix (2.18 and 2.22) and the plastic multiplier matrix (2.19 and 2.23), the linear programming problem can then be formulated by equation (2.17) and solved in terms of the discontinuity displacement vector d, the plastic multiplier p and the load factor λ, representing the minimum collapse live load, equal to the energy dissipation in the system.

Chapter 3

Box2D Physics Engine

3.1 Introduction of Box2D algorithm

Box2D is an open-source two-dimensional physics engine able to simulate rigid body contact collisions or interactions and has been widely applied in computer games. It adopts a time-stepping scheme in which the whole execution process is discretised into a number of sub-time steps and each sub-time step can be regarded as an independent problem. All rigid bodies are generated and oriented spatially with assigned velocities initially, along with the calculation of contact forces via the velocity-based contact model preventing any inter-penetration between rigid bodies by applying impulses or velocity jumps, and the free body motion is governed by the Newton–Euler equations. New velocities and positions will be updated at the end of each time step by the semi-implicit integration scheme. The contact model in Box2D is based on the constraint method (Kenny, 2004; Pytlos, 2015) and very similar to the analytical method proposed by (Baraff, 1989, 1997) in which inter-particle penetration is not allowed and this is achieved by impulses given on colliding rigid bodies, whereas the distinct element method uses the penalty method (Cundall and Strack, 1978) in an explicit manner in its contact model in which small overlap between rigid bodies is allowed and the contact force is proportional to their overlap depth. Therefore, the contact models of Box2D and DEM are built at the velocity level and the acceleration or force level respectively and should be considered as one of their main differences. Box2D is more akin to the contact dynamics model (Jean, 1999; Krabbenhoft, Huang, Da Silva and Lyamin, 2012; Krabbenhoft, Lyamin, Huang and da Silva, 2012; Meng et al., 2018; Radjai and Richefeu, 2009), although the latter adopts the fully implicit integration scheme.

3.2 Box 2D program structure

Box2D version 2.3.1 is being used in this study. Either graphical user interface (GUI) mode or non-GUI mode can be selected when running Box2D based on specific requirements. The code structure written in C++ is shown as below:

```cpp
#ifndef DEMTEST_H
#define DEMTEST_H

#define GUI

class TestContactListener : public b2ContactListener {

    public:

    void PostSolve (b2Contact* contact, const b2ContactImpulse* impulse) {
        //Solve contacts;
    }
};

#ifdef GUI
class DEMTest : public Test {

    public: DEMTest() {
        //Declare parameters system settings;
        //Model set-up;
    }
#endif

#ifndef GUI
int main () {
    //Declare parameters system settings;
    //Model set-up;
#endif

    //Run the test;
    #ifdef GUI
    #void Step(Settings* settings) {
        Test::Step(settings);
    #endif

    #ifndef GUI
    while (run_simulation) {
        world.Step(timeStepSize, velocityIterations, positionIterations);
    #endif

    }

    #ifdef GUI
    static Test* Create() {
        return new DEMTest;
    }
    #endif
};

#endif
```

Depending on whether we need to use GUI, we can choose two different environments to build the
model: either define a derived class ("DEMTest" in this example) inherited from the base class "Test"
to run the Testbed GUI in Box2D, or establish directly within the main() function without activating
GUI. Then we can declare a series of user-defined parameters which will be used in the simulation
and assign their values in the derived class or the main() function. The time-stepping simulation is
run within Step() function or while loop. To solve the contacts between two colliding particles, we
need to define a derived class ("TestContactListener" here) inherited from the "b2ContactListener"
beforehand and implement PostSolve() function within the class to gather collision results.

3.3 Contact model

Two randomly-shaped polygonal rigid bodies in relative motion are shown in Figure 3.1 and will be used to explain the contact model in Box2D. In this figure, p_1 and p_2 are assumed to be two potential contacting points belonging to each body, and will coincide in an upcoming collision event (the algorithm to detect potential contacts will be introduced in section 3.4). $\vec{n}$ is a normal unit vector pointing from body 2 to body 1 indicating the separating direction once collision occurs. It is considered that the normal unit vector $\vec{n}$ is along the direction of the relative displacement velocity at a vertex-vertex contact and the normal direction at an edge-edge contact. The relative position can be described by the separation distance d:

$$d = (\vec{\boldsymbol{p}}_1 - \vec{\boldsymbol{p}}_2) \cdot \vec{\boldsymbol{n}} \tag{3.1}$$

The two rigid bodies should be in contact with each other when $d \leq 0$. It is hard to justify whether the two bodies are separating, colliding or resting when $d = 0$, therefore, the relative velocity $v_{rel,n}$ should also be considered to calculate their subsequent movement tendency:

$$v_{rel,n} = (\dot{\vec{\boldsymbol{p}}}_1 - \dot{\vec{\boldsymbol{p}}}_2) \cdot \vec{\boldsymbol{n}} \tag{3.2}$$

In order to prevent any existing or potential colliding activity occurring, two non-penetration constraints along the normal and tangential directions and their corresponding derivatives can be formulated and constrained as follows:

$$C_n = (\vec{\boldsymbol{p}}_1 - \vec{\boldsymbol{p}}_2) \cdot \vec{\boldsymbol{n}} \geq 0 \tag{3.3}$$

$$C_t = (\vec{\boldsymbol{p}}_1 - \vec{\boldsymbol{p}}_2) \cdot \vec{\boldsymbol{t}} = 0 \tag{3.4}$$

$$\dot{C}_n = (\dot{\boldsymbol{p}}_1 - \dot{\boldsymbol{p}}_2) \cdot \vec{\boldsymbol{n}} \geq 0 \tag{3.5}$$

$$\dot{C}_t = (\dot{\boldsymbol{p}}_1 - \dot{\boldsymbol{p}}_2) \cdot \vec{\boldsymbol{t}} = 0 \tag{3.6}$$

$\dot{\boldsymbol{p}}$ is the contact point velocity and can be calculated by:

$$\dot{\boldsymbol{p}} = \boldsymbol{v} + \boldsymbol{\omega} \times (\vec{\boldsymbol{p}} - \vec{\boldsymbol{x}}) \tag{3.7}$$

where $\boldsymbol{v}$ and $\boldsymbol{\omega}$ are the translational velocity and the angular velocity of rigid bodies, $\vec{\boldsymbol{x}}$ is the body mass centre vector in the Cartesian coordination system. The contact conditions are summarised in Table 3.1.

Consider the case in which two rigid bodies are already in contact ($C_n \leq 0$) or potentially in penetration ($C_n = 0$ & $\dot{C}_n < 0$) in the contact normal direction. Let $\vec{\boldsymbol{J}}$ be the impulse applied on the rigid bodies in contact to avoid overlap and equal to $\vec{\boldsymbol{F}} \Delta t$, where $\vec{\boldsymbol{F}}$ is the contact force and Δt is the time step size set in Box2D whose default value is $1/60$ s. Pytlos (2015) did a systematic parametric study on the accuracy settings on the time step size Δt and the number of velocity iterations per time

Table 3.1: List of relative contact conditions

Relative position constraints	Relative velocity constraints	Contact conditions
$C_n > 0$		separated
$C_t \neq 0$		sliding
$C_n = 0$	$\begin{vmatrix} \dot{C}_n > 0 \\ \dot{C}_n < 0 \end{vmatrix}$	touching and separating touching and penetrating
$C_t = 0$	$\begin{vmatrix} \dot{C}_t \neq 0 \\ \dot{C}_t = 0 \end{vmatrix}$	sliding non-sliding
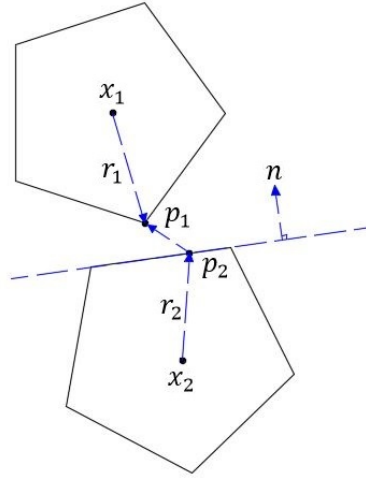
Figure 3.1: Two rigid bodies in relative motion.

step by comparing the collapse loads of a voussoir arch bridge under a point load between Box2D and LimitState:RING, and found that the number of velocity iteration per time step decreases as the time step size does when satisfying the accuracy requirement. He noted that while this statement only applies to the specific model, further analysis should be conducted for other applications. Pytlos et al. (2015) used the default time step size in the biaxial modelling and obtained accurate results. As the quasi-static state is maintained in the modelling for this study as will be shown in section 5.2, the number of velocity iterations per time step is still kept as the default value. The translational velocity change $\Delta \vec{v}$ and the angular velocity change $\Delta \vec{\omega}$ can be calculated by the given impulse:

$$\Delta \vec{v} = \frac{j_n \vec{n}}{m} \tag{3.8}$$

$$\Delta \vec{\omega} = \frac{\vec{r}^{\perp} \cdot j_n \vec{n}}{I} \tag{3.9}$$

where m is the rigid body mass, I is the second moment of inertia, $\vec{r}$ is the vector pointing from the centre of the body to the contact point ($\vec{p} - \vec{x}$) and the symbol $\perp$ is the perpendicular operator representing counterclockwise rotation by $90°$.

Assume the symbol "$-$" represents the pre-impulse condition, and "$+$" represents the post-impulse

condition, therefore,

$$\Delta \vec{v} = \vec{v}^+ - \vec{v}^- \tag{3.10}$$

$$\Delta \vec{\omega} = \vec{\omega}^+ - \vec{\omega}^- \tag{3.11}$$

By arranging equations (3.2), (3.7), (3.8), (3.9), (3.10) and (3.11), we can obtain the magnitude of the applied normal impulse:

$$j_n = \frac{v_{rel,n}^+ - v_{rel,n}^-}{\frac{1}{m_1} + \frac{1}{m_2} + \frac{(\vec{r}_1^\perp \cdot \vec{n})^2}{I_1} + \frac{(\vec{r}_2^\perp \cdot \vec{n})^2}{I_2}} \tag{3.12}$$

The coefficient of restitution e is defined as:

$$e = -\frac{v_{rel,n}^+}{v_{rel,n}^-} \tag{3.13}$$

Sandeep et al. (2021) studied the coefficient of restitution of fairly regular-shaped Leighton Buzzard sand (LBS) colliding with granite and metal base blocks by conducting impact experiments and found that the coefficient of restitution lies within 0.73 to 0.85 and 0.5 to 0.7 for LBS-granite block and LBS-brass/stainless steel block collisions respectively when the impact velocity is within $1.5\,\mathrm{m/s}$ to $2.5\,\mathrm{m/s}$. In conventional DEM, the coefficient of restitution is directly correlated with the damping coefficient which cannot be physically measured as the coefficient of restitution can. It was numerically found that the coefficient of restitution has little or even no influence on granular soil behaviours (e.g. Grima and Wypych (2011); Simons et al. (2015); Yan et al. (2015)). In Box2D the coefficient of restitution is stipulated as the larger value between two contacting rigid bodies: $e = \max(e_1, e_2)$, however this may not always be true in reality, and hence, the coefficient of restitution e is kept as 0 in this study which is reasonable in the quasi-static state. As a result, j_n can be transformed into a new form:

$$j_n = \frac{-(e+1)(\dot{\vec{p}}_1^- - \dot{\vec{p}}_2^-) \cdot \vec{n}}{\frac{1}{m_1} + \frac{1}{m_2} + \frac{(\vec{r}_1^\perp \cdot \vec{n})^2}{I_1} + \frac{(\vec{r}_2^\perp \cdot \vec{n})^2}{I_2}} \tag{3.14}$$

It is important to mention that Baraff (1989, 1997) solved the resting contact problem resorting to quadratic programming. The contact solver of Box2D simply generates an impulse that will zero the relative velocity in the normal collision direction in dealing with resting contacts, and this is easy to implement and also time-efficient.

Relative sliding between contacting rigid bodies is inhibited. Analogous to the formula of j_n, the magnitude of applied tangential impulse j_t is:

$$j_t = \frac{-(\dot{\vec{p}}_1^- - \dot{\vec{p}}_2^-) \cdot \vec{t}}{\frac{1}{m_1} + \frac{1}{m_2} + \frac{(\vec{r}_1^\perp \cdot \vec{t})^2}{I_1} + \frac{(\vec{r}_2^\perp \cdot \vec{t})^2}{I_2}} \tag{3.15}$$

The magnitude of j_t is restricted by application of Coulomb's friction law:

$$-\mu j_n \leq j_t \leq \mu j_n \tag{3.16}$$

where μ is the coefficient of friction stipulated equal to $\sqrt{\mu_1 \mu_2}$ in Box2D which is different from the minimum friction coefficient law used in the Hertz contact model in PFC codes. However, as this is not the main object in this study, the default interface friction coefficient setting in Box2D was inherited. The whole dynamic solving process for the contact model can be described by the pseudo-code given in Figure 3.2.

The free motion of a rigid body under external forces follows the Newton-Euler equation. Assume $\vec{\boldsymbol{F}}(t)$ and $\tau(t)$ to be external forces and torques applied on each rigid body at time step t, where the time step size is Δt. For one rigid body in contact with other n bodies, we have:

$$\vec{\boldsymbol{F}}(t) = \sum_{i=i}^{n} \vec{\boldsymbol{F}_i} \tag{3.17}$$

$$\tau(t) = \sum_{i=1}^{n} \vec{r}_i^{\perp} \cdot \vec{\boldsymbol{F}_i} \tag{3.18}$$

Based on the Newton's Second Law, the tentative translational and angular velocities at time $t + \Delta t$ are:

$$\vec{\boldsymbol{v}}^{-}(t + \Delta t) = \vec{\boldsymbol{v}}(t) + \Delta t \frac{\vec{\boldsymbol{F}}(t)}{m} \tag{3.19}$$

$$\omega^{-}(t + \Delta t) = \omega(t) + \Delta t \frac{\tau(t)}{I} \tag{3.20}$$

When the non-penetration criterion is broken, a normal impulse must be exerted on the rigid bodies, thus the post non-penetration velocities are:

$$\vec{\boldsymbol{v}}^{+}(t + \Delta t) = \vec{\boldsymbol{v}}^{-}(t + \Delta t) + \frac{j_n \vec{\boldsymbol{n}}}{m} \tag{3.21}$$

$$\omega^{+}(t + \Delta t) = \omega^{-}(t + \Delta t) + \frac{\vec{r}^{\perp} \cdot j_n \vec{\boldsymbol{n}}}{I} \tag{3.22}$$

If the non-sliding criterion is not satisfied, the tangent impulse will be applied to the bodies and the post non-sliding velocities are:

$$\vec{\boldsymbol{v}}^{++}(t + \Delta t) = \vec{\boldsymbol{v}}^{+}(t + \Delta t) + \frac{j_t \vec{\boldsymbol{t}}}{m} \tag{3.23}$$

$$\omega^{++}(t + \Delta t) = \omega^{+}(t + \Delta t) + \frac{\vec{r}^{\perp} \cdot j_t \vec{\boldsymbol{t}}}{I} \tag{3.24}$$

The impulses are applied on the contacting rigid bodies iteratively until the iteration reaches a prescribed number or the impulses are small enough. After their velocities are updated, the new

Algorithm for Box2D contact model
___
if $C_n > 0$
   separated contact;
   do nothing;
else if $C_n < 0$
      the rigid bodies are in penetration;
      if $\dot{C}_n \leq 0$
       collision continues;
       compute an normal impulse j_n to instantly change their relative normal velocity;
      else if $\dot{C}_n > 0$
         separating contact;
         do nothing;
      end
      if $\dot{C}_t \neq 0$
       compute an impulse j_t to zero their relative tangential velocity;
      else if $\dot{C}_t = 0$
         they will not slide along the tangential direction;
         do nothing;
      end
else if $C_n = 0$
      the rigid bodies are in contact;
      if $\dot{C}_n > 0$
       separating contact;
       do nothing;
      else if $\dot{C}_n = 0$
         resting contact;
         do nothing;
         if $\dot{C}_t \neq 0$
          compute an impulse j_t to zero their relative tangential velocity;
         else if $\dot{C}_t = 0$
            they will not slide in the tangential direction;
            do nothing;
         end
      else if $\dot{C}_n < 0$
         colliding bodies;
         compute an impulse j_n to instantly change their relative normal velocity;
         if $\dot{C}_t \neq 0$
          compute an impulse j_t to zero their relative tangential velocity;
         else if $\dot{C}_t = 0$
            they will not slide in the tangential direction;
            do nothing;
         end
      end
end
___

Figure 3.2: Pseudo-code for solving contact models in Box2D

positions $\vec{x}$ and rotations Ω can also be updated:

$$\vec{x}(t + \Delta t) = \vec{x}(t) + \Delta t \vec{v}^{++}(t + \Delta t) \tag{3.25}$$

$$\Omega(t + \Delta t) = \Omega(t) + \Delta t \omega^{++}(t + \Delta t) \tag{3.26}$$

The iteration process will terminate until the three conditions are satisfied:

- Fixed number of iterations is reached, and both position iteration number and velocity iteration number control the iteration limit.

- Corrective impulses become small enough.

- Velocity errors become small enough.

In Box2D, a relatively small magnitude of bias impulse is added to the normal impulse to mitigate the "bounce" or "jitter" effects which are common in velocity based constraints. In each iteration, a small penetration δ_{slop} between rigid bodies is allowed (Catto et al., 2006) and the bias velocity is given as:

$$v_{bias} = \frac{\beta}{\Delta t} \max\left(0, \delta - \delta_{slop}\right) \tag{3.27}$$

in which β is a bias factor approximately 0.1 to 0.3 and δ is the inter-particle overlap. Then, the normal impulse becomes:

$$j_n = \frac{-(e+1)(\dot{\vec{p}}_1^- - \dot{\vec{p}}_2^-) \cdot \vec{n} + v_{bias}}{\frac{1}{m_1} + \frac{1}{m_2} + \frac{(\vec{r}_1^\perp \cdot \vec{n})^2}{I_1} + \frac{(\vec{r}_2^\perp \cdot \vec{n})^2}{I_2}} \tag{3.28}$$

3.4 Contact detection algorithm

The distance computation algorithm in Box2D is based on the Gilbert–Johnson–Keerthi distance algorithm (Gilbert et al., 1988) able to determine the minimum distance between two convex objects. An online source about this algorithm as implemented in Box2D was given by Catto (2010). The contact detection is achieved by measuring the distance between two approaching convex polygons, and this can be simplified into the case of measuring the distance between a polygon vertex point and its neighbouring polygon, and simplified even further to considering a point and a triangular polygon. The simplest point-edge case illustrated in Figure 3.3 will be analysed firstly in which a point Q is projected onto a line segment AB at point G. Barycentric coordinates can be used to represent the coordinate of point G as a weight sum of the coordinates of points A and B:

$$G(u, v) = uA + vB$$

, where u and v are the barycentric coordinates and their sum is always equal to one since they are fractional lengths of the line segment AB. There are three different relative positions between point G and the line segment AB, and this can be represented by the sign combinations of the barycentric
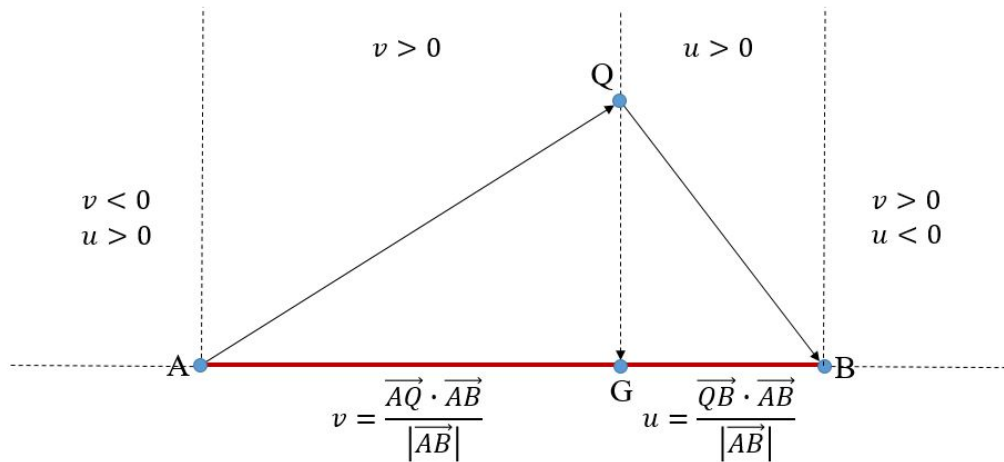
Figure 3.3: Barycentric coordinates of a point passing a line segment.

coordinates. Analogous to the barycentric coordinates of a point with a line segment, they can be developed for areas as shown in Figure 3.4. In this case, the barycentric coordinates substitute the
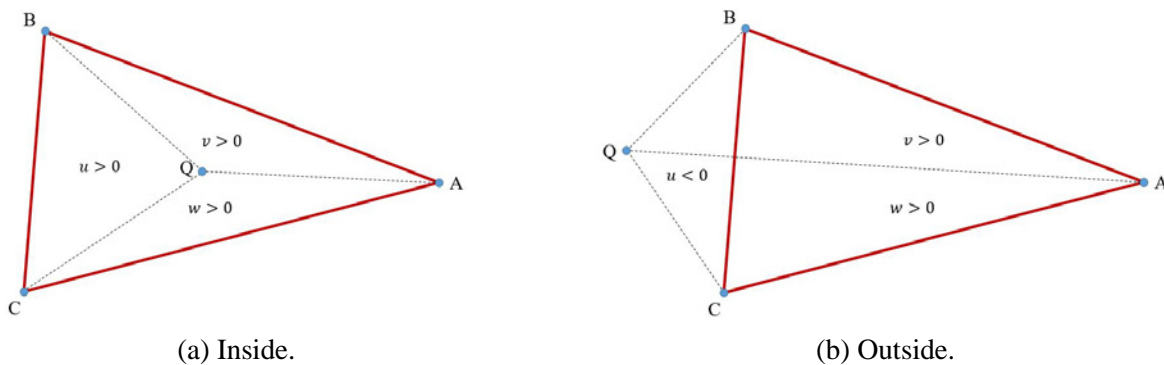

(a) Inside.   (b) Outside.

Figure 3.4: Barycentric coordinates of a point with a triangle.

fractional areas of the partial triangles:

$$Q(u, v, w) = uA + vB + wC$$

The polygon vertices are defined following counterclockwise direction, therefore the barycentric coordinate sign will be different between the inside case (Figure 3.4a) and the outside case (Figure 3.4b).

Using different barycentric coordinate sign combinations, the relative positions between a point and a triangle can be illustrated as Figure 3.5. The problem to calculate the distance between a point and a triangle or find the closest point on the triangle can be converted to the problem to carve the plane into Voronoi regions. It is apparent that the point and its closest point on the triangle should lie into the same Voronoi region, hence the problem can then be simplified to calculate the distance between a point and a line segment. The vertex regions are firstly tested, followed by the edge regions, and if none of them are satisfied based on the barycentric coordinate sign combinations, the point should lie within the interior of the triangle.
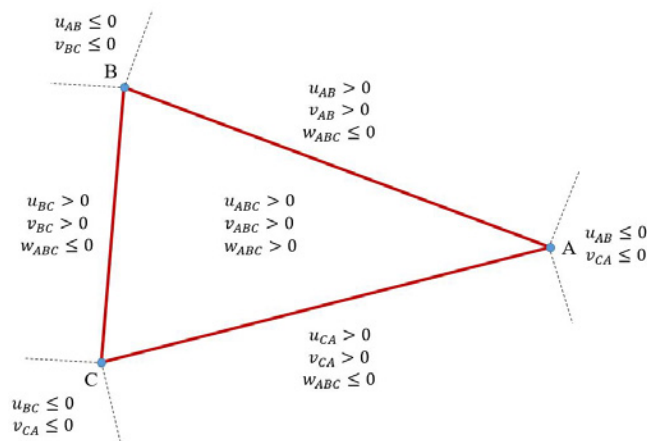
Figure 3.5: Voronoi regions.

Having been able to solve the minimum distance between a point and a triangle, the distance between a point and a convex polygon can be worked out by the Gilbert–Johnson–Keerthi (GJK) distance algorithm following the process illustrated in Figure 3.6. To find the closest point of Q on

| (a) Step 1. | (b) Step 2. | (c) Step 3. |
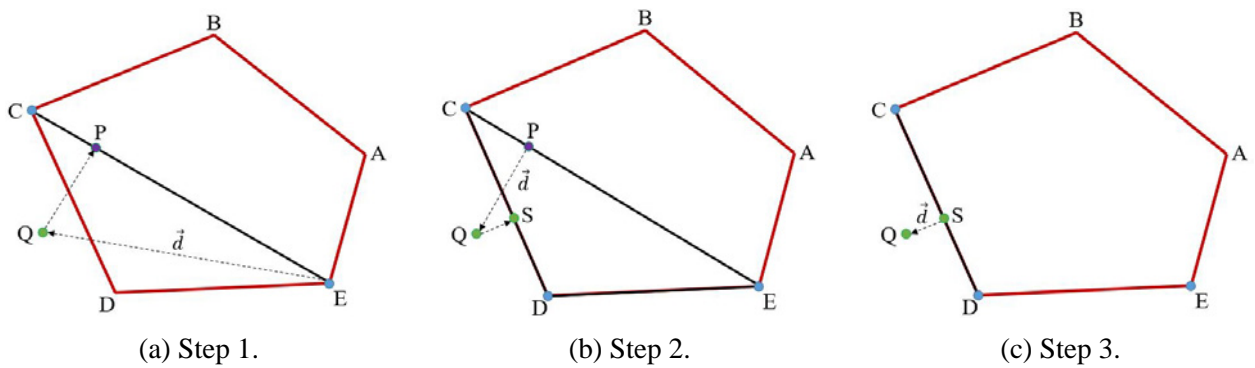
Figure 3.6: Searching the closest point on a convex polygon.

the convex polygon, an arbitrary vertex in this case E is selected as a support point and a vector $\vec{d}$ pointing from E to Q can be found as shown in Figure 3.6a, then the furthest vertex point C on the polygon along the direction $\vec{d}$ is determined as another support point. The closest point on the line segment EC can be found and denoted as P. The vector $\vec{d}$ can be updated as pointing from P to Q and a new support point D is added to the group which is furthest vertex on the polygon along the updated direction $\vec{d}$, resulting in creating a triangle ECD as shown in Figure 3.6b. The closest point S on the created triangle can then be determined as the approach explained aforementioned. To keep the support point number not more than 3, the support point E not related to the newest closest point S will be excluded from the support point group, hence the process will restart from the case of Q and the line segment CD as shown in Figure 3.6c. Because no more new support point can be added, the process will terminate and the closest point on the convex polygon from the point Q is S.

Based on the GJK distance approach, the relative position between two neighbor polygonal-shaped particles can be solved iteratively by Minkowski difference (or geometry difference). It is defined and computed by the combination of two polygons X and Y via $Y_i - X_i$ in which X_i and

Y_i are the points belong to polygons X and Y. One of the properties of Minkowski difference is the distance between the origin and the support point along direction $\vec{d}$ on the combined polygon Z is equal to the difference between the distance between the origin and the support point on polygon Y along direction $\vec{d}$ and that between the origin and the support point on polygon X along the opposite direction $-\vec{d}$. Therefore, there is no need to build the entire combined polygon Z explicitly to calculate the support point on the combined polygon Z. Another property of Minkowski difference is the distance between the two polygons is equal to the distance between the origin and the combined polygon Z created by Minkowski difference. Using this approach, the computational cost can be substantially reduced especially for convex polygons of large numbers of vertices.

Sometimes it may happen to see that two objects go through each other without collision detected. This may be caused by collision filtering options set to control the allowed collision targets or collision "SetEnabled(false)" option in "PreSolve" function in b2ContactListener class in Box2D. Another possible reason for unobserved collision is due to the "tunneling" effect, which can be avoided by computing the first time of impact (TOI) with a sub-stepping solver to move the objects to TOI in order to solve the collision event, and the contact skin which is used to keep polygonal rigid bodies slightly separated with small margins in between.

3.5 Contact skin

It is important to declare that touching and contacting are two different terms in Box2D and can be checked by calling "IsTouching" function defined in "b2Contact" class and "BeginContact" function in "b2ContactListener" class, respectively. The function "IsTouching" returns a boolean value telling if the two rigid bodies are in collision, while the "b2Contact" checks if their axis-aligned bounding boxes (AABBs) start to collide. Figure 3.7a illustrates the contacting case when the AABBs of two polygons intersect and this will be added to the contact list although this does not mean they are actually in collision. It is computationally efficient when adopting this approach to exclude the computation for not contacting particles. The collision event happens at the time step when the two polygons start to touch as Figure 3.7b shows.

(a) Contacting.   (b) Colliding.
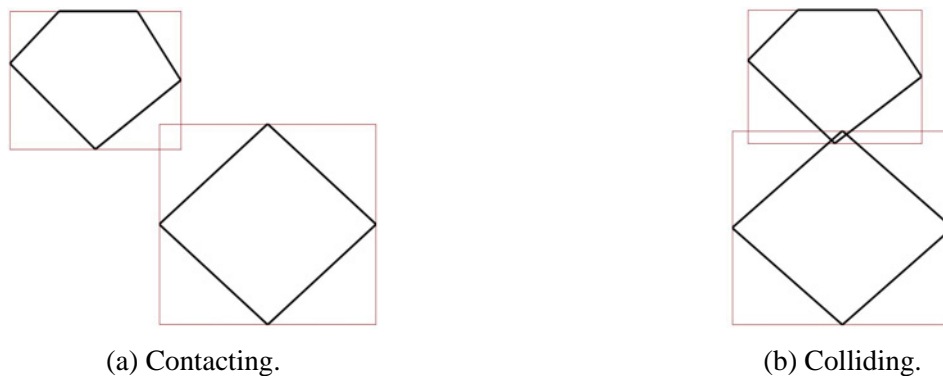
Figure 3.7: Contacting and colliding events.

It can happen that collision is not detected when a polygonal rigid body is rather small and the prescribed time step size is not small enough. In this case, two rigid bodies will pass each other in a process called "tunneling". To prevent this phenomenon happening, a skin surrounding each generated polygonal body is created, as a result, the penetration depth is the skin thickness minus the true distance. When the skin margins of two contact polygonal bodies touch, they start to collide as the case shown in Figure 3.8. The default value of the contact skin is set as $0.1\,\mathrm{m}$ in Box2D. Pytlos (2015) conducted a simple toppling failure test of a block on an incline to test the contact skin effects on the results and reported that the contact skin effects could be neglected if its value is not larger than $0.001\,\mathrm{m}$ in a simulation involving particles larger than $0.1\,\mathrm{m}$.
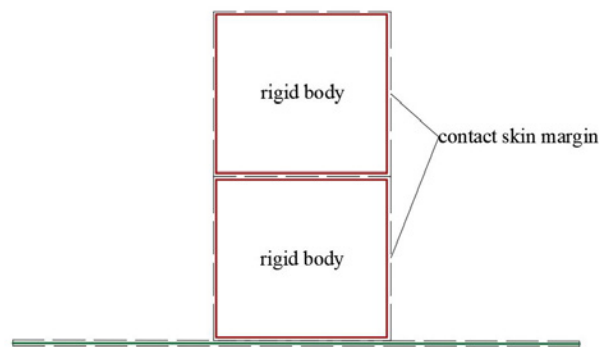
Figure 3.8: Contact skin.

In some special circumstances analysing granular soil deposit packing effects on its mechanical behaviours, the contact skin should be modelled coupled with the created polygonal grains as in Figure 3.9. This void-free packing was created using Voronoi tessellation. If the polygon skin space is not considered, inter-particle contact forces will propagate therefore breaking the original structure and also causing disturbances. Therefore, when considering the packing effects or modelling polygonal grains using the constructive approaches in situ rather than using the dynamic approaches, it would be better to involve the contact skin in modelling.

3.6   Summary

In this chapter, the physics engine Box2D contact model and its contact detection algorithm are introduced. The Box2D contact model is similar to that applied in contact dynamics, in which the unilateral condition is satisfied and the solver is based on the velocity level. The greatest difference with the distinct element method is that inter-particle overlap is not allowed in Box2D. The time integration scheme used in Box2D is the semi-implicit method, adopting the advantage of the explicit method (conventional distinct element method and molecular dynamics) which is easier to handle compared with the fully-implicit method, also the advantage of the fully-implicit method (contact dynamics) for greater stability hence no damping ratio definition is required which can bring more difficulties in simulation. The time step size in Box2D can be larger than that in other conventional
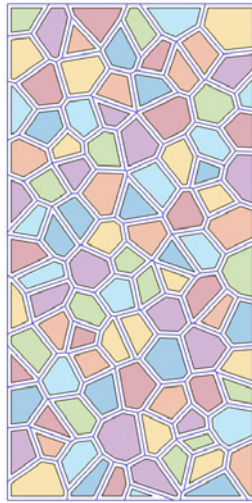
Figure 3.9: Void-free packing created considering contact skin effects.

DEMs by several orders of magnitude because of the non-smoothness property since the sub-particle scale or inter-particle elastic behaviour is ignored. As a result, there is a huge potential in accelerating the simulation in granular soil modelling compared with other methods. The contact skin is used to avoid tunneling phenomenon happening in the contact detection. For the case of using the constructive approaches to generate in-situ packings constituted with polygonal grains, inter-particle contact forces will develop and disturbances will propagate within the whole deposit if contact skins are not considered, therefore, polygonal grains should be modelled taken contact skins into account to avoid local rearrangements occurring.

Chapter 4

Random Convex Polygonal Particle Generation Technique

4.1 Voronoi Tessellation

A Voronoi diagram, firstly proposed by Russian mathematician Georgy Voronoy (Voronoi, 1908), is the partitioning of a plane domain into a set of regions within each of which the interior points are closer to its initially generated and distributed random seed point than others. This process is dual to Delaunay triangulation, also named Voronoi tessellation or Dirichlet tessellation. In geotechnics, it is often used to simulate polygonal convex granular soil grains due to its high computational efficiency and randomness in particle shape (Galindo-Torres et al., 2010; Galindo-Torres and Pedroso, 2010; Mollon and Zhao, 2012; Peña et al., 2007). The methods in polygonal particle modelling using Voronoi tessellation adopted in this study generally refer to the work published by Mollon and Zhao (2012) but have been modified to be applicable to physics engine Box2D and LimitState:GEO. The whole process of Voronoi tessellation is divided into four steps when implemented in MATLAB.

Step 1) Firstly, a number of seed points are specified and distributed randomly inside a prescribed domain, then the seeds closest to the boundary of the domain are selected as shown in Figure 4.1a. A built-in function in MATLAB could be called to create a Voronoi diagram based on these seeds however the outmost regions are unconfined by boundaries.

Step 2) In order to build boundaries for the outmost regions, a new domain boundary is constructed which is slightly larger than the original one to prevent any initial seed point lying on it, causing the corresponding subdomain to be infinitely small. A group of new seed points symmetrical to the red points next to the boundaries in Step 1) about each boundary edge are added in Figure 4.1b. A new Voronoi diagram is obtained where the outmost subdomains are confined with boundaries.

Step 3) The unconfined Voronoi cells exceeding the domain boundary are weeded (Figure 4.1c) and the Voronoi cells next to the boundaries (denoted by red points in Figure 4.1a) are confined.

It is worth mentioning that Figure 4.1a is created from Voronoi cells for which the outermost cells have no boundaries, while for Figure 4.1c, all cells are constrained by boundaries, however, the MATLAB function used to create Voronoi tessellation cannot help to build the boundaries for the outermost cells and their vertex coordinates are represented by infinity.

Step 4) This step is optional. In order to model voids in the deposit, the Voronoi cells are modified by chamfering process as Figure 4.1d shows. In most cases, the created Voronoi-based particles in MATLAB will be imported one by one into Box2D and then deposited under gravitational environment, therefore this step is only for the case generating packings in situ for example in LimitState: GEO.
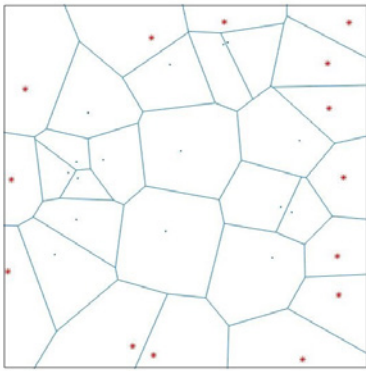
(a) A Voronoi diagram without boundaries.
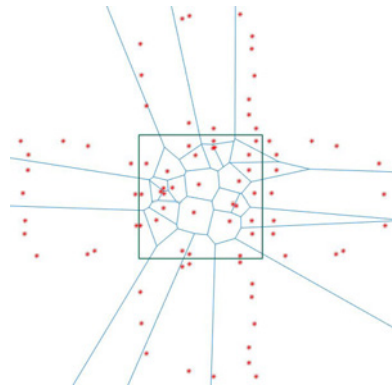
(b) Complimentary seed points.
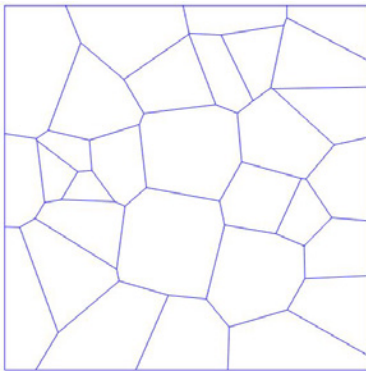
(c) A newly-built Voronoi diagram with boundaries.
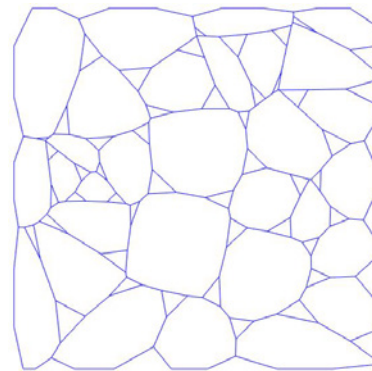
(d) Created Voronoi-based particles.

Figure 4.1: Using Voronoi tessellation to generate random polygonal particles.

The distribution of the initial seed points influences greatly on the created Voronoi cells, such as their size, circularity and orientation distributions, which further influence the mechanical properties of granular packings. The uniform and Halton sequence distribution methods used to allocate the initial seeds and their created Voronoi tessellations are shown in Figure 4.2a and Figure 4.2b respectively. The Halton sequence is constructed by a deterministic approach using coprime numbers as bases (detailed description please refer to e.g. Kocis and Whiten (1997)), applied to generate a number of points of low discrepancy in a space. It is apparent to distinguish that the uniform method makes the final Voronoi cells distributed over a wider range of particle sizes than the Halton sequence

method, while grains are more uniform in size distribution if their seeds are allocated by the Halton sequence algorithm. Another way to generate more uniformly-sized cells is to divide the whole do-

(a) Uniform distribution.   (b) Halton sequence distribution.
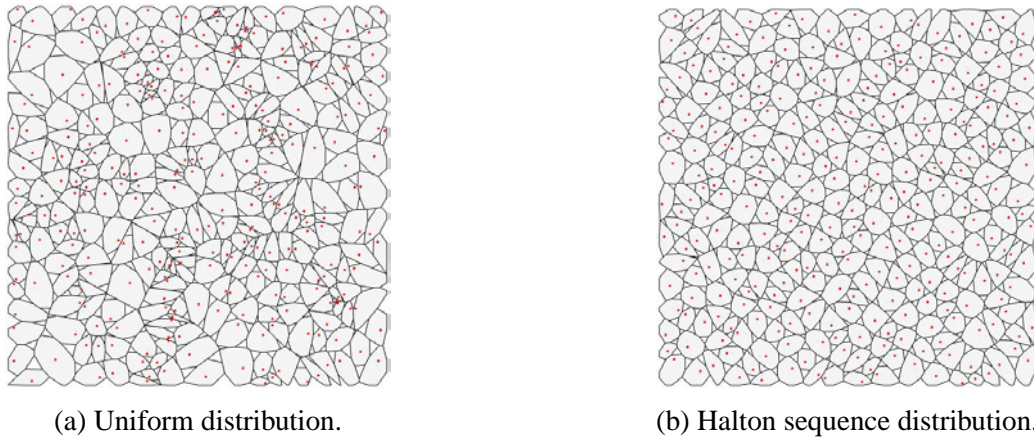
Figure 4.2: Two different types of seeds distribution.

main by a certain number of grids at the beginning and position seeds inside each block as Figure 4.3a displays, however, the contacts are primarily aligned along the horizontal and vertical directions, hence particle interlocking effects are inhibited compared with packings without preferable orientations. If the domain boundary is rotated by an angle, for example $60°$, then a corresponding Voronoi diagram is created and afterwards the particles are rotated back to their original place, the contact directions will be mainly kept along $30°$ and $60°$ to the horizontal direction, as shown in Figure 4.3b. It is therefore possible to choose different packings depending on certain requirements for various analyses .

(a) No orientation.   (b) Oriented at $30°$ and $60°$.
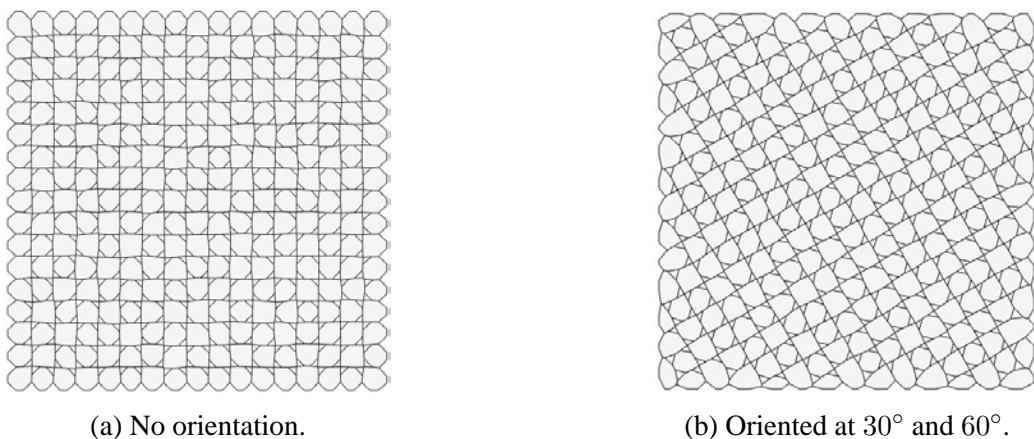
Figure 4.3: Voronoi-based packings controlled by grids.

4.2 Inverse Monte-Carlo (IMC) method

As mentioned in section 4.1, various seed generation algorithms can be adopted to alter Voronoi tessellation in size and orientation distributions, however, this method can not strictly guarantee math-

ematical evaluations and take other particle shape characteristics into account. The inverse monte-Carlo (IMC) method put forward by Mollon and Zhao (2012) is a potent way to solve this problem, by means of driving the Voronoi cell shape distribution approaching to a target one through a stochastic iterative process as described below.

Step 1) Generate initial seed points randomly and then create Voronoi tessellation based on these generators (Figure 4.4a). Then calculate the discrepancy between the actual distribution and the target distribution using the error function:

$$E = \sqrt{\sum_{i=1}^{n}(h_i - H_i)^2} \tag{4.1}$$

where E is the discrepancy, and h and H are the actual and target Voronoi cell shape descriptor values respectively. Figure 4.4b depicts the discrepancy rank from high to low labelled by numbers above the columns from the desired size distribution denoted by the red curve.
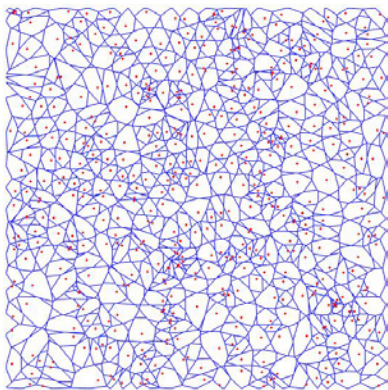
(a) Generate original Voronoi tessellation. (b) Voronoi cell size distribution and the target.
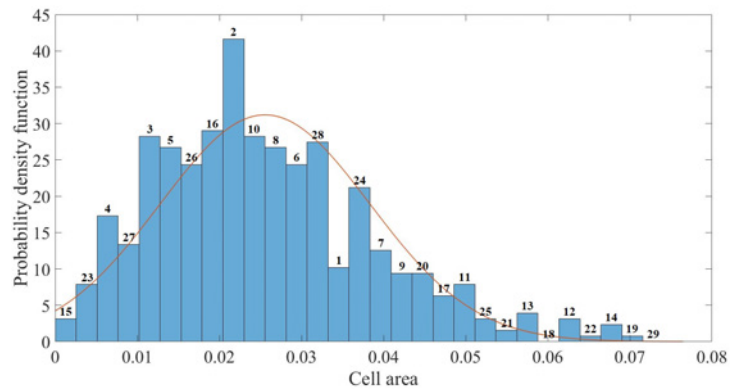
Figure 4.4: Step 1 in IMC.

Step 2) If the discrepancy E is lower than the prescribed tolerance value, it indicates the current distribution satisfies the requirement, if not, one of the seeds is translated to a series of new positions and the updated discrepancy is calculated until it drops. For computational efficiency, the ready-for-being-translated seeds should be selected according to their corresponding group ranks. The maximum iteration number in this procedure should be specified beforehand, and if the iteration step exceeds the maximum iteration number, the seed will be stopped moving and a next one will be chosen to continue iteration.

After each iteration, it is necessary to recalculate the actual distribution of the Voronoi tessellation. It is highly time-consuming to generate and calculate the Voronoi tessellation iteratively especially when a large group of seeds are involved. In order to enhance the computational efficiency, the seed movement is constrained by its surrounding cells within the first layer (inside the green zone in Figure 4.5a) and this means it is only necessary to recreate a new Voronoi tessellation within the three adjacent layers (Figure 4.5b and Figure 4.5c)

because the Voronoi cells will not be influenced outside the third layer (colored in red). In the example shown in Figure 4.5, the selected seed in red is translated to a new position in black. Finally, the newly generated Voronoi cells can be combined with the previous intact ones (Figure 4.5d) and their distributions and corresponding discrepancies are calculated.
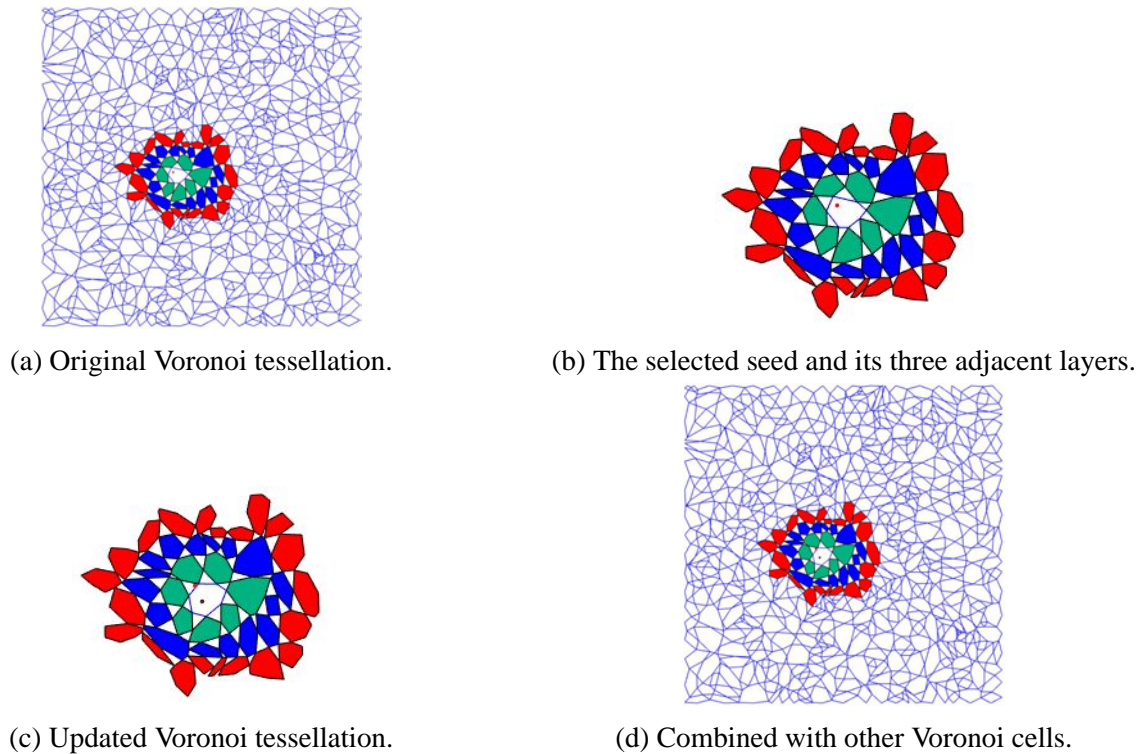

(a) Original Voronoi tessellation.

(b) The selected seed and its three adjacent layers.

(c) Updated Voronoi tessellation.

(d) Combined with other Voronoi cells.

Figure 4.5: Step 2 in IMC.

Step 3) The iteration will not terminate until the overall discrepancy is reduced below a certain specified threshold. If several different particle shape properties need to be controlled simultaneously, their individual discrepancies from the target values can be calculated and summed by equation (4.1). The process will terminate when the discrepancy summation decreases below the prescribed threshold. Another approach is to calculate the discrepancies respectively during each iteration and terminate when they are all reduced below the target discrepancy thresholds.

Two examples of IMC application in targeting particle size and circularity distributions are shown in Figure 4.6 and Figure 4.7. Circularity is defined as the ratio of grain inscribed circle radius to its circumscribed circle radius (Blott and Pye, 2008). The red curves in the plots represent the target distributions and the blue histograms are actual distributions.

4.3   Summary

This chapter gives a full introduction on the random convex polygonal particle generation technique. Voronoi tessellation is a fast and easy-to-implement constructive approach to generate random con-

(a) Initial Voronoi diagram colored by cell size.

(b) Target Voronoi diagram colored by cell size.

(c) Initial cell size distribution.

(d) Target cell size distribution.
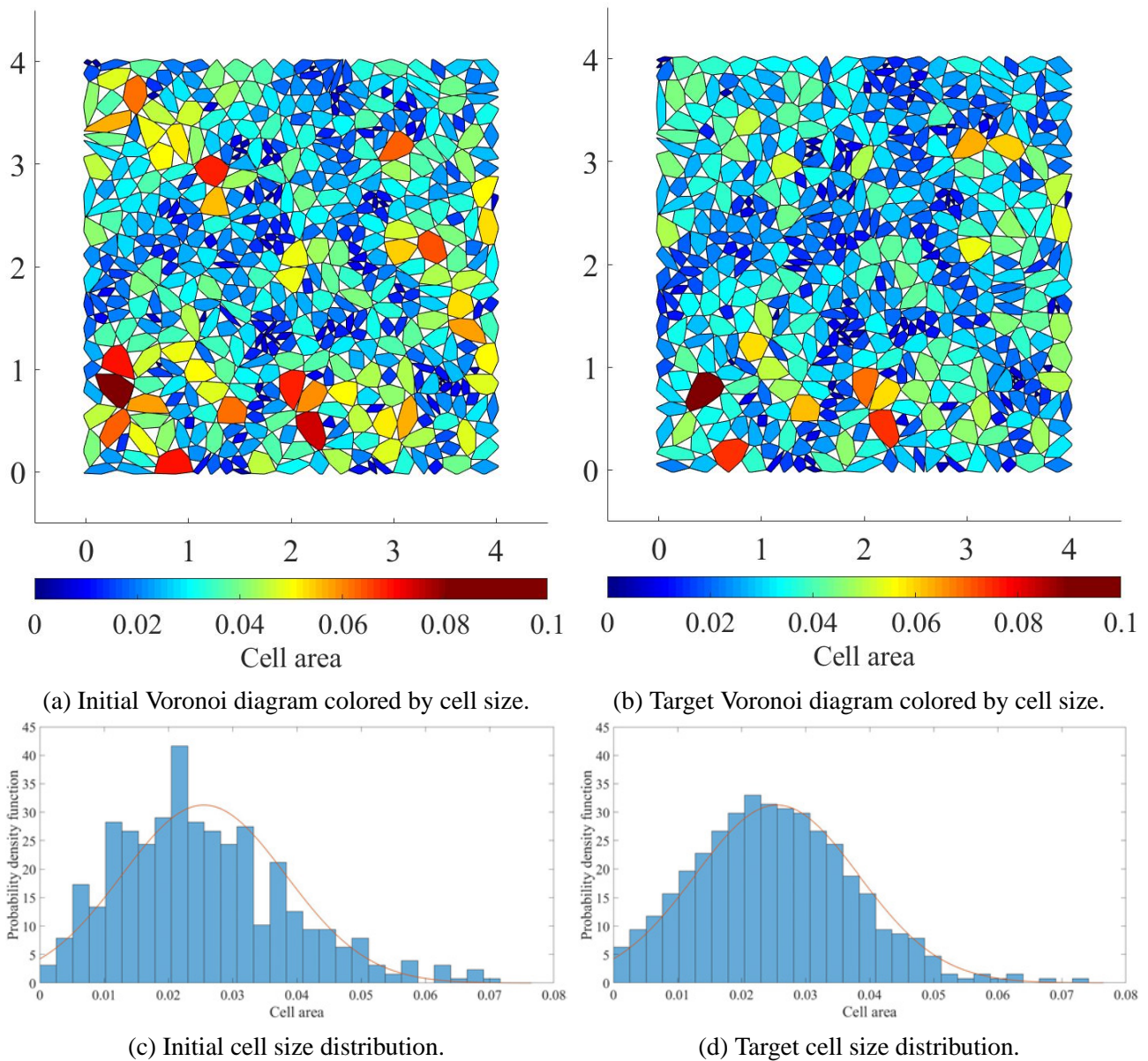
Figure 4.6: IMC method to modify the cell area distribution.

vex polygonal particles. It can be applied in Box2D simulation to replace commonly used spherical particles. Another advantage of this constructive particle generation method is that it can be directly applied to build in-situ packings without necessity to be within a dynamic environment (e.g. build packings in LimitState:GEO). The inverse Monte-Carlo method can be applied to target the distributions of specific particle shape characteristics (e.g. size and circularity), however, computational efficiency and convergency factors deserve to be analysed and studied in future. This approach is also applicable in 3D modelling.

(a) Initial Voronoi diagram colored by cell circularity.

(b) Desired Voronoi diagram colored by cell circularity.

(c) Initial cell circularity distribution.

(d) Desired cell circularity distribution.
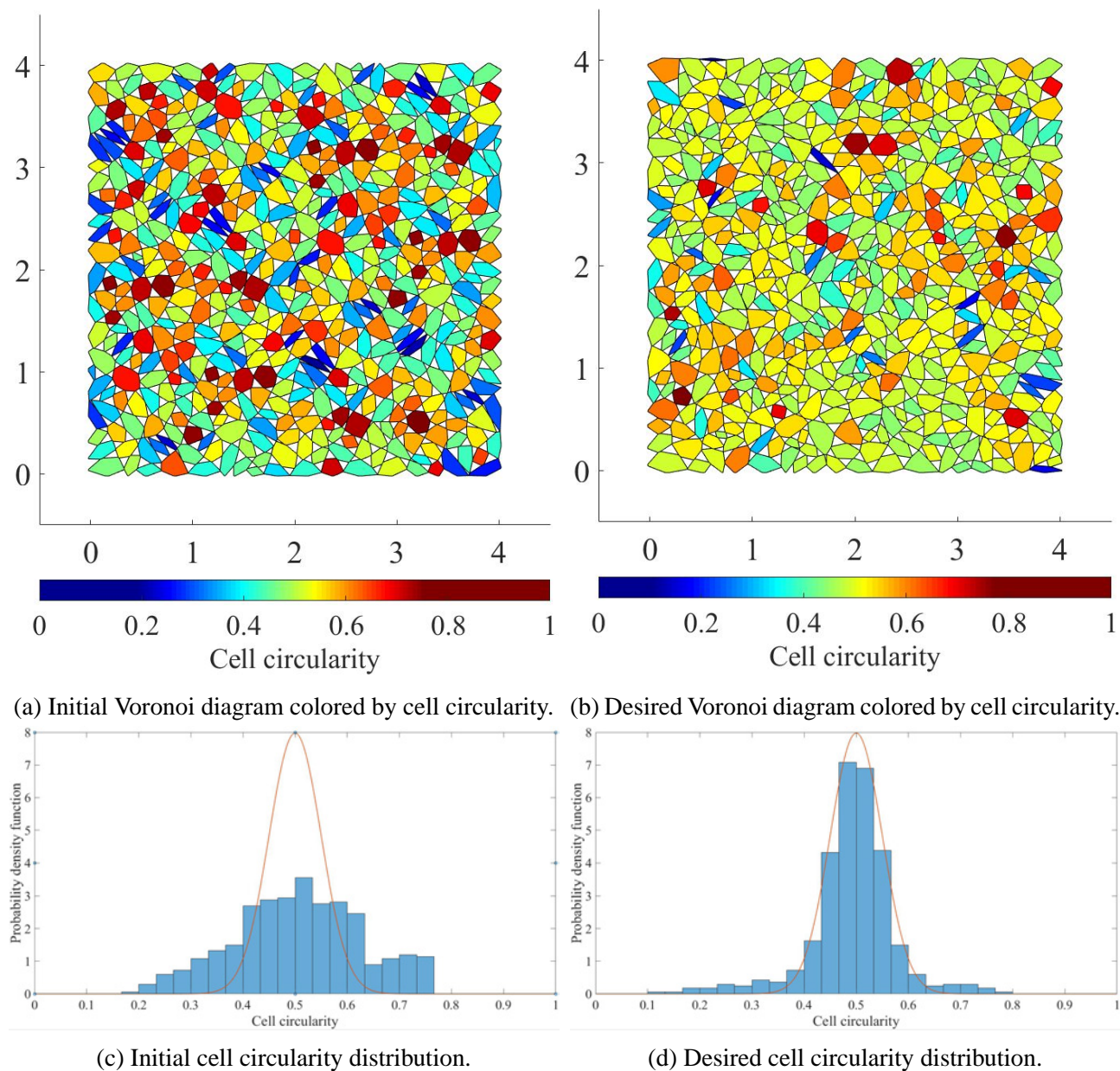
Figure 4.7: IMC method to modify the Voronoi cell circularity distribution.

Chapter 5

Effects of Particle Shape and Packing on Soil Properties

5.1 Review of previous works

Because of the limitation of computational power, spherical particles are appreciated in DEMs for simplicity and simulation speed, especially in engineering problems where a huge number of particles are required, such as excavations, strip footings and retaining walls. Spherical particles have always been considered to underestimate the shear strength of real granular soils due to weak interlocking effects and inter-particle frictions. Many researches have been conducted to compare spherical assemblies with other shapes, and some of these will be reviewed and summarised in this section.

Jensen et al. (2001) used the two-dimensional DEM approach to analyse particle shape effects on clustered and non-clustered granular soil mechanical properties systematically and reported that both angularity and roughness will increase the granular packing void ratio under the same compaction effort compared with round grains, however, the initial void ratio does not influence the critical state shear stress but merely peak shear strength. They also concluded that dense and clustered samples exhibit higher peak strengths, larger dilations and greater average rotations than loose and non-clustered samples due to inter-particle interlocking effects. Mirghasemi et al. (2002) studied particle shape effects by modelling equilateral and equal-sized polygonal particles of various numbers of edges to study both particle shape and packing effects on their behaviours in DEM and reported that angularity will increase void ratios, mean coordination numbers and shear strengths, and inhibit relative rotations, in addition, different packings will also behave diversely in mechanical properties. for example, assemblies that can perfectly fill a 2D space behave differently with others for which angularity increase will decrease void ratios after isotropic compaction. Wang et al. (2011) had similar findings with Mirghasemi et al. (2002) comparing circular, triangular and quadrilateral particles in 2D shear tests and 3D hopper flow DEM simulations. Matsushima and Konagai (2001) found that the particle surface roughness will enhance the grain column stability because of larger moment transmission at contacts, and directly increase the peak strength in 2D DEM models. Later, Matsushima (2005)

carried out additional 2D DEM simulations and observed the surface angularity increase can make
the shear strength (mobilised friction angle) higher because irregular particles tend to produce plural
contact points and thus increase the moment resistance. Santamarina and Cho (2004) believed that
particle angularity and roughness will add difficulty to particle rotation and slippage respectively and
also enhance the dilation in dense packings based on some experimental works. It was observed by
Cho et al. (2006) that particle shape irregularity will reduce small strain stiffnesses by shear wave
velocity tests but higher critical friction angles. Shin and Santamarina (2013) conducted laboratory
experiments using sand mixtures of round and angular grains to study particle angularity effects on
granular soil mechanical behaviours and proved that with the angular particle mass fraction increase,
the void ratio, the small strain stiffness modulus (contrary to the results obtained by Cho et al. (2006))
and the critical state friction angle will increase. Lu and McDowell (2007) used PFC3D modelling
sphere clumps compared with spherical particles in box tests and proved that average contact forces
among spherical clumps are less that those among spheres due to greater homogeneity in clumps
because of higher mean contact numbers, and relative rotations were found to be resisted in clumps
by interlocking in the loading-unloading simulation. Peña et al. (2007) studied anisotropy effects
on shear strength comparing elongated and isotropic samples by means of molecular dynamics and
observed wider shear bands and smaller accumulated rotations in elongated samples. It was stated by
Azéma et al. (2017) in their 3D contact dynamics model that the shear strength will increase as the
particle shape deviates from sphericity and the proportion of non-spherical particles increases. There
will be an approximately linear increase of the normalised shear strength (ratio of the deviatoric stress
over the mean stress) as particle elongation increases and it also increases with particle angularity to
a maximum degree and saturates to a constant value.

In this chapter, the particle shape and packing effects on granular soil behaviour will be studied
via biaxial test models based on physics engine Box2D. The aims of this study are:

1. Study the particle shape effects (e.g. circularity and particle size and shape variations) on their
   mechanical behaviours (e.g. coordination number, strain localisation and mobilised friction
   angle). Compare the observations with previous findings to demonstrate the simulation perfor-
   mance in physics engine Box2D is trustworthy, therefore providing more confidence for further
   studies.

2. Develop more techniques applied in Box2D in simulating particulate media systems, for ex-
   ample, graphical interpretation approaches (e.g. local volumetric strain and local void ratio
   plots during a simulation process by means of open-source language Asymptote to draw vector
   graphics).

3. Investigate the packing effects on soil behaviours by establishing perfect Voronoi-based pack-
   ings (without void) to compare with poorly packed (randomly dropped) packings in global
   response. This is able to provide useful information on whether there is benefit to be had by
   packing (larger) particles deliberately in practice (enhanced dry stone walling). In addition,
   this methodology builds a bridge between discrete element methods and continuum methods

because the perfect Voronoi packing can be regarded as a meshing approach for a continuum domain however adopting the discrete element method to simulate the dynamic response in strength. How initial void ratio and mean coordination number influence the peak strength will also be studied.

4. Through studying particle shape effects on granular soil behaviours, it is possible to establish a repository to relate soil mechanical properties with specific particle shapes, and this would help in determining soil strengths according to their particle shape characteristics in geotechnical design.

5.2   Biaxial test model set-up

Overview

The entire biaxial test simulation process is divided into three stages: particle and deposit generation (test set-up), axial and horizontal confining stress application and biaxial shearing stages. The main parameters in the simulation system are summarised in Table 5.1. The inter-particle friction coefficient was set to 0.4663 (the inter-particle friction angle to be $25°$), close to 0.5 as set by Peña (2008). The rolling resistance is not taken into account in the Box2D contact model. The constraint solver in Box2D comprises a velocity phase and a position phase, used to update rigid body velocities and positions respectively. In each time step, a number of iterations of constraint solves are required because any single constraint solved will influence other constraints. The contact skin thickness was set to be 0.001 m which is ten times smaller than the default value because as proved by Pytlos (2015) that contact skin thickness effects can be ignored when it is smaller than 0.001 m in a system involving rigid bodies whose circumscribed circle diameter is larger than 0.1 m. The time step size, the velocity iteration number and the position iteration number were set as defaults following the Box2D guidance.

Particle and deposit generation

One way to create a polygonal particle is randomly attaching its vertices along a circle of a prescribed size and controlling its aspect ratio to obtain either isotropic or elongated shape. Another way is using Voronoi tessellation to create more random polygonal particles. The biaxial container width was initially set as the product of the initial particle number along the biaxial container bottom boundary (or scaling ratio) and the particle average size. Samples of different densities were generated by changing particle friction coefficient during the deposition stage. A position for each particle which was created individually was specified randomly in the domain above a height of 10-particle size from the biaxial container bottom. Then the particles deposited under gravity onto the bottom until they reach the "sleep " state. The particles lying outside the biaxial container height would be excluded from the system. The gravity acceleration was then gradually reduced to zero

Table 5.1: List of main parameters.

Parameters	Values
Box2D default parameters	
Time step size	$1/60\,\text{s}$
Number of velocity iterations per time step	8
Number of position iterations per time step	3
Contact skin thickness	$0.001\,\text{m}$
Particle characteristics	
Density	$2660\,\text{kg/m}^3$
Restitution coefficient	0
Particle bounding circle diameter[1]	$1.0\,\text{m}$
Non-elongated particle aspect ratio	1.0
Elongated particle aspect ratio	1.875
Test set-up parameters	
Particle friction coefficient[2]	$0.05 \sim 1.0$
Gravity acceleration[3]	$0.1\,\text{m/s}^2$
Particle number along the biaxial container width (scaling ratio)	40
Ratio of sample height to width	2
Maximum top platen velocity in the confining stage	$0.01\,\text{m/s}$
Biaxial test parameters	
Top and bottom boundary friction coefficients	0.4663
Particle friction coefficient	0.4663
Confining pressure	$1\,\text{kPa}$
Top platen velocity	$0.005\,\text{m/s}$
Gravity acceleration	$0\,\text{m/s}^2$
Axial strain limit	15%

[1] Not for Voronoi-based particles.

[2] By altering the friction coefficients during deposition to obtain packings of different densities.

[3] For packings generated by deposition.

and the inter-particle friction coefficient during the deposition stage was altered to the target value step by step in order to avoid causing disturbance to the system. The term "sleep" in Box2D means a rigid body is in rest and not involved in computation hence saving CPU space. There are three conditions that must be satisfied for a rigid body turning into "sleep" state and they are the minimum time that a body stays still (b2_timeToSleep) and the linear (b2_linearSleepTolerance) and the angular (b2_angularSleepTolerance) velocity tolerances, respectively, as listed in Table 5.2. The Box2D contact model parameter default settings (see section 3.3) were inherited except that the contact skin thickness was changed to $0.001\,\text{m}$ as tested by Pytlos (2015) and Pytlos et al. (2015).

Confining stress application and biaxial shearing stage

The axial confining stress was imposed via a servo-controlled process (e.g. Thornton and Antony (2000), Cheung and O'Sullivan (2008)). The radial boundaries were simulated by membranes which

Table 5.2: Parameters used to check rigid body state conditions.

Parameters	Default values
b2_timeToSleep	0.5 s
b2_linearSleepTolerance	0.01 m/s
b2_angularSleepTolerance	$2\pi/180$ rad/s

were modelled by the outermost particles (Bardet, 1994) in the horizontal direction. These particles were targeted by constructing directional ray-cast lines defined in Box2D as shown in red horizontal lines in Figure 5.1. These ray-cast lines were distributed evenly from the bottom platen to the top and changing in position as shearing continued. Once the particles which were firstly intersected with the ray-cast lines were found, horizontal force (F) inserted by a single ray-cast line was applied on each particle based on the density (ρ_{ray}) of the ray-cast lines (equal to the average number of the ray-cast lines allocated on a single particle), the sample height (H) and the target confining pressure (σ) following the equation:

$$F = \frac{\sigma H d}{\rho_{ray} H_0} \tag{5.1}$$

in which d is the average particle size and H_0 is the initial sample height. The horizontal force was applied directly on a particle centre where the particle intersected with a ray-cast line. Therefore, larger particles would intersect with more ray-cast lines and be applied more constant horizontal forces F during a single time step. The axial confining pressure and shear stress were applied by a
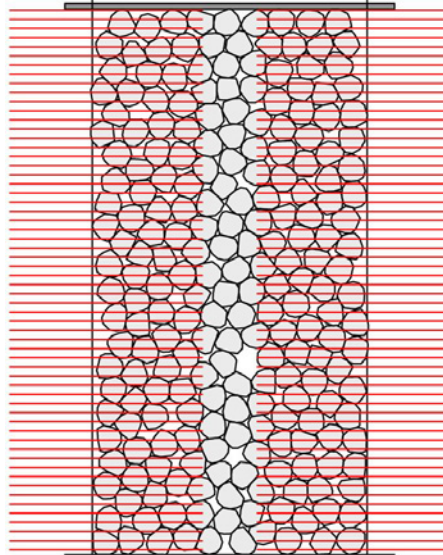
Figure 5.1: Illustration of horizontal confining process.

rigid top platen. During the shearing process, the shear stress was increased via a strain-controlled method, in which the top platen movement velocity was set constant until a prescribed axial strain was reached. The top platen velocity was set to be small enough in order to maintain the quasi-static condition in which samples behave irrespective of the strain rate. The dimensionless inertial number I

is normally used to identify different states of a granular system: quasi-static, dense flow and dynamic regimes (Da Cruz et al., 2005) and defined as:

$$I = \frac{\dot{\gamma}d}{\sqrt{P/\rho}}$$

(5.2)

The inertia number quantifies the ratio of inertia forces to external forces given to the granular media. It is reported that granular media will stay within the quasi-static regime if I is far less than 10^{-1} to 10^{-3} (Katagiri et al., 2014; MiDi, 2004; Perez et al., 2016; Radjai and Richefeu, 2009). Five biaxial test simulations involving 3500 discs were conducted using a computer facilitated with $16\,\text{GB}$ RAM and $3.2\,\text{GHz}$ i7-8700 CPU to look at the effects of biaxial shearing strain rate on granular soil behaviours in Box2D. The particle number was selected considering both simulation cost and data quality, determined by setting the scaling ratio to be 40 in order to diminish the model scaling effects as will be discussed in Chapter 6. The particle friction coefficient during set-up stage was set to be 0.1. The calculated inertia numbers and the running durations are listed in Table 5.3. The model set-up process before shearing started cost around 8 minutes to run.

Table 5.3: Summary of programme running durations.

Strain rate (m/s)	Inertia number	Running time
0.1	1.63×10^{-1}	10 min 39 s
0.05	8.15×10^{-2}	12 min 57 s
0.005	8.15×10^{-3}	55 min 18 s
0.001	1.63×10^{-3}	252 min 11 s
0.0005	8.15×10^{-4}	489 min 37 s

The results are shown in Figure 5.2 and it is apparent to see that their convergence for simulations under strain rates equal to and smaller than $0.005\,\text{m/s}$. For the simulations run under strain rates to be $0.1\,\text{m/s}$ and $0.05\,\text{m/s}$, the initial behaviours oscillate and deviate obviously with others. The strain rate effects on critical state behaviours are not significant in this series of simulations. Therefore, setting the strain rate to be $0.005\,\text{m/s}$ was considered accurate in results and time efficient.

5.3 Particle shape and size effects

5.3.1 Particle distribution

To analyse effects of particle shape and size distributions on mechanical behaviours of granular assemblies, samples constituted of five different random polygonal particles in different size distributions were generated in Box2D: polysized discs, monosized non-elongated (isotropic) and elongated dodecagons, polysized elongated dodecagons and polysized and polyshaped Voronoi-based polygons as shown in Figure 5.3. The circumscribed circle radius of polysized discs and elongated dodecagons was set between $0.2\,\text{m}$ and $0.8\,\text{m}$ and the size distribution was controlled by initialisation of the
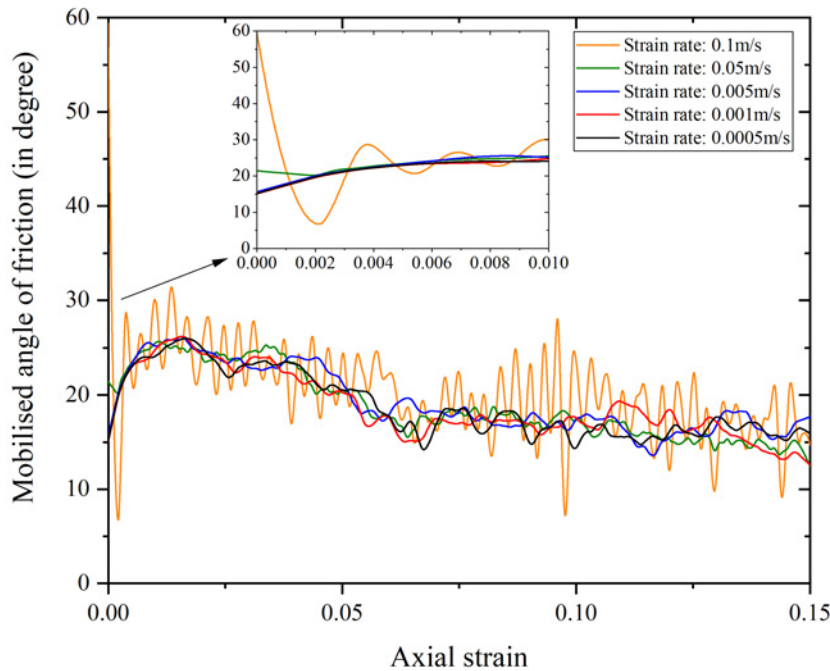
Figure 5.2: Mobilised friction angle versus axial strain for discs run by various strain rates.

pseudo-random number generator in C++. The circumscribed circle radius of monosized dodecagons was 0.5 m. A number of simulations were conducted after altering the random number generator setting in defining particle shape, initial position and the friction coefficient during the particle deposition stage in order to compare the particle shape and size effects on the void ratio (Figure 5.5) and the mean coordination number (Figure 5.6). Their size and circularity distributions are shown in Figure 5.4. The particle size is normalised by their corresponding mean values and the normalised size distribution ranges of monosized particles are quite narrow in magnitude compared with others even though a small variation due to their random particle shapes still exists. The circularity (cf. platiness) is defined as the ratio of the largest inscribed circle diameter of a particle to its smallest circumscribed circle diameter (Cho et al., 2006) and its distributions are identical for monosized and polysized elongated dodecagonal particles and represented together in the graph. Table 5.4 and Table 5.5 list average particle average sizes and circularities for differently shaped particles created in the models. A number of prior simulations were carried out to find the particle aspect ratio value in order to make the mean particle circularity of created elongated dodecagonal particles closest to that of the created Voronoi-based polygons to minimise the circularity difference in order to study the particle shape variation effects, and the aspect ratio was set to be 1.875 shown in Table 5.1. The circularity distributions for the Voronoi-based particles are wider than others due to their greater particle shape variation. It is observed that the random number setting has little effect on particle size and circularity distributions.

(a) Polysized discs.

(b) Monosized non-elongated dodecagons.

(c) Monosized elongated dodecagons.

(d) Polysized elongated dodecagons.

(e) Voronoi-based polygons.
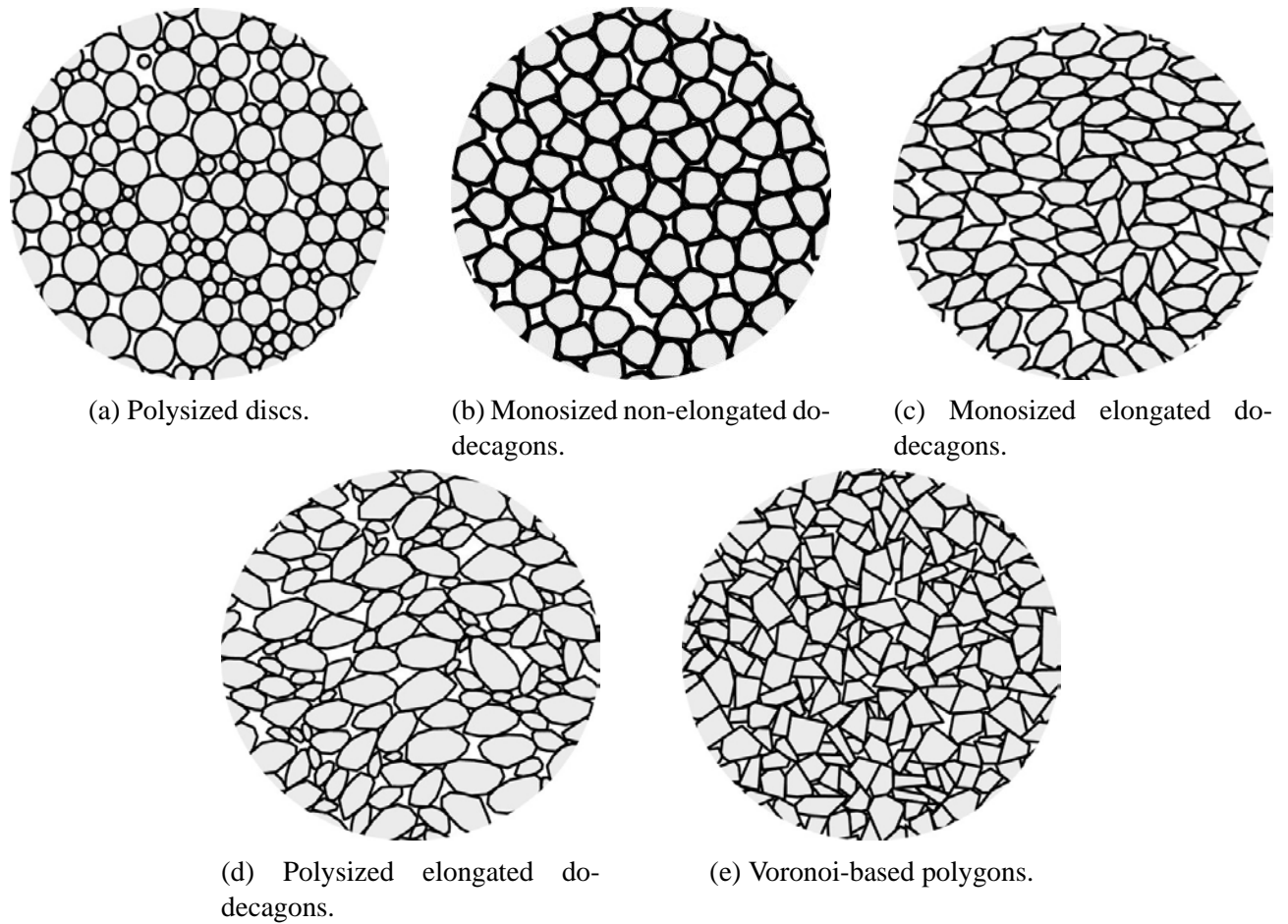
Figure 5.3: Grain shapes.

Table 5.4: Average sizes for different particle shapes (m^2).

Rand number	Disc	Non-elongated dodecagon	Monosized elongated dodecagon	Polysized elongated dodecagon	Voronoi-based polygon
1	0.881	0.700	1.312	1.490	1.002
2	0.875	0.701	1.312	1.452	1.002

Table 5.5: Circularities for different particle shapes.

Rand number	Non-elongated dodecagon	Elongated dodecagon	Voronoi-based polygon
1	0.805	0.493	0.493
2	0.804	0.493	0.492

The particle size and minimum diameter distribution curves are shown in Figure 5.4c and 5.4d respectively calculated and plotted based on the generated particles. The uniformity coefficient U and the coefficient of curvature Z can then be calculated based on the plot of particle minimum diameter distribution curve according to the equations (5.3) and (5.4) as given in geomechanics textbooks (e.g.
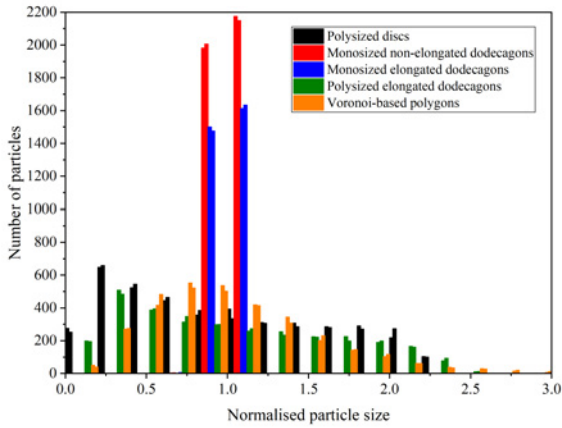
(a) Normalised particle size distributions (normalised by mean particle size).
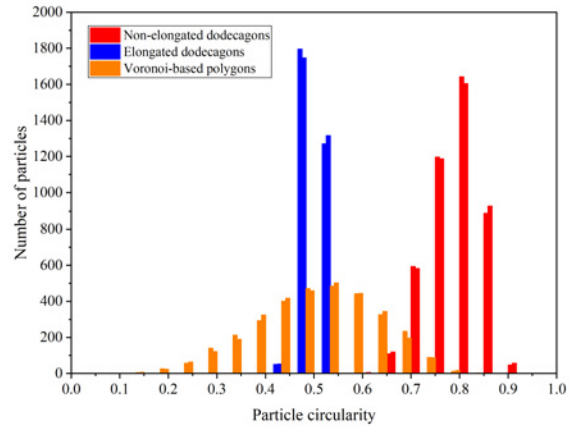
(b) Particle circularity distributions.
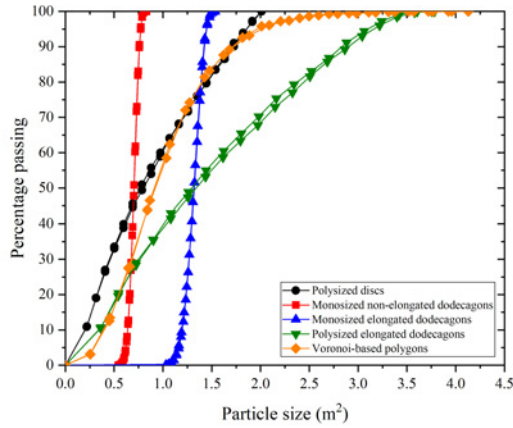
(c) Cumulative particle size distribution curves.
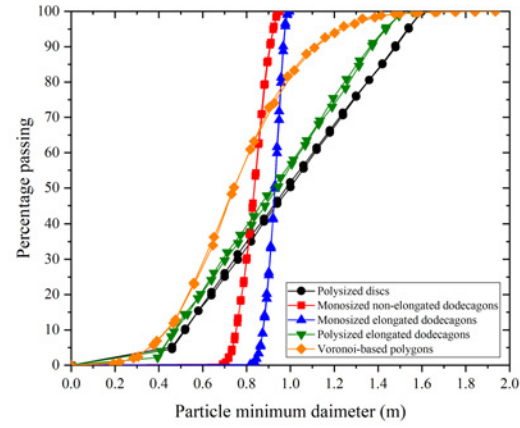
(d) Cumulative particle minimum diameter distribution curves.

Figure 5.4: Particle shape distributions for all particle shapes generated by two different random number settings.

Powrie (2018)).

$$U = D_{60}/D_{10} \tag{5.3}$$

$$Z = (D_{30})^2/(D_{60}D_{10}) \tag{5.4}$$

where D_{60}, D_{30} and D_{10} are known as the largest particle minimum diameter in the smallest 60%, 30% and 10% of particles respectively. The uniformity coefficient U helps to indicate the general curvature shape and slope of the particle size distribution curve. Well-graded soils generally possess U values larger than 10 and Z values raging between $1-3$. The soils of U values smaller than 10 can be regarded as being uniformly-graded. The approximate U and Z values for the five samples generated under the random number at 1 are calculated as shown in Table 5.6. Although the samples

made of polysized particles exhibit higher U values than others, all the U values are below 10 and the Z values oscillate around 1.

Table 5.6: Distribution curve characteristics.

Descriptor	Disc	Non-elongated dodecagon	Monosized elongated dodecagon	Polysized elongated dodecagon	Voronoi-based polygon
U	1.164	1.131	1.072	2.966	1.860
Z	0.972	1.000	1.005	0.743	1.034

5.3.2 Sample compression

Packing void ratios and mean coordination numbers before and after imposing confining pressures (set to $1\,\text{kPa}$ as Pytlos et al. (2015) to accelerate the confining process) are compared in Figure 5.5 and 5.6, and their percentage increases are given in Table 5.7. It is found that the packings made of polysized elongated dodecagons have the greatest compressibility due to their variations in particle size and large platiness in particle shape, causing distinct rearrangements due to rotation and translation within the domain once being confined, however, there the average particle contact number increase after being confined for this type of packing is not significant. Similarly, the Voronoi-based polygon samples exhibit relatively high compressibility because of their large shape variation. The mean coordination numbers for the packings made of monosized elongated dodecagons increased the most compared with other samples. A relatively large increase in the contact number is also found in the packings of monosized non-elongated dodecagons and this causes significant increases in density after being confined. The polysized disc packings possess the lowest compressibility because of the largest circularity. As a conclusion, the contact numbers for monosized polygonal particle packings raise more compared with polysized polygonal particle packings, and particle size and shape variations, lower circularity (causing anisotropy in orientation) and resultant particle contact number increase can enhance the compressibility.

Under the same friction coefficient during deposition, the Voronoi-based polygonal particles were found to be able to develop into the most densest packings when the friction coefficient is below 0.7 because of greatest variations both in particle size and particle shape. Circular particles can deposit into denser samples than dodecagonal particles when the friction coefficient is over 0.3 and this coincides with previous observations (e.g. Jensen et al. (2001)) because of circularity. A significant difference between circular and angular particles is that the deviation between the highest and the lowest void ratio for circular particles is much smaller than that for angular particles. It is observed that the elongated particle samples are denser than the non-elongated particle samples deposited by the same process because the anisotropy in orientation of elongated particles can help form into a denser packing. The polysized elongated samples can deposit into denser packings when the friction coefficient is smaller than 0.3. Therefore, particle size variation can provide more space changing in density. Based on these results, it is found the particle shape variation can help create denser packings

over particle size variation (considering the elongated dodecagons and the Voronoi-based polygons). In addition, the density states affected by particle shape are kept consistent after being confined.
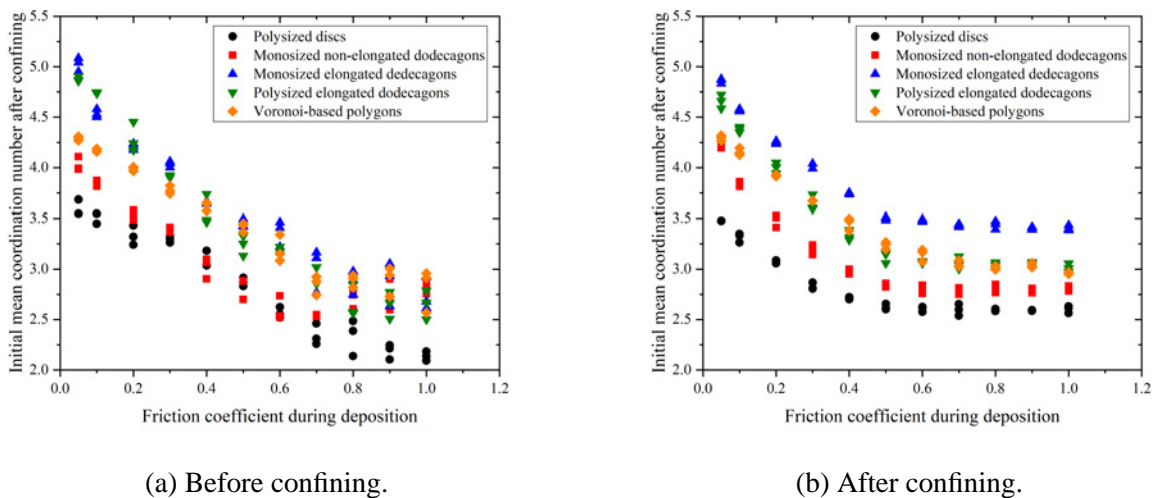

(a) Before confining.
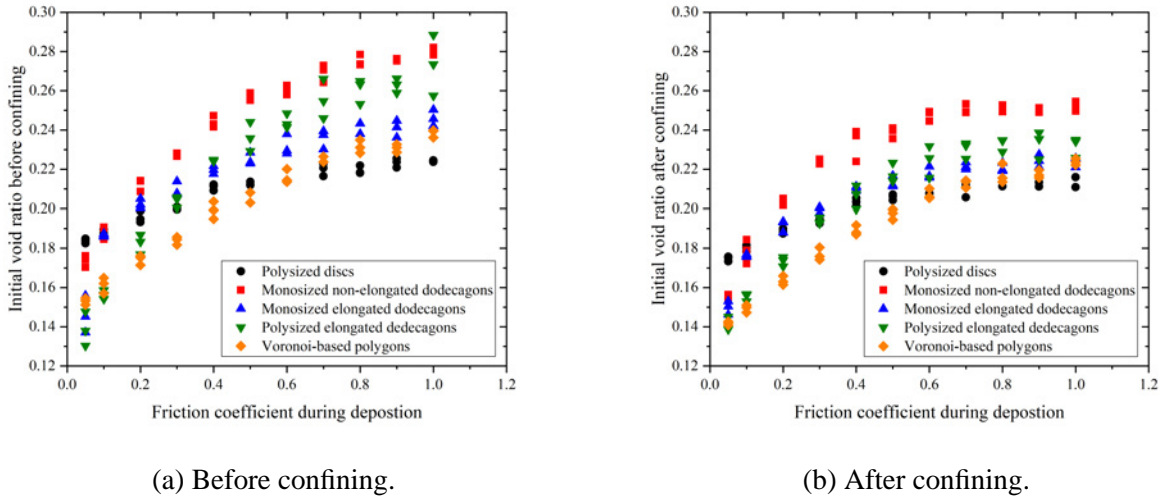
(b) After confining.

Figure 5.5: Initial void ratios before and after confining stage for different samples created under different particle friction coefficients during deposition stage.

Void ratio and mean coordination do not change apparently after the friction coefficient exceeds 0.7 for all types of packings as sliding effects dominate during the confining process instead of rolling effects. The mean coordination number is more influenced by the circularity as shown in Figure 5.6 that the non-elongated dodecagonal and disc samples exhibited lower mean contact numbers than other samples, and both particle size and shape variations will reduce the mean contact numbers when considering the elongated and the Voronoi-based samples. Therefore, circularity dominates the effects on mean coordination number compared with particle size and shape variations.

(a) Before confining.

(b) After confining.

Figure 5.6: Initial mean coordination numbers before and after confining stage for different samples created under different particle friction coefficients during deposition stage.

52

Table 5.7: Average void ratio and contact number increases after being confined.

Packings	Void ratio	Mean coordination number
Polysized discs	-3.894%	1.034%
Monosized non-elongated dodecagons	-6.612%	1.716%
Monosized elongated dodecagons	-5.275%	7.597%
Polysized elongated dodecagons	-7.195%	0.846%
Voronoi-based polygons	-5.619%	0.557%

5.3.3 Biaxial shearing

Soil strength

In order to study the particle shape effects on mechanical behaviours of cohesionless granular soils, two relatively dense and one relatively loose samples in initial states were created for each particle shape, because packing (void ratio) is another one factor influencing soil behaviours (peak and critical shear strengths) besides particle shape. The deposition friction coefficient was increased up to 0.6 to create loose dodecagon samples, while for the other four loose samples, particles were created under the deposition gravity of $0.02\,\mathrm{m/s^2}$ and in a domain of height of 1.35 times the initial height from the biaxial bottom boundary.

Figure 5.7 shows the results of the normalised deviatoric stress (q) by the mean stress (p) with the deviatoric strain up to 16%. The normalised deviatoric stress represents the slope of the critical state line (CSL) in q-p space (normally interpreted as the parameter M). It is apparent to see that the critical state normalised deviatoric stress is only influenced by average particle circularity instead of particle size and shape variations since the Voronoi-based samples possess identical critical normalised deviatoric stresses (around 1.0) as the monosized and polysized elongated dodecagon samples, and because particle shape and size variations can only influence the initial density states, with which the critical state behaviours are not related (for example Jensen et al. (2001)). The normalised deviatoric stresses in critical states or the slopes of the CSL in the $q - p$ space are captured from Figure 5.7 and summarised in Table 5.8. The mobilised friction angle versus axial strain is shown in Figure 5.8 and their critical friction angles for the samples are picked up listed in Table 5.8. The disc samples exhibit the lowest critical strength, and as the circularity decreases, the critical strength increases, because inter-particle rotation is strongly inhibited between more angular particles, hence producing additional shear strength. In the critical state, the energy will mainly dissipate from inter-particle sliding and rotation under the condition that the volume is unchanged, therefore the samples constituted of more angular particles possess higher critical strength. In the biaxial test model, the mean stress p is equal to $\frac{1}{2}(\sigma_1 + \sigma_3)$, in which σ_1 and σ_3 are the axial stress and confining stress respectively, hence, $M = 2\sin\phi$, where ϕ is the mobilised friction angle. It is also observed that as the particle circularity decreases, the granular samples require larger deformation or skeleton rearrangements to reach critical states. The developed axial strains up to the critical states for the initially dense disc samples, the non-elongated dodecagon samples and the elongated dodecagon and Voroni-based sam-

ples are roughly 10%, 12% and 13% respectively. For the initially loose samples, their critical axial strains are approximately 8%, 11% and 12% respectively. By comparing the axial strain at which the peak strength developed for the initially dense samples, it is found that particle size and shape variations could help postpone the failure or yielding occurring as slightly longer time required for rearrangements prior to reach maximum shearing strength than the monosized and monoshaped particle samples. The initial density state is the dominant factor influencing the peak strength able to be developed. The global void ratio and the volumetric strain changes as shearing proceeds are shown in Figure 5.9 and 5.10. The denser the initial packing is, the larger the peak strength will be reached. The initially dense and loose packings exhibit dilative and contractive behaviours as expected. In general, the samples made of more angular particles exhibit more volumetric dilation and/or contraction.

Table 5.8: Critical state soil strength values.

Packings	CSL slope	Mobilised friction angle (ϕ)	$\sin \phi$
Discs	0.498 (26.5°)	14.4°	0.249
Non-elongated dodecagons	0.704 (35.1°)	20.6°	0.352
Elongated dodecagons & Voronoi-based polygons	0.902 (42.1°)	26.8°	0.451

The mean coordination number evolution is depicted in Figure 5.11. The monosized elongated dodecagon samples possess the largest mean coordination number in critical states, stabilising at 3.77 and 3.56 for initially dense and loose packings respectively. Both particle size and shape variations will decrease the mean coordination number. The polysized elongated dodecagon samples and the Voronoi-based polygon samples stabilise in critical states at 3.42 and 3.28, and 3.30 and 3.10 for their initially dense and loose packings respectively. The critical state mean coordination numbers for initially dense and loose monosized non-elongated dodecagons samples are around 3.22 and 2.95. Peña (2008) found that the mean coordination numbers for the elongated and isotropic particle samples oscillated around 3.4 and 3.0 respectively by means of 2D DEM and the results obtained in Box2D agree well with their findings, slightly more than the minimum contact number to be 3 for 2D frictional granular particles in static equilibrium as proved by Edwards (1998) theoretically. With regard to the disc samples, the critical mean coordination numbers are at roughly 2.85 for both initially dense and loose samples and this is because the shear band zone in these samples occupy a larger volume (as will be shown in Figure 5.16) therefore the global values deviate less with the local values in the shear band zones. Similarly, the critical global void ratios are closer in magnitude for initially dense and loose packings of discs compared with other samples as shown in Figure 5.9. If purely measuring the local void ratio in the failure zone, the critical values should converge irrespective of the initial density states.

At axial strain 15%, mean contact numbers for each normalised particle size are calculated and the results are shown in Figure 5.12. As monosized particles do not deviate greatly in size, only polysized particles are involved in the calculation. It is consistent that as average particle size increases, there will be more particles contacted with it. This indicates smaller particles are located among larger par-
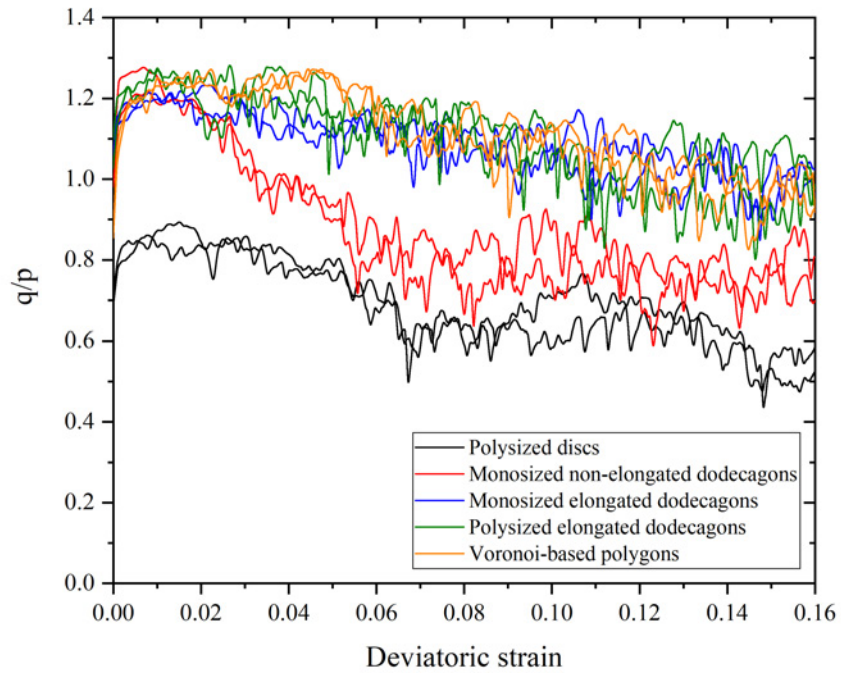
(a) Relatively dense packings.
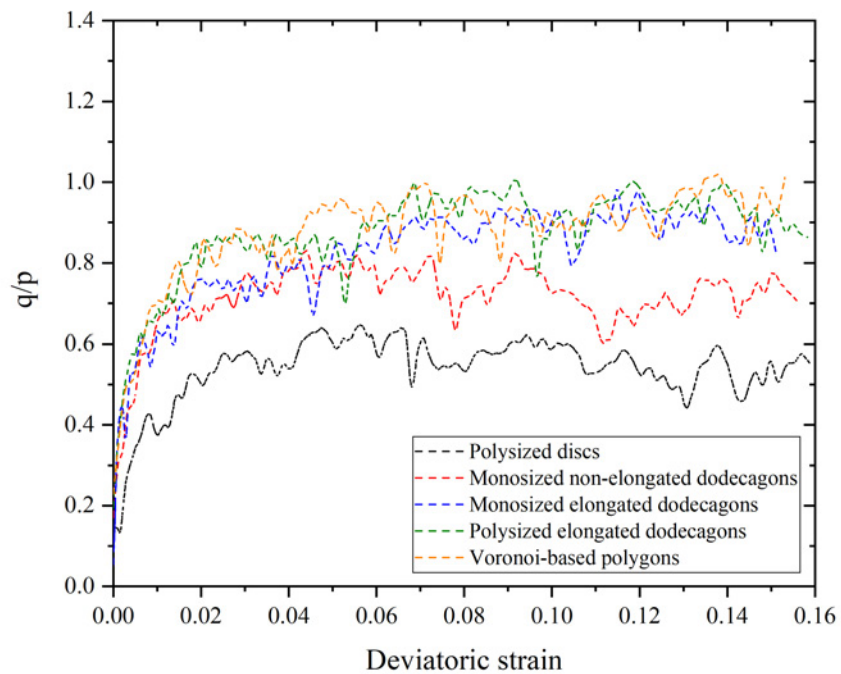
(b) Relatively loose packings.

Figure 5.7: Normalised deviatoric stress by mean stress versus deviatoric strain for different samples.
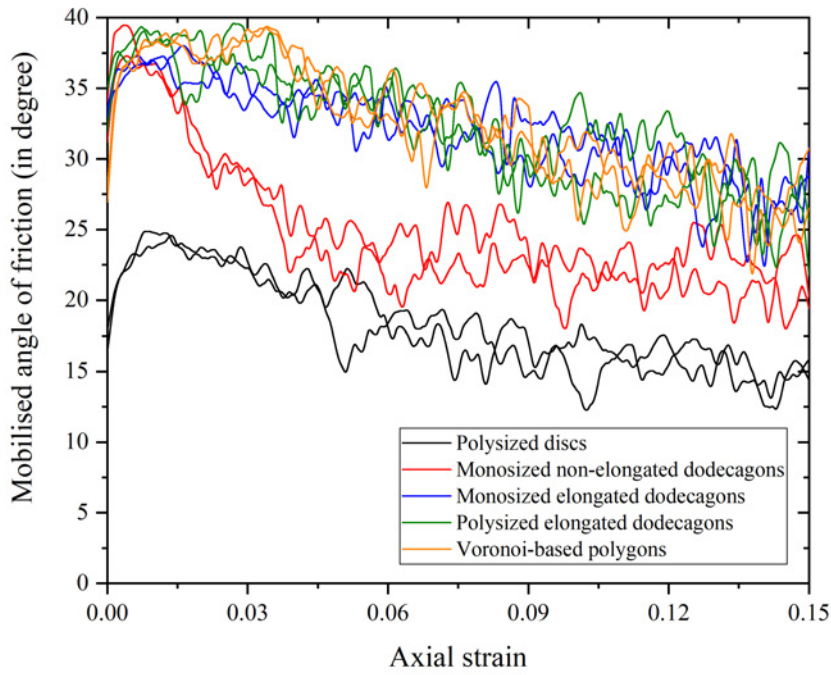
(a) Relatively dense packings.
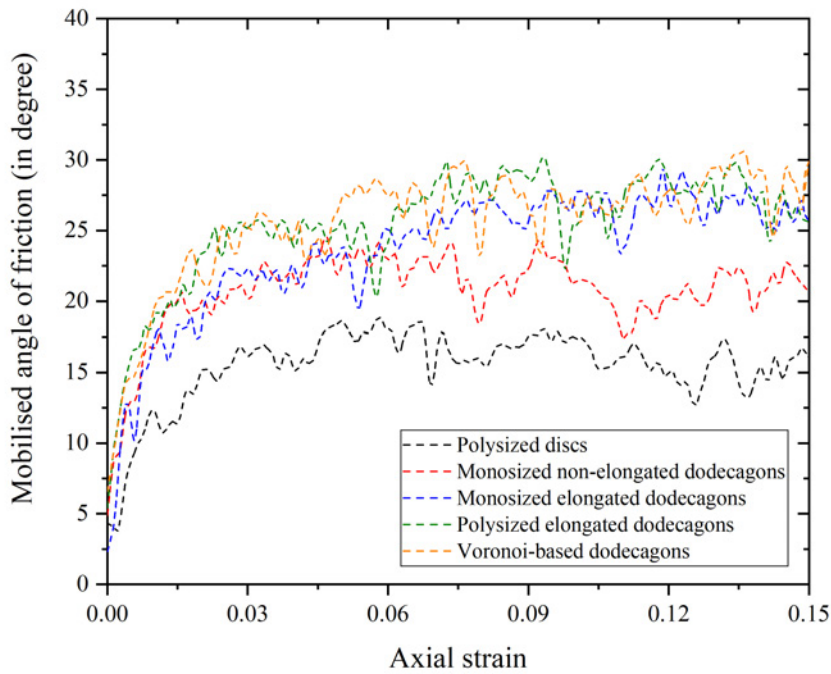
(b) Relatively loose packings.

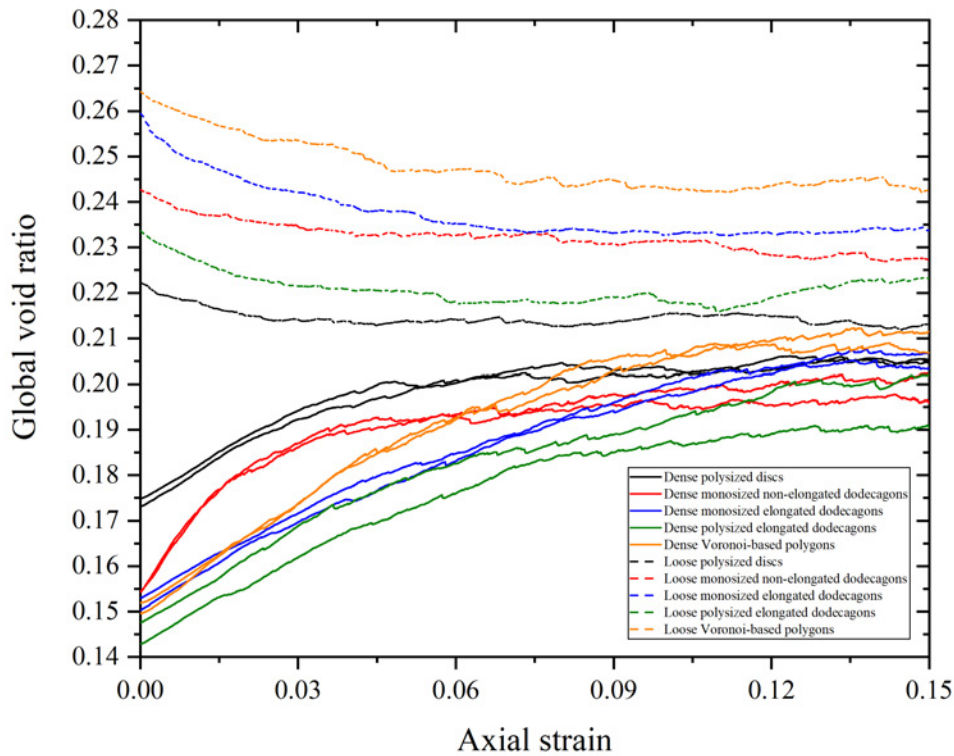Figure 5.8: Mobilised friction angle versus axial strain for different samples.

Figure 5.9: Global void ratio for samples of various initial density states.

ticles and sustain weaker contact forces. Under the same group of normalised particle size, particles in the denser samples possess higher contact numbers than in the looser samples as expected. Due to particle shape variation effects, the Voronoi-based particles in the initially dense state have the highest mean contact numbers for the largest particles in size, however, the mean contact numbers are quite small for the largest assemblies in the initially loose state.

Particle rotation increments

The average absolute particle rotation increments during a single time step (rotation velocity) along 20 different layers at axial strain 15% are compared in Figure 5.13. The relative height is defined as average height of a layer normalised by the total height at the axial strain. In critical states, the particles in initially dense and loose samples rotate in parallel velocities. The rotation velocity is highly dependent on the particle circularity. Particle size and shape variations will slightly increase the particle rotation velocity as the curves representing the polysized elongated dodecagon samples lie between the Voronoi-based polygon curves and the monosized elongated dodecagon curves.
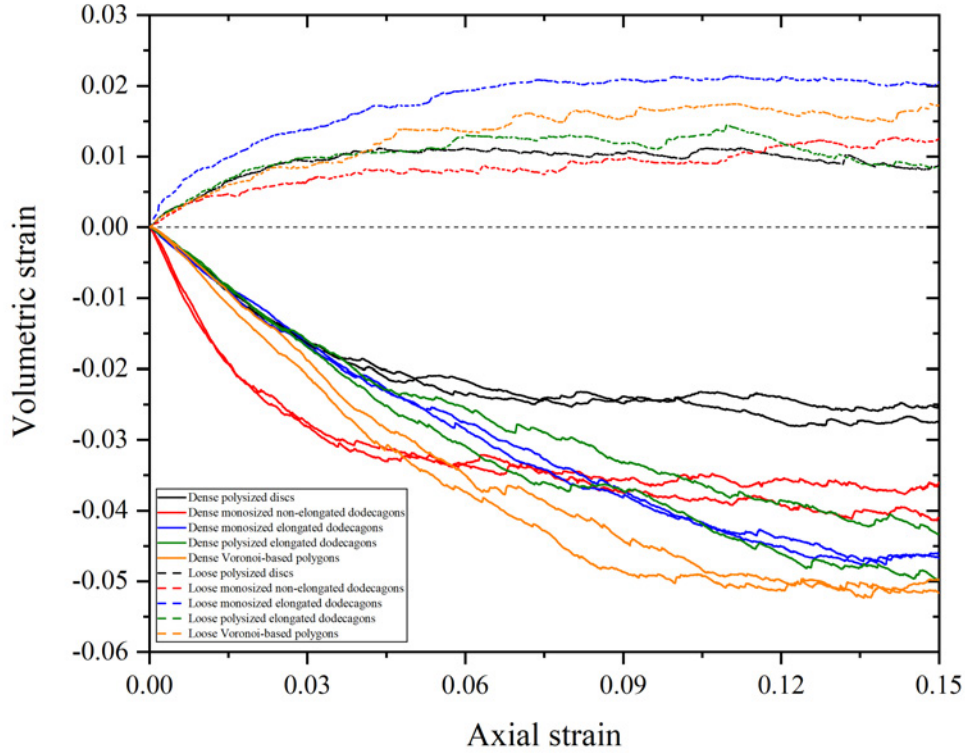
Figure 5.10: Volumetric strain for samples of various initial density states.

Second-order fabric tensor

The second-order fabric tensor (O'Sullivan, 2011) is the most commonly used fabric tensor to determine the most preferred orientation of particles under loading and quantify the anisotropy magnitude, and its form is given by equation (5.5) as:

$$\Phi_{ij} = \frac{1}{N_c} \sum_{k=1}^{N_c} n_i^k n_j^k \tag{5.5}$$

in which n_i^k and n_j^k are branch vectors connecting the centroid of the particle k to one of the contact points with other particles relative to the directions i and j, and N_c is the contact number for particle k. In two-dimensional Cartesian coordinate system, the unit branch vector n_i^k can be represented by equation (5.6) in which θ is the angle with regard to the horizontal axis, then equation (5.5) can be expanded into 2×2 symmetric matrices (5.7) and (5.8):

$$n^k = \begin{pmatrix} n_x^k \\ n_y^k \end{pmatrix} = \begin{pmatrix} \cos \theta^k \\ \sin \theta^k \end{pmatrix} \tag{5.6}$$
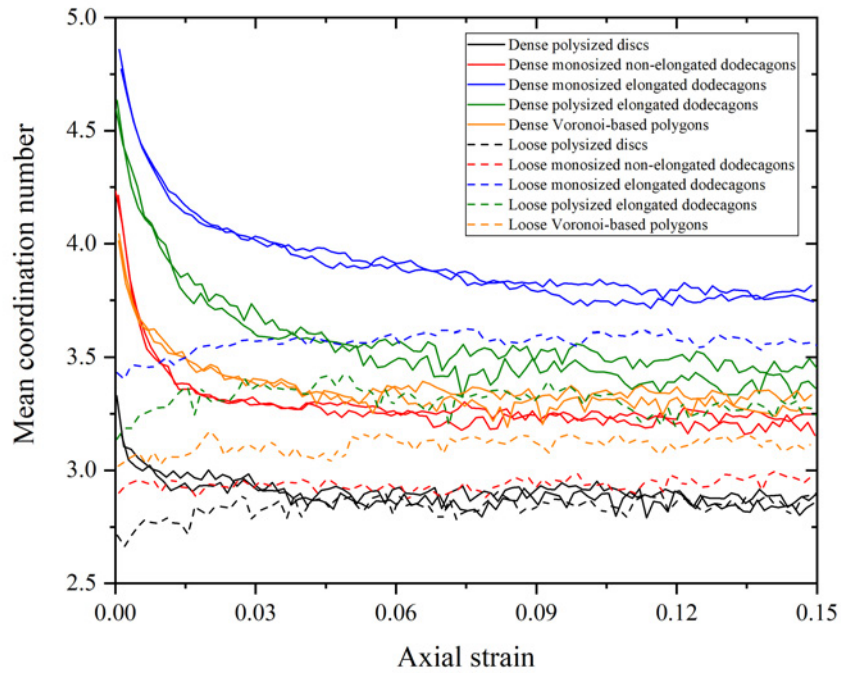
Figure 5.11: Mean contact numbers for samples in initially dense and loose states.
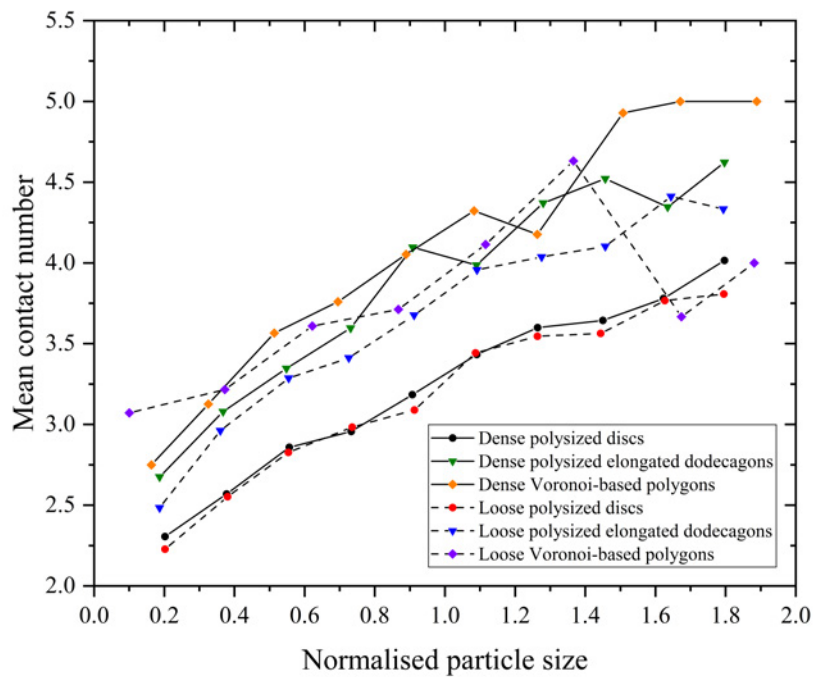
Figure 5.12: Average contact numbers for samples in dense and loose states.

$$\begin{pmatrix} \Phi_{xx} & \Phi_{xy} \\ \Phi_{yx} & \Phi_{yy} \end{pmatrix} = \frac{1}{N_c} \begin{pmatrix} \sum_{k=1}^{N_c} n_x^k n_x^k & \sum_{k=1}^{N_c} n_x^k n_y^k \\ \sum_{k=1}^{N_c} n_y^k n_x^k & \sum_{k=1}^{N_c} n_y^k n_y^k \end{pmatrix} \tag{5.7}$$

(a) Relatively dense packings.

(b) Relatively loose packings.
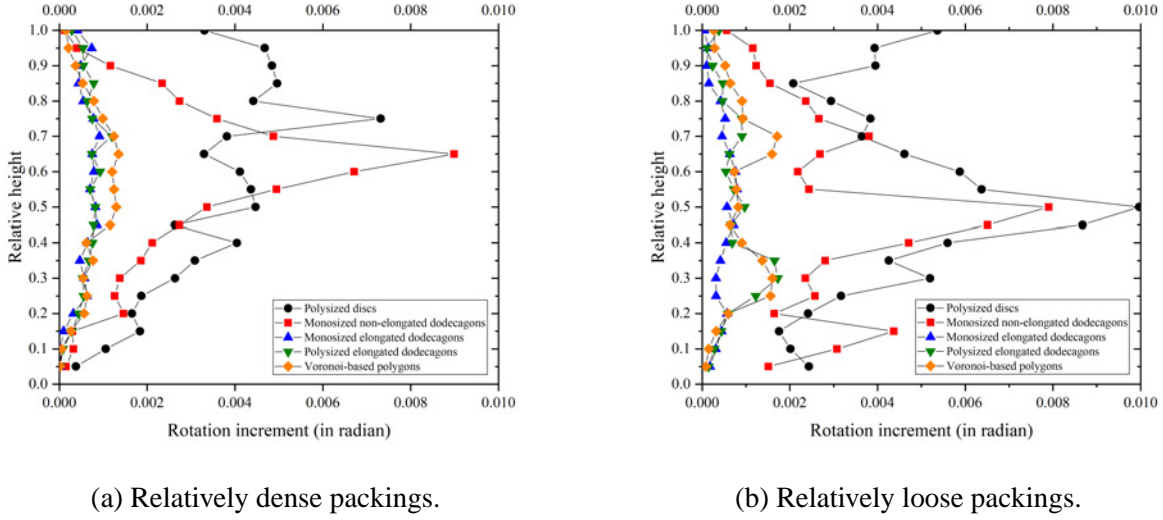
Figure 5.13: Particle average rotation increments at different relative heights at axial strain 15%.

$$
\begin{pmatrix} \Phi_{xx} & \Phi_{xy} \\ \Phi_{yx} & \Phi_{yy} \end{pmatrix} = \frac{1}{N_c} \begin{pmatrix} \sum_{k=1}^{N_c} \cos^2 \theta^k & \sum_{k=1}^{N_c} \cos \theta^k \sin \theta^k \\ \sum_{k=1}^{N_c} \sin \theta^k \cos \theta^k & \sum_{k=1}^{N_c} \sin^2 \theta^k \end{pmatrix} \tag{5.8}
$$

The trace of the fabric tensor for particle k is 1:

$$
\Phi_{xx} + \Phi_{yy} = 1 \tag{5.9}
$$

The mean fabric tensor F_{ij} for a granular media consisting of N_p particles can be computed by equation (5.10):

$$
F_{ij} = \frac{1}{N_p} \sum_{p=1}^{N_p} \Phi_{ij} \tag{5.10}
$$

Once Φ_{ij} is obtained, the principal fabric tensors Φ_1 and Φ_2 indicating the most and least preferred orientations can be derived by equation (5.11). This is an analytical approach alternative to the eigenvalue method to calculate the principal components of fabric tensors (O'Sullivan, 2011).

$$
\begin{pmatrix} \Phi_1 \\ \Phi_2 \end{pmatrix} = \frac{1}{2} (\Phi_{xx} + \Phi_{yy}) \pm \frac{1}{2} \sqrt{(\Phi_{xx} - \Phi_{yy})^2 + \Phi_{xy}^2} \tag{5.11}
$$

In order to involve the stress effects which are not considered in the fabric tensor, the stress tensor is defined as equation (5.12) with its corresponding average value defined in equation (5.13) in which f is the contact force and V_p is the particle volume.

$$
\sigma_{ij}^p = \frac{1}{V_p} \sum_{k=1}^{N_c} n_i^k f_j^k \tag{5.12}
$$

$$
\sigma_{ij} = \frac{1}{N_p} \sum_{p=1}^{N_p} \sigma_{ij}^p \tag{5.13}
$$

Evolutions of the ratio of two principal components of the fabric tensor Φ_1/Φ_2 (principal fabric tensor ratio) along the vertical and horizontal directions respectively, and also the stress tensor (principal stress tensor ratio) σ_1/σ_2 for the initially dense packings are shown in Figure 5.14 and 5.15. The principal fabric tensor ratios are over 1.0 for all the samples as the samples are sheared along the vertical direction and this is consistent with the contact force chains captured in Figure 5.41 to 5.46. It is less different between vertical and horizontal directions for the non-elongated dodecagon and disc samples because of their more isotropic particle shapes. The strain softening behaviours are not observed in the elongated dodecagon and Voronoi-based samples if only considering the contact normals, while evident when taking the stress effects into account.
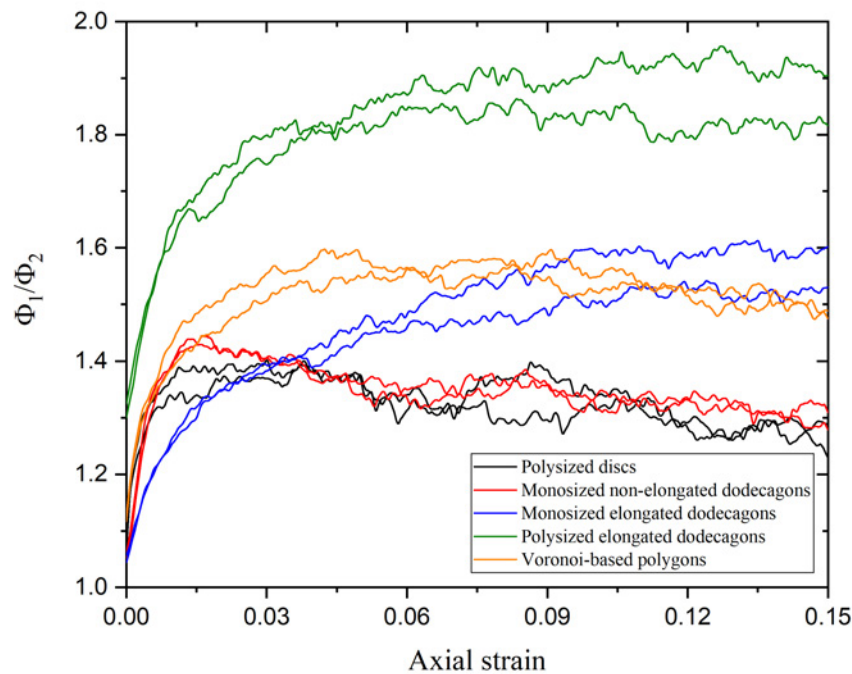
Figure 5.14: Evolution of the principal fabric tensor ratios.
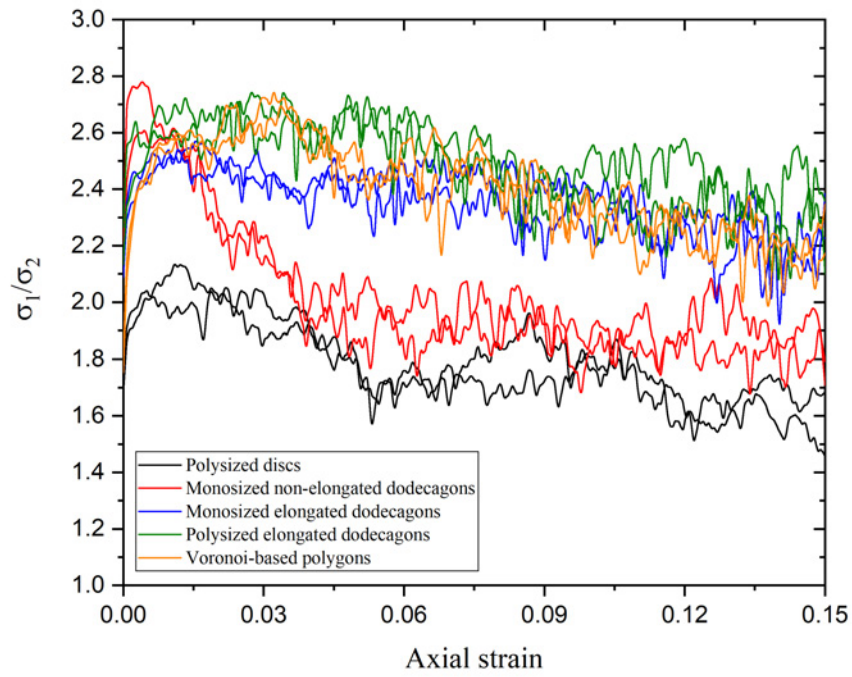
Figure 5.15: Evolution of the principal stress tensor ratios.

5.3.4   Graphical interpretation approaches

Particle rotation/displacement and shear banding

To study the microscopic behaviours effected by particle shapes, particle rotations at axial strain 15% are accumulated and illustrated in Figure 5.16 to Figure 5.20. It is clear to distinguish the shear band zones developed in all initially dense samples. Based on the Mohr circles of stress, the shear band should align along the direction of $45° + \phi/2$ (according to Table 5.8) from the horizontal, while the shear band directions for these dense packings from Figure 5.16a to 5.20b are around $42°$, $45°$, $42°$, $40°$ and $50°$ respectively measured by protractor, and the deviation from the theoretical values is because the Mohr-Coulomb failure criteria are derived from continuum mechanics and less accurate in discrete systems. It is also possibly due to the existing frictional forces between the top and bottom platens and the contacting particles. The total particle rotations for the elongated dodecagon and Voronoi samples are found to be inhibited significantly due to lower average particle circularities compared with the disc and non-elongated dodecagons. Otherwise, the polygonal particle samples can develop much more highlighted and concentrated shear bands than the disc samples.

(a) Dense polysized disc sample.   (b) Loose polysized disc sample.
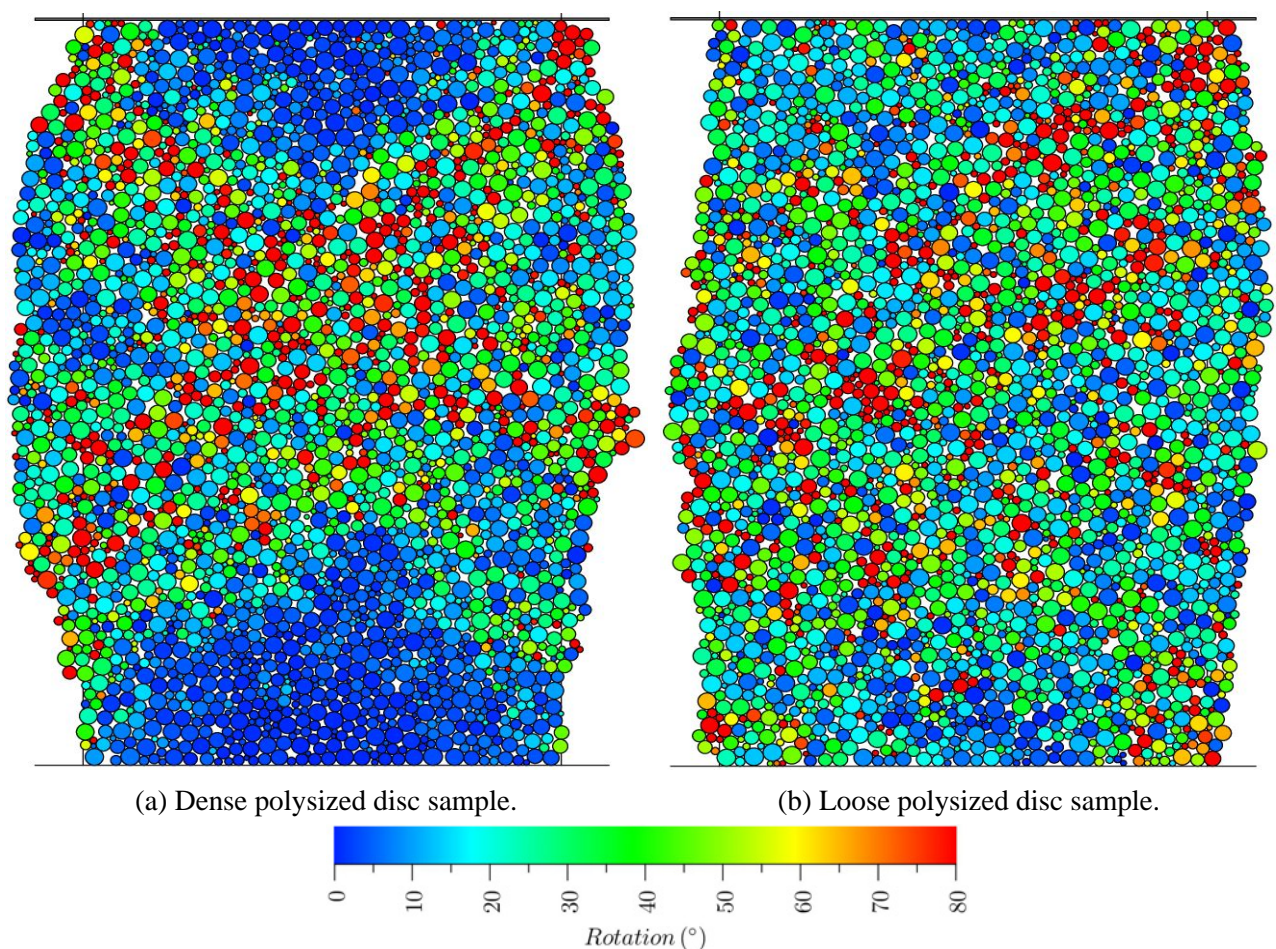
Figure 5.16: Particle total rotation diagram at axial strain 15% for polysized disc samples.

(a) Dense monosized non-elongated dodecagon sample.(b) Loose monosized non-elongated dodecagon sample.
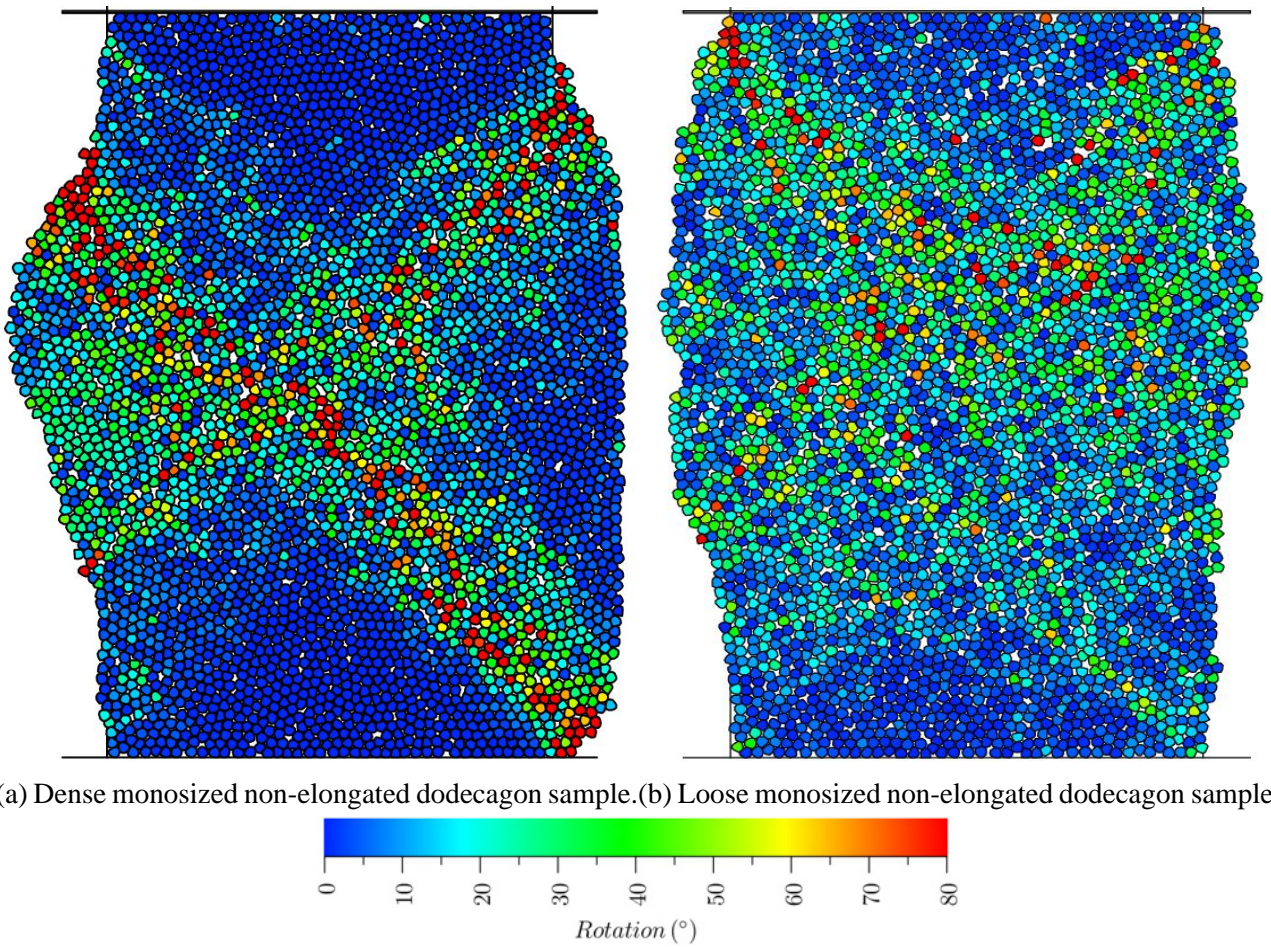
Figure 5.17: Particle total rotation diagram at axial strain 15% for monosized non-elongated dodecagon samples.

(a) Dense monosized elongated dodecagon sample.

(b) Loose monosized elongated dodecagon sample.
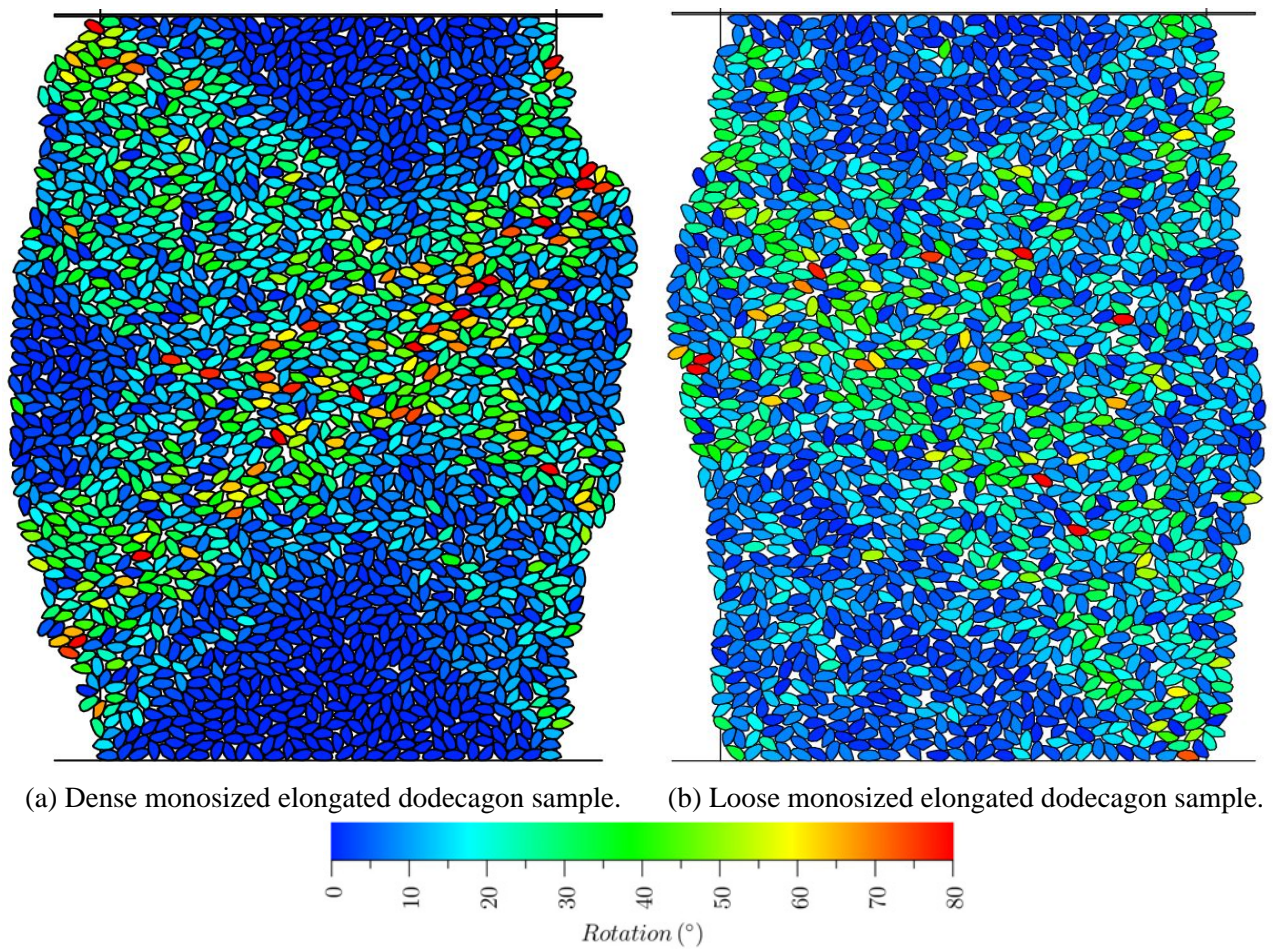
Figure 5.18: Particle total rotation diagram at axial strain 15% for monosized elongated dodecagon samples.

(a) Dense polysized elongated dodecagon sample.　　(b) Loose polysized elongated dodecagon sample.
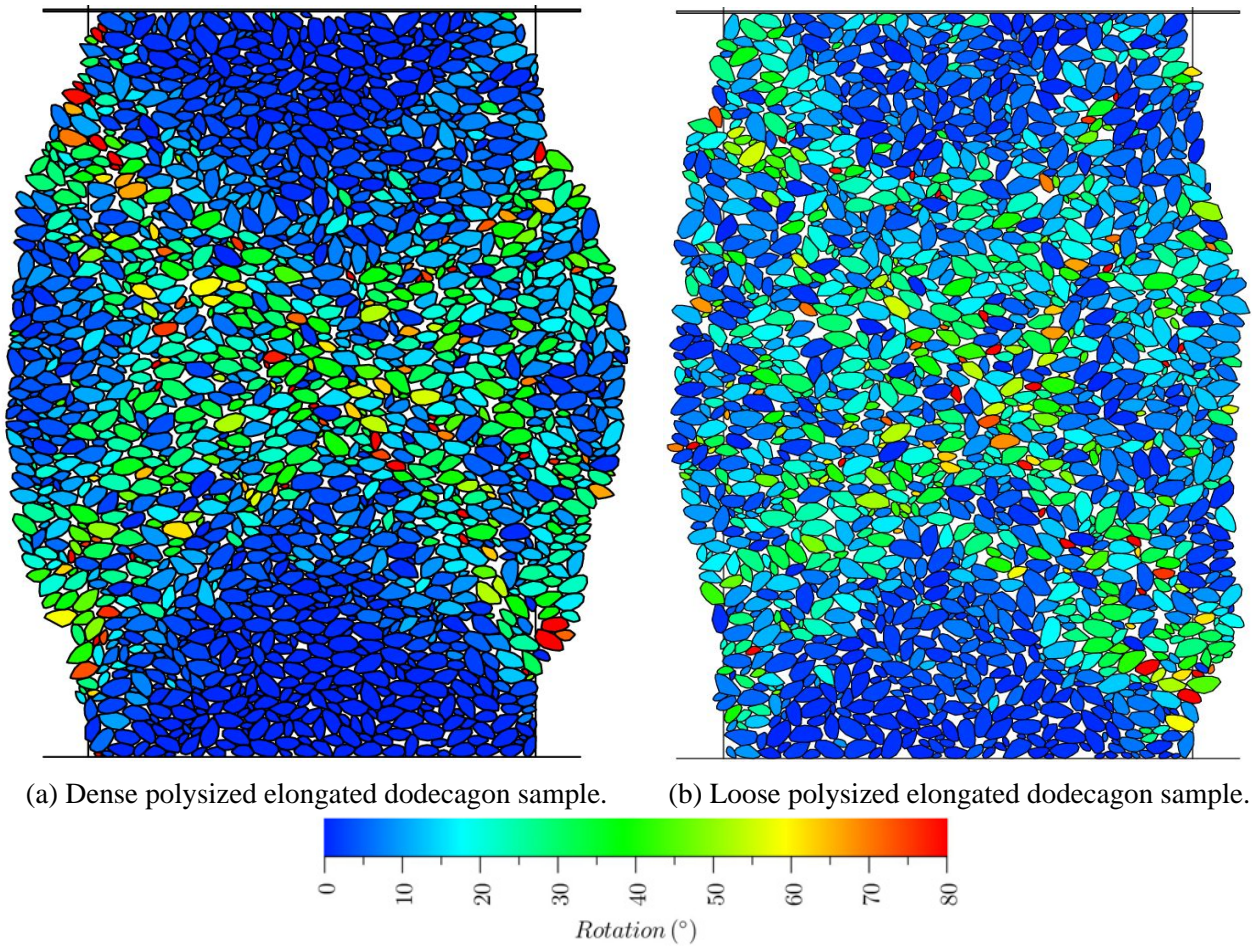
Figure 5.19: Particle total rotation diagram at axial strain 15% for polysized elongated samples.

(a) Dense Voronoi-based polygon sample.   (b) Loose Voronoi-based polygon sample.
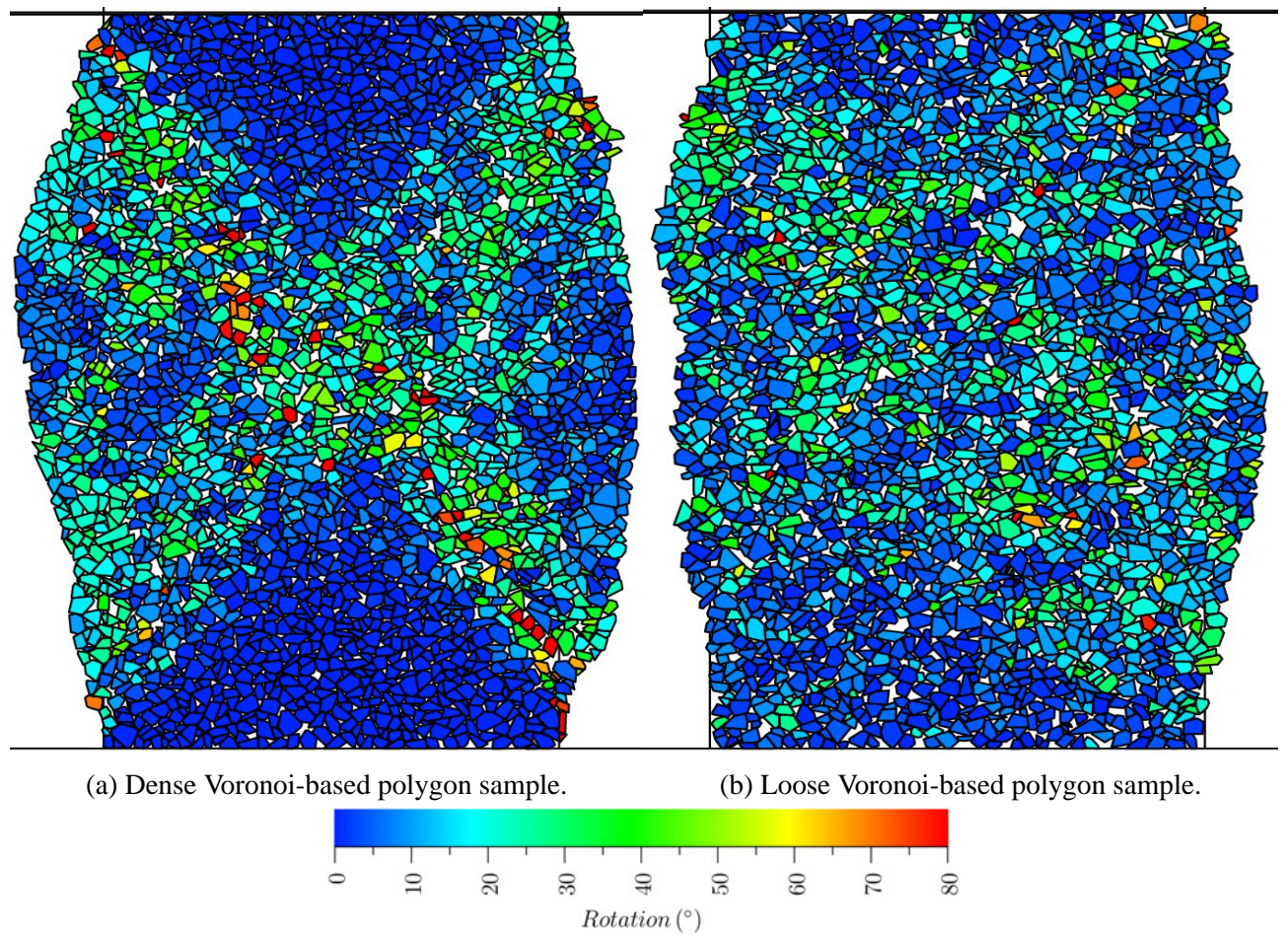
Figure 5.20: Particle total rotation diagram at axial strain 15% for Voronoi-based particles.

The overall particle displacements are illustrated in Figure 5.21 to Figure 5.25. The largest movements are concentrated within the upper triangular zones in all cases and the particles within the bottom zones remain static in translation. The particles in the middle zones move both downwards and outwards, and the outward displacements cause volumetric dilation in dense samples.

(a) Dense polysized disc sample.   (b) Loose polysized disc sample.

Total displacement (*m*)
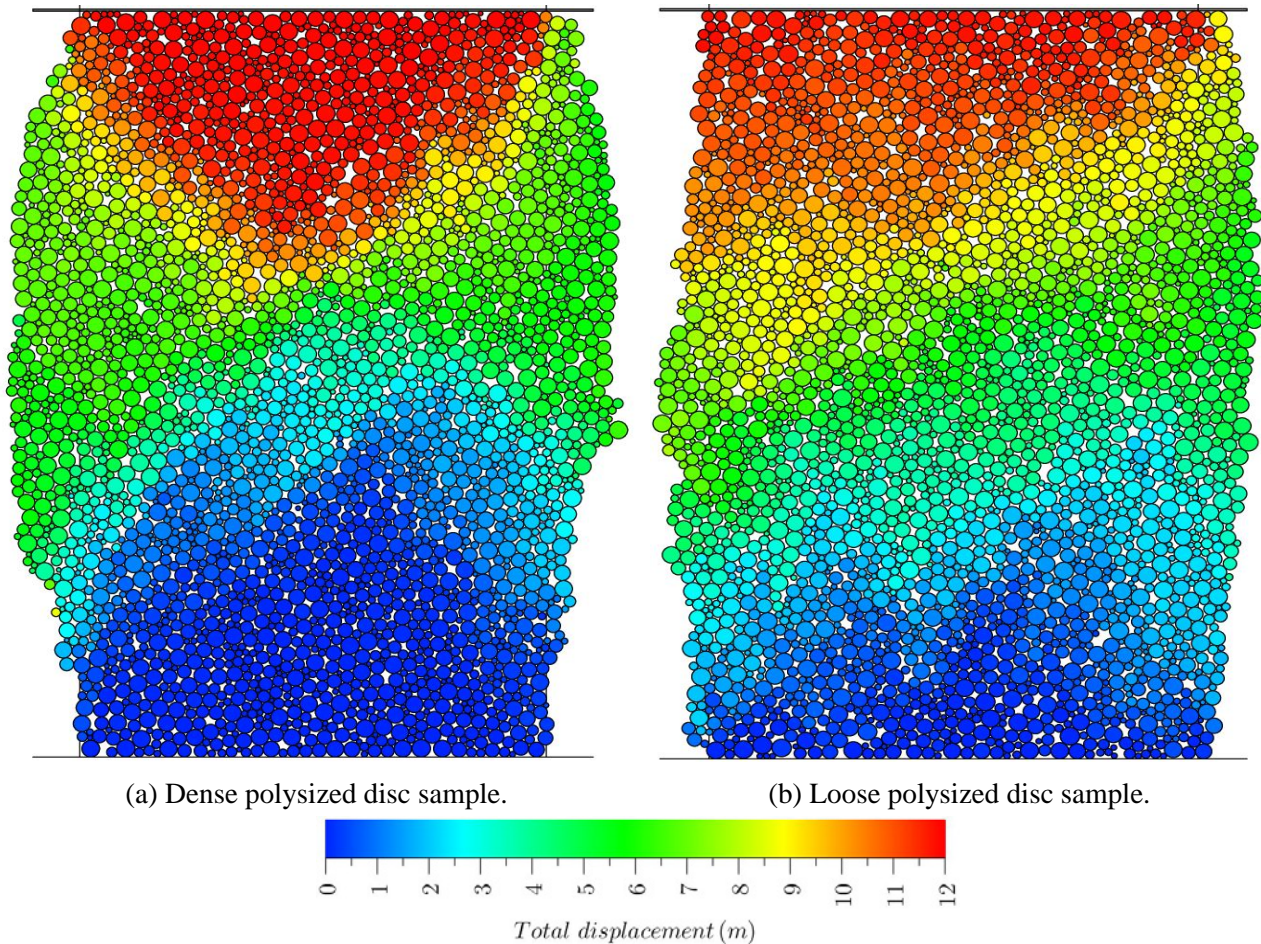
Figure 5.21: Particle total displacement diagram at axial strain 15% for polysized disc samples.

(a) Dense monosized non-elongated dodecagon sample.(b) Loose monosized non-elongated dodecagon sample.
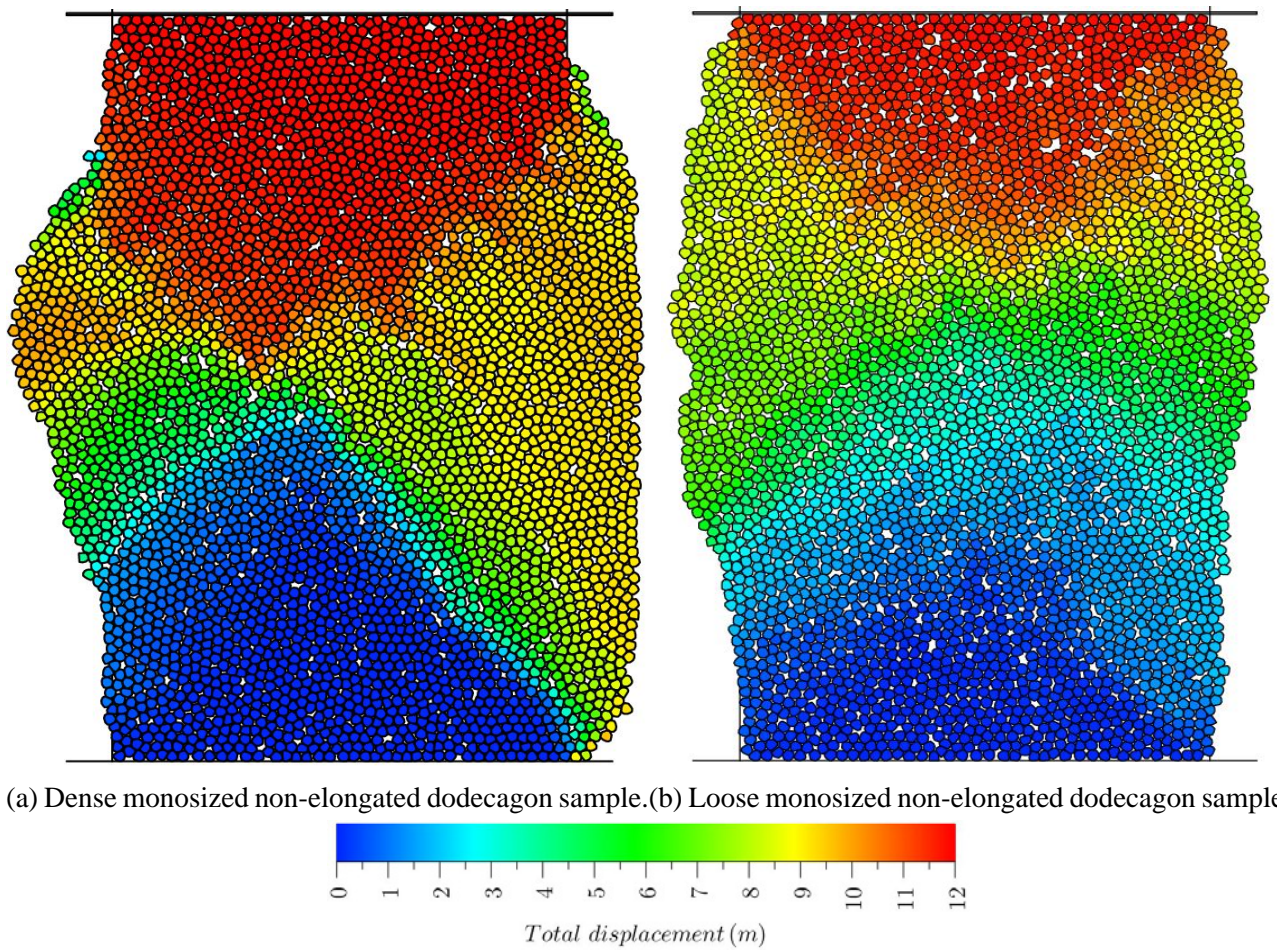
Figure 5.22: Particle total displacement diagram at axial strain 15% for monosized non-elongated dodecagon samples.

(a) Dense monosized elongated dodecagon sample.   (b) Loose monosized elongated dodecagon sample.

Total displacement (m)
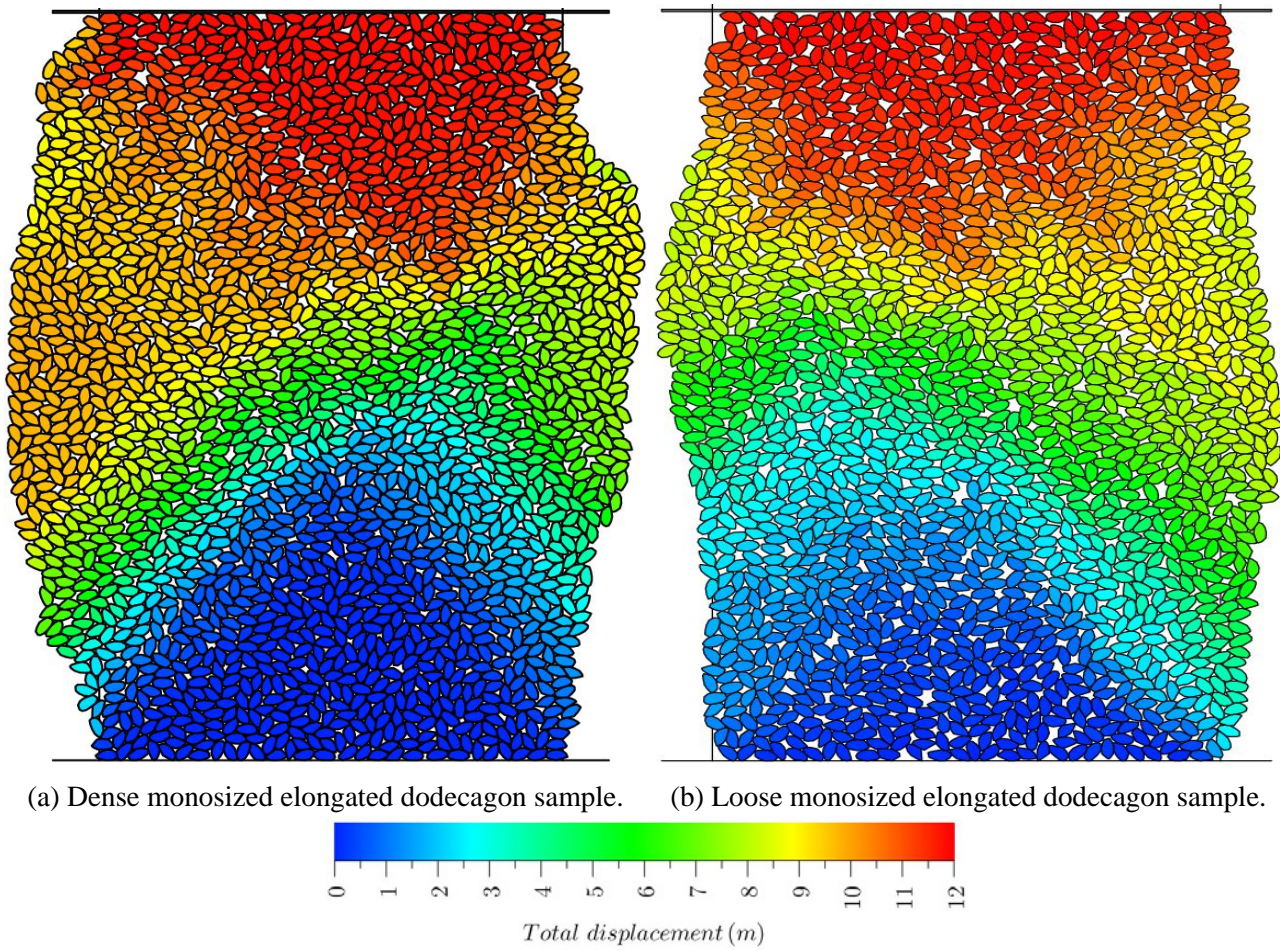
Figure 5.23: Particle total displacement diagram at axial strain 15% for monosized elongated samples.

(a) Dense polysized elongated dodecagon sample.   (b) Loose polysized elongated dodecagon sample.
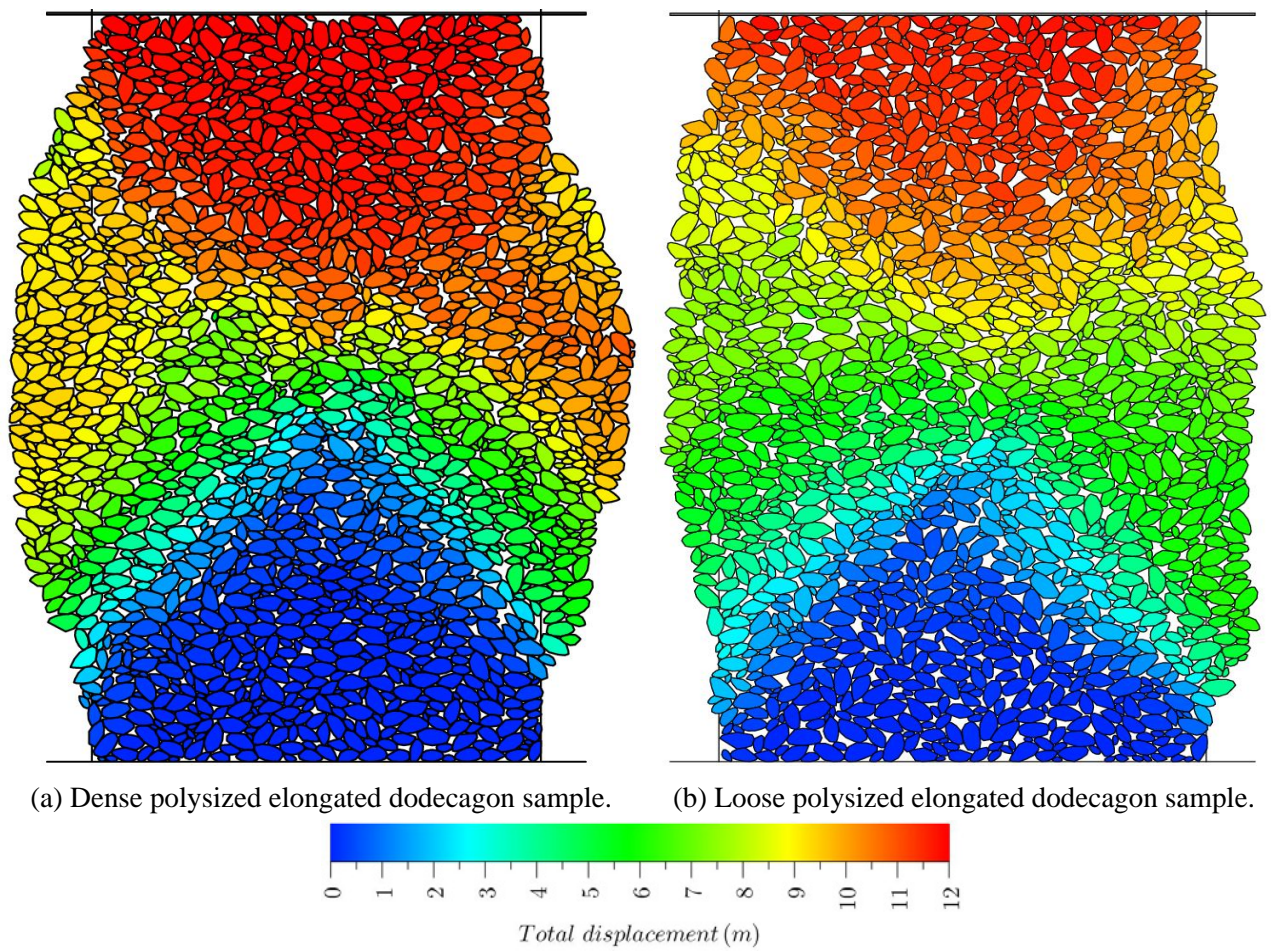
Figure 5.24: Particle total displacement diagram at axial strain 15% for polysized elongated samples.

(a) Dense Voronoi-based polygon sample.

(b) Loose Voronoi-based polygon sample.
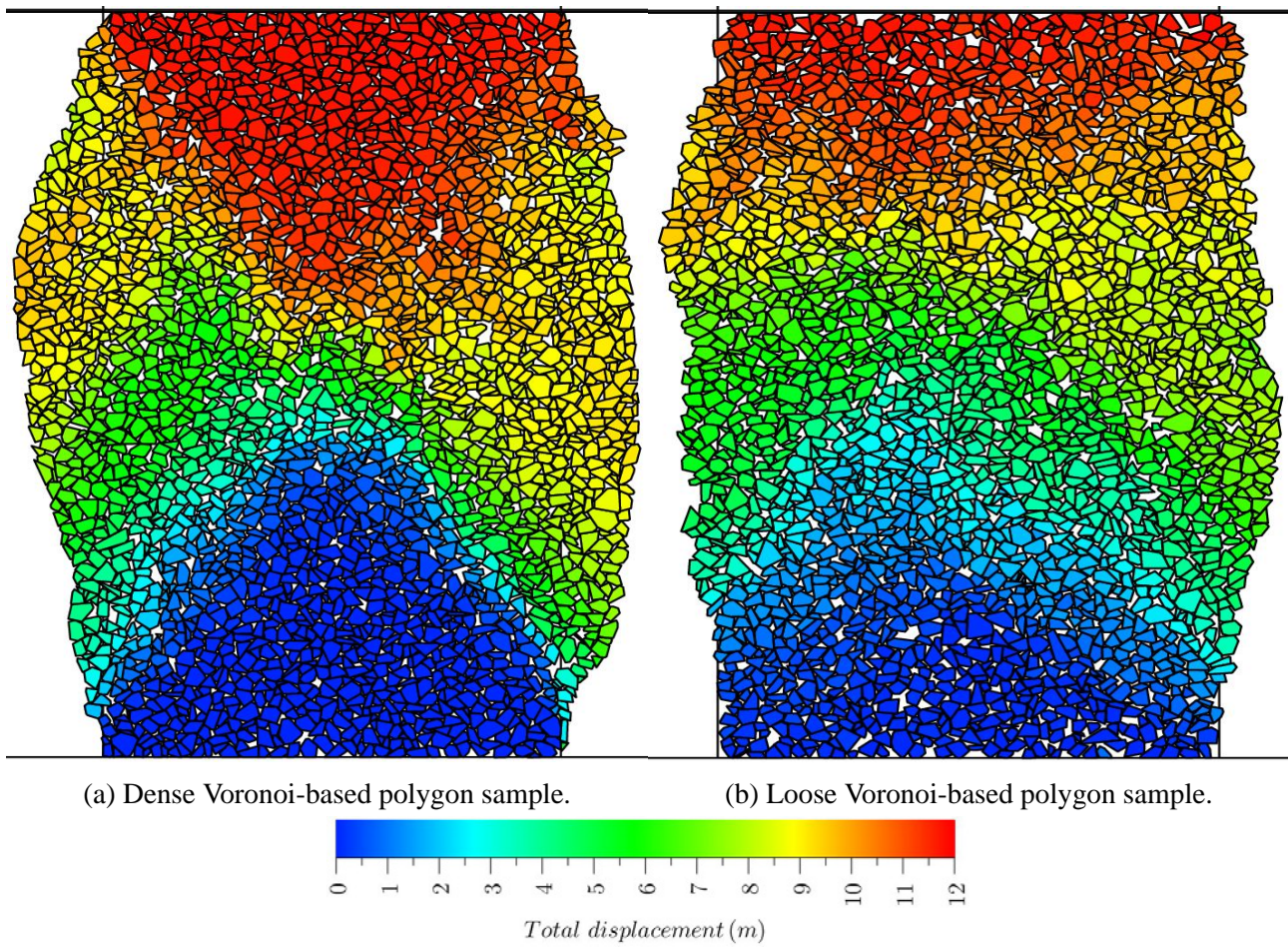
Figure 5.25: Particle total displacement diagram at axial strain 15% for Voronoi-based samples.

Local volumetric strain

To analyse the local volumetric strain rates in critical states, Delaunay triangulation was applied to calculate the volumetric change based on the nodes selected as the centroids of the particles in a single time step and their relative translational velocities. A Delaunay triangulation is used to divide a set of points into groups of triangles by maximising their interior minimum angles in order to avoid sliver triangles, and no point is allowed to lie in the circumcircle of any created triangle. Figure 5.26 to Figure 5.30 plot local volumetric strain in a single time step at axial strain 15% in which the black circles and the red circles represent volumetric contraction and dilation respectively. It can be observed that the local volumetric strain rates are similar between the initially dense and loose samples while more evenly distributed in the loose samples as no clear concentrated failure zones are developed. Local volumetric strain rates in the disc and non-elongated dodecagon samples are comparatively more significant due to their large particle circularities, while by comparing Figure 5.28b with 5.29b and 5.30b, volumetric strain rates increase evidently due to particle size and shape variations. Moreover, larger negative and positive volumetric strain rates concentrate within the shear bands in initially dense packings and balance off in magnitude, resulting in constant volumes.

(a) Dense polysized disc sample.   (b) Loose polysized disc sample.
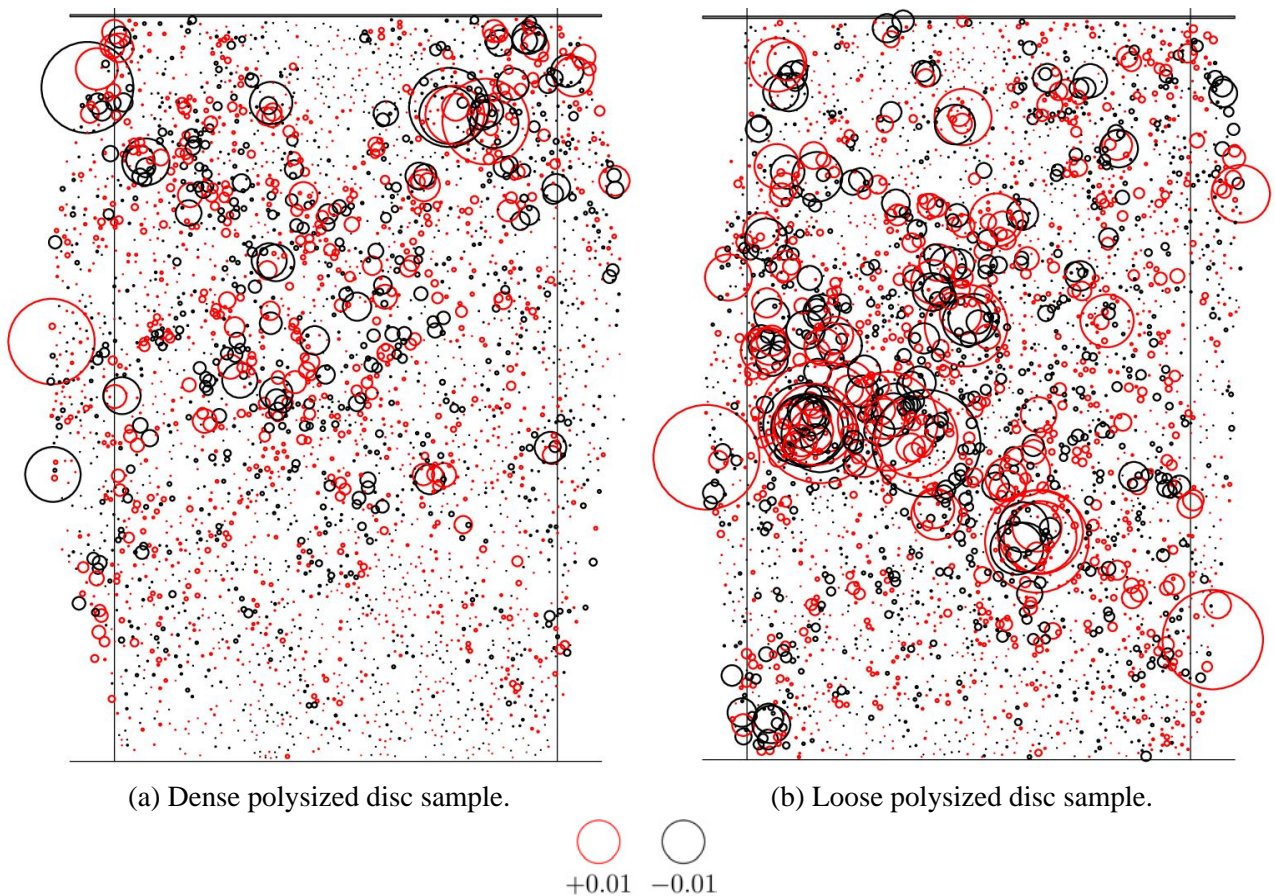
+0.01   −0.01

Figure 5.26: Local volumetric strain in a single time step at axial strain 15% for polysized disc samples.

(a) Dense monosized non-elongated dodecagon sample.(b) Loose monosized non-elongated dodecagon sample.

Figure 5.27: Local volumetric strain in a single time step at axial strain 15% for monosized non-elongated dodecagon samples.
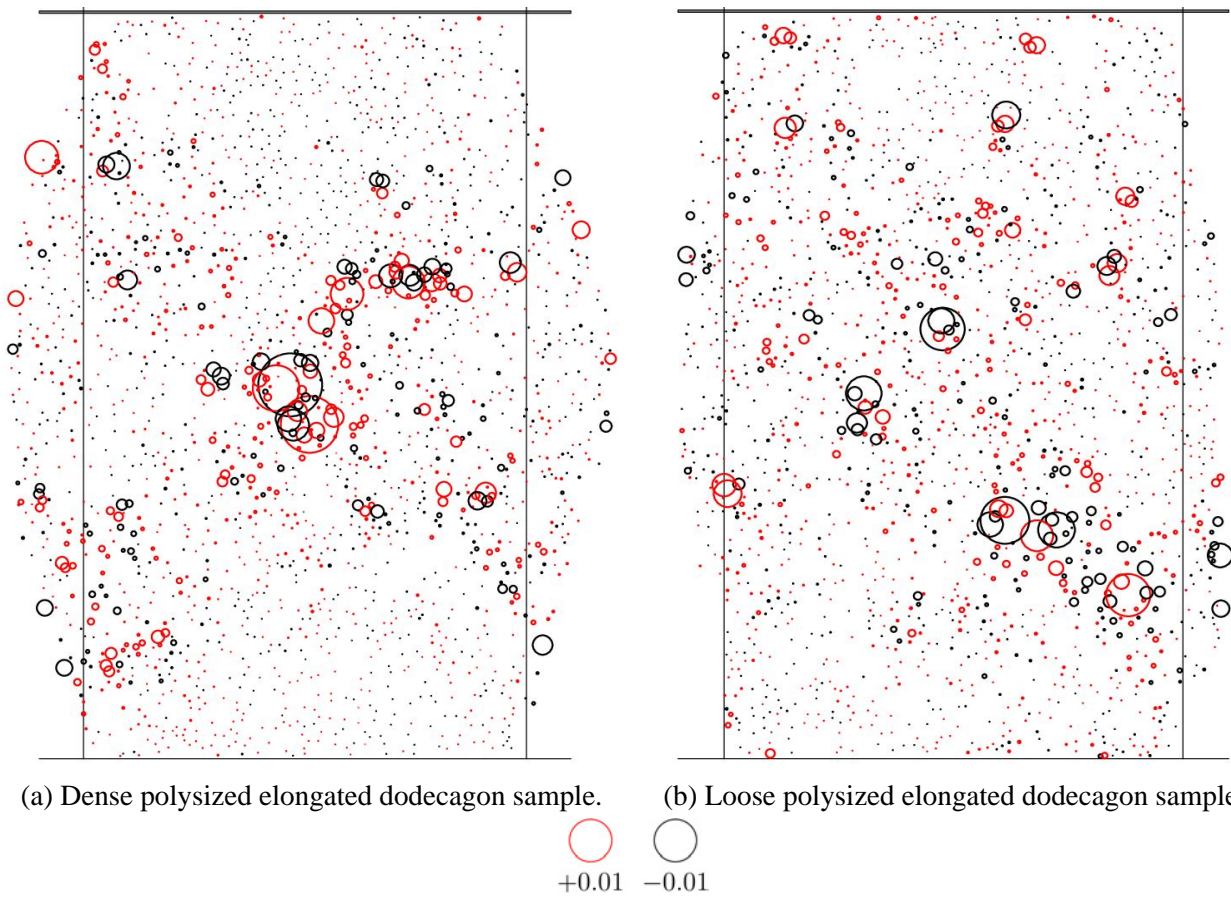
(a) Dense monosized elongated dodecagon sample.   (b) Loose monosized elongated dodecagon sample.
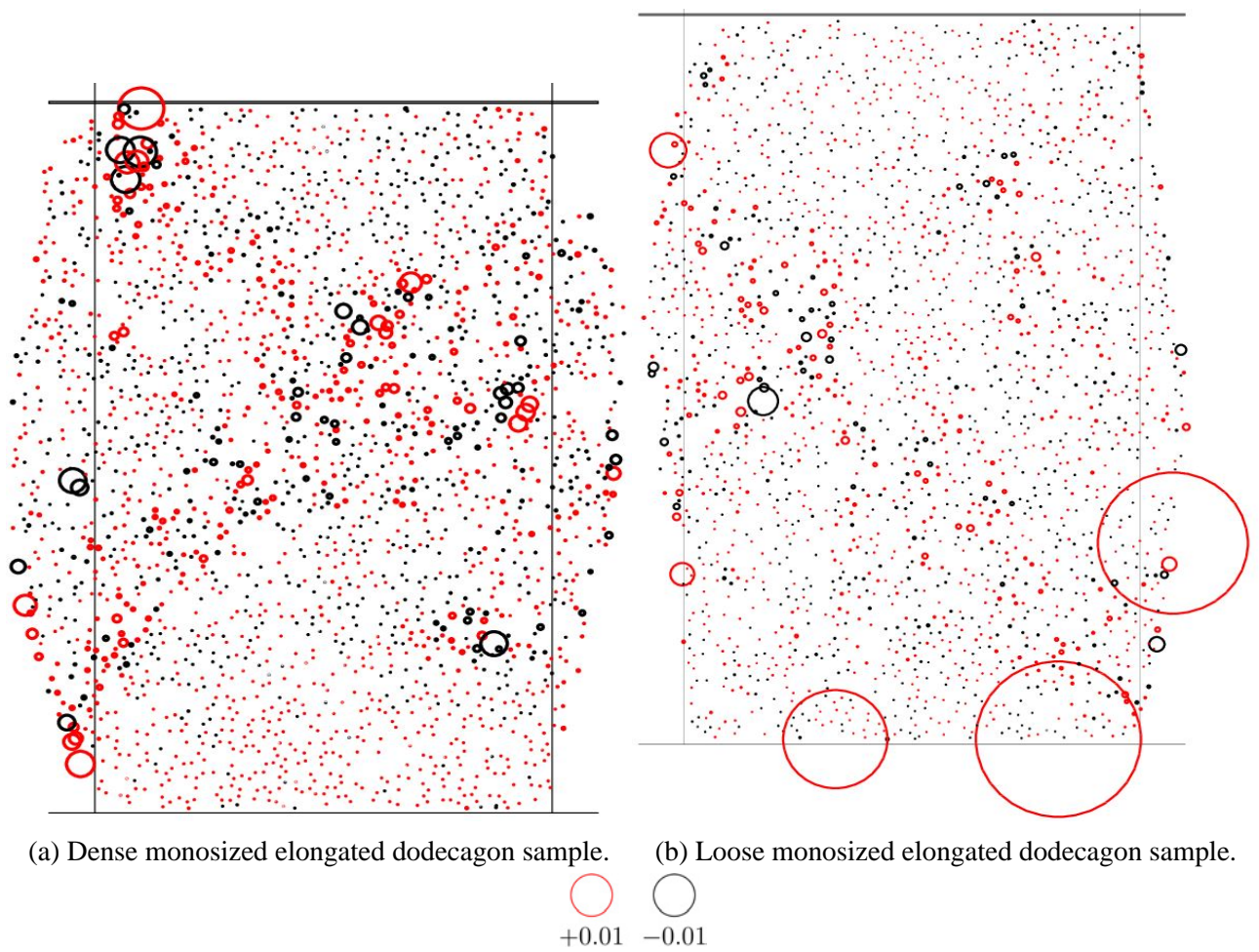
Figure 5.28: Local volumetric strain in a single time step at axial strain 15% for monosized elongated dodecagon samples.

(a) Dense polysized elongated dodecagon sample. (b) Loose polysized elongated dodecagon sample.

$+0.01$ -0.01

Figure 5.29: Local volumetric strain in a single time step at axial strain 15% for polysized elongated dodecagon samples.

(a) Dense Voronoi-based polygon sample.

(b) Loose Voronoi-based polygon sample.
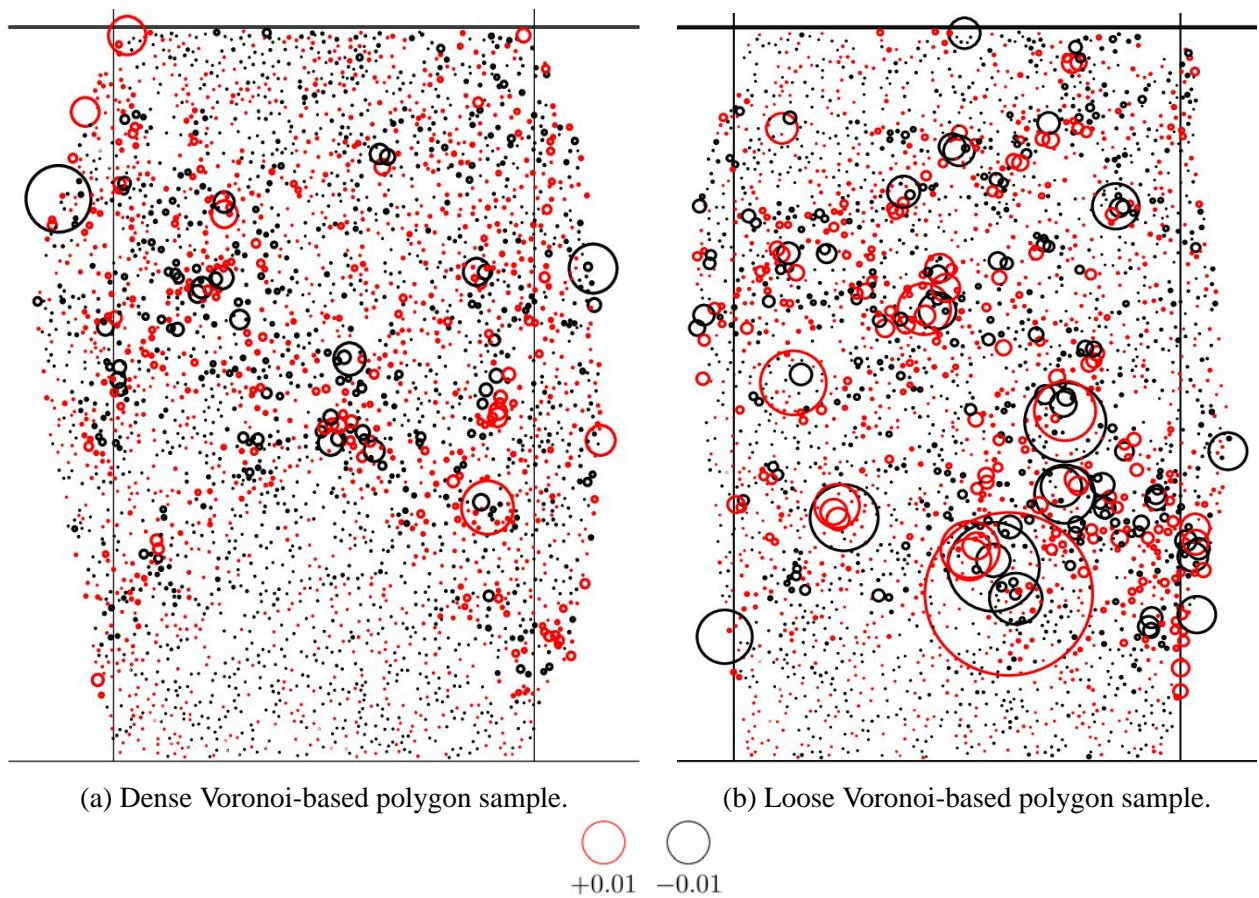
Figure 5.30: Local volumetric strain in a single time step at axial strain 15% for Voronoi-based samples.

Local void ratio

The local void ratios were also computed at critical state as plotted in Figure 5.31 to Figure 5.35. In order to avoid the boundary effects, only central zones (within the initial biaxial container width of 40 particle size) were involved in the computation. At an axial strain of 15%, the central zone in each sample of initial biaxial width was divided into a set of subdomains and the void ratio was calculated according to total intersections of particles within each domain with its boundary. Local void ratios are generally larger in the shear bands in the dense samples compared with the values outside the strain localisation zones, and as particle circularity decreases and also as particle size and shape vary, the local void ratio will correspondingly become larger. In critical states, the local void ratios around the shear bands from Figure 5.31a to 5.35b are roughly 0.20, 0.22, 0.25, 0.30 and 0.35 respectively.

(a) Dense polysized disc sample.   (b) Loose polysized disc sample.
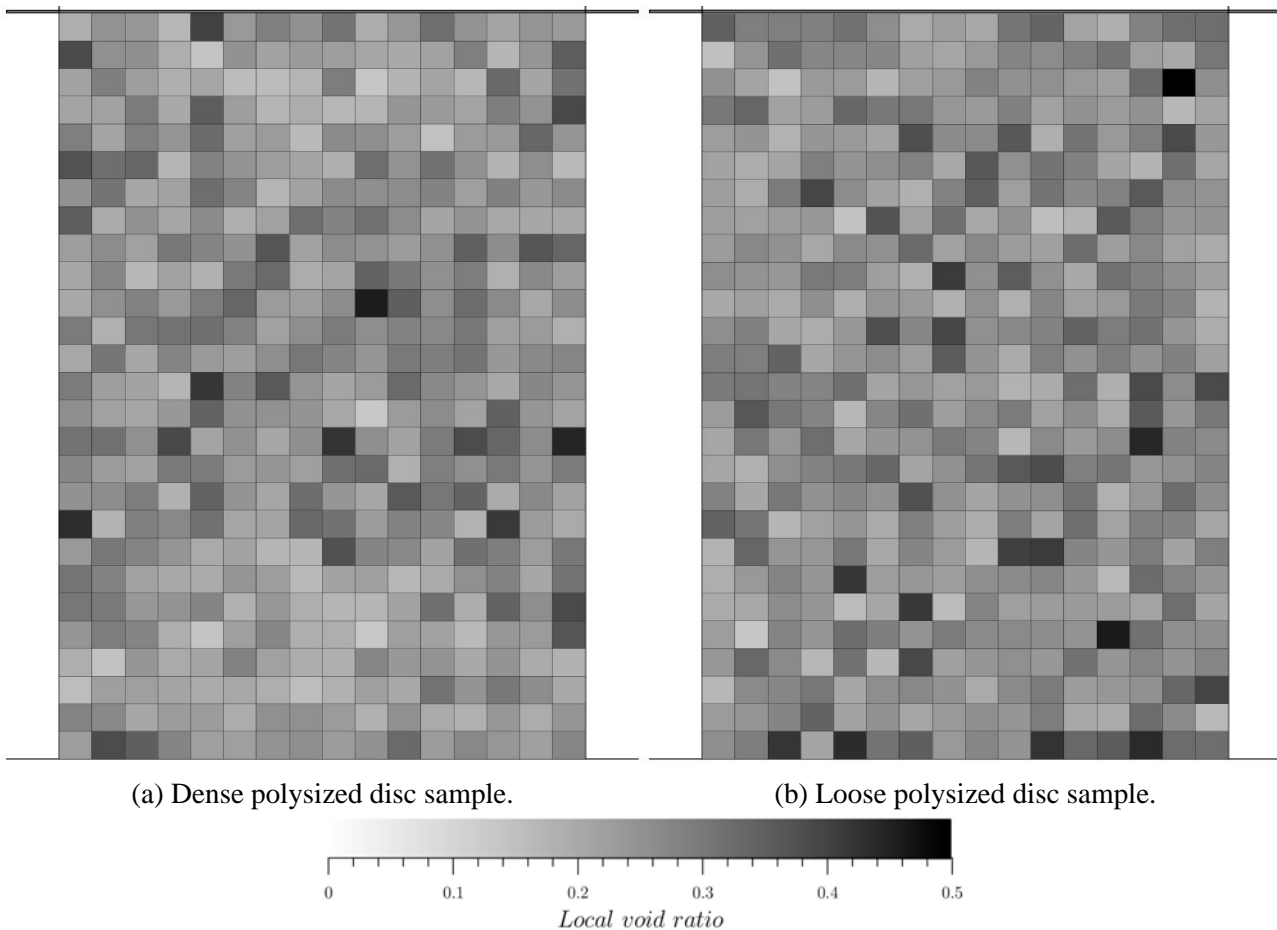
Figure 5.31: Sample local void ratio diagram at axial strain 15% for polysized disc samples.

(a) Dense monosized non-elongated dodecagon sample.(b) Loose monosized non-elongated dodecagon sample.
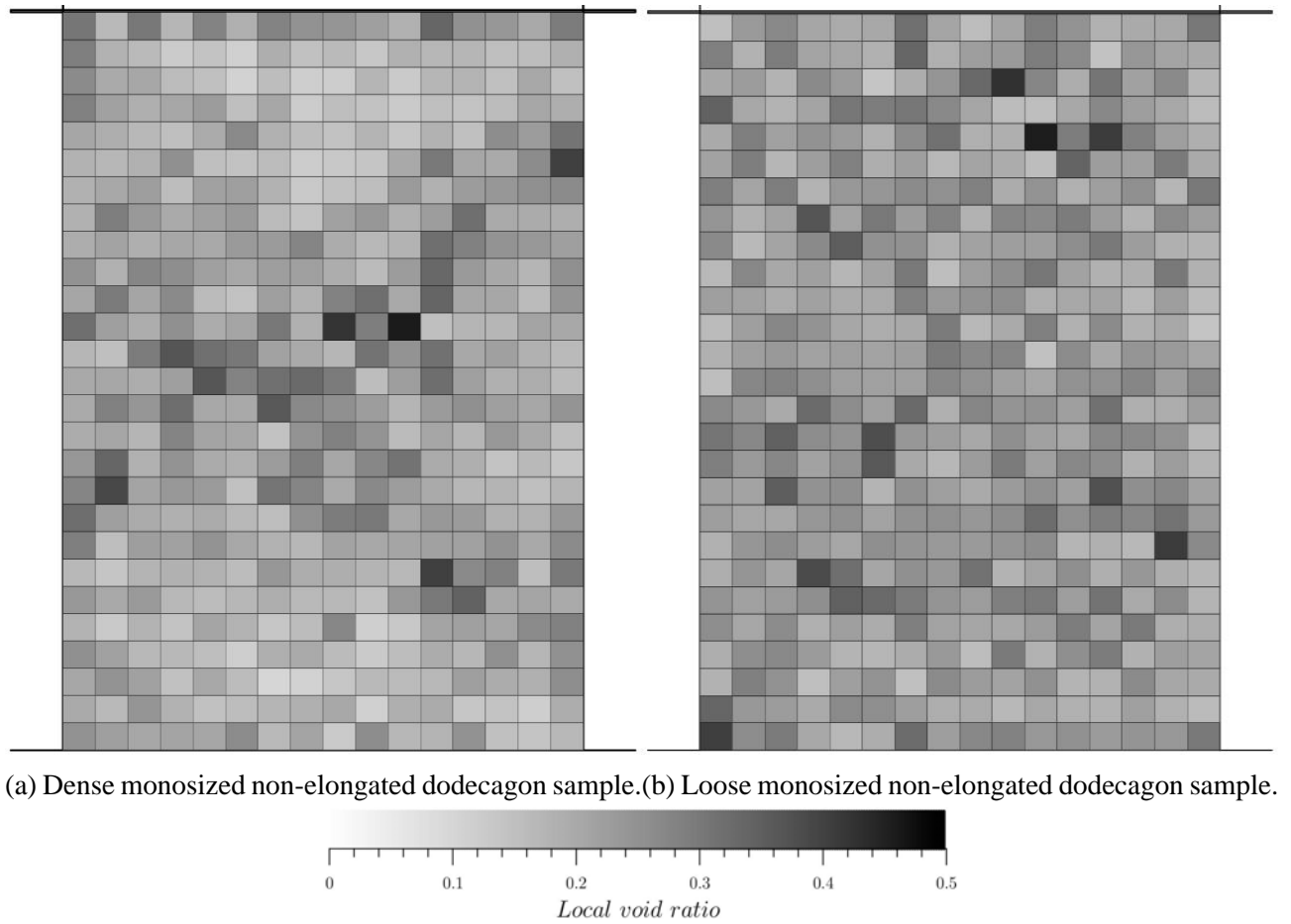
Figure 5.32: Sample local void ratio diagram at axial strain 15% for monosized non-elongated do-decagon samples.

(a) Dense monosized elongated dodecagon sample.   (b) Loose monosized elongated dodecagon sample.
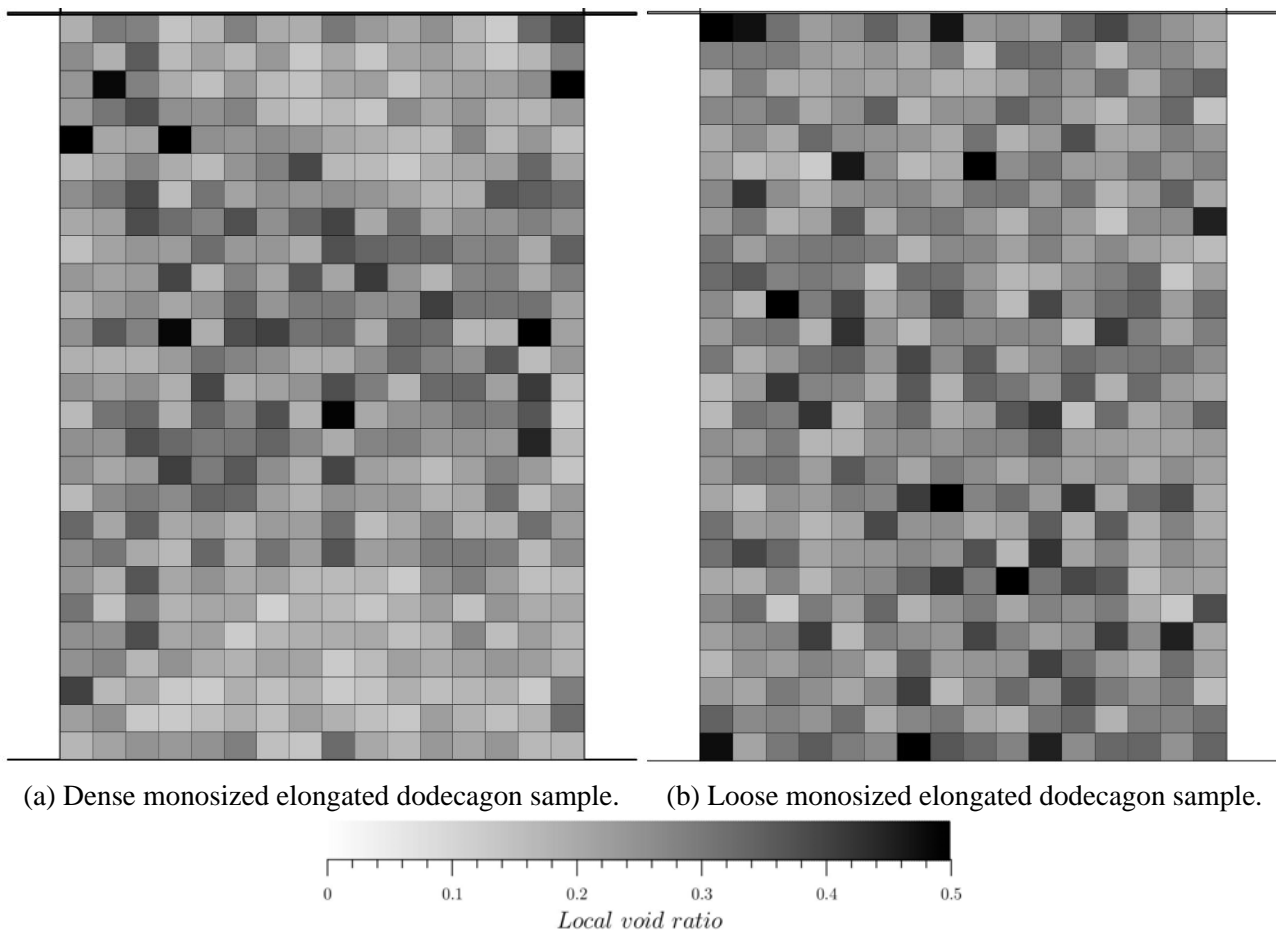
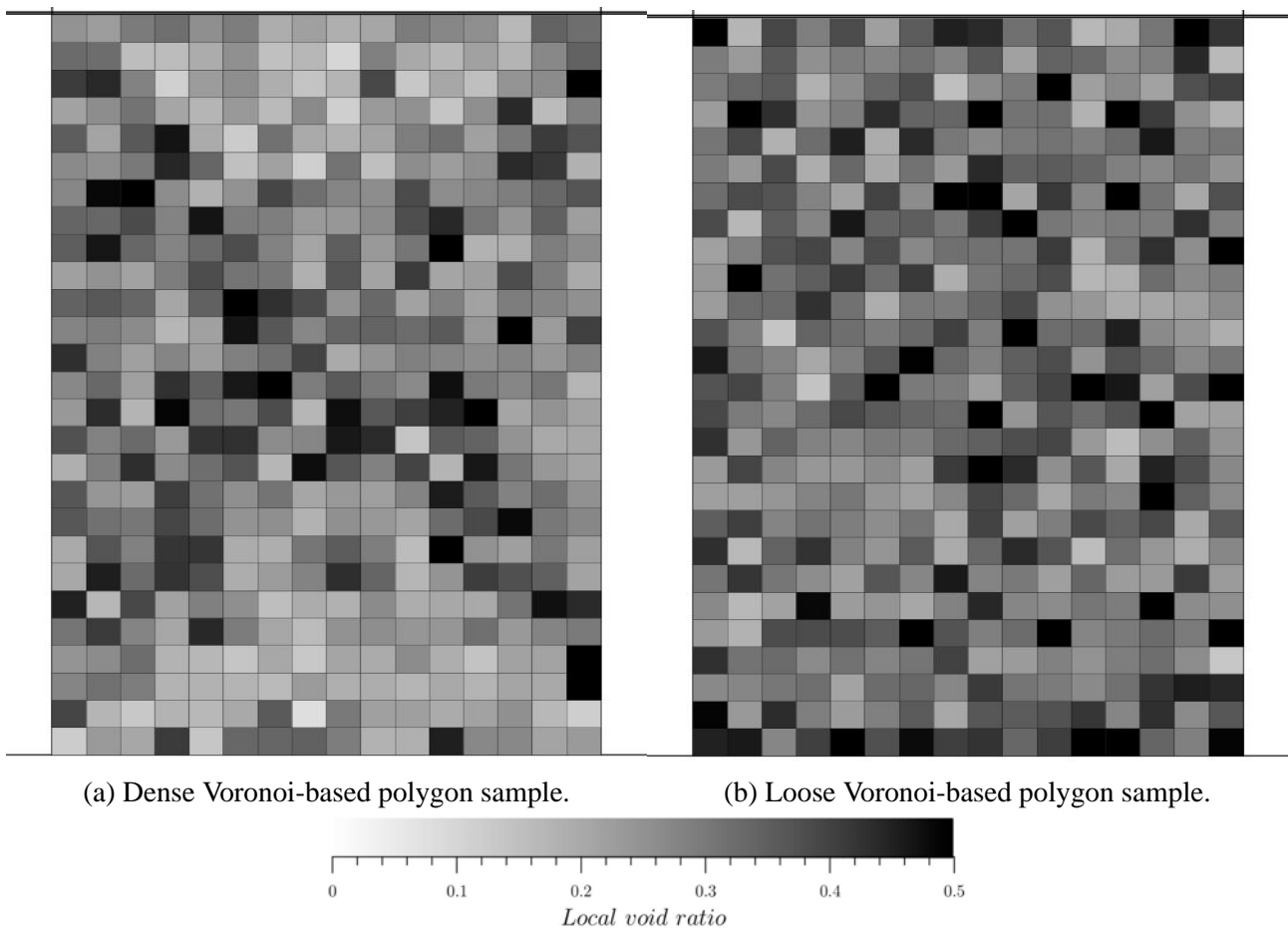Figure 5.33: Sample local void ratio diagram at axial strain 15% for monosized elongated dodecagon samples.

(a) Dense polysized elongated dodecagon sample.   (b) Loose polysized elongated dodecagon sample.
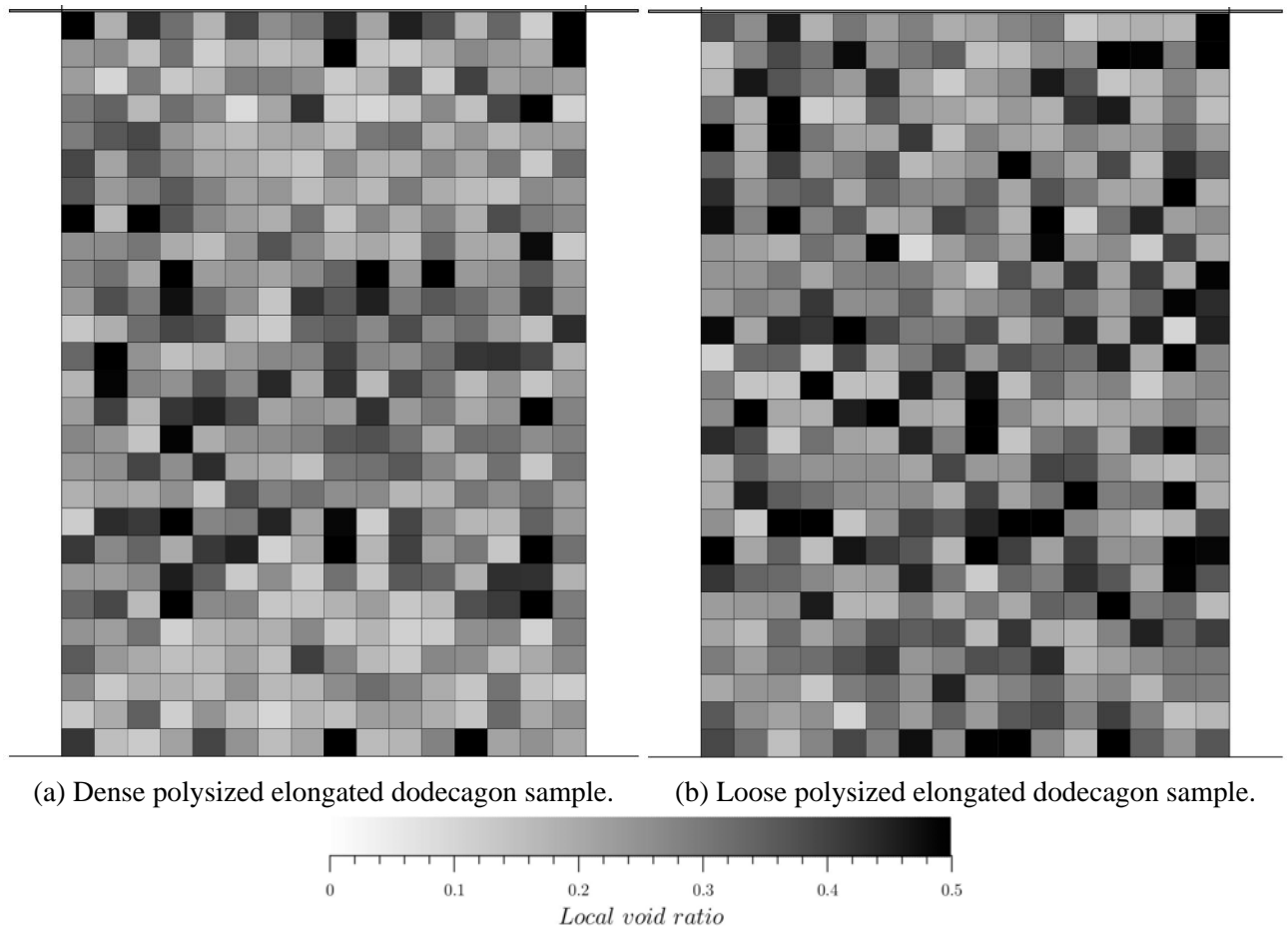
Figure 5.34: Sample local void ratio diagram at axial strain 15% for polysized elongated dodecagon samples.

(a) Dense Voronoi-based polygon sample.   (b) Loose Voronoi-based polygon sample.

Local void ratio

Figure 5.35: Sample local void ratio diagram at axial strain 15% for Voronoi-based samples.

Particle contact numbers

Particle contact numbers in critical states are illustrated in Figure 5.36 to Figure 5.40. Mean coordination numbers are relatively lower in shear band zones than elsewhere. Particles within the top and bottom zones possess more contacts with surrounding particles. This agrees with previous discussions that in the rupture zones particles experience more rotations, and local volumetric strain rates and void ratios exhibit larger values.

(a) Dense polysized disc sample.   (b) Loose polysized disc sample.
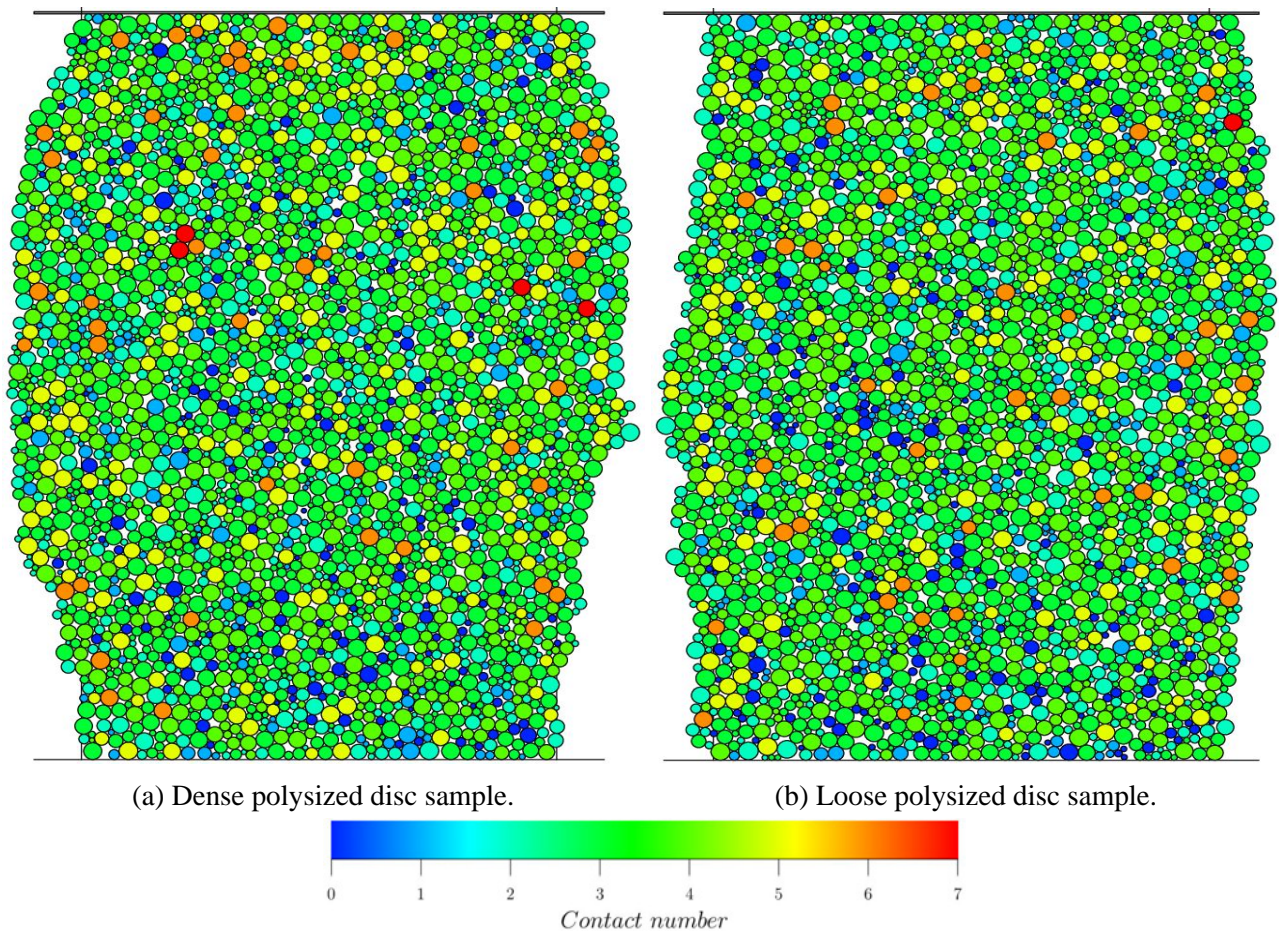
Figure 5.36: Particle contact number diagram at axial strain 15% for polysized disc samples.

(a) Dense monosized non-elongated dodecagon sample.(b) Loose monosized non-elongated dodecagon sample.
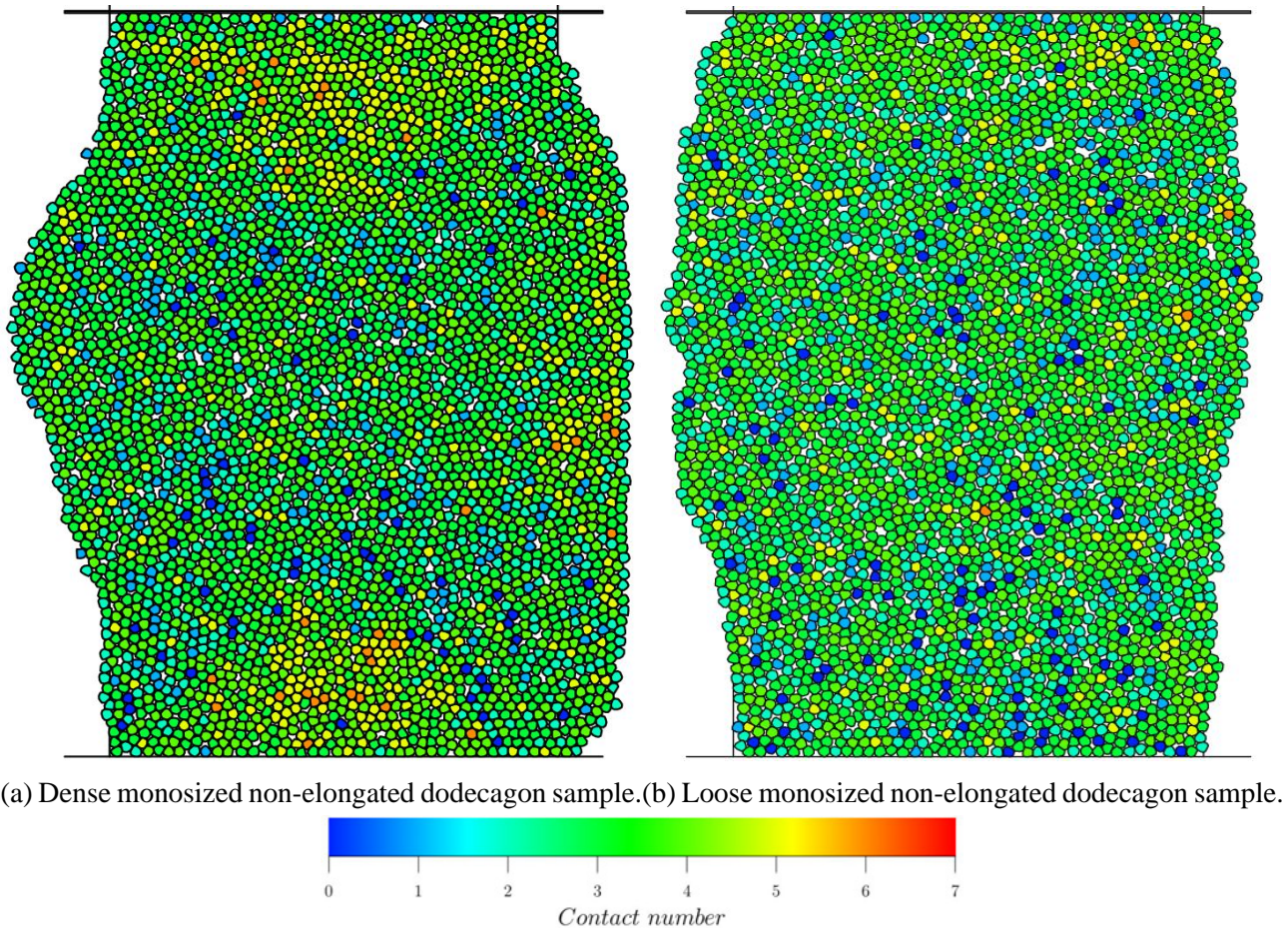
Figure 5.37: Particle contact number diagram at axial strain 15% for monosized non-elongated dodecagon samples.

(a) Dense monosized elongated dodecagon sample. (b) Loose monosized elongated dodecagon sample.
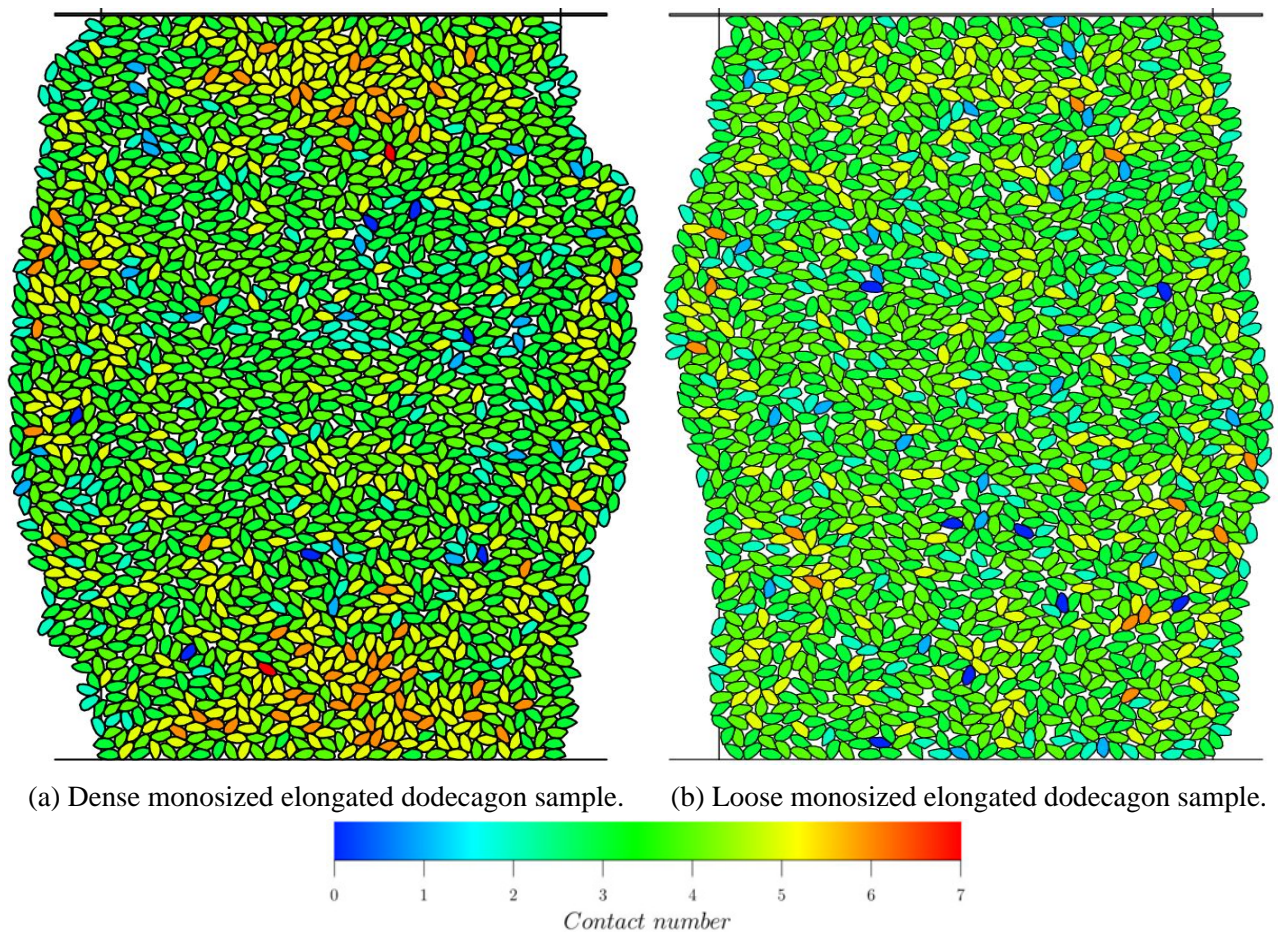
Figure 5.38: Particle contact number diagram at axial strain 15% for monosized elongated dodecagon samples.

(a) Dense polysized elongated dodecagon sample.   (b) Loose polysized elongated dodecagon sample.
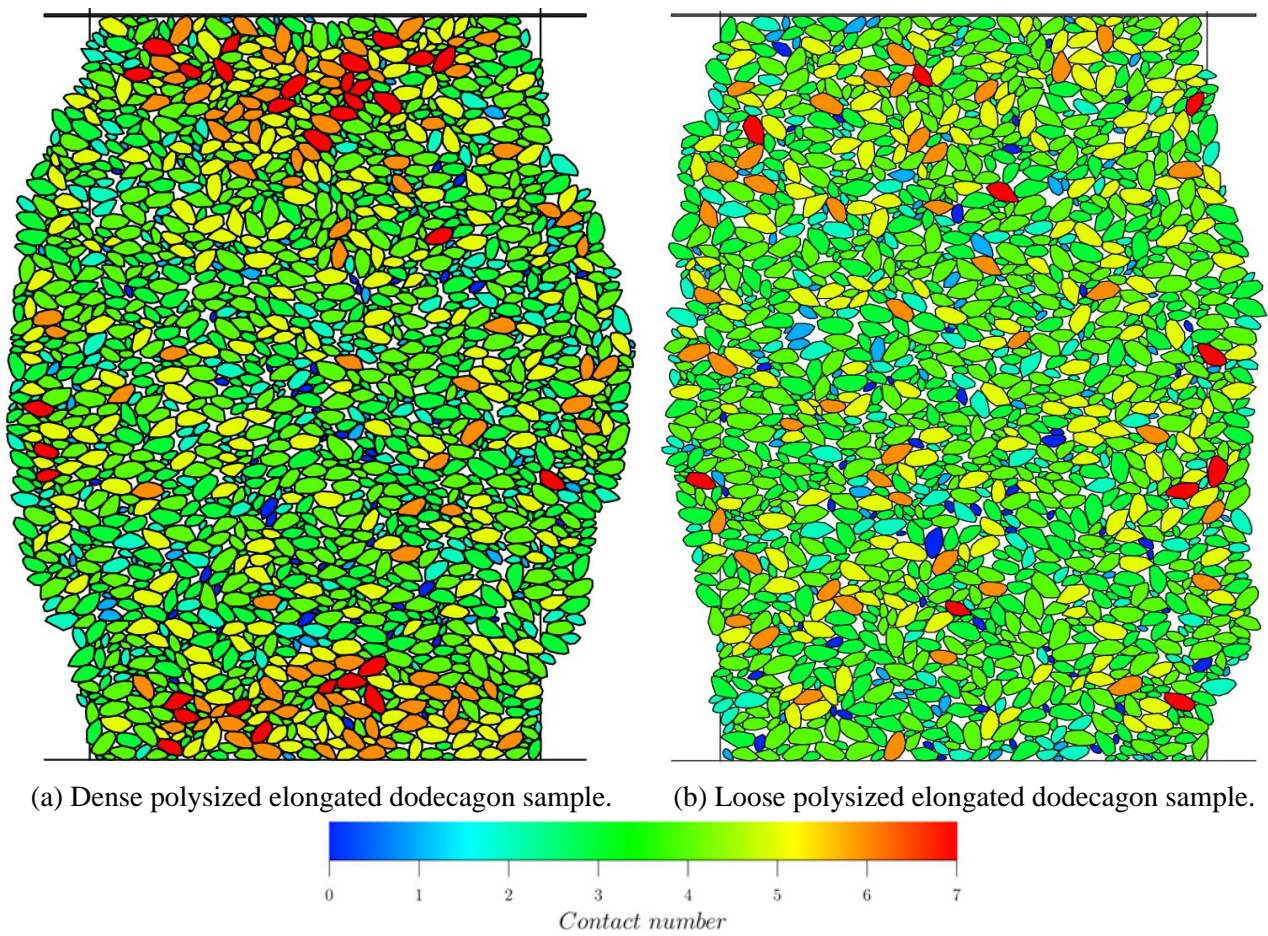
Figure 5.39: Particle contact number diagram at axial strain 15% for polysized elongated dodecagon samples.

(a) Dense Voronoi-based polygon sample.   (b) Loose Voronoi-based polygon sample.
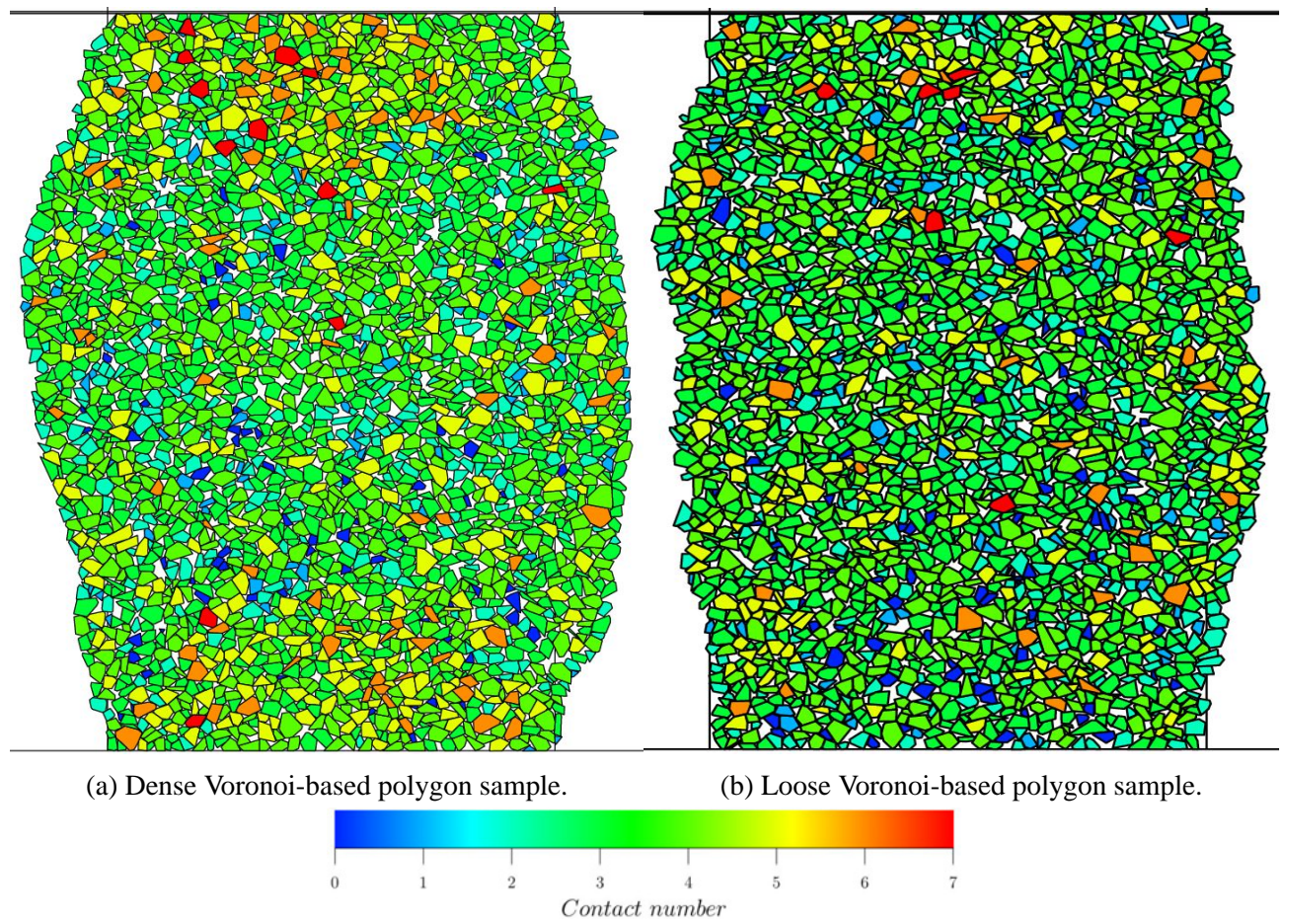
Figure 5.40: Particle contact number diagram at axial strain 15% for Voronoi-based samples.

Normal contact force chains

Normal contact force chains can also be obtained by Box2D as shown in Figure 5.41 to 5.45 and Figure 5.46 at axial strain 15% and 2% respectively. The contact forces transmit from the top platen downwards and gradually dissipate in the radial direction. In the rupture zones where significant sliding and rotating occur for the denser packings, the normal contact forces are relatively weaker and this is because the particles are sliding along a direction deviated from the vertical shearing direction. At axial strain of 2% at which all the initially dense samples are developing towards the peak deviatoric stress, a greater volume of contacts are developed along the vertical direction, and in greater magnitude as illustrated in Figure 5.46. When looking at Figure 5.46a and 5.46d, it is observed that relatively large local space without normal contact force chains exist and this proves that contact force are more likely to be transmitted among larger particles. Table 5.9 lists the average normal contact forces comparing their values at peak and critical states for samples in different initial density states. Untouched contacts are excluded in the calculation. The initially dense samples can develop higher average normal contact forces at peak states and this is also shown in 5.46. The angular particles are able to undertake larger normal contact forces as comparing the elongated dodecagons and the Voronoi-based polygons with the discs and non-elongated dodecagons because less relative rotation between particles will help form stabler contacts. By comparing the monosized elongated dodecagons with the polysized elongated dodecagons, it is found that the particle size variation contributes to produce greater normal contact force chains as smaller particles position among larger particles, not involved into contact force transmission. Because the particle shape variation increases the possibility to form unstable contacts which can disturb surrounding skeletons once being forced, the normal contact forces produced among Voronoi-based polygons are not as strong as those developed among polysized elongated dodecagons. In terms of the initially loose samples, the average normal contact forces in critical states are higher as their mobilised strengths are still growing at axial strain 2%. By studying the influences of particle shape effects on contact force chains, a better understanding of the particle crushing phenomena can be obtained. Crushing results from excessive contact forces rather than soil grain load bearing capacity in reality, as particle crushing as shearing progresses will change soil microscopic skeletons and as a result dramatically weaken the soil strength. However, particle crushing does not need to be worried about in this study because of the rather low stress levels simulated compared with the real condition.
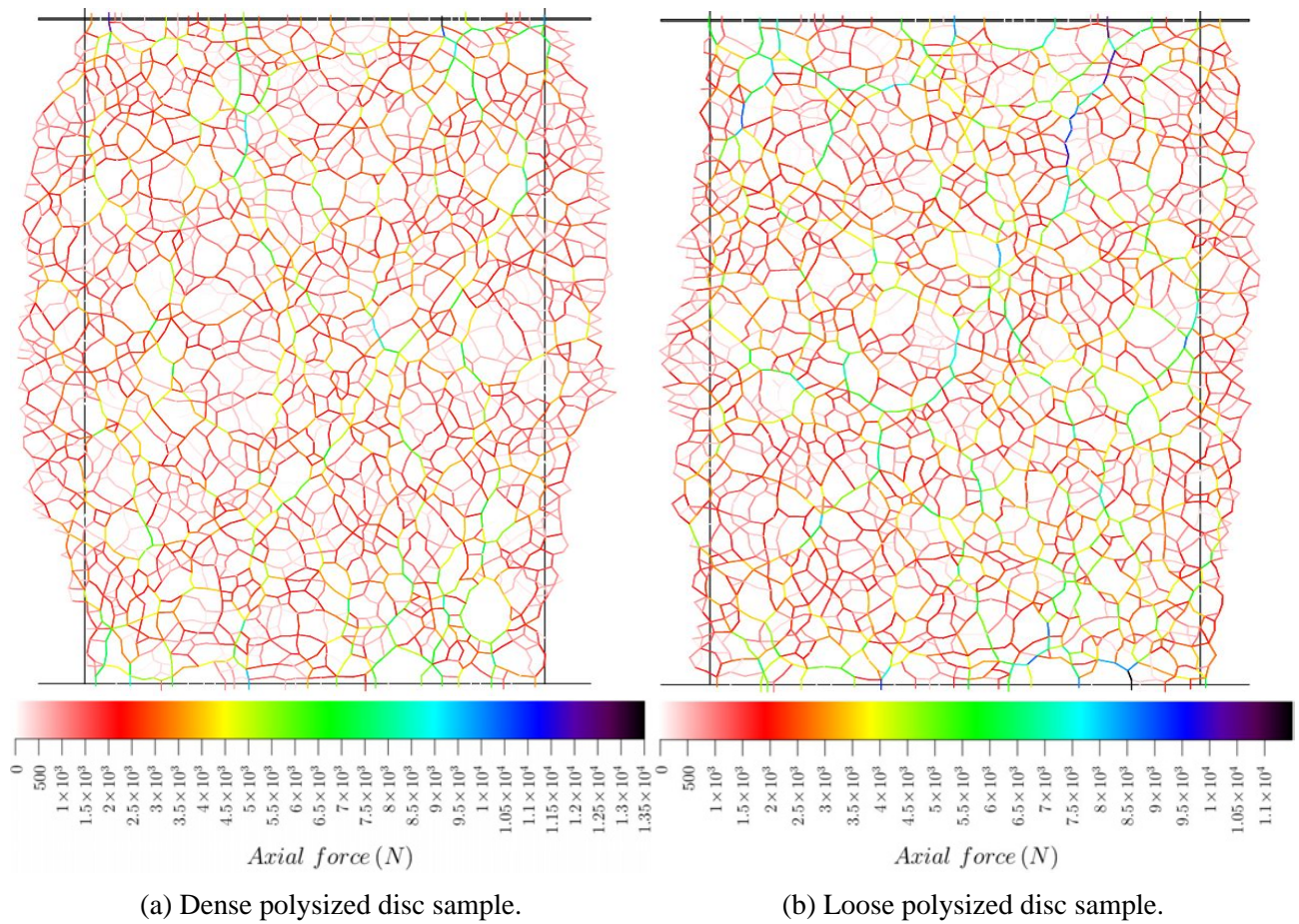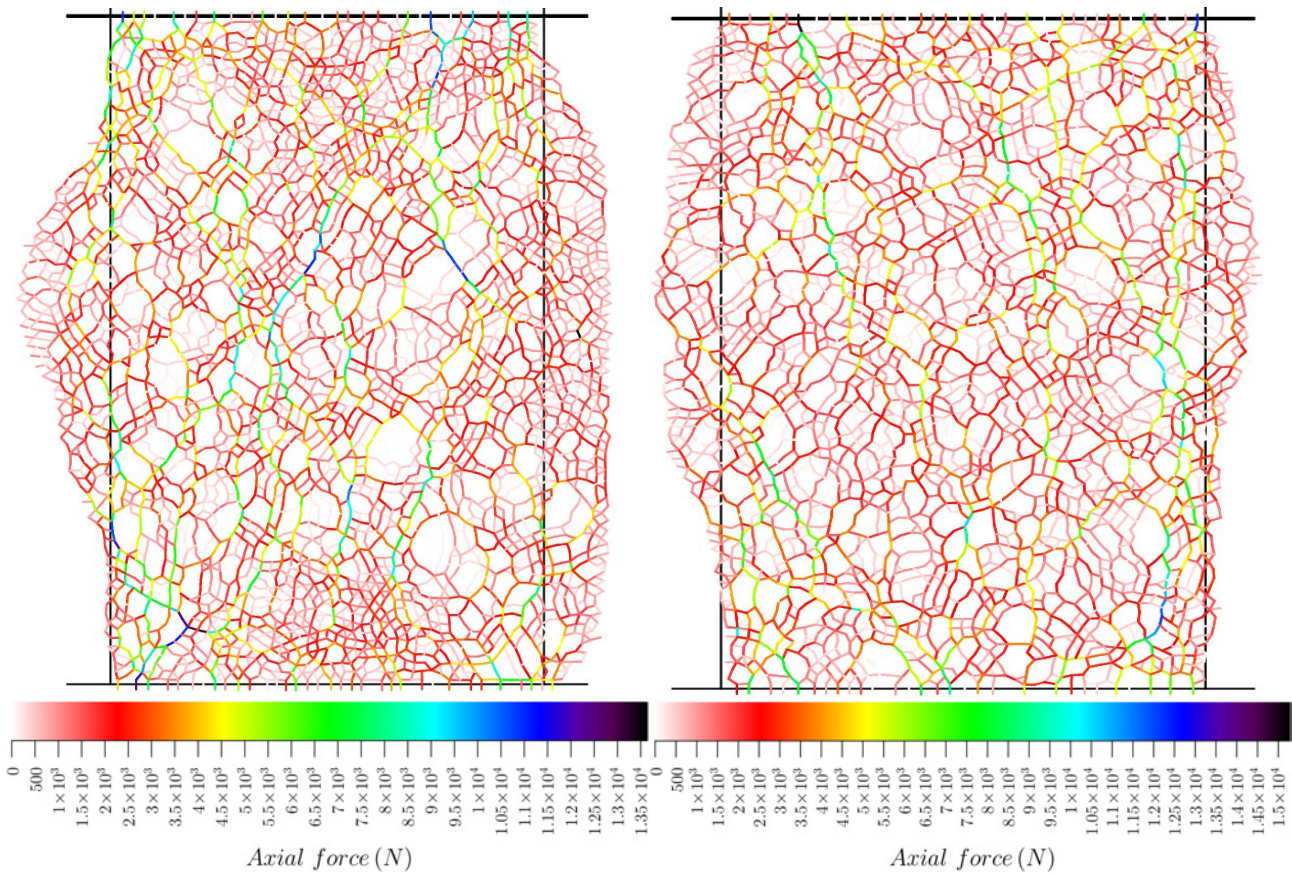
(a) Dense polysized disc sample.

(b) Loose polysized disc sample.

Figure 5.41: Particle contact force chains at axial strain 15% within polysized disc samples.

Table 5.9: Average normal contact forces at peak and critical states.

Packings	States	Average contact forces (N)	
		Dense	Loose
Polysized discs	peak state	2210.89	1804.06
	critical state	1915.14	1994.82
Monosized non-elongated dodecagons	peak state	2482.67	1922.1
	critical state	1880.44	1830.24
Monosized elongated dodecagons	peak state	3243.01	2292.88
	critical state	3091.50	3005.51
Polysized elongated dodecagons	peak state	4235.48	2583.78
	critical state	4140.00	3178.37
Voronoi-based polygons	peak state	3418.76	2653.28
	critical state	2536.55	3036.41

(a) Dense monosized non-elongated dodecagon sample.(b) Loose monosized non-elongated dodecagon sample.

Figure 5.42: Particle contact force chains at axial strain 15% within monosized non-elongated dodecagon samples.
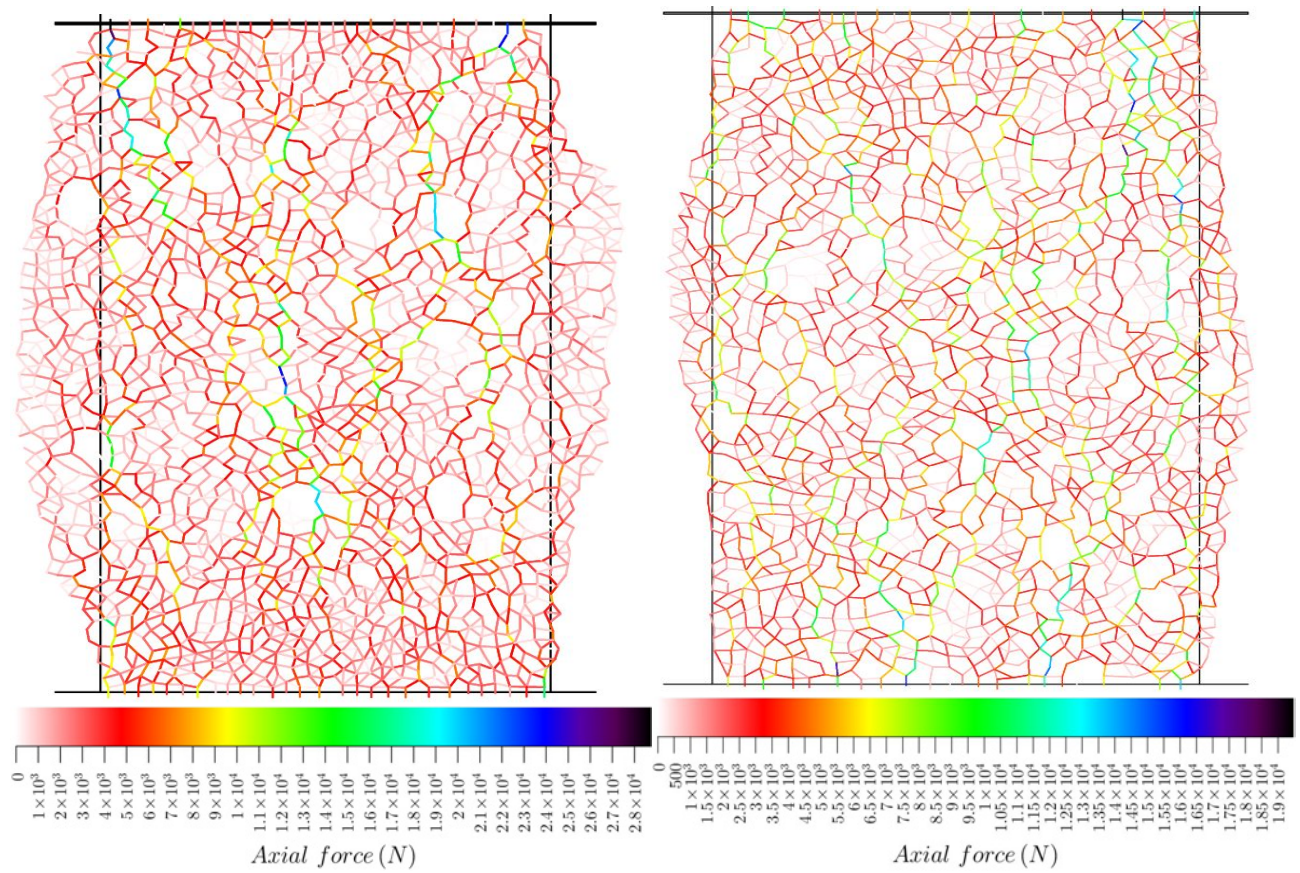
(a) Dense monosized elongated dodecagon sample.   (b) Loose monosized elongated dodecagon sample.
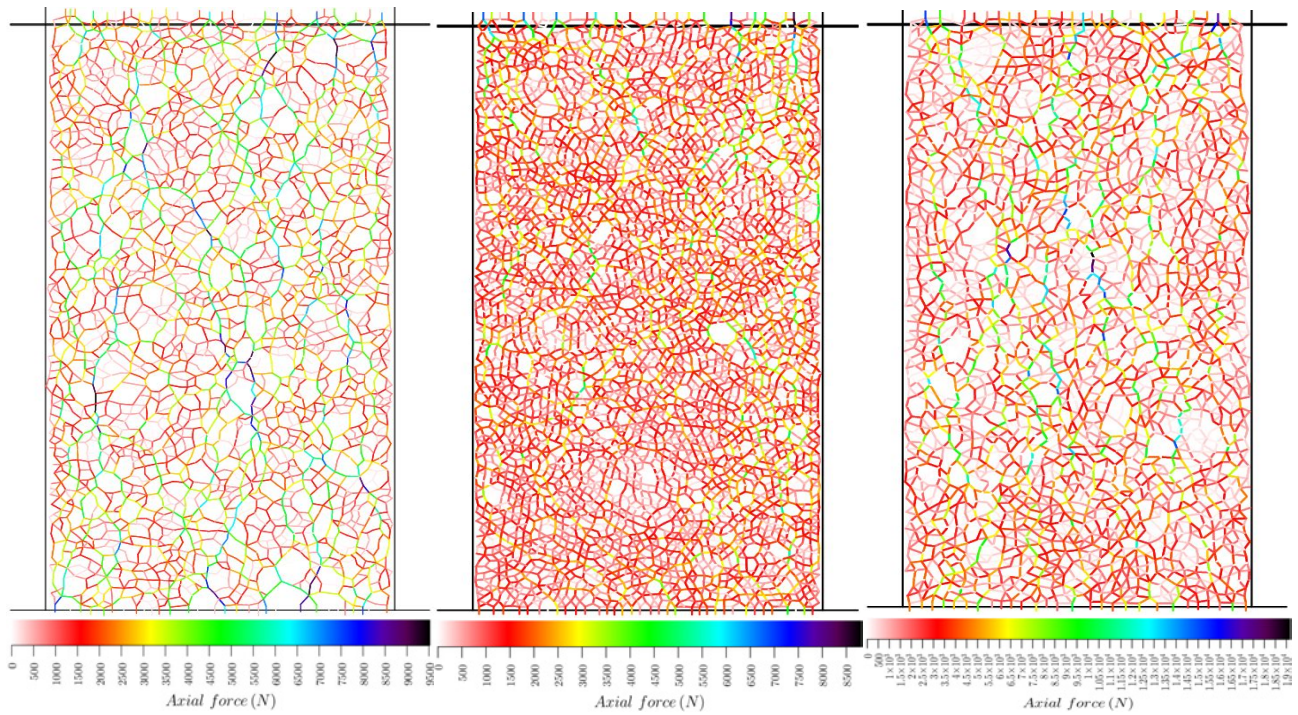
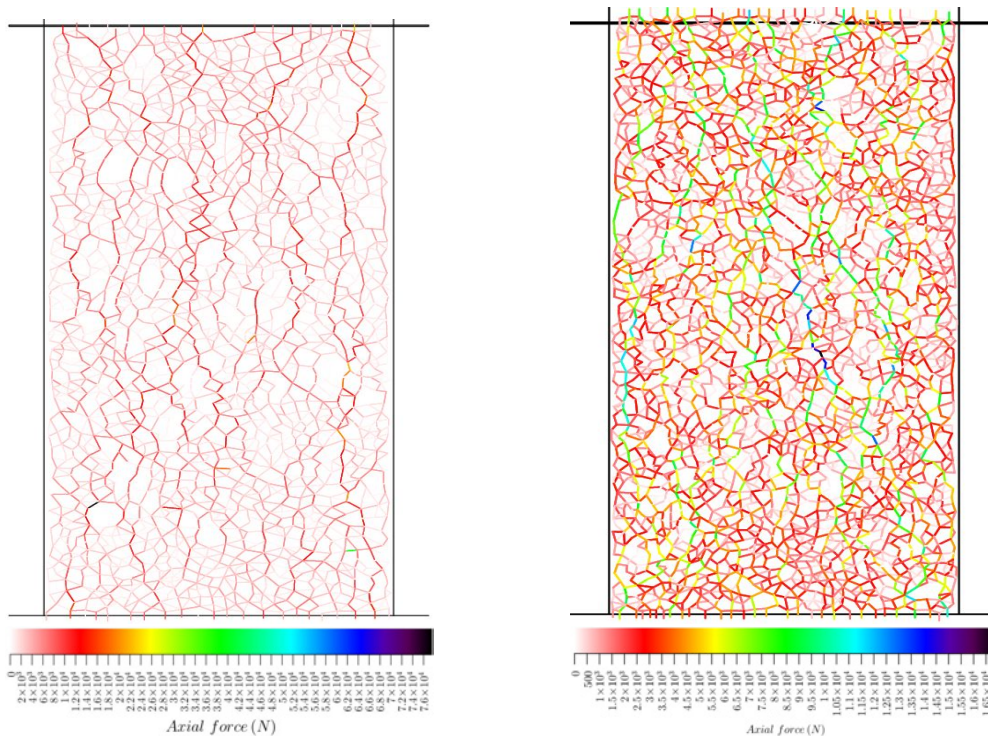Figure 5.43: Particle contact force chains at axial strain 15% within monosized elongated dodecagon samples.
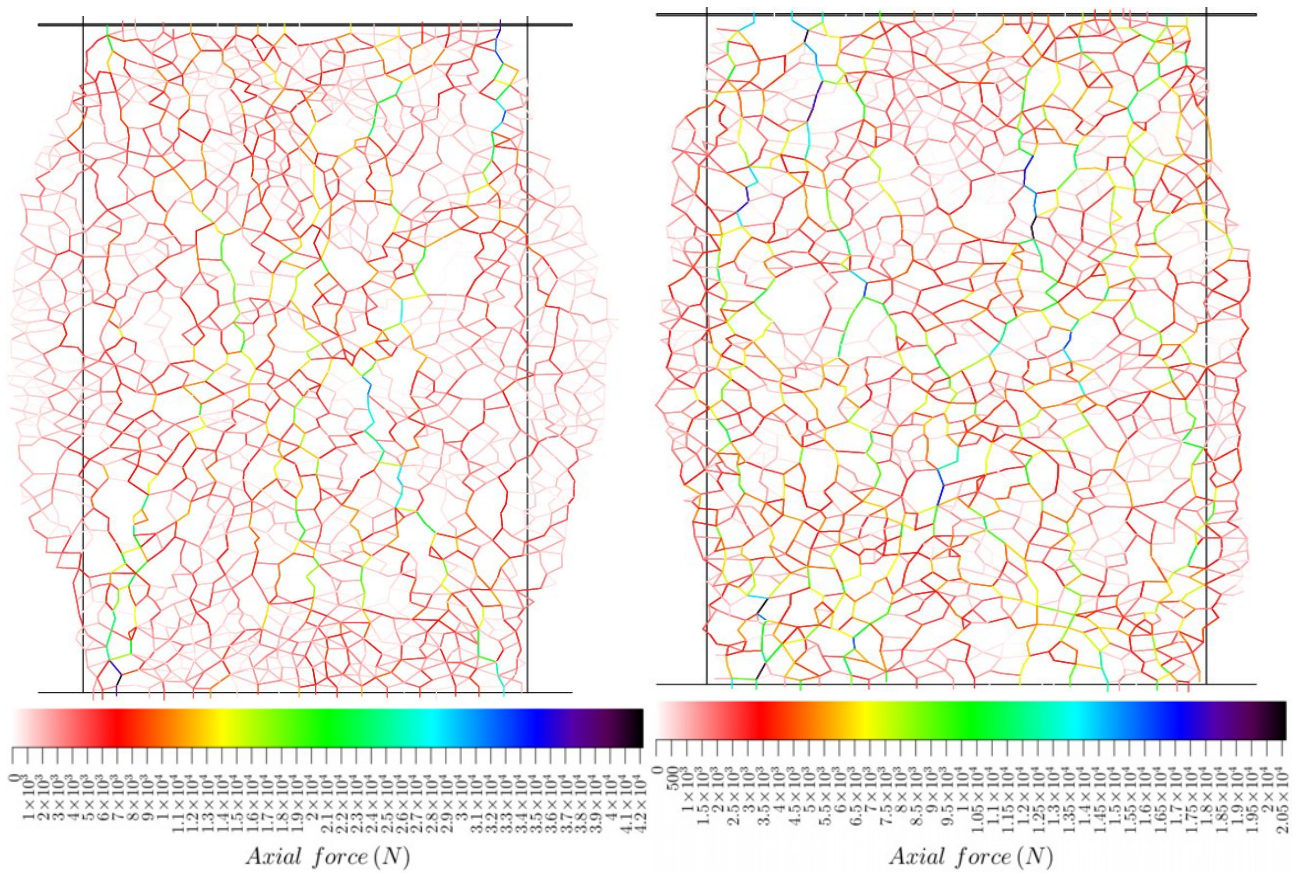
(a) Dense polysized elongated dodecagon sample.

(b) Loose polysized elongated dodecagon sample.

Figure 5.44: Particle contact force chains at axial strain 15%c within polysized elongated dodecagon samples.

(a) Dense Voronoi-based polygon sample.

(b) Loose Voronoi-based polygon sample.

Figure 5.45: Particle contact force chains at axial strain 15% within Voronoi-based samples.

(a) Dense polysized disc sample.

(b) Dense monosized non-elongated dodecagon sample.

(c) Dense monosized elongated dodecagon sample.

(d) Dense polysized elongated dodecagon sample.

(e) Dense Voronoi-based sample.

Figure 5.46: Particle contact force chains at axial strain 2%.

5.4 Packing effects

In addition to particle shape effects, packing effects are also crucial factors influencing granular soil behaviours. In this part, two kinds of Voronoi packings (as shown in Figure 5.47) were built by constructive methods directly in situ to obtain a packing without void (Figure 5.47a) and the other with voids but still with the original edge-edge contacts by modifying particles whereby particle corners are removed by a cutting-edge approach (Figure 5.47b) so as to study the perfect packing effects (perfectly fill a two-dimensional domain) and contact effects (i.e. edge-edge contact area variation) on granular soil properties. To obtain the voids in Figure 5.47b, each vertex connected by one or more polygons in Figure 5.47a were replaced by a polygon of which the edge number is equal to the polygon number surrounding the vertex. The results will also be compared with those obtained by simulations in which packings were created by dynamic methods (particles were dropped into the biaxial container bottom boundary under gravity).
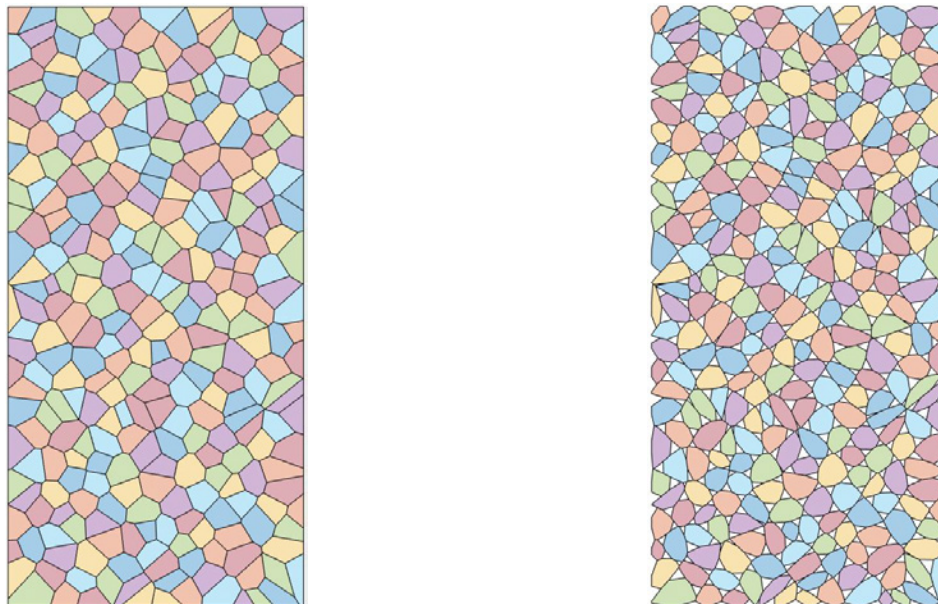
(a) Original Voronoi packing without void.   (b) Voronoi-based particles modified by cutting-edge.

Figure 5.47: Schematic graphs of Voronoi packings.

The average particle circularities and void ratios after the confining process are listed in Table 5.10. The Voronoi tessellations were constructed based on the initial seeds allocated by the Halton sequence algorithm. 3200 particles were created for each packing involved in simulation. The system parameter set-up is identical to the description in Table 5.1 except that the axial strain limit is extended to 20%. The average circularities are quite similar and the void ratio changes because of the confining procedure are rather limited due to the nature of the packings established by the constructive method. The in-situ Voronoi packings following application of the confining stress are shown in Figure 5.48 and the original particle and contact arrangements were almost undisturbed. The negligible void ratio existing in the Voronoi packing in Figure 5.48a was brought by the contact skin effects.

Figure 5.49 plots how the mobilised angle of friction changes as shearing continues. The peak

Table 5.10: Particle and packing parameters before shearing starts.

| Packings	Particle and packing parameters after confining	
	Particle circularity	Packing void ratio
In-situ built Voronoi packing without void (1)	0.569	0.0036
In-situ built Voronoi packing with void (2)	0.614	0.1478
Voronoi packing built by dynamic method using particles from (1)	0.569	0.1624
Voronoi packing built by dynamic method using particles from (2)	0.614	0.1564

(a) Voronoi packing without void. (b) Voronoi packing with void.
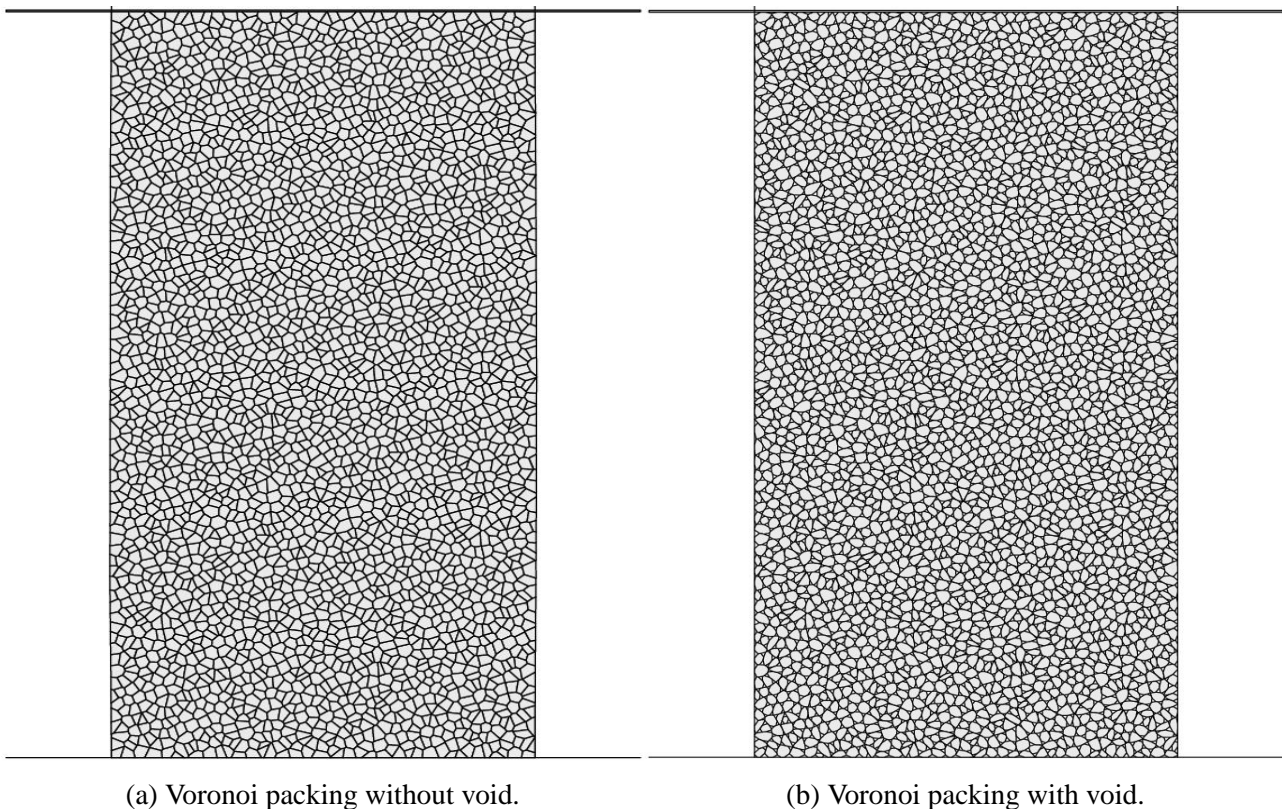
Figure 5.48: Voronoi packings built by constructive methods after confining process.

strengths for both samples initially established by in-situ Voronoi-based well-packed particles are reached quite earlier (at around 0.37% and 0.17%) compared with the other two samples (at around 1%) made by deposited Voronoi-based particles. The two well-packed Voronoi samples reach far higher values of peak strength, which are $72°$ (3.078 in tan) and $53°$ (1.33 in tan) respectively, than the other two samples, which are around $37.6°$ (0.77 in tan) and $36.1°$ (0.729 in tan) respectively. It is important to note that the initial void ratios before shearing starts for the two samples created by the deposition approach and the one sample created by in-situ built Voronoi packing with void are very

close, however, the in-situ Voronoi packing exhibits significantly larger peak strength than the other
two samples. Although there are disparities in magnitudes of void ratio, these disparities can not be
responsible for the large differences in peak strengths if comparing the two samples created by the
deposition approach. Therefore, the contact condition is the primary reason causing the peak strength
difference. The global mean coordination number is plotted against axial strain in Figure 5.50. The
two samples prepared by in-situ Voronoi packings take the values of 5.08 and 4.90 after the confining
process terminates, while the mean coordination numbers of the other two samples are 4.26 and 4.37
just after the shearing starts. The large global mean coordination number difference explains why
the samples exhibit different peak strengths even though their initial void ratios are similar. This also
proves that the initial mean coordination number is a crucial parameter determining the peak strength
able to be reached besides the initial packing density condition. The packing effects are not observed
in critical states and the Voronoi packings using the same group of particles (1) and (2) exhibit $26.2°$
(0.49 in tan) and $24.0°$ (0.45 in tan) in the critical friction angle respectively, because of the particle
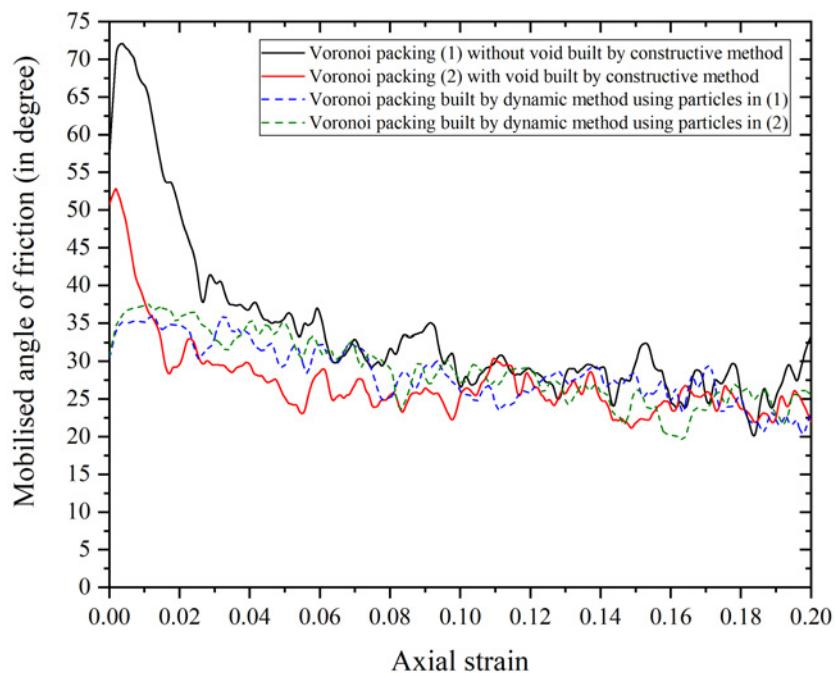shape effects (circularity).

Figure 5.49: Mobilised friction angles for samples built by different packings.

The two in-situ built Voronoi packings possess much greater initial mean coordination numbers
(may not be equal because the mean coordination number was measured after confining), neverthe-
less their values drop rapidly until the peak strengths are reached, followed by slight increases until
critical state values are achieved as shown in Figure 5.50. This resilient behaviour in global mean
coordination number is not observed for the other two Voronoi-based samples made by the deposition
approach. In addition, the well-packed Voronoi sample without voids needs a longer time to rearrange

its contact conditions than the other sample with voids. The critical state global mean coordination number is dependent on the particle circularity and initial packing contact and density conditions. Although there are discrepancies in mean coordination number at the critical states, it is hard to distinguish the critical strengths for these samples in Figure 5.49. Similar with the mean coordination number developments, the well-packed Voronoi packing with void reaches the critical state prior to the one without void.
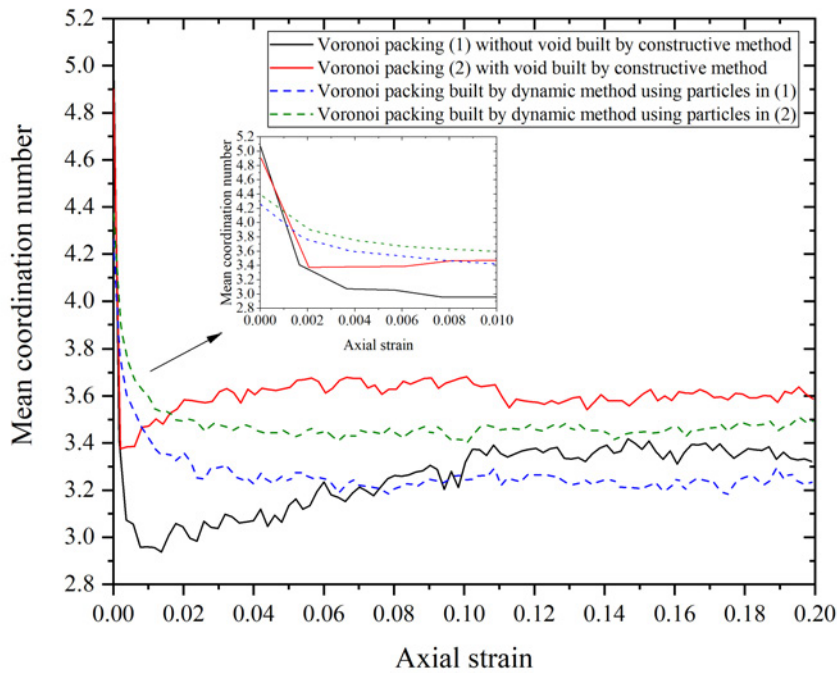
Figure 5.50: Mean contact number evolutions for samples built by different packings.

Figure 5.51 to 5.54 illustrate the particle total rotation courses for the four packings at different axial strains. Both of the well-packed Voronoi packings develop comparatively clearer zones within which particles rotate more than others and these zones are further developed into rupture zones in the critical states. The rupture zones in the well-packed Voronoi packings are much more distinguishable than those in the other two samples and their widths are also smaller especially in the well-packed Voronoi packing without void. Due to larger global mean coordination number at the onset of shearing, inter-particle rotations are inhibited in the well-packed Voronoi samples and this causes rotations occurring mainly within the rupture zones which are developed consistently at the same locations from the beginning of shearing. In contrast, the particle rotations are distributed more widely and randomly in other two samples, and this is one of the reasons causing relatively wider shear bands. The important thing to note is that the maximum and average particle rotations within the shear band regions in the well-packed Voronoi packings are larger than those in other two samples. This indicates that the rapid drops of mean coordination numbers occurred in the shear band zones, along with dilatancy in volume providing space for skeleton rearrangements. From the perspective of energy

balance, the energy dissipated by particle rotation is reduced outside the failure zones, and this must be compensated by that within the failure zones, causing greater particle rotations. The shear band angles for the well-packed Voronoi packings and the other two packings are 53° and 45° respectively. As discussed in section 5.3, the theoretical value for the shear band angle relative to the horizontal direction should be around 58° derived from the Mohr-Coulomb failure criteria, and the values for the well-packed Voronoi packings are rather closer to the theoretical value and that is because the theoretical value is based on the continuum mechanics and the original well-packed Voronoi packings can perfectly fill in a two-dimensional domain.

(a) Axial strain 0.4%.
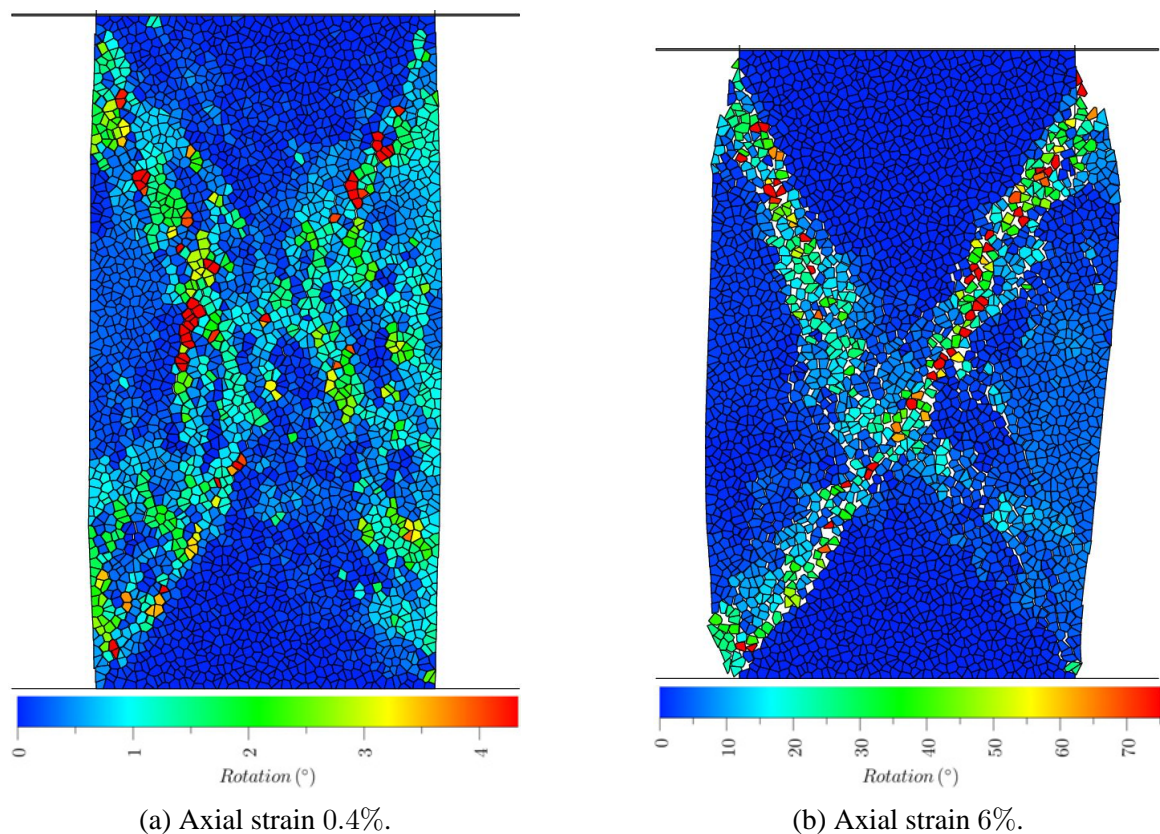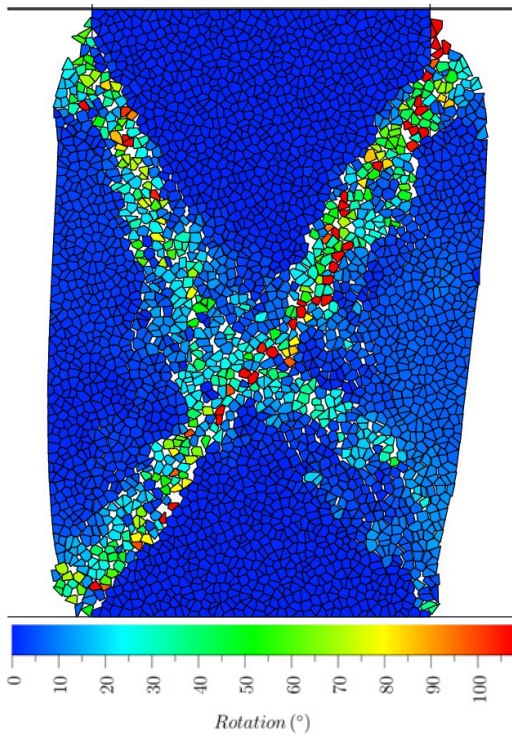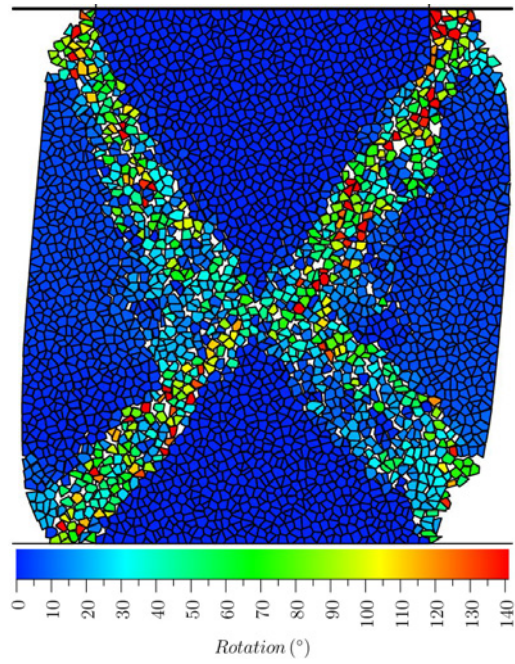

(b) Axial strain 6%.

Figure 5.55 plots the particle contact numbers for each well-packed Voronoi packing at axial strain 20%. It is observed the particles in the triangular zones adjacent to the top and bottom boundaries possess greatest contact numbers and the particles within the shear band zones possess the least contact numbers. This proves the beforementioned conclusion that the shear band zones start to dilate from shearing begins providing more space to rearrange and resulting in decrease in mean coordination number and greater inter-particle rotations until failure.

The local volumetric strain rates are also computed and plotted in Figure 5.56. Relatively larger volumetric strain rates are observed mainly distributed over the strain localisation domain in all cases, indicating larger volumetric strains occurring. It is also observed that the positive volumetric strain rates are similar to the negative ones within the whole domains when comparing the red and black circle sizes and amounts, meaning that the volumetric strains are constant in the critical states.
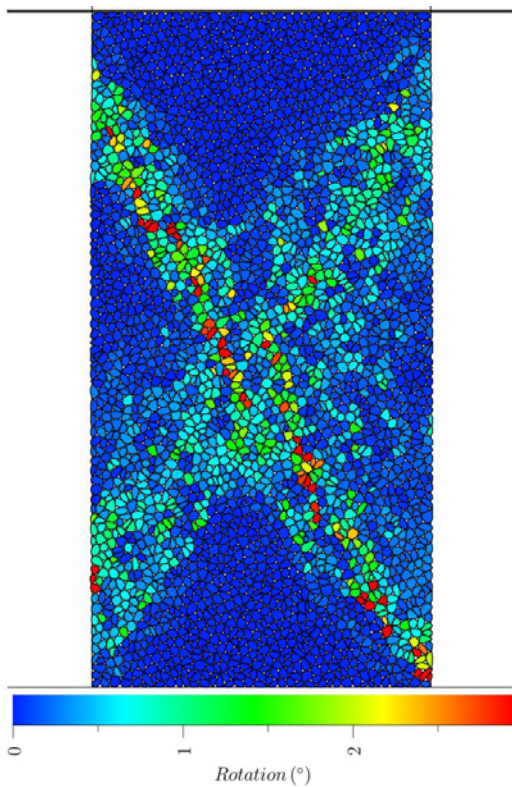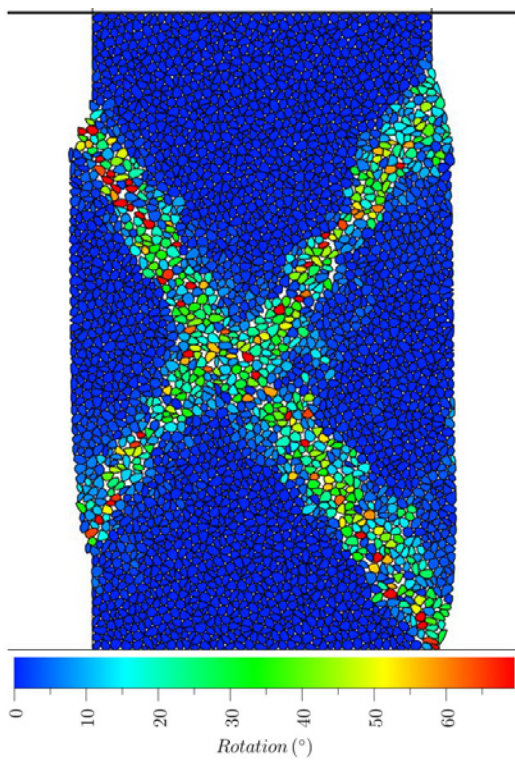
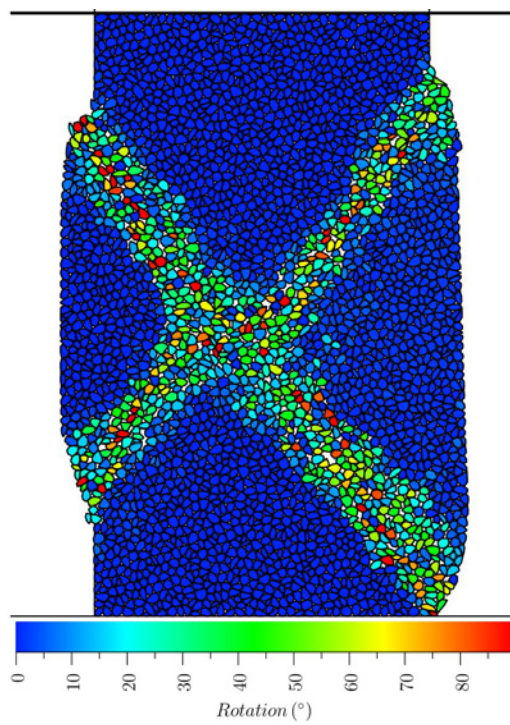(c) Axial strain 10%.

(d) Axial strain 20%.

Figure 5.51: Particle total rotation diagram for in-situ Voronoi packing without void.
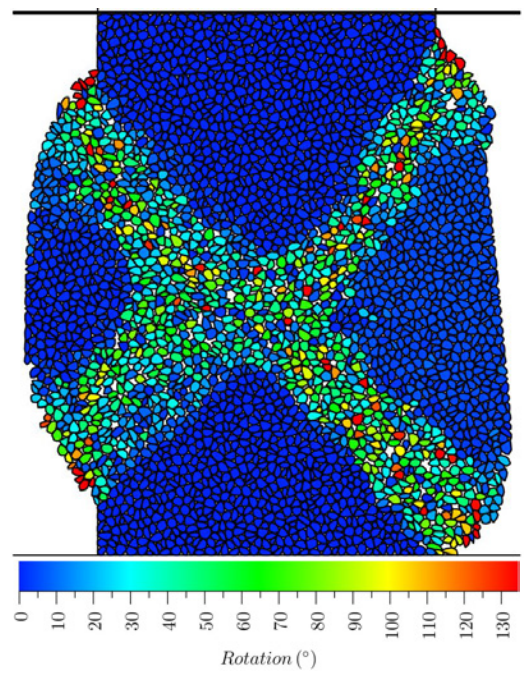

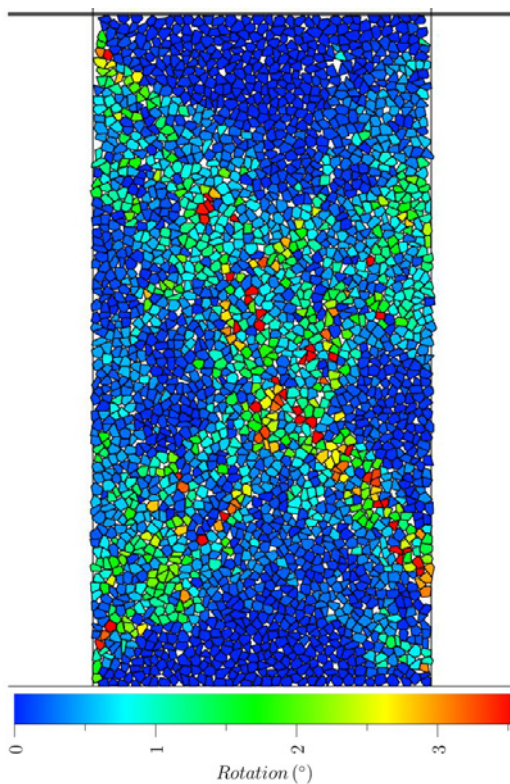(a) Axial strain 0.2%.

(b) Axial strain 6%.
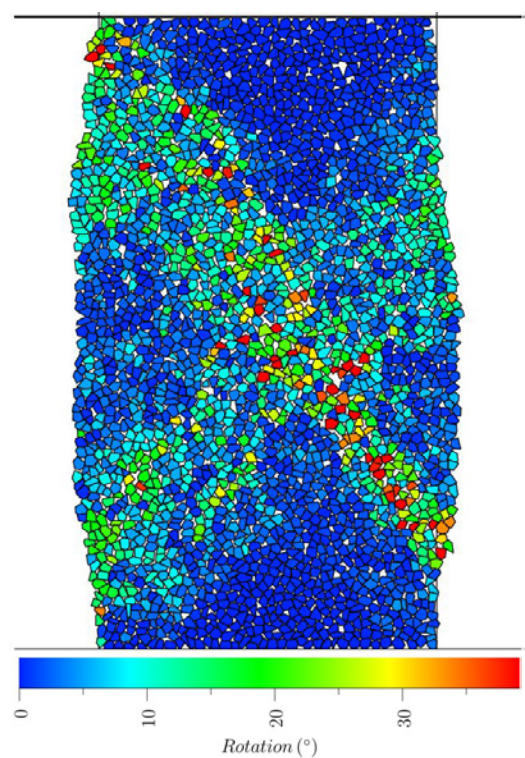
(c) Axial strain 10%.

(d) Axial strain 20%.

Figure 5.52: Particle total rotation diagram for in-situ Voronoi packing with void.
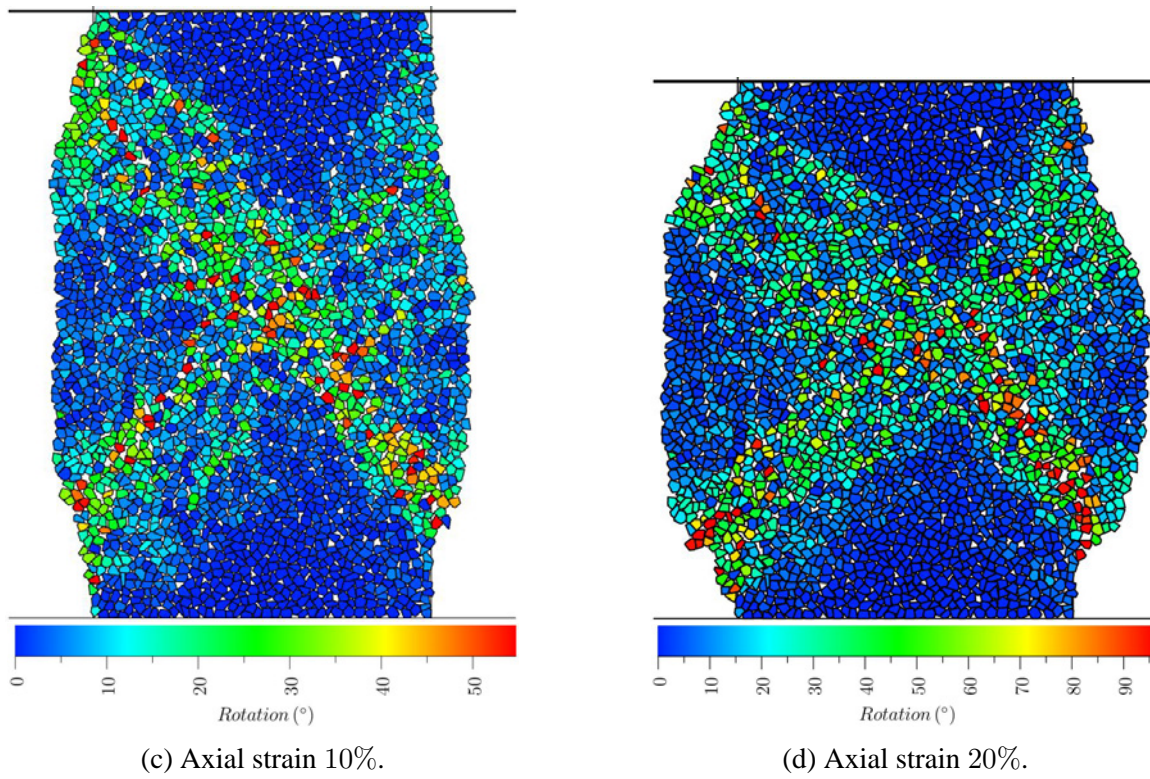

(a) Axial strain 0.4%.

(b) Axial strain 6%.

(c) Axial strain 10%.

(d) Axial strain 20%.

Figure 5.53: Particle total rotation diagram for Voronoi packing (1) prepared by deposition.

(a) Axial strain 0.4%.

(b) Axial strain 6%.

(c) Axial strain 10%.
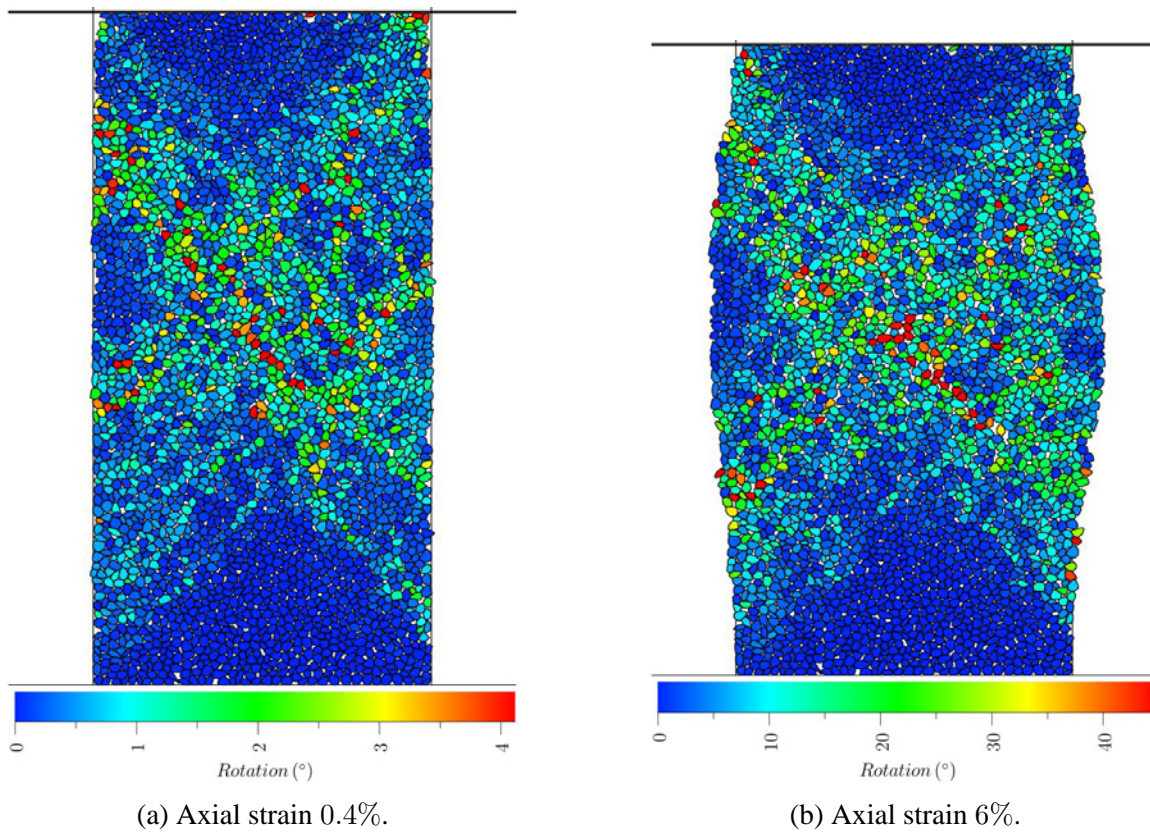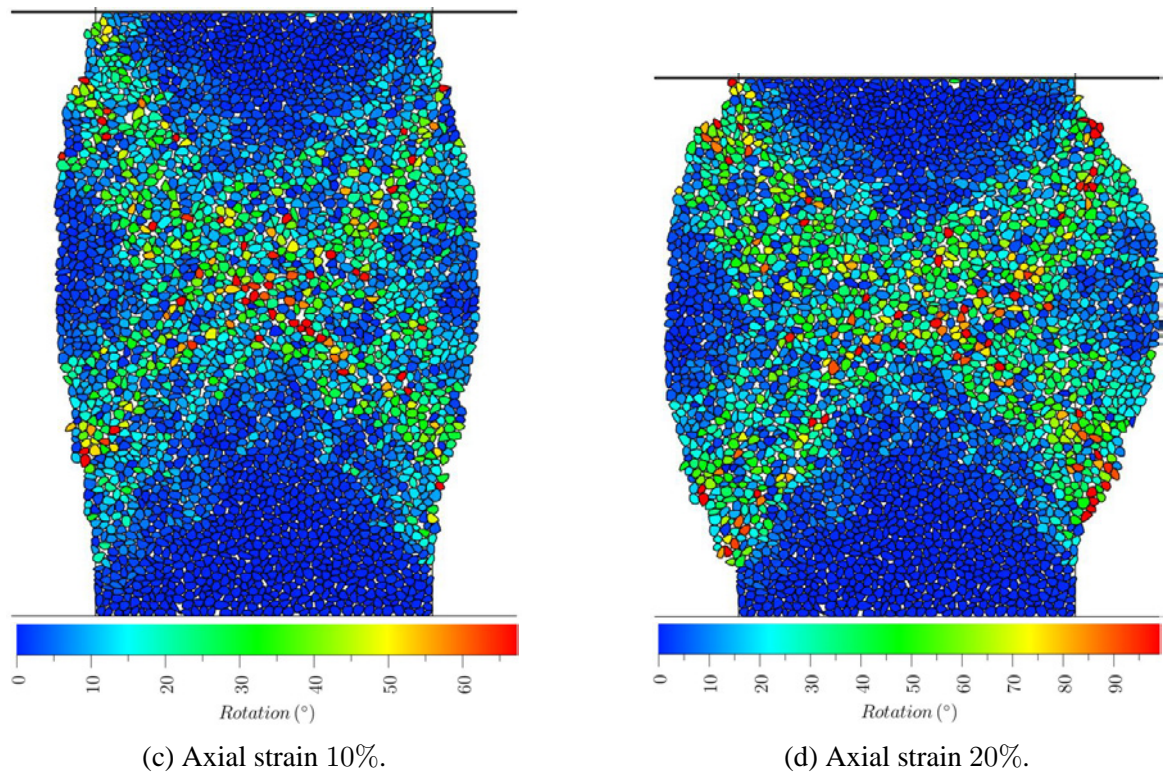
(d) Axial strain 20%.

Figure 5.54: Particle total rotation diagram for Voronoi packing (2) prepared by deposition.

(a) Voronoi packing without void.

(b) Voronoi packing with void.
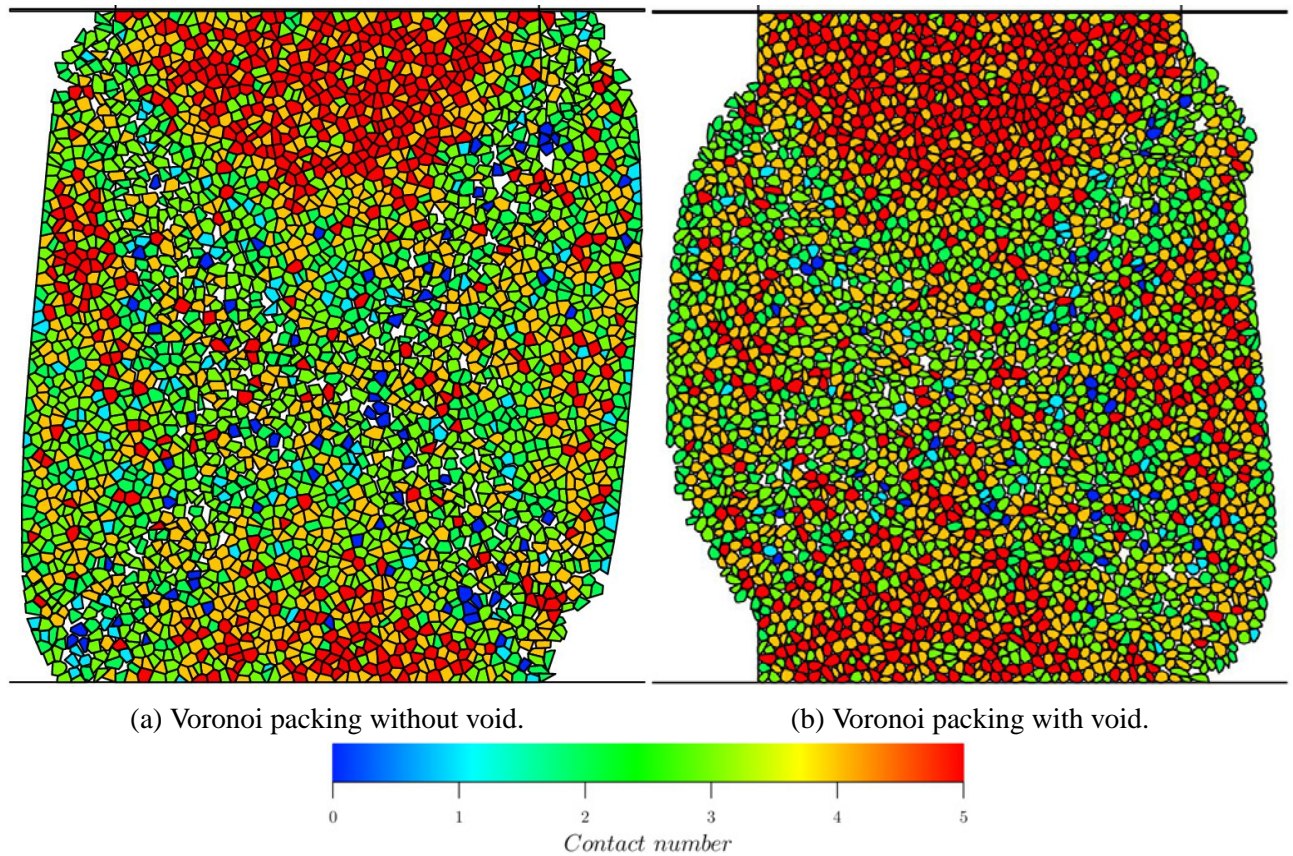
Figure 5.55: Particle contact numbers for Voronoi packings built by constructive method at axial strain 20%.

(a) Voronoi packing built in situ without void (1).

(b) Voronoi packing built in situ with void (2).

(c) Voronoi packing built by deposition using particles in (1).

(d) Voronoi packing built by deposition using particles in (2).

+0.01 −0.01

Figure 5.56: Local volumetric strain in a single time step at axial strain 20%.

5.5   Summary

In this chapter, five different particle shapes were deposited into granular packings of different initial densities under gravity in biaxial test simulation in order to study particle shape effects on both macroscopic and microscopic mechanical beha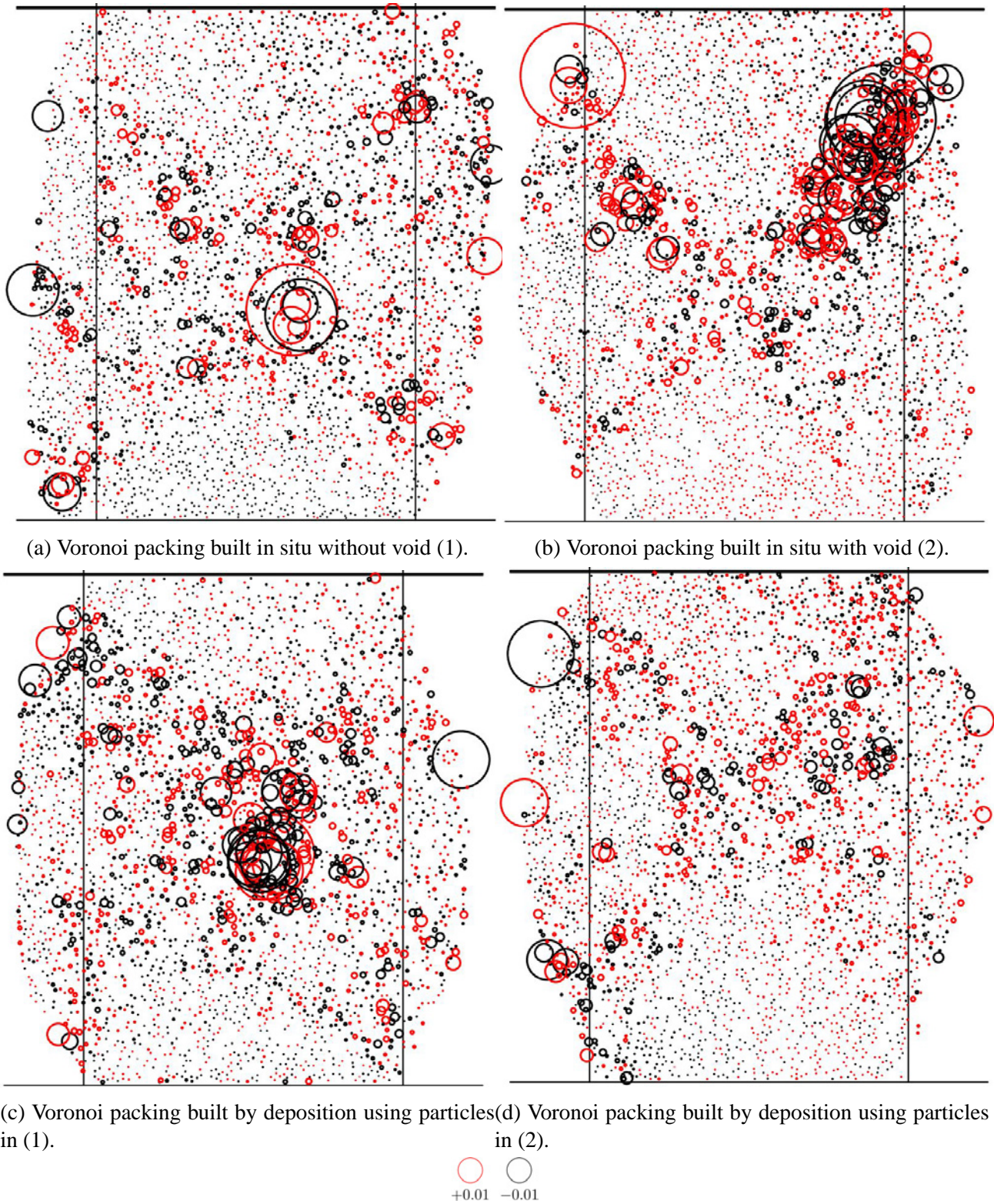viours. The Box2D system settings and the biaxial model set-up were introduced in section 5.2. A series of prior simulations were conducted to study the particle shape effects on initial void ratios and mean coordination numbers of the granular assemblies created by altering the friction coefficients during the deposition process under constant gravity before and after confining. Their mechanical behaviours were investigated and compared both qualitatively (by building new graphical interpretation approaches) and quantitatively. To study the packing effects, in-situ Voronoi-based granular packings were constructed in order to compare their behaviours with the packings created by the deposition approach. This new study can help us to analyse the behaviours of perfectly-packed discrete packings deliberately structured in practice and also provide an approach to investigate continuums by discrete element methods. The main conclusions observed will be summarised in this part.

Particle shape effects on compressibility

The sample compressibility after confining process was studied. It was found that the polysized elongated dodecagon samples possess the greatest compressibility after confining because of their particle shape variation and large particle shape platiness. The monosized elongated dodecagon samples exhibit highest increase in mean coordination number after confining. It was therefore concluded that:

1. Samples made of monosized and monoshaped grains exhibited the most significant increase in inter-particle contact numbers after confining.

2. Particle size and shape variations, lower circularity and inter-particle contact number increase will all contribute to the density increase after being confined.

Particle shape effects on soil strength

Both relatively dense and loose samples for each particle shape in initial density states were created and sheared in biaxial tests until the axial strain reached 15%. It was observed that:

1. The critical shear strength is purely correlated with particle circularity and not found influenced by particle size and shape variations and initial packing density states. More angular particles are inhibited in particle rotation and observed to possess higher critical friction angles.

2. The peak strength is found being irrespective of the particle circularity and merely effected by initial packing density states, however, particle size and shape variations will delay failure happening due to skeleton rearrangements. In addition, as particle circularity decreases, samples need to undertake larger deformation to reach the critical state.

3. The mean coordination number decreases as particle circularity increases and also as particle size and shape vary.

4. The principal stress tensor ratio is more accurate in capturing the peak and critical behaviours than the principal fabric tensor ratio with shearing processes.

5. To visualise the microscale mechanism in the critical state, particle total rotations and displacements, local volumetric strain rates and void ratios, particle contact numbers and normal contact force chains in critical states were captured. Very clear shear band zones were observed in the dense samples. It was proved that particle rotation is inhibited significantly among more angular particles. This also contributes to form stabler inter-particle contacts able to sustain larger normal contact forces without considering the soil grain crushing effects. Normal contact forces were observed to be transmitted mainly by larger particles resulting in greater normal contact force chains formed due to particle size variation effects. In the contrary, the particle shape variation will impede larger normal contact force generated. Relatively large local volumetric strains and void ratios were found to concentrate within the strain localisation regions where normal contact forces are weaker and this is consistent with less contacts among particles in the rupture zones on the other hand.

Packing effects on mechanical behaviours

In order to study the packing effects on granular soil behaviours, an in-situ perfectly-packed Voronoi packing without void and a similar packing with void but maintain the inter-particle contacts the same were built to compare with two samples created by the deposition approach using the same Voronoi-based grains. The main observations are:

1. The two in-situ well-packed Voronoi-based packings reach their peak strengths earlier than the poorly-packed samples because of the restrained skeleton rearrangements. Their peak strengths are 91.5% and 46.8% higher than the peak strengths developed in the other two samples made by deposition. The large mean coordination number is the dominant reason for the significant high peak strength under the condition that the initial void ratio is relatively similar. The packing effects disappear in critical states and the critical friction angle is purely dependent on particle shape effects.

2. The two in-situ well-packed Voronoi-based packings exhibit intense decreases from higher mean coordination numbers than for the other two samples once being sheared, followed by slight rebounds before reaching critical magnitudes. However, there is no rebound in mean coordination number occurring in the other two poorly-packed samples. In critical states, the well-packed samples possess slightly higher mean coordination numbers than the poorly-packed samples.

3. By plotting the particle accumulated rotation diagrams, much more apparent strain localisation regions were observed in the well-packed packings, and the particles outside the failure regions are less disturbed.

5.6 Discussion

Global void ratio

In terms of global void ratio shown in Figure 5.9, the critical void ratios do not converge for initially dense and loose samples, and the same phenomenon is also observed in Figure 5.11. This is different from the global response of mobilised friction angle in the critical state that its value will converge irrespective of the initial density states as shown in Figure 5.8. It is worth interrogate the local void ratio within the strain localisation regions in a later study.

Graphical interpretation approach

In order to observe the microscopic behaviours, a set of post-processed graphical interpretation approaches have been developed for Box2D, which can give a range of insights on actual micro evolutions within granular samples, thus help people understand the background mechanics and further predict real soil behaviours, for instance, most likely local failure zones, based on simple measurements of particle size distribution, particle shape and etc. Additional graphical interpretation approaches like shear strain distributions developed by Wang et al. (2007) are also deserved to be investigated.

Contact condition

By studying packing effects, we can better understand the interlocking effects and further study the dry stone structures which have been widely applied as retaining walls. The inter-particle contact number was found to be a crucial factor influencing the peak strength. However, the influences of inter-particle length at an edge-edge contact on the peak strength are not clear when comparing the two in-situ Voronoi packing peak strengths. It is worth investigating the reasons causing the peak strength of the Voronoi packing (1) 35.8% higher than that of the Voronoi packing (2), such as the contact length, the initial void ratio and mean coordination number, or a combination effect. Detailed studies considering the inter-particle condition, for example, the effects of the portion of inter-pariticle edge-edge contacts (stabler than the vertex-vertex and vertex-edge contacts), will be conducted to further explore the packing effects on soil behaviours.

Chapter 6

Study on Model Scaling Effects on Granular Soil Small Strain Stiffness

The model scaling effects is often observed in centrifuge tests (e.g. Pearson and Shepley (2018)). However, there are always discrepancies in small-strain stiffnesses measured by different experiment facilities due to the device sensitivity and accuracy. Therefore, this chapter will discuss the model scaling effects on the small-strain stiffness of granular cohesionless soils using the discrete element modelling technique Box2D. The influence of confining pressure on the small-strain shear modulus will also be investigated to compare with the data obtained by other numerical modelling techniques.

6.1   Review of previous works

The stress-strain behaviour of soil is highly non-linear and stiffness decay as soil deforms has been investigated for decades. The soil stiffness decay can be illustrated by a characteristic S-shaped reduction curve on a semi-logarithmic domain as shown in Figure 6.1. The stiffness of soil is constant when associated with shear strains under the order of magnitude of 0.0001% and this strain region is termed very small strain, within which granular skeleton deformations do not change soil fabric structure and localise at contacts between particles, therefore, reflecting the stiffness and stability of the undisturbed or initial granular fabric structure and the nature of inter-particle contacts. The strain region from 0.0001% to 0.1% is small strain as the stiffness decays rapidly, and the strain region over 0.1% is defined as large strain in which stiffness is relatively small. Stiffnesses in different ranges of strains are measured by different laboratory equipments and differences in observation always exist between different laboratory facilities and also between laboratory tests and back-calculation based on in-situ observations. For instance, Hardin and Drnevich (1972) reported that small strain stiffness measured by a dynamic method: the resonant column test, is significantly larger than that measured by the conventional static triaxial test due to the accuracy and measurement limitations of the devices. In this perspective, more versatile numerical investigations of soil small-strain stiffness become complementary with laboratory tests and can provide additional verifications to experimental results. Soil

108

stiffness at small-strain levels has great importance in engineering activities, in particular for prac-tical problems involved in the strain range between 0% and 0.1%. In this chapter, the small strain stiffness of granular soil simulated by different particle shapes will be discussed by using physics en-gine Box2D. Although small-strain stiffness has been investigated using various numerical analyses by many researchers, there is still a gap in numerical solutions on model scaling effects on the small strain stiffness.

Small-strain stiffness is usually measured by static and dynamic laboratory tests. Because it is difficult to measure soil behaviour using local gauges in the small strain range, dynamic tests are more preferable in many situations. The bender element method developed by Shirley and Hampton (1978) has been widely used as a dynamic approach by observing the shear wave velocity (V_s) which can be used to calculate shear modulus ($G = \rho V_s^2$). Cyclic tests and torsional tests are able to statically obtain soil mechanical properties by unloading and reloading processes. The main difference between dynamic and static tests is upon the loading rate. In terms of static tests, the loading rate is kept at a very small level in order to make the soil behaviour maintain quasi-static, that also means the velocity profile of the system is independent on the shearing rate. A dimensionless inertia parameter $I = \frac{\dot{\gamma}d}{\sqrt{P/\rho}}$ is possible to be used to identify the shear strain rate $\dot{\gamma}$ in plane shearing tests for satisfying the quasi-static state if $I \leq 10^{-3}$ or 10^{-1} ensuring no inertia effects involved, where d and ρ denote average particle diameter and density, and P represents the applied compression pressure as discussed in section 5.2. Although the loading rate does not influence the initial stiffness of dry sands at the stage when soil performs elastic, the loading rate should also be controlled to be small enough to keep the developed strain within the very small strain range once shearing happens, and strain rate becomes increasingly more important after soil deforms into non-linear state before reaching the critical or steady state.
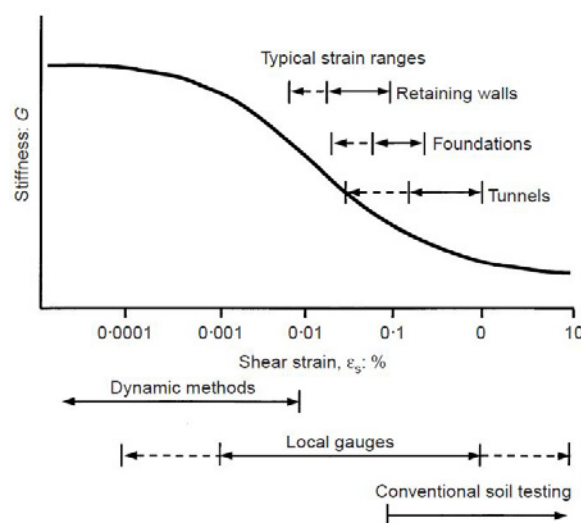

Figure 6.1: Characteristic stiffness-strain behaviour of soil with typical strain ranges for laboratory tests and structures (Atkinson, 2000).

Both theoretical analysis (e.g. Cundall and Strack (1983)) and experimental observations (e.g. Hu et al. (2011), Omar and Sadrekarimi (2014) and Scott (1987)) thus far have been conducted focusing

on general behaviours of granular soils under the particle or specimen size effects. There have also been many laboratory experiments performed to study the initial small-strain stiffness of cohesionless sands and cohesive clays, among which, Hardin and Drnevich (1972) observed that both granular soils and clays exhibit the maximum shear modulus when shear strain is smaller than the order of magnitude 10^{-4} using the resonant column device. Typically, granular soils being confined by pressures ranging between 10 kPa and 1 MPa exhibits elastic behaviours under strain increments of the order of 10^{-5} to 10^{-4} respectively, as reported by Agnolin and Roux (2007), using molecular dynamics to model granular soil simulated by spherical beads, and this strain range agrees with what Hicher (1996) found, that is granular assemblies and clay exhibit reversible behaviour if the strain amplitude is lower than 3×10^{-5} and 10^{-4}. Chang et al. (1991), Cho et al. (2006), Enomoto (2016) and Yu and Richart Jr (1984) also observed initial elastic behaviours of granular soils under the strain of order 10^{-5} to 10^{-4}. It was found by Kokusho (1980) via an improved triaxial apparatus under cyclic loading condition that the secant shear modulus converges to a certain value when the shear strain is below 10^{-5}. Dobry and Ng (1992) simulated spherical media using DEM in the strain range from 10^{-4} to 10^{-1} and regarded the tangent shear modulus at 10^{-4} as the maximum. Lo Presti et al. (1997) and Santos and Correia (2000) also studied the shear modulus for different soils in the range of small to medium strain levels (10^{-6} to 10^{-2}) under cyclic loading conditions.

Void ratio and effective stress are two dominant factors influencing the initial stiffness of granular materials (Enomoto, 2016). In order to describe the effects caused by void ratio, a void ratio function (Hardin and Black, 1968; Wichtmann and Triantafyllidis, 2009) is commonly applied to normalise the void ratio influence:

$$F(e) = \frac{(2.17 - e)^2}{1 + e} \qquad \text{(for round grains)}$$

$$F(e) = \frac{(2.97 - e)^2}{1 + e} \quad \text{or} \quad 0.3 + 0.7e^2 \qquad \text{(for angular grains)}$$

Another general form of the void ratio function was proposed by Lo Presti et al. (1997) as:

$$F(e) = e^{-x}$$

In terms of spherical particles, the parameter x is approximately $\frac{2}{3}$ (Santos and Correia, 2000).

Many researches have been conducted to find the relationship between the initial stiffness of various granular soils constituted with different types of particles, void ratio and also mean pressure. Hardin and Black (1966) established the following equation to commonly represent the relationship:

$$G_0 = F(e)\sigma_0^n = A\frac{(a - e)^2}{1 + e}\sigma_{atm}^{1-n}\sigma_0^n$$

in which e is the void ratio, σ_0 and σ_{atm} are the isotropic confining pressure and the atmospheric pressure, and A, a and n are variants altering with particle shapes. These variants were also found to be related with particle size distributions and Wichtmann and Triantafyllidis (2009) used the following

equations to correlate these variants with coefficient of uniformity ($C_u = d_{60}/d_{10}$):

$$a = 1.94e^{-0.066C_u}$$

$$n = 0.4C_u^{0.18}$$

$$A = 1563 + 3.13C_u^{2.98}$$

Hardin and Black (1966) observed the values of A for round and angular grains are 690 and 320, respectively, with n to be 0.5. Zeghal and Tsigginos (2015) also found that particle shape influences the $F(e)$ term instead of n. It was analysed theoretically and simulated using molecular dynamics by Walton (1987) and Agnolin and Roux (2007) who found that the shear modulus of spherical grains increases proportionally to $\sigma_0^{\frac{1}{3}}$, and n is 0.35 as the DEM simulation using spherical particles proved by Jung et al. (2010), while as reported by Hardin and Black (1966), Kokusho (1980) and Lo Presti et al. (1997), n lies in the range between 0.5 and 0.6 as the confining pressure changes. Based on the observation given by Cascante and Santamarina (1996), n is equal to $\frac{1}{3}$ for spherical grains and $\frac{1}{2}$ for polygonal grains.

The coordination number is also a factor able to significantly affect the initial stiffness of granular soil according to the results provided by DEM simulation by Dobry and Ng (1992) and Zeghal and Tsigginos (2015) and a unique relation function correlating the mean coordination number and the mean pressure with the initial shear modulus of granular media is given as:

$$G_0 = \alpha(M_n - M_0)^m \sigma_0^r$$

where M_n is the coordination number, σ_0 is the isotropic confining pressure, and α, M_0, m (influenced by particle shape) and r are coefficients obtained by non-linear least-squares regression analysis. It is also pointed out that the only possible reason that the stress history influences the initial stiffness is that it has changed the mean coordination number, and since the void ratio can not be determined by a unique mean coordination number, it is not accurate to estimate the initial stiffness by void ratio. As observed by Walton (1987), the initial stiffness is sensitive to the average coordination number. Another reason to replace the void ratio with the mean coordination number in this equation is that some particles in an assemblage cannot enhance the stability of the fabric structure and hence the void ratio cannot provide enough evaluation on the contact stability compared with the contact number. This also coincides with what Dobry and Ng (1992) observed via DEM software CONBAL-2, and the results show that for two samples under the same consolidation pressure, one of higher void ratio exhibits greater shear modulus than the other of lower void ratio because of the average coordination number effects. Zeghal and Tsigginos (2015) obtained two sets of coefficients based on regular fabric synthetic grains and spherical grains respectively:

$$G_0 = 12434(M_n - 4.68)^{0.76}\sigma_0^{0.34} \qquad \text{(for regular fabric synthetic grains)}$$

$$G_0 = 16851(M_n - 4.17)^{0.7}\sigma_0^{0.35} \qquad \text{(for spherical grains)}$$

Dobry and Ng (1992) adopted a very similar expression based on the results obtained by two-dimensional DEM simulations using discs:

$$G_0 = 682 M_n^{1.04} \sigma_0^{0.304}$$

Oztoprak and Bolton (2013) derived a new shear modulus equation to estimate the very-small-strain (0.0001%) shear modulus (G_0) for sandy soils based on the constructed database involving 454 previous physical tests to measure the S-shaped shear modulus degradation curve as shown in Figure 6.1. A modified hyperbolic equation was then established to fit the secant shear modulus curve. Three curve fitting characteristic parameters which are the elastic threshold strain up to which the elastic shear modulus (G_0) is constant, the reference strain at which the secant shear modulus reduces to $0.5 G_0$ and the curvature parameter controlling the secant shear modulus reduction rate respectively, were highlighted. It was also observed that the secant shear modulus of a sandy soil with a more disperse particle size distribution starts to degrade at a smaller shear strain compared with a sample with a more uniform particle size distribution because of premature slip between large and small particle contacts due to strain incompatibility, while the secant shear modulus of a sand sample with more uniform particles degrades faster. The grain size distribution effects on small-strain shear modulus G_0 of quartz sand with subangular grain shape were also investigated by Wichtmann and Triantafyllidis (2009) by conducting resonant column tests because the well-known empirical Hardin's equation (Hardin and Black, 1966) significantly overestimates the well-graded granular soils. It was reported that the small-strain shear modulus is not dependent on the mean grain size (d_{50}) at a constant void ratio while it strongly decreases as the coefficient of uniformity (C_u) increases. The dependence of the pressure wave (P-wave) velocity, the constrained elastic modulus and the Poisson's ratio respectively on the grain size distribution at the small strain level was later studied by Wichtmann and Triantafyllidis (2010). The P-wave velocity and the elastic modulus were observed to follow the same tendency as the small-strain shear modulus affected by C_u, while the Poisson's ratio was found to increase with C_u. All these parameters do not depend on d_{50}. The particle shape effects on the small-strain shear wave (S-wave) velocity which can be calculated by: $V_s = \alpha(\frac{\sigma'_{mean}}{1\,kPa})^\beta$ was measured by Cho et al. (2006) and it was observed that the particle roundness, sphericity and regularity decreases make the α factor reduce while the β factor increase. Giang et al. (2017) also studied the particle shape effects on the small-strain stiffness of calcareous sand by bender element tests. The empirical formula (Hardin and Richart, 1963): $G_0 = Ae^{-B}(\frac{p'}{100\,kPa})^n$ was adopted in their research. They found that the particle angularity and shape variation can increase G_0 due to a better fabric for shear wave propagation, and the factor A decreases while B and n increase as the particle angularity increases.

Additional studies on the small-strain shear wave velocity and shear modulus have been carried out under the help of DEM techniques by simulating bender element tests. O'Donovan et al. (2012) conducted a two-dimensional DEM simulation by building a sample made of hexagonally packed uniformly-sized discs in PFC2D to capture particle responses (particle displacement velocities, representative particle mean and shear stresses) under shear wave excitation starting from the bottom.

The shear wave velocity was found to be proportional to the inter-particle contact spring stiffness and inversely proportional to the square root of the particle density, and insensitive to the viscous damping ratio when the viscous damping ratio is below 0.1. A new Fourier decomposition approach was also proposed to be able to accurately calculate the propagation duration of the shear wave. Ning and Evans (2013) investigated the excitation frequency, particle size and confining pressure effects on the shear wave velocities of cylindrical spherical assemblies of grains via DEM. It was found that the mean particle size has less of an impact on the shear wave velocity while the resonant frequency will increase as the mean particle size decreases. The small-strain stiffness was detected to increase with the confining pressure as physical experiments show. The anisotropic stress state effects on the small-strain shear wave velocity and shear modulus were also analysed by O'Donovan et al. (2015) and Nguyen et al. (2018). The shear wave velocity was observed to be strongly influenced by the stresses along the directions of propagation and oscillation of the shear wave, however, independent of the stress orthogonal to the plane containing the shear wave excitation. In addition, a new rough-surface contact model was proposed by Otsubo et al. (2017) and Otsubo and O'Sullivan (2018) to analyse the particle surface roughness effects on the small-strain shear modulus of samples modelled by uniform spheres facilitated by the 'Lammps' molecular dynamics code. The particle surface roughness was found to be able to decrease the small-strain stiffness particularly under a low confining pressure condition, while this effect gradually attenuates as the confining pressure increases.

Specimen size effect also shows significant influence on the soil sample strength properties such as stiffness and critical strength, and localisation zone. As observed by Bažant et al. (1991), the strength of cemented granular materials may drop as much as 60% to 70% as the specimen size increases by two orders of magnitude. Additionally, the shear band width was found to be as 8 to 10 times the particle diameter (Roscoe, 1970; Vardoulakis and Graf, 1985; Oda and Kazama, 1998; Alshibli and Sture, 2000). It was also reported by Pearson and Shepley (2018) that the footing stiffness will increase as the ratio of the footing width to the average particle diameter increases by using centrifuge tests.

6.2 Model scaling effects on small-strain stiffness

In this section, granular soil samples constituted of three different types of particles: random dodecagonal particles, regular hexagonal particles and Voronoi-based polygonal particles were studied and compared with respect to the model scale effects on small-strain stiffness. These three kinds of packings have their own characters as Voronoi-based polygons deviate greatly both in particle size and shape compared with mono-sized random dodecagons and regular hexagons, and crystallisation often occurs in packings made of unique hexagonal particles, which can clearly influence soil behaviour.

6.2.1   Model set-up

Figure 6.2 shows the three packings made of two-dimensional random convex polygonal particles. To generate polygonal grains of specific numbers of edges (dodecagons or hexagons), their circumscribed circle size was firstly determined (their radii equal to $0.5\,\mathrm{m}$ in this study). The particle vertices were then to be specified in sequence according to the shape aspect ratio (set to be 1 in this study representing no elongation).

All the particles were created above the bottom boundary at a distance of 10 particle sizes, and dropped down to the bottom under the gravity until coming into rest. The particle friction coefficient could be altered in order to obtain packings of desired density states. The particles above the stipulated container height were than excluded from the samples. The particle friction was changed to 0.4663 gradually followed by total sample weight measurement procedure until the system was stable. The created dodecagonal particles were of similar sizes and the hexagonal particles were unique in size. The greater variations both in particle size and circularity for the Voronoi-based polygonal particles will make these samples behave differently with other samples. The algorithm to create Voronoi tessellation was introduced in section 4.1. The Halton sequence algorithm was adopted to allocate the initial seeds for the Voronoi tessellation. Figure 6.3 plots the particle size and circularity distributions created by different random number generators, annotated with their average values also given in Table 6.1. It can be found that the generated Voronoi-based samples vary greatly both in particle size and circularity and the average circularity is far smaller than that of dodecagonal samples, while the average particle sizes are relatively close in magnitude.

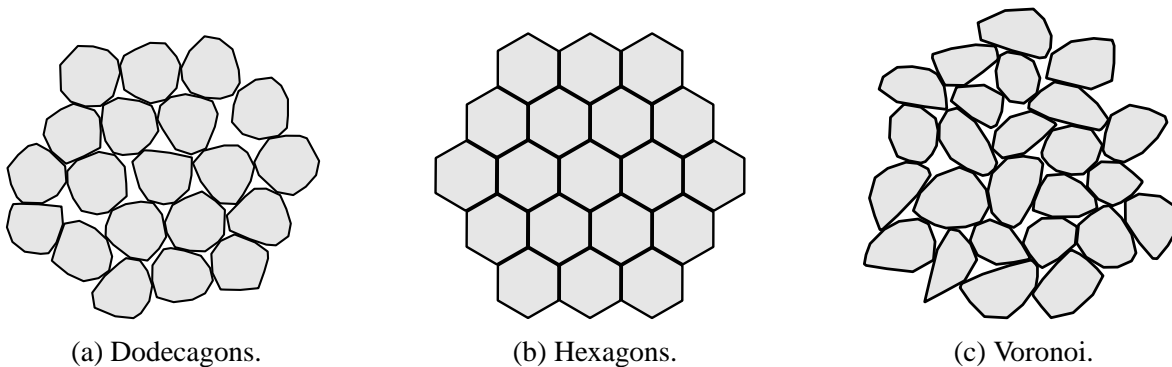(a) Dodecagons.　　　　(b) Hexagons.　　　　(c) Voronoi.

Figure 6.2: Example particle samples.

The horizontal and vertical confining stresses were applied after the preparation stage. The horizontal confining stress was applied by the stress-controlled algorithm (Cheung and O'Sullivan, 2008) step by step onto the outmost particles found and updated via ray-cast lines evenly distributed along the vertical direction in each time step as introduced in section 5.2. The ray density was calculated under the condition that each particle could be allocated 3 rays so that no boundary particles were missed and computational efficiency was maintained. The vertical confining stress was applied by the "servo-controlled" algorithm (Thornton and Antony, 2000; Pytlos et al., 2015), which means that the velocity of the top platen when confining the granular sample was modified according to the calcu-
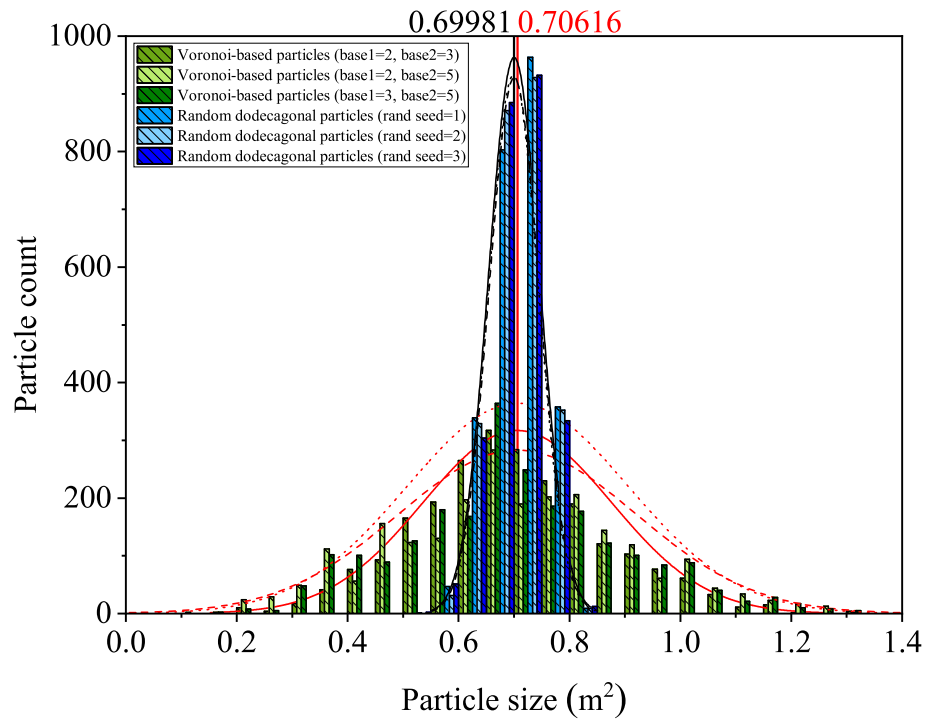
(a) Particle shape area distribution.
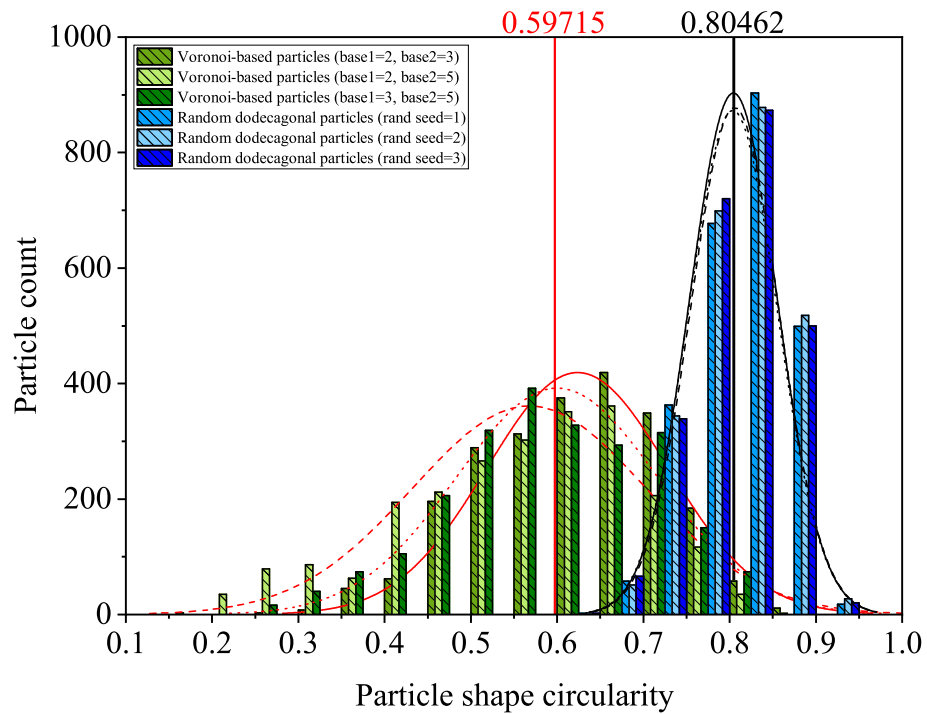
(b) Particle shape circularity distributions.

Figure 6.3: Particle shape descriptor distribution.

lated deviation of the measured vertical confining stress apart from the target vertical confining stress required to achieve in each time step.

After the confining process was finished, the shearing process was started during which the top platen was velocity-controlled. The shearing velocity was required to satisfy the condition that the inertial number calculated by equation (5.2) was smaller than 10^{-4} in order to maintain the quasi static condition. The main Box2D system and model parameters chosen in these simulations are summarised in Table 6.2.

Table 6.1: List of particle shape descriptors

Shape descriptions	Packings	Dodecagons	Hexagons	Voronoi
Average sizes (m^2)		0.700	0.650	0.706
Average circularities		0.805	0.866	0.597

Table 6.2: List of system and set-up parameters.

Parameters	Values
Box2D default parameters	
Time step size	$1/60\,$s
Number of velocity iterations per time step	8
Number of position iterations per time step	3
Contact skin thickness	$0.001\,$m
Particle characteristics	
Density	$2660\,$kg/m^3
Restitution coefficient	0
Particle bounding circle diameter[1]	$1.0\,$m
Particle aspect ratio	1.0
Test set-up parameters	
Particle friction coefficient[2]	$0.05 \sim 0.466$
Ratio of biaxial container height to width	2
Gravity acceleration	$0.1\,$m/s^2
Sample slenderness ratio	2
Maximum top platen velocity in the confining stage	$0.01\,$m/s
Biaxial test parameters	
Top and bottom platen friction coefficients	1.0
Particle friction coefficient	0.466
Confining pressure	$1\,$kPa
Top platen velocity	$0.0005\,$m/s
Gravity acceleration	$0\,$m/s^2
Deviatoric strain limit	0.002%

[1] For dodecagonal and hexagonal particles.

[2] By altering this value during the deposition stage to generate packings of various density states.

6.2.2 Methodology

The strain-stress relationship is modified to equations (6.1) to (6.4) because the intermediate stress and strain in the triaxial model are no longer involved into consideration in the biaxial model.

$$
\begin{pmatrix} s \\ t \end{pmatrix} = \begin{pmatrix} \frac{1}{2} & \frac{1}{2} \\ 1 & -1 \end{pmatrix} \begin{pmatrix} \sigma'_1 \\ \sigma'_3 \end{pmatrix}
\tag{6.1}
$$

$$
\begin{pmatrix} \sigma'_1 \\ \sigma'_3 \end{pmatrix} = \begin{pmatrix} 1 & \frac{1}{2} \\ 1 & -\frac{1}{2} \end{pmatrix} \begin{pmatrix} s \\ t \end{pmatrix}
\tag{6.2}
$$

$$
\begin{pmatrix} \delta\epsilon_v \\ \delta\epsilon_t \end{pmatrix} = \begin{pmatrix} 1 & 1 \\ \frac{1}{2} & -\frac{1}{2} \end{pmatrix} \begin{pmatrix} \delta\epsilon_1 \\ \delta\epsilon_3 \end{pmatrix}
\tag{6.3}
$$

$$
\begin{pmatrix} \delta\epsilon_1 \\ \delta\epsilon_3 \end{pmatrix} = \begin{pmatrix} \frac{1}{2} & 1 \\ \frac{1}{2} & -1 \end{pmatrix} \begin{pmatrix} \delta\epsilon_v \\ \delta\epsilon_t \end{pmatrix}
\tag{6.4}
$$

The relationship between the principal strain and the principal stress in the biaxial model can be established by equation (6.5):

$$
\begin{pmatrix} \delta\epsilon_1 \\ \delta\epsilon_3 \end{pmatrix} = \frac{1}{E} \begin{pmatrix} 1 & -\nu \\ -\nu & 1 \end{pmatrix} \begin{pmatrix} \delta\sigma'_1 \\ \delta\sigma'_3 \end{pmatrix}
\tag{6.5}
$$

By transforming equation (6.3), the following is obtained:

$$
\begin{pmatrix} \delta\epsilon_v \\ \delta\epsilon_t \end{pmatrix} = \frac{1}{E} \begin{pmatrix} 2(1-\nu) & 0 \\ 0 & \frac{1}{2}(1+\nu) \end{pmatrix} \begin{pmatrix} \delta s \\ \delta t \end{pmatrix}
\tag{6.6}
$$

If the stiffness parameters K and G are defined as:

$$
\frac{1}{K} = \frac{2}{E}(1-\nu)
\tag{6.7}
$$

$$
\frac{1}{G} = \frac{1}{2E}(1+\nu)
\tag{6.8}
$$

the stiffness matrix can be obtained as follows:

$$
\begin{pmatrix} \delta\epsilon_v \\ \delta\epsilon_t \end{pmatrix} = \begin{pmatrix} \frac{1}{E} & 0 \\ 0 & \frac{1}{G} \end{pmatrix} \begin{pmatrix} \delta s \\ \delta t \end{pmatrix}
\tag{6.9}
$$

$$
\begin{pmatrix} \delta s \\ \delta t \end{pmatrix} = \begin{pmatrix} E & 0 \\ 0 & G \end{pmatrix} \begin{pmatrix} \delta\epsilon_v \\ \delta\epsilon_t \end{pmatrix}
\tag{6.10}
$$

Parameter definitions:

ϵ_1 – axial strain; ϵ_3 – horizontal strain;

σ_1 – axial stress; σ_3 – horizontal stress;

ϵ_v – volumetric strain; ϵ_t – distortional strain;

s – mean effective stress; t – distortional stress;

ν – Poisson's ratio; E – Young's modulus;

K – bulk modulus; G – shear modulus.

.

The model scaling ratio was defined as the ratio of biaxial model width W to the particle average diameter d as shown in Figure 6.4. The model scaling effects on the small-strain stiffness which was described by the shear modulus G were studied in this research. In order to achieve the desired
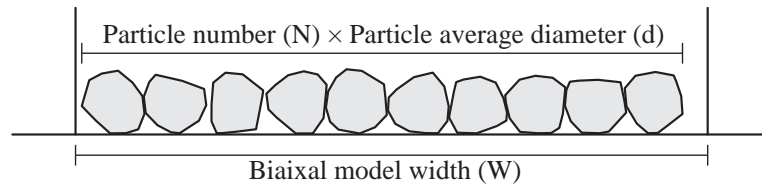
Figure 6.4: Ratio: W/d.

scaling ratio in a model, the biaxial width was calculated by the multiplication of the particle size and the scaling ratio and the particle size was unchanged in each simulation.

As proposed by Head et al. (1998) that the width of a triaxial specimen should be at least of a diameter of $4 - 5$ times that of the largest particle for granular materials. Therefore the scaling ratios were chosen as 10, 15, 20, 25 and 30 for dodecagonal and hexagonal samples, and 10, 20 and 30 for Voronoi-based samples. In total 51 models were established for each scaling ratio condition by altering the particle friction coefficient in the range of 0.05 to 0.466 during the deposition stage in order to obtain deposits of various density states. Figure 6.5 illustrates the depositional friction coefficient effects on the packing densities after the confinement process. Consistent with the observations in Figure 5.5, the Voronoi-based samples are able to deposit into denser packings than the dodecagonal samples under the same efforts due to their larger mean contact numbers which arise due to the larger variations in particle size and shape and the lower circularity. In addition, the crystallisation phenomenon was found able to help the hexagonal samples reach the densest states.

6.2.3   Simulation results

Void ratio and mean coordination number effects on small-strain stiffness

Figure 6.6 plots the small-strain secant shear modulus which is taken as the slope of the deviatoric stress-strain plot as represented in equation (6.10) with respect to void ratio (Figure 6.6a) and mean coordination number (Figure 6.6b) respectively for dodecagonal samples of different scaling ratios at
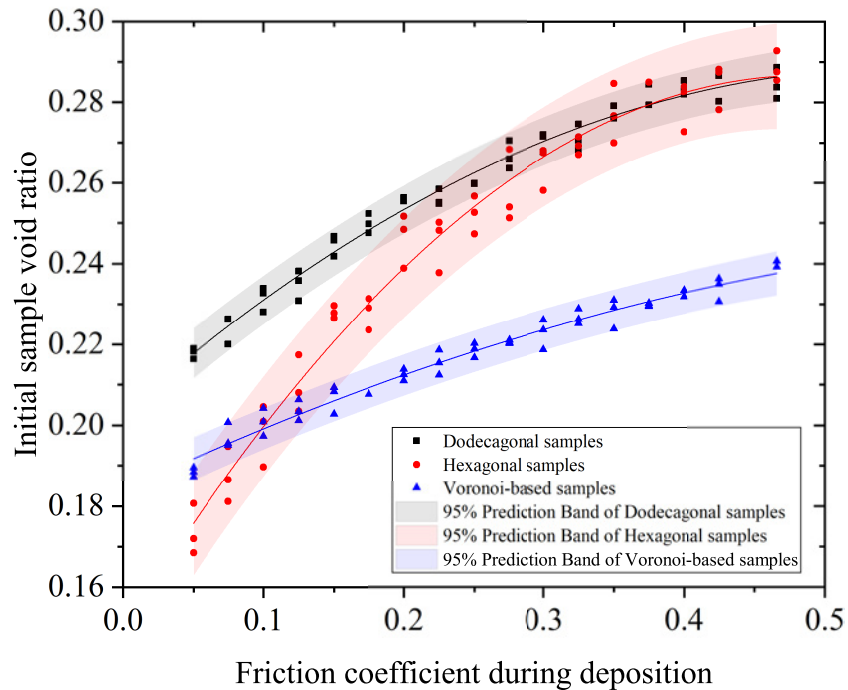
Figure 6.5: Deposit void ratios created by altering friction coefficients during deposition at a scaling ratio of 30.

a deviatoric strain level up to 2×10^{-5}. It is found that the initial stiffness increases as the scaling ratio increases for samples of the same density state, however, it decreases (though to a lesser extent) as the scaling ratio increases for samples with the same mean coordination number.

Eight samples of different scaling ratios were chosen as labelled in Figure 6.6 and 6.7 to further interrogate the findings by means of assessing their microscopic behaviours in detail. The studied samples were selected based on the criteria that they deviate greatly in stiffness but exhibit near identical void ratios or mean coordination numbers, in order to best observe the implicit reasons causing the different behaviours purely due to scaling effects, and they all sit on the vertical dashed lines at constant void ratio in Figure 6.6a and mean coordination number in Figure 6.6b. Their reciprocal relationships are also plotted and labelled in Figure 6.7.

Because the boundary particles contact with fewer neighbour particles and these particles occupy a larger volume in smaller samples, samples at higher scaling ratios are observed to possess larger mean coordination numbers at the same density state due to this boundary effect as shown in Figure 6.7. Conversely, samples of higher scaling ratios tend to be looser in packing density at the same mean coordination numbers as Figure 6.7 indicates. Cundall and Strack (1983) proposed a theoretical solution to relate the granular sample structure stability with the number of particles and their contacts, and concluded that collapse is more likely to happen in larger assemblies under the same contact conditions. This study extends this conclusion, highlighting that samples of larger mean coordination numbers (and therefore denser packings) exhibit larger stiffness at small strain levels.
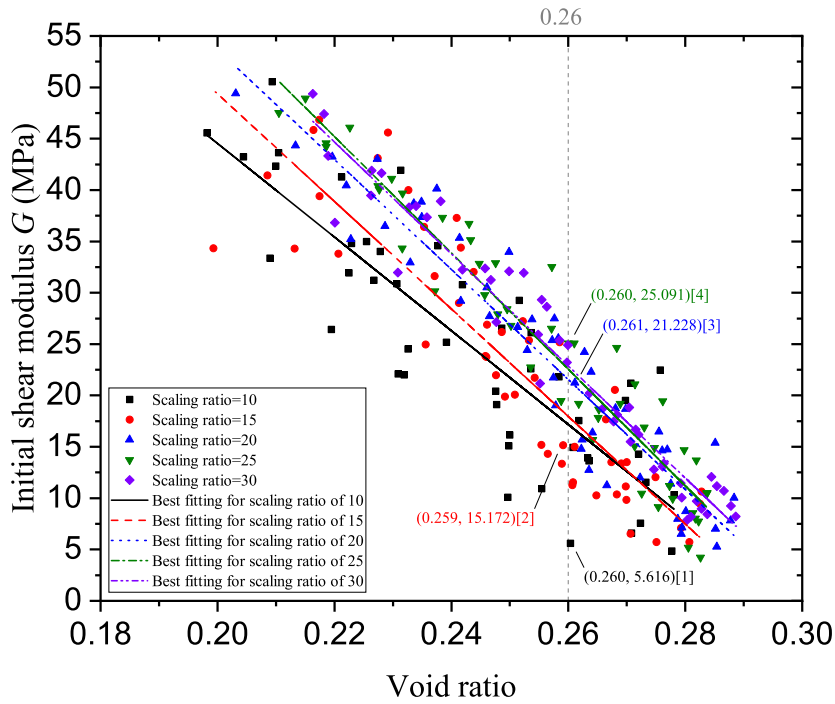
(a) Small-strain stiffness versus void ratio.
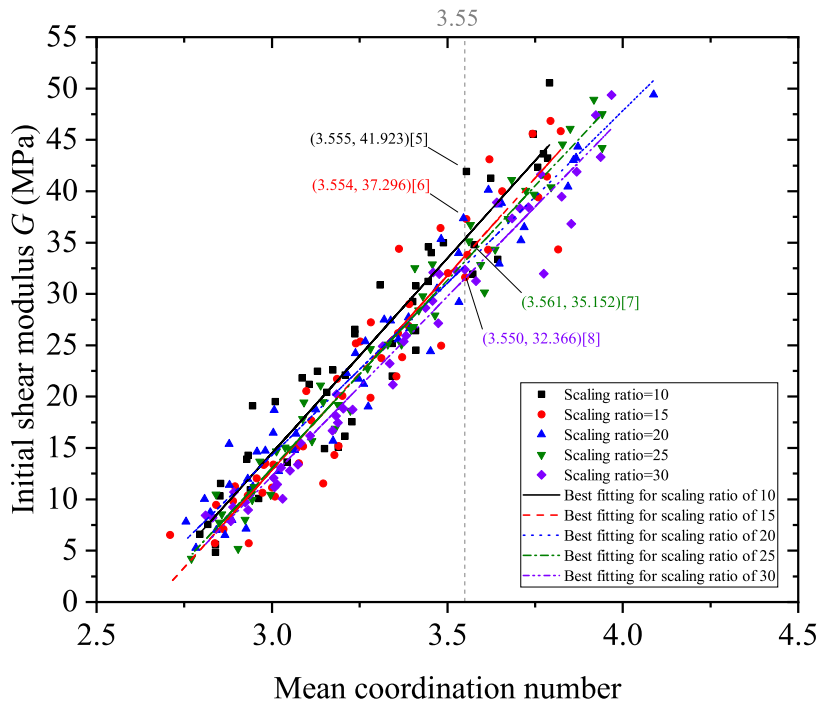
(b) Small-strain stiffness versus mean coordination number.

Figure 6.6: Plot of Small-strain stiffness versus void ratio (a) and mean coordination number (b) for dodecagonal samples of different scaling ratios.
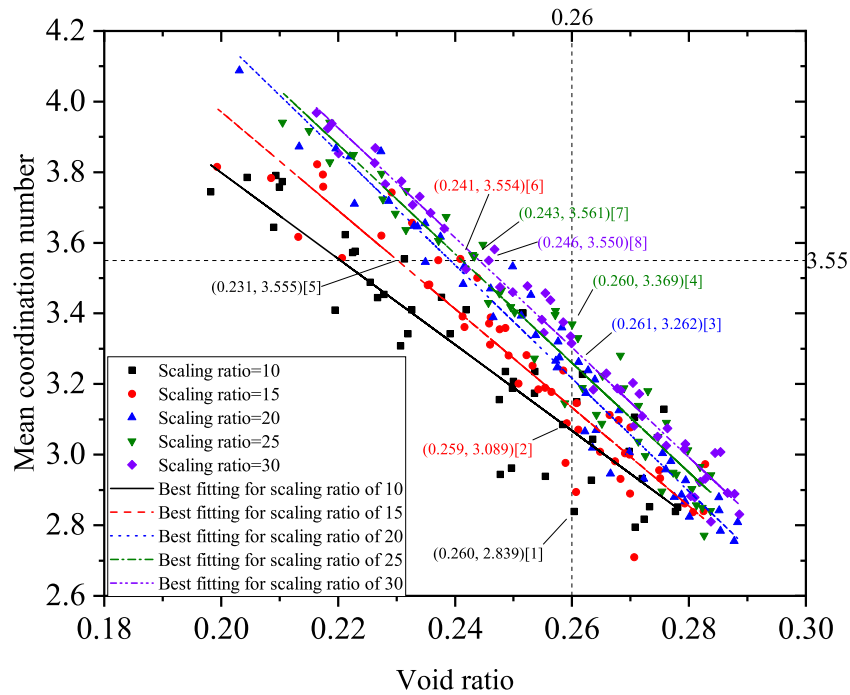
Figure 6.7: Comparison for samples of different scaling ratios in terms of mean coordination number and void ratio.

The void ratio effects on the initial stiffness for packings constituted of hexagonal and Voronoi-based particles are analysed in Figure 6.8a and 6.8b respectively. The scaling ratio effects in hexagonal samples are not significant due to the close packing clusters (crystallisation phenomenon) which are easy to develop randomly in these packings, giving strong local load bearing capacity and hence increasing the stiffness. The Voronoi-based samples exhibit consistent behaviour with the dodecagonal samples when their void ratios are below 0.224, that the small-strain stiffness increase follows the scaling ratio increase. However, this phenomenon is not maintained for all density conditions and reverses after the void ratio exceeds 0.224 as the packings become looser. It is hypothesised that this is due to which existing unstable contact between particles generated during deposition and the confining stage and is more common for vertex-vertex or vertex-edge contacts. These unstable contacts will collapse immediately after shearing starts but were still taken into account when calculating the mean coordination number.

To verify this hypothesis, two samples of void ratios 0.247 and 0.239 and scaling ratios of 10 and 30 respectively were selected to compare their particle total rotations which can reflect the unstable contact dissipation events. Their mean coordination numbers correspond to 3.384 and 3.497 respectively. The smaller sample was found to be much stiffer than the larger sample although the larger sample is packed in denser state at the initial stage and has greater mean coordination number at deviatoric strain levels up to 0.002%. Figure 6.9 captures the particle total rotations for these two samples and it is easy to observe that more particles distributed across the whole sample rotate significantly in

the larger sample, indicating collapse of unstable contacts will make the stiffness decrease. However, there are still not enough evidences showing the scaling ratio effects on the small-strain stiffness for the Voronoi-based packings based on the obtained data.
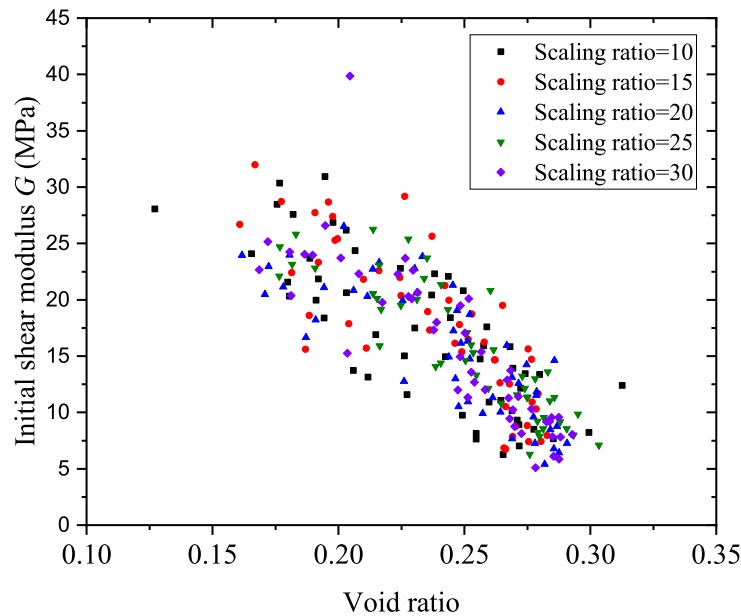
(a) Hexagonal samples.
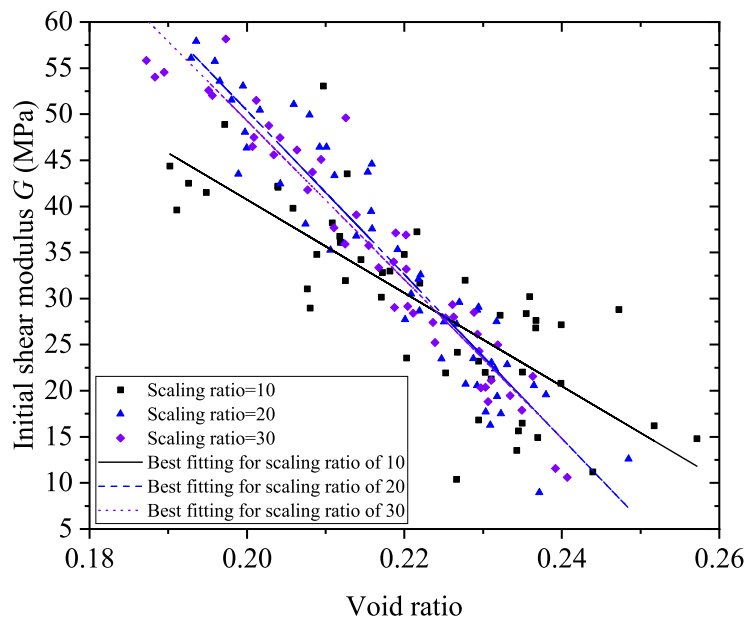
(b) Voronoi-based samples.

Figure 6.8: Relationship between small-strain stiffness and void ratio for hexagonal (a) and Voronoi-based samples (b) for differently-scaled samples.
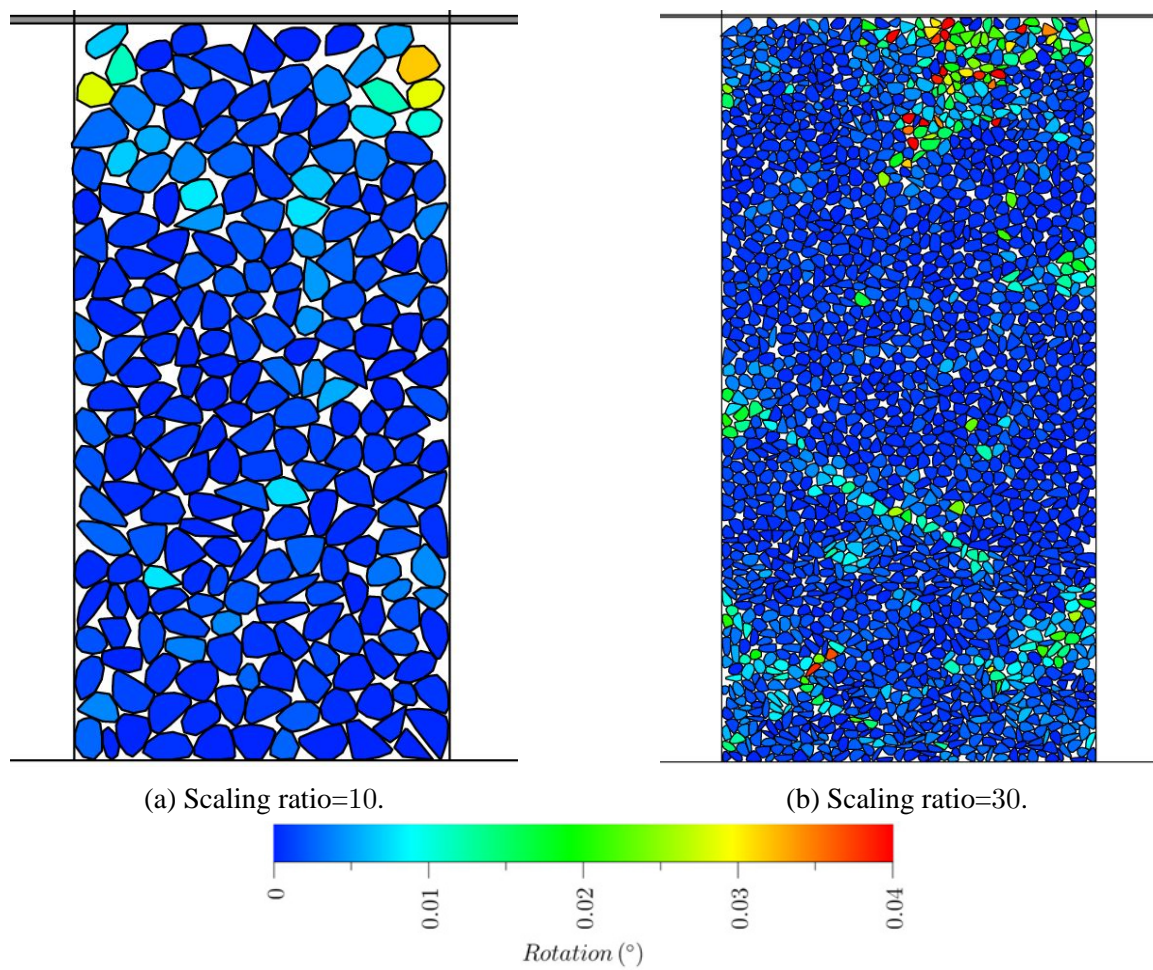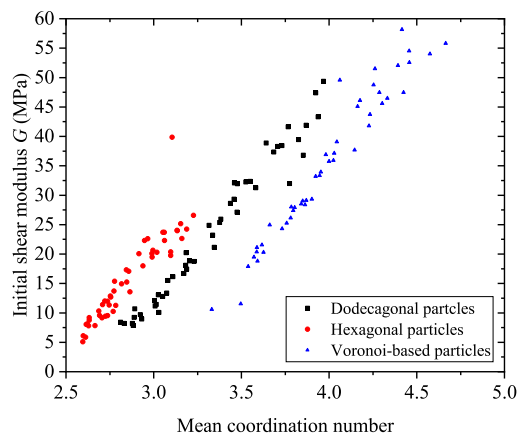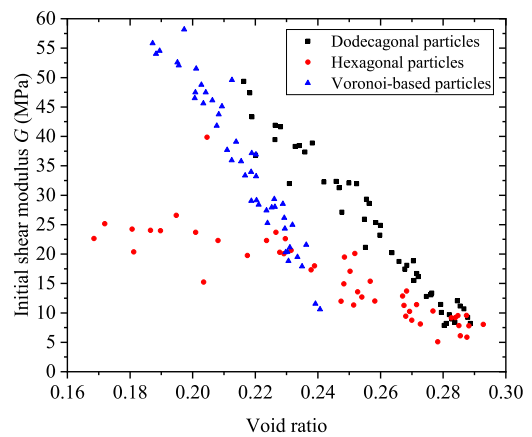
(a) Scaling ratio=10.

(b) Scaling ratio=30.

Figure 6.9: Particle total rotation diagram at deviatoric strain 0.002% for Voronoi-based samples of void ratios 0.247 and 0.239 and scaling ratios of 10 and 30 respectively.

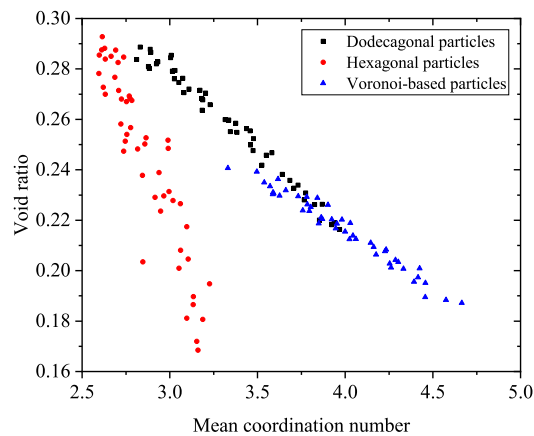**Packing effects on small-strain stiffness**

Figure 6.10 compares three different packings at the same scaling ratio of 30 (minimise the boundary effects) in terms of their variations in mechanical properties. The mean coordination numbers of the three types of packings lie within different ranges due to their different particle shape characteristics as shown in Figure 6.10a,. The mean coordination number for the hexagonal samples varies between 2.6 and 3.2, while for the dodecagonal and the Voronoi samples, it ranges from 2.8 to 4.0, and from 3.3 to 4.7, respectively. It is reasonable to see that the hexagonal grains are easier to be deposited into denser states because of the unique particle geometry and potential crystallisation randomly occurring within the sample, and therefore exhibit stronger stiffness than the dodecagonal samples when their mean coordination numbers are of the same magnitudes. On the other hand, the dodecagonal packings exhibit higher stiffness than the hexagonal packings at the same density states as a result of their greater mean coordination numbers as shown in Figure 6.10b. It is also found from Figure 6.10c that the relationship between void ratio and mean coordination number for polygonal particles is highly dependant on the packing nature rather than the particle size and shape variations because the void ratio for the hexagonal samples decreases by around 2 times as that for the other two samples when the mean coordination number increases by the same amount although each packing has its own range within which these values can alter. From Figure 6.10a and Figure 6.10b it is apparent to see that the dodecagonal packings behave stiffer than the Voronoi samples if the mean coordination numbers or the void ratios are the same even though these two types of packings possess very close mean coordination numbers when their density states are the same. This supports the conclusion that it is the greater variations in particle size and shape among the Voronoi-based particles providing more potential space for relative movements and rotations that reduces the stiffness of the overall sample.

(a) Initial stiffness versus mean coordination number.

(b) Initial stiffness versus void ratio.

(c) Void ratio versus mean coordination number.

Figure 6.10: Mechanical properties of various packings at scaling ratio of 30.

6.2.4 Discussion

To analyse how packing and scaling ratio influence the small-strain stiffness from microscopic perspectives, a number of snapshots for different packings at deviatoric strain 0.002% have been captured. All the scaled vectors represent the displacements accumulated from the start of shearing.

Figure 6.11 to Figure 6.13 compare the total horizontal and vertical relative displacements (normalised by the model initial width and height respectively to eliminate differences caused by variant model scaling ratios) and rotations for the selected four dodecagonal samples of different scaling ratios labelled in Figure 6.6a and 6.7. The boundary particles in smaller samples tend to move outward (as shown in Figure 6.11a and Figure 6.11b) because these particles which are constrained by less contacted particles occupy a larger volume, resulting in larger vertical movement when sheared by the same magnitude of vertical deviatoric stress (i.e. a lower stiffness) as shown in Figure 6.12. The top layer particles are observed to displace more in the vertical direction than the lower particles. There is also a slight tendency that the particles undergo more vertical displacements above the region within which the particles move outward greatly. Furthermore, the smaller the scaling ratio, the more the particles can potentially rotate because of lower mean coordination numbers due to the boundary effects. This phenomenon is illustrated by the increasing percentage volume of particles undergoing noticeable rotations as the scaling ratio reduces (Figure 6.13).

Significant outward displacements in the horizontal direction are observed in Figure 6.14c and Figure 6.14d when the mean coordination number is nearly constant because of the larger volume of initial void also providing more space for particle rotation in Figure 6.16. The symmetric horizontal movements shown in Figure 6.14d caused even vertical displacements of the top layer particles in Figure 6.15d. This micro-skeleton rearrangement eventually results in larger total vertical relative displacements observed in largely-scaled samples in Figure 6.14.
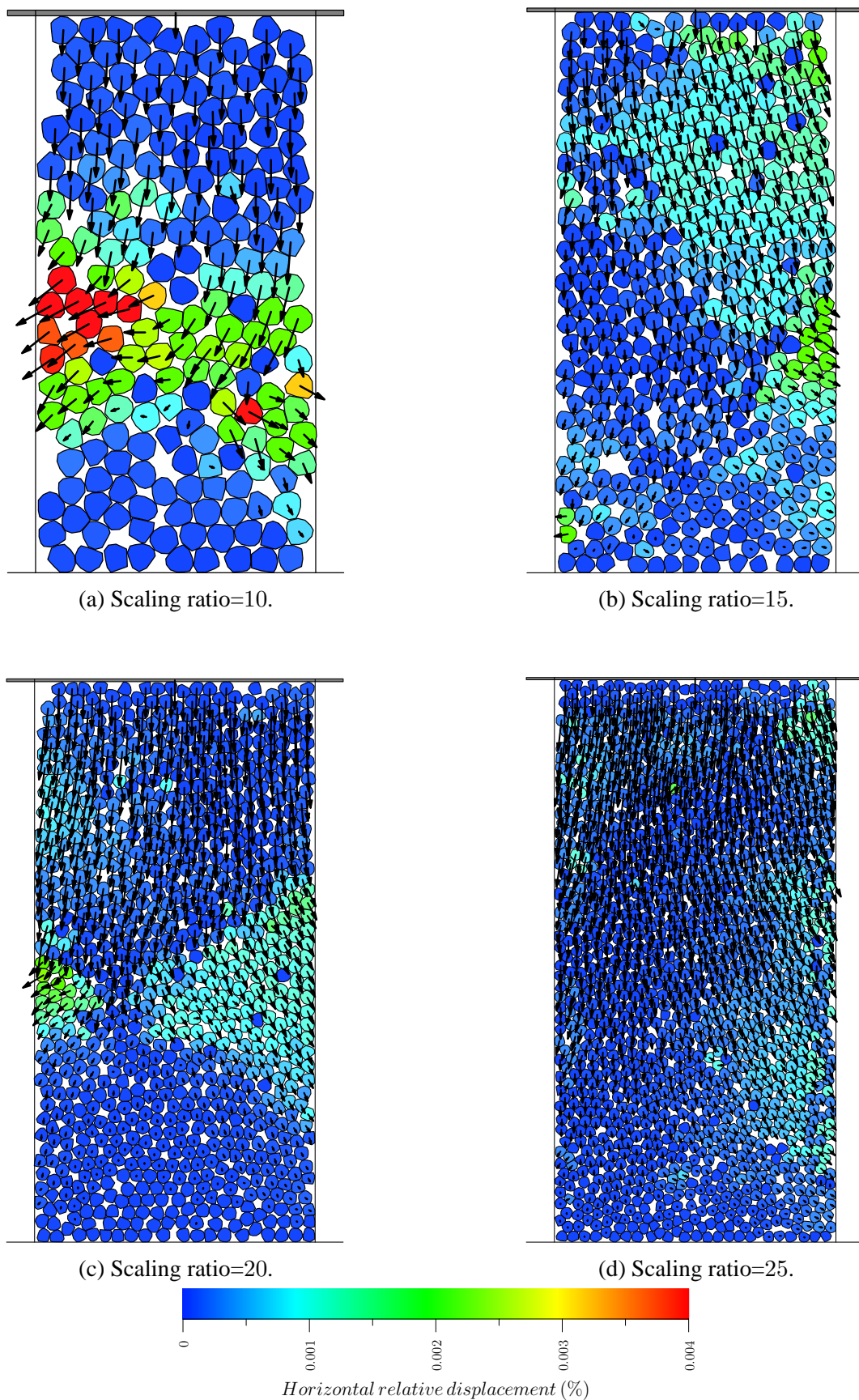
(a) Scaling ratio=10.

(b) Scaling ratio=15.

(c) Scaling ratio=20.

(d) Scaling ratio=25.

Horizontal relative displacement (%)

Figure 6.11: Particle total horizontal relative displacements and accumulated displacement vectors at deviatoric strain 0.002% for dodecagonal samples of void ratios around 0.26.
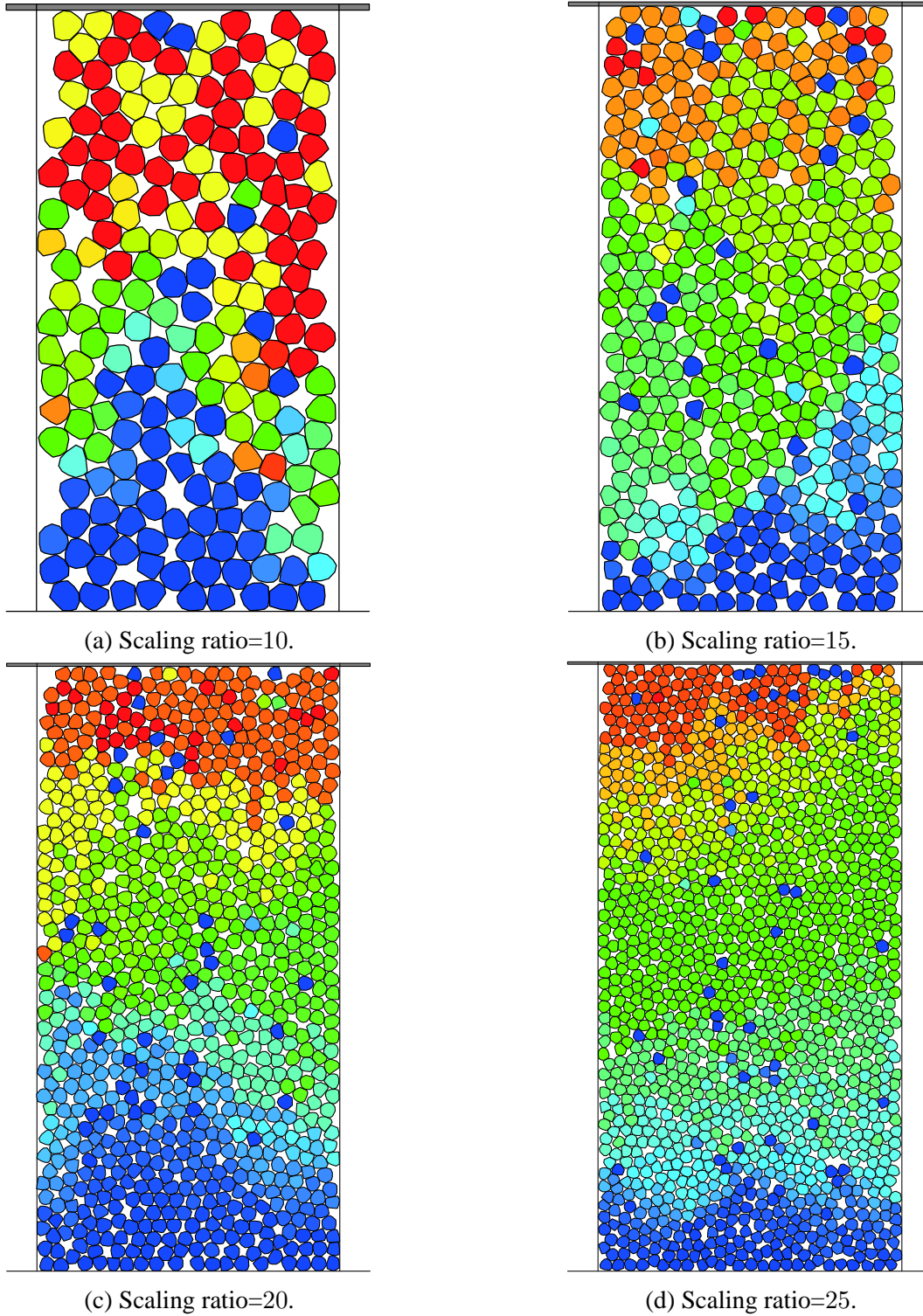
(a) Scaling ratio=10.

(b) Scaling ratio=15.

(c) Scaling ratio=20.

(d) Scaling ratio=25.

Figure 6.12: Particle total vertical relative displacements at deviatoric strain 0.002% for dodecagonal samples of void ratios around 0.26.
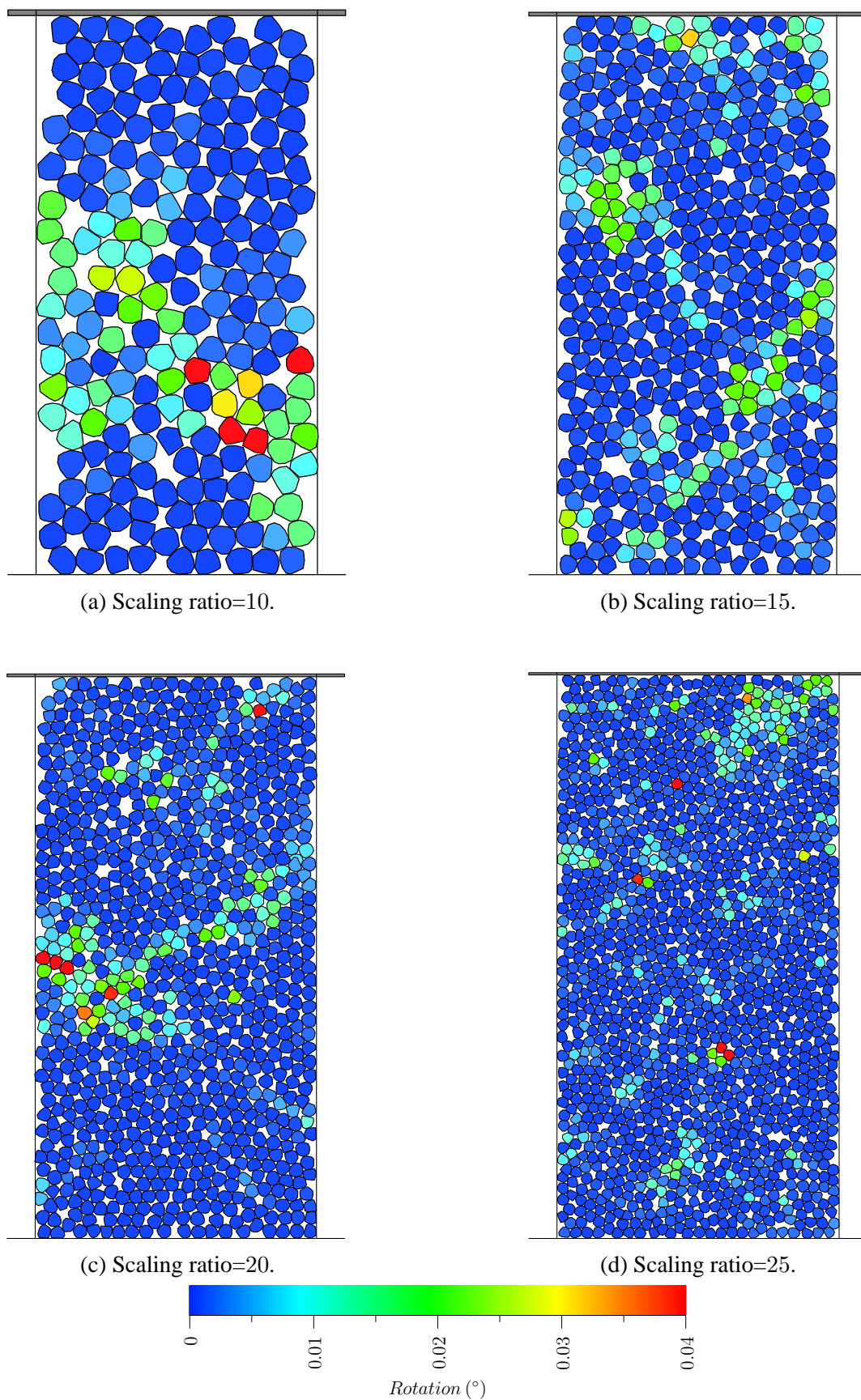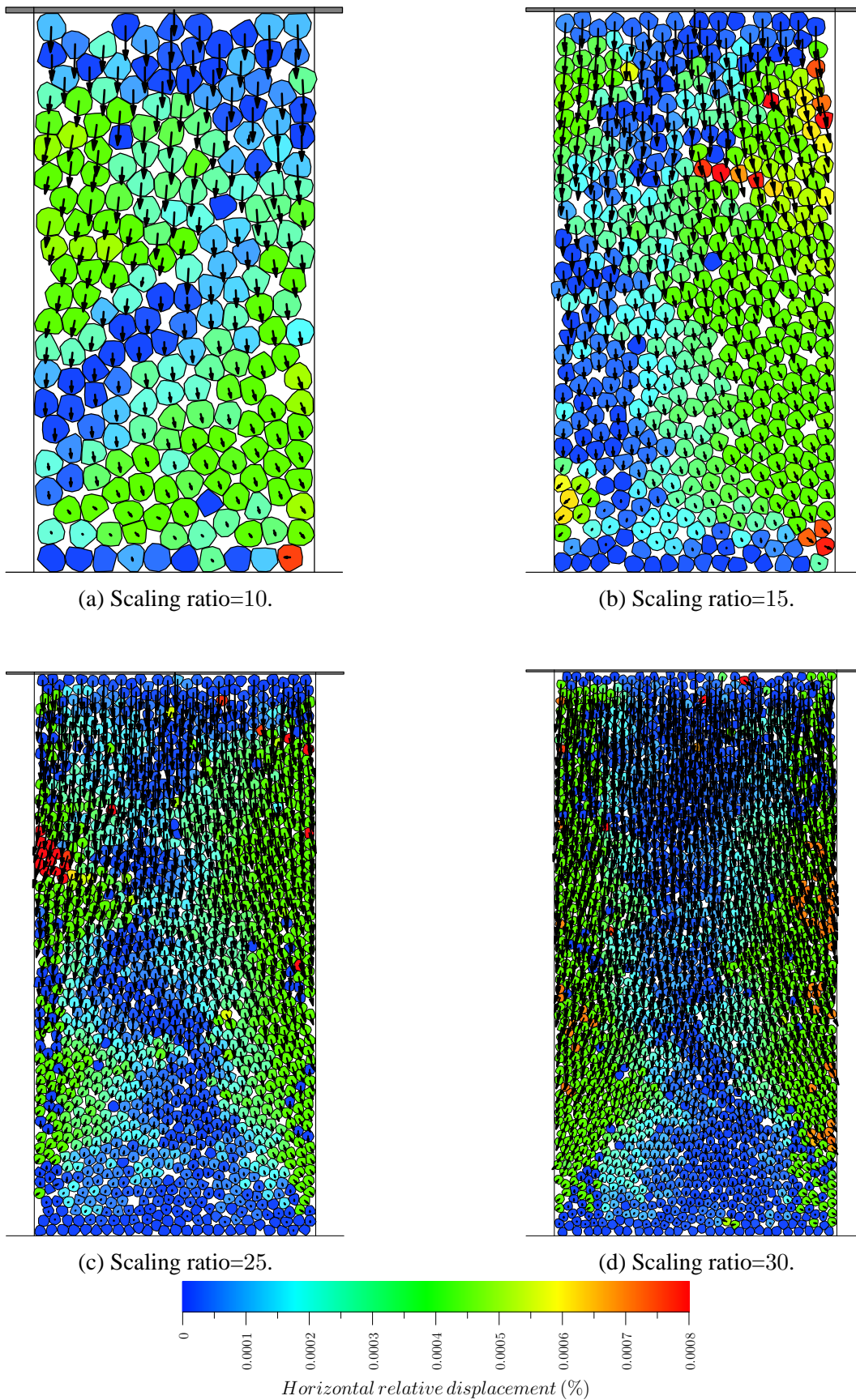
(a) Scaling ratio=10.

(b) Scaling ratio=15.

(c) Scaling ratio=20.

(d) Scaling ratio=25.

$Rotation$ (°)

Figure 6.13: Particle accumulated rotation diagram at deviatoric strain 0.002% for dodecagonal samples of void ratios around 0.26.

(a) Scaling ratio=10.

(b) Scaling ratio=15.

(c) Scaling ratio=25.

(d) Scaling ratio=30.

Horizontal relative displacement (%)

Figure 6.14: Particle total horizontal relative displacements and accumulated displacement vectors at deviatoric strain 0.002% for dodecagonal samples of mean coordination numbers around 3.55.
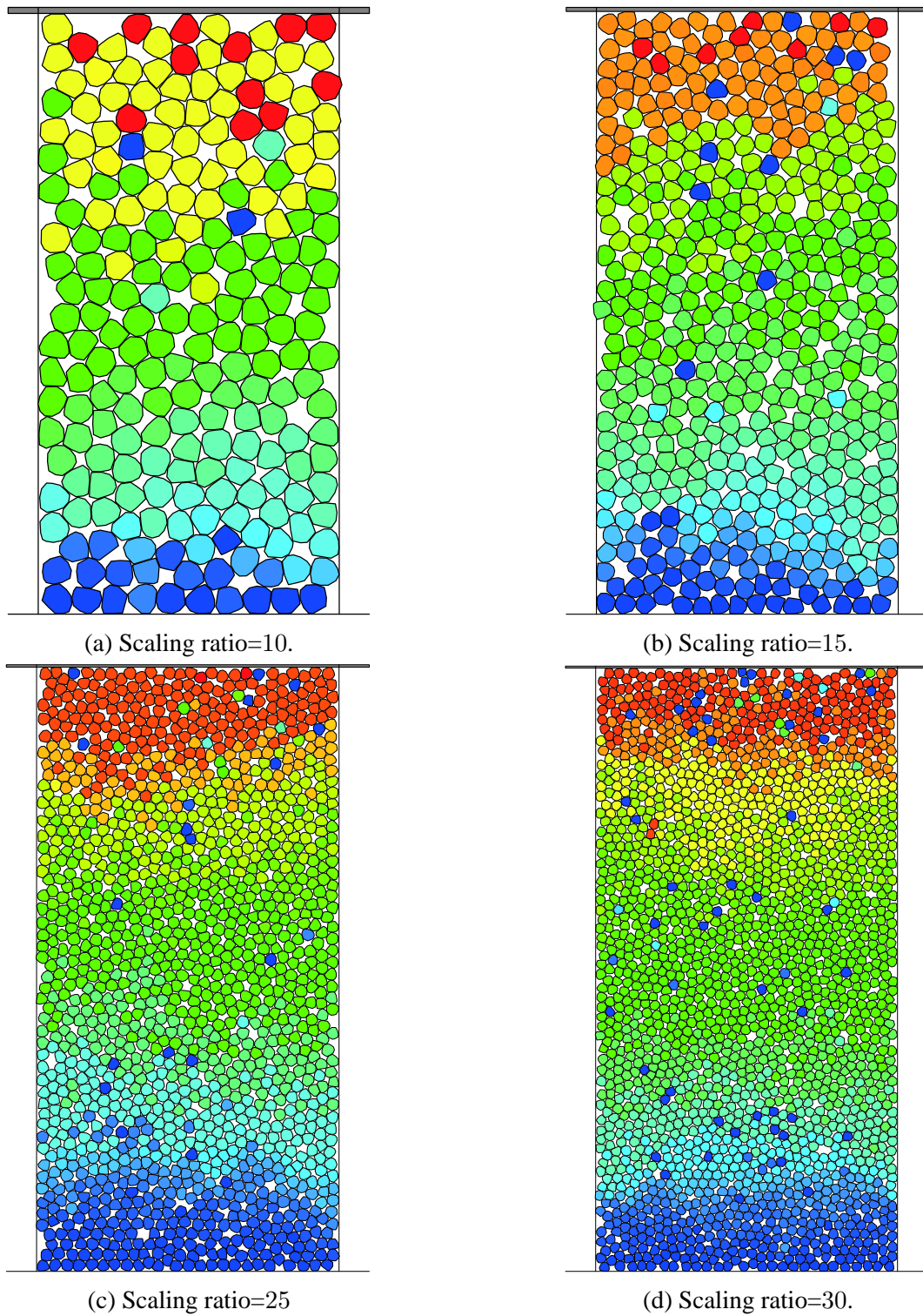
(a) Scaling ratio=10.

(b) Scaling ratio=15.

(c) Scaling ratio=25

(d) Scaling ratio=30.

Figure 6.15: Particle total vertical relative displacements deviatoric strain 0.002% for dodecagonal samples of mean coordination numbers around 3.55.
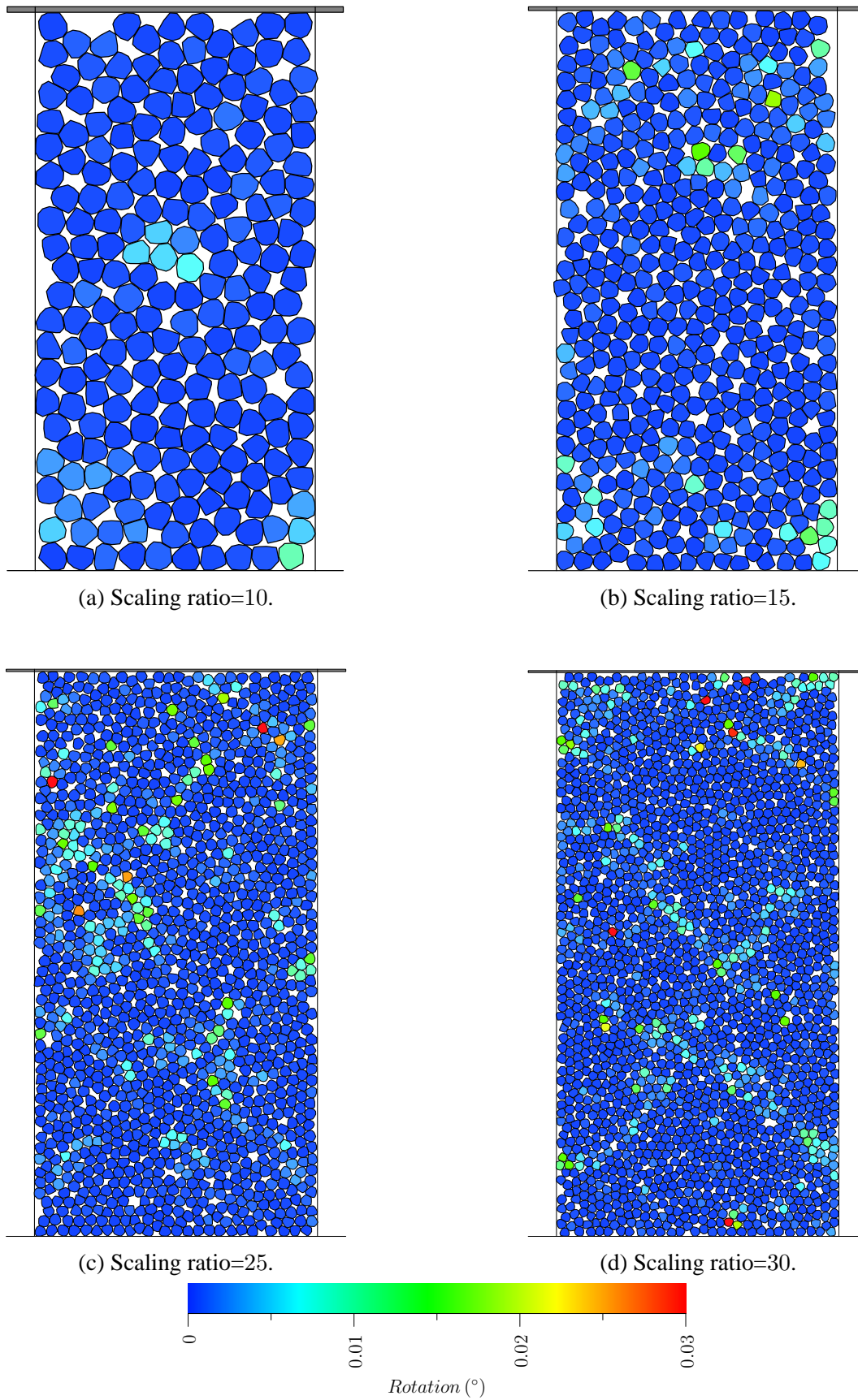
(a) Scaling ratio=10.

(b) Scaling ratio=15.

(c) Scaling ratio=25.

(d) Scaling ratio=30.

$Rotation$ (°)

Figure 6.16: Particle accumulated rotation diagram at deviatoric strain 0.002% for dodecagonal samples of mean coordination numbers around 3.55.

Two dodecagonal packings were selected to be compared with a hexagonal packing and a Voronoi-based packing at two different mean coordination numbers as illustrated in Figure 6.17 and Figure 6.18 in order to analyse the packing effects on stiffness. It can be seen in Figure 6.17b and Figure 6.17d that a large number of stable local close clusters have been developed, and the particles in dodecagonal packings tend to move outward to the right to a large extent as shown in Figure 6.17a. Otherwise, rotations in hexagonal particles are observed to be inhibited apparently when comparing Figure 6.17c and Figure 6.17d.

The void ratios of the dodecagonal and Voronoi-based packings shown in Figure 6.18 are 0.228 and 0.224. Instead, the main difference in stiffness is caused by particle size and shape variations. Since particle shape variation can ease particle rotation especially at the vertex-vertex or vertex-edge contacts (Figure 6.18d), and the particle size variation will make smaller particles move or rotate more surrounded by larger particles (Figure 6.18b), the mono-sized and mono-shaped particle packings can exhibit stabler performance (i.e. greater stiffness) than the Voronoi-based samples especially during the very initial stage during which a small shear force can disturb the micro skeleton.

(a) Displacements for the dodecagonal sample.

(b) Displacements for the hexagonal sample.

$Horizontal\ relative\ displacement\ (\%)$

(c) Total rotations for the dodecagonal sample.

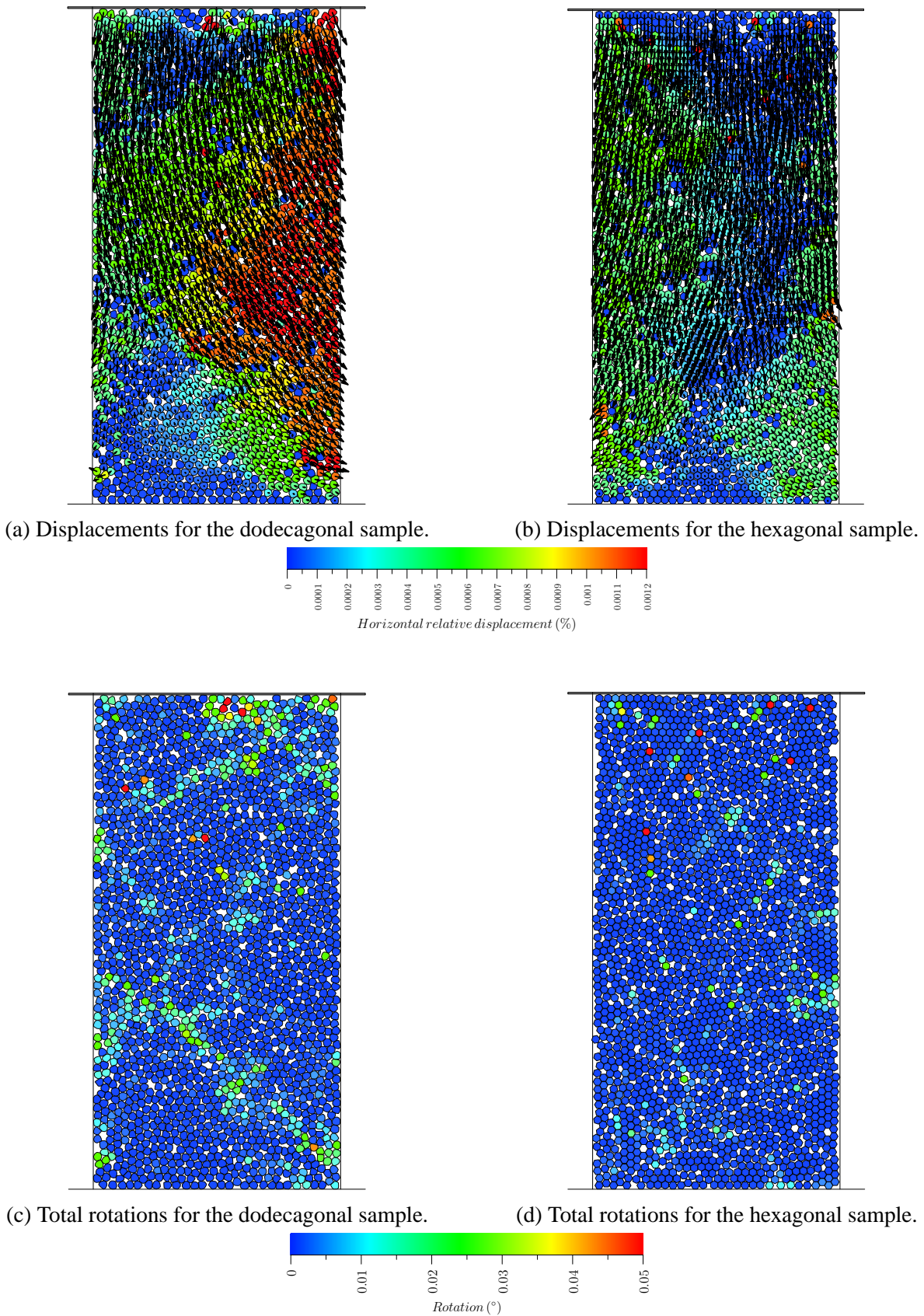(d) Total rotations for the hexagonal sample.

$Rotation\ (°)$

Figure 6.17: Particle total horizontal relative displacements and rotations for dodecagonal and hexagonal samples of mean coordination numbers and void ratios 3.005 and 0.284, 2.996 and 0.231 respectively.
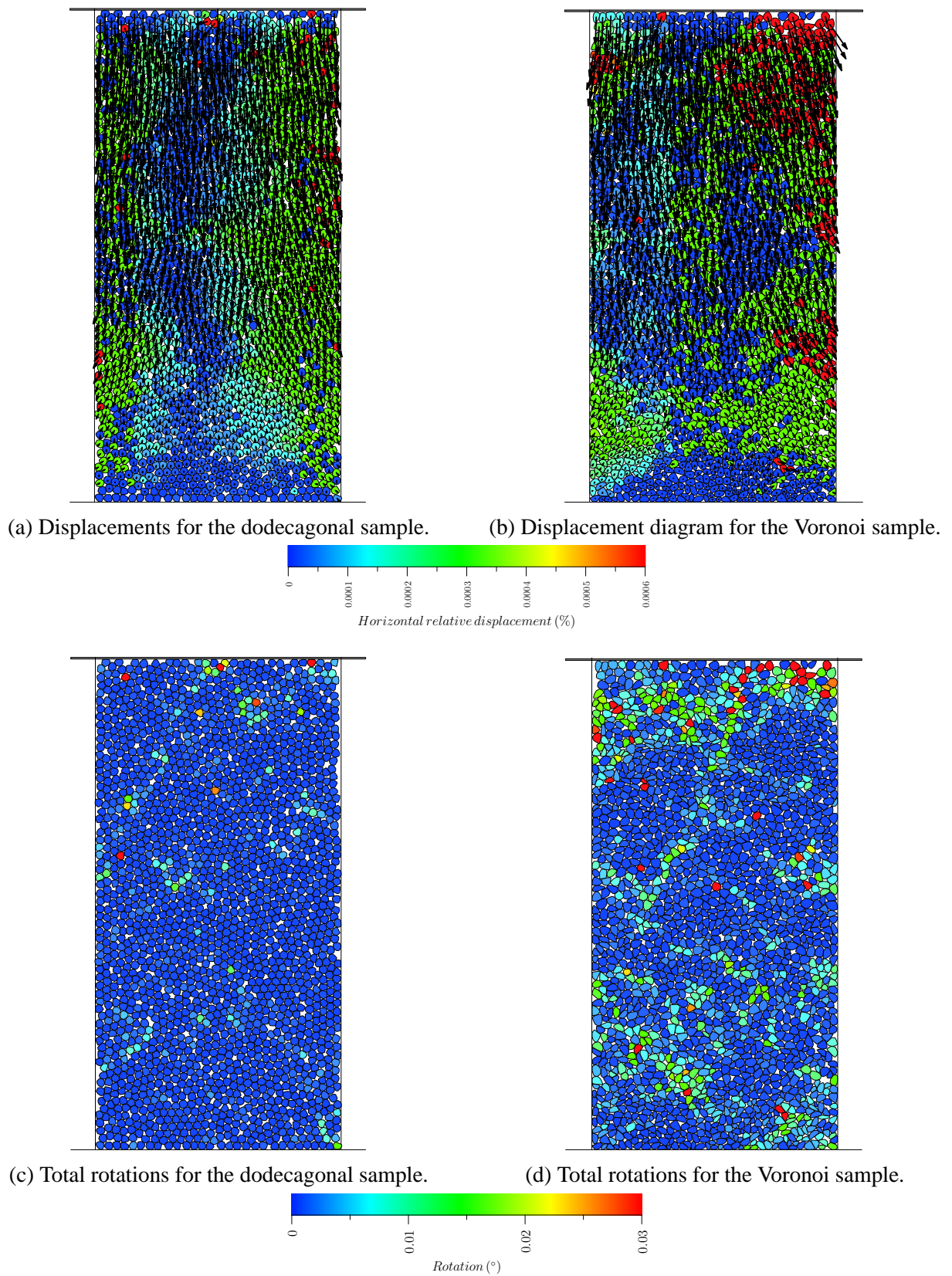
(a) Displacements for the dodecagonal sample.

(b) Displacement diagram for the Voronoi sample.

$Horizontal\ relative\ displacement\ (\%)$

(c) Total rotations for the dodecagonal sample.

(d) Total rotations for the Voronoi sample.

$Rotation\ (°)$

Figure 6.18: Particle total horizontal relative displacements and rotations for dodecagonal and Voronoi samples of mean coordination number 3.76.
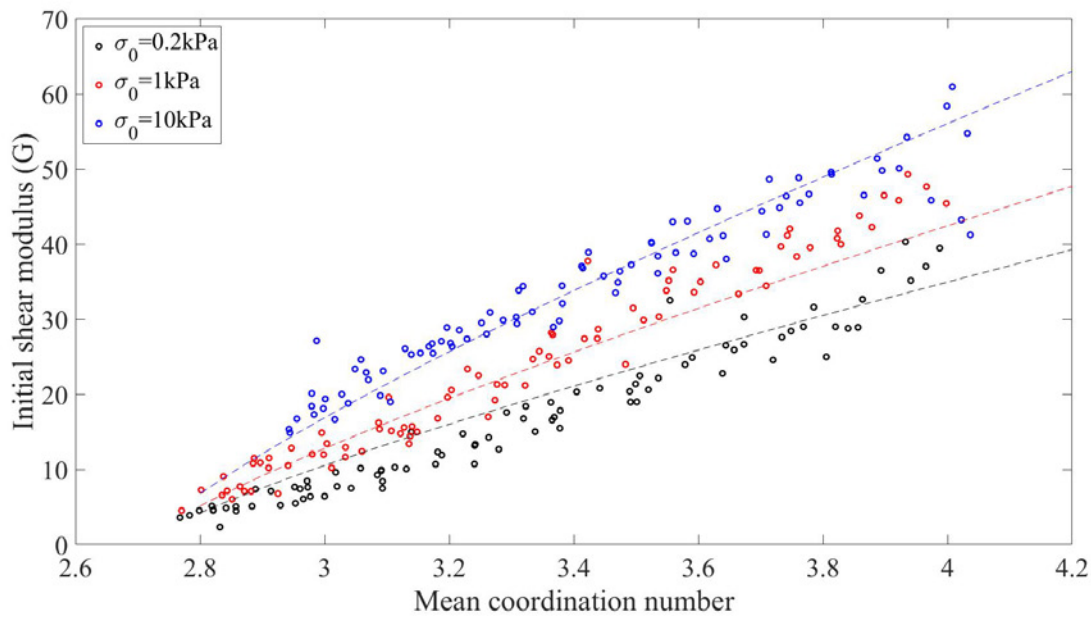
6.3 Confining pressure effects on small-strain stiffness

The effects of confining pressure on initial stiffness of granular soil samples made of different parti-
cles were studied. Particles were deposited into samples of different initial densities by altering the
deposition friction coefficient in each biaxial container for which the model scaling ratio was kept at
30. For each particle shape, 255 simulations were conducted and divided into three groups confined at
0.2 kPa, 1 kPa and 10 kPa respectively. Equations (6.11) and (6.12) were adopted to compare the re-
lationship between initial shear modulus and mean coordination number and void ratio respectively.
The parameters obtained by non-linear least-squares regression analysis are listed in Table 6.3 and
6.4. Figure 6.19 and 6.20 present the simulation results and corresponding best-fitting curves.
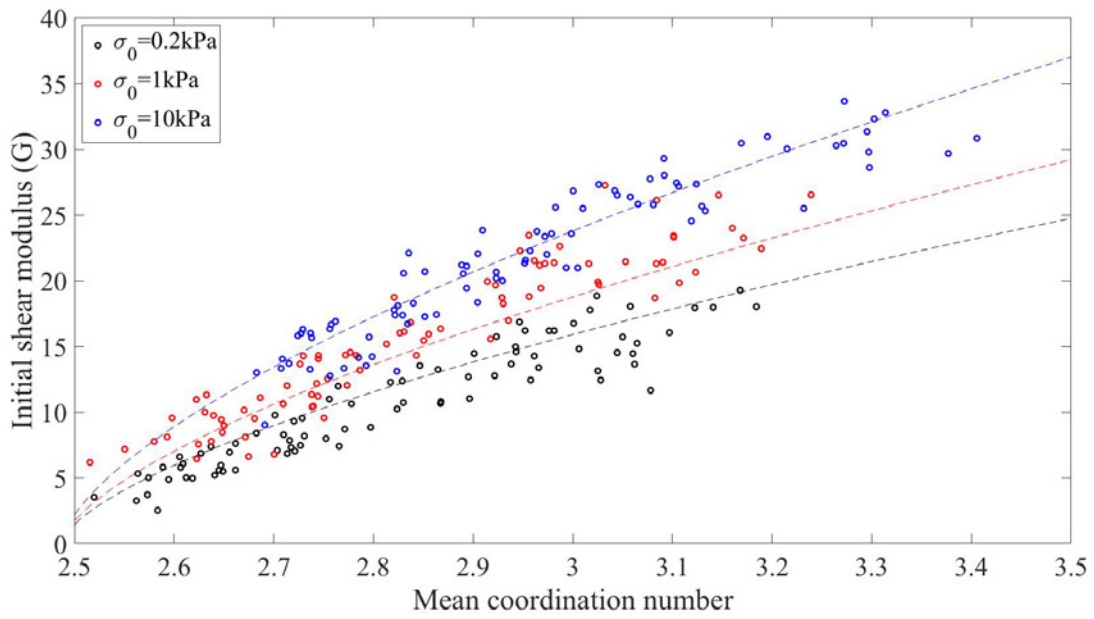
$$G_0 = \alpha(M_n - M_0)^m \sigma_0^r \tag{6.11}$$

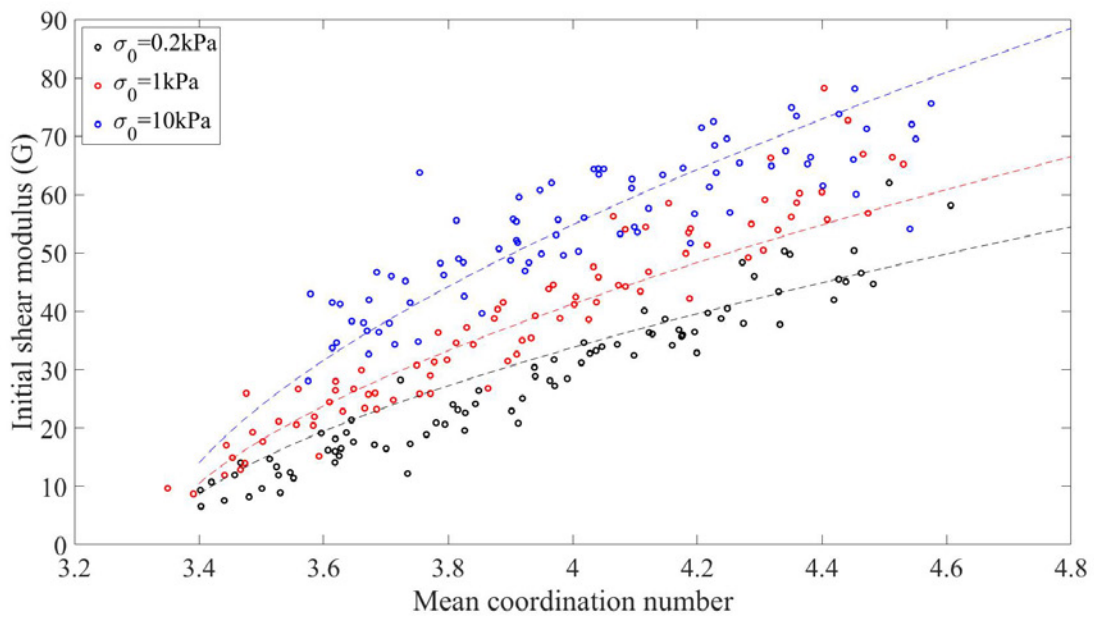Table 6.3: List of best-fitting parameters in equation (6.11).

Parameters / Samples	α	M_0	m	r
Dodecagons (ratio=30)	34.37	2.704	0.8126	0.1207
Hexagons (ratio=30)	28.95	2.487	0.6501	0.1029
Voronoi tessellation (ratio=30)	52.57	3.329	0.609	0.124

(a) Dodecagonal samples.
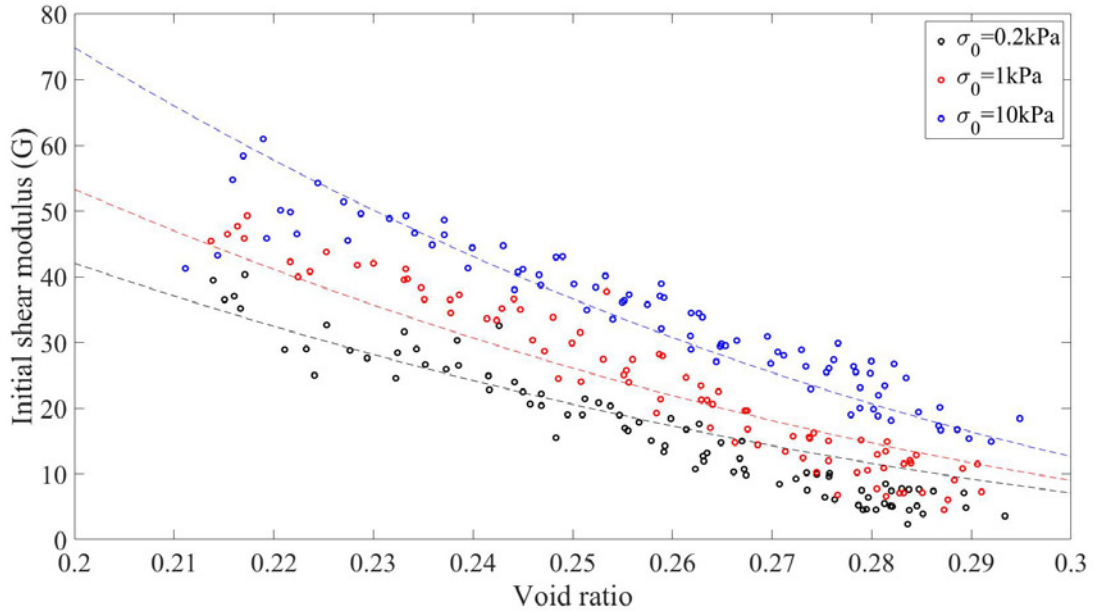
(b) Hexagonal samples.

(c) Voronoi-based samples.

Figure 6.19: Confining pressure effects on small-strain stiffness for different samples related with mean coordination number.

$$G_0 = F(e)\sigma_0^n = A\frac{(a-e)^2}{1+e}\sigma_0^n \tag{6.12}$$

Table 6.4: List of best-fitting parameters in equation (6.12).

| Parameters \ Samples	A	a	n
Dodecagons (ratio=30)	2093	0.3748	0.1474
Hexagons (ratio=30)	199.6	0.5486	0.1625
Voronoi tessellation (ratio=30)	3242	0.329	0.1505

In equation (6.11), it is clearly shown that parameters α, M_0 and r increases as particle circularity decreases. Parameter m for the hexagonal particles is lower than that for the dodecagonal particles and this may be due to packing effects. In principle, M_0 is the minimum mean coordination number for each particle shape in quasi-static equilibrium condition. Parameters A, a and n in equation (6.12) are also dependent on particle shape and packing effects as A increases with decrease of particle circularity while a and n for the hexagonal particles are also influenced by packing effects. The confining pressure increase can enhance the small-strain stiffness of granular soils as a result of constraint of movement in the horizontal direction by stronger confinement, especially at initially denser states in which mean coordination number is higher as shown in Figure 6.19 and 6.20. The small-strain stiffness difference caused by confining pressure is less significant for samples in initially looser states. The best-fitting curves are observed to agree better with the initial shear modulus data for higher confining pressures. Equation (6.11) was found to be more accurate than equation (6.12) in capturing the confining pressure effects on initial stiffness of granular soils. This is because although void ratio is correlated with mean coordination for a specific packing as shown in Figure 6.10c, mean coordination number can better reflect the true packing natures in force transmission and particle contact condition, both of which will influence soil strength and stability.

(a) Dodecagonal samples.
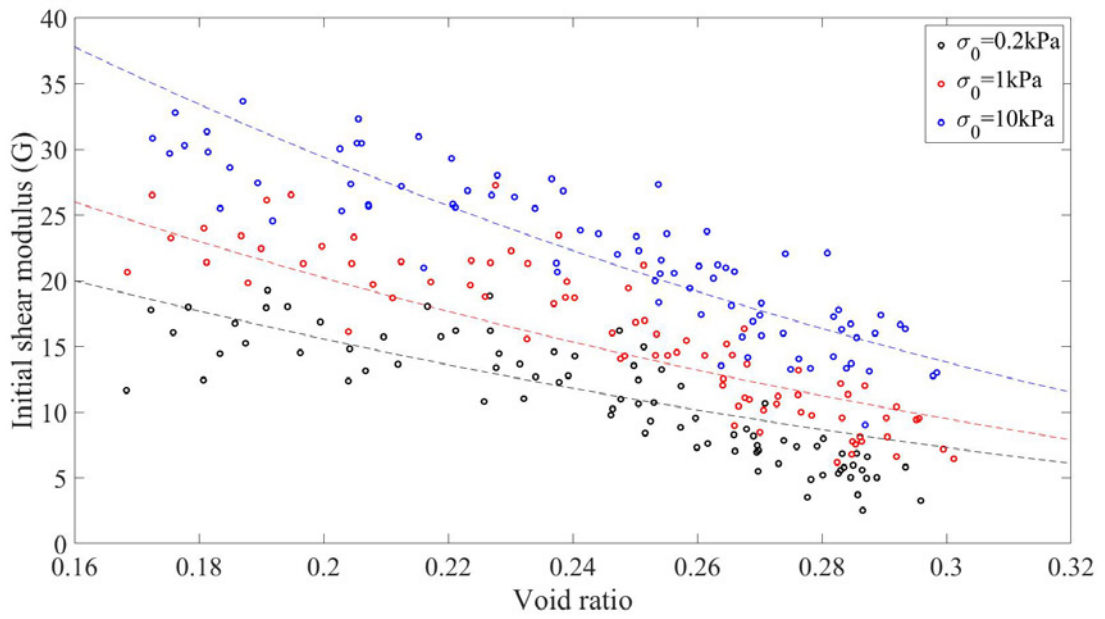
(b) Hexagonal samples.
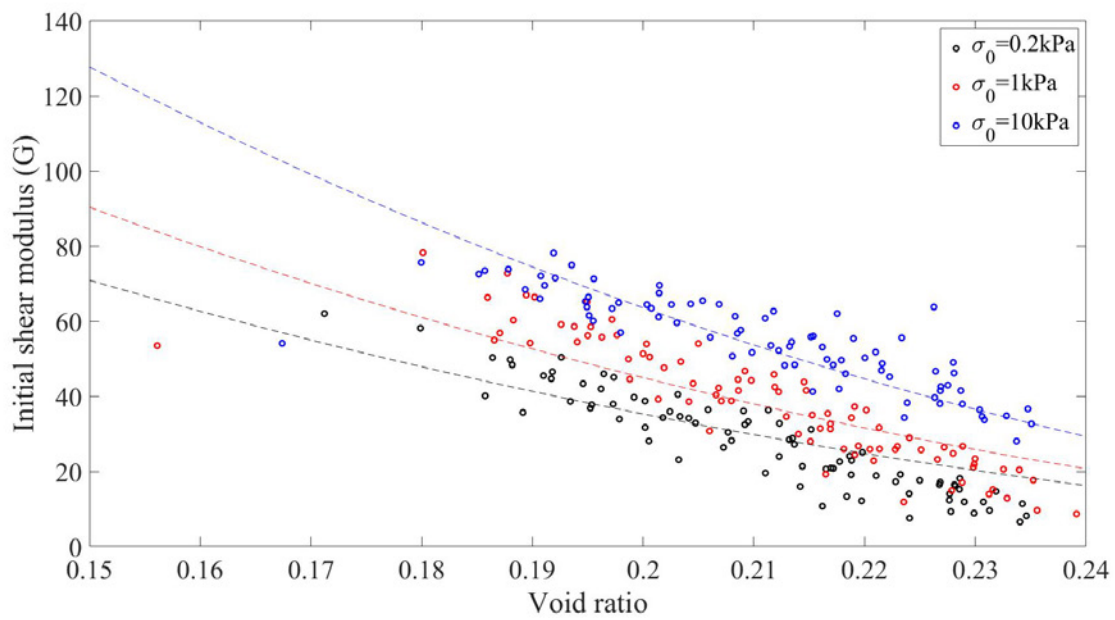
(c) Voronoi-based samples.

Figure 6.20: Confining pressure effects on small-strain stiffness for different samples related with void ratio.

6.4 Summary

A large number of biaxial simulations have been conducted using physics engine Box2D to study the biaxial model scaling ratio and packing effects (made of random dodecagonal particles, regular hexagonal particles and Voronoi-based particles respectively) on the small-strain stiffness (described by shear modulus G in this study). The mechanical descriptors were redefined based on the parameters proposed in the triaxial system to fit for the biaxial system. The main observations are:

1. Increasing the scaling ratio will cause stiffness to increase under the same void ratio and this effect is only observed in dodecagonal samples.

2. Samples made by mono-sized and mono-shaped particles possess higher small-strain stiffnesses than Voronoi-based samples in which particle size and shape deviate greatly. The samples deposited by unique regular hexagonal grains exhibit highest stiffnesses due to the close packing nature (or crystallisation effects) under equal mean coordination condition, however, the samples show the lowest stiffness under equal void ratio condition.

3. There is a small but measurable effect on small strain stiffness when changing the scaling ratio and this needs caution in numerical modelling. The difference is hypothesised to be caused by the relative volume of particles undergoing rotation and outward movement which increases as the scaling ratio decreases in otherwise identical conditions due to reduced constraints at the boundaries.

4. The confining pressure in biaxial tests were found able to influence soil initial stiffness much more apparently than the model scaling effects. Soil exhibits higher initial stiffness under higher confining pressure. By comparing with void ratio, mean coordination number is shown more pronounced than than void ratio in correlating with the initial stiffness under confining pressure effects for different packings.

Based on the data obtained in this study, it was found that the model scaling effects will degrade when exceeding 25. It is possible to predict the small-strain stiffness according to the initial void ratio and particle shape. In addition, although the mean coordination number is more correlated with the initial shear modulus than the void ratio under the confining pressure effects because this parameter reflects the inter-particle contact condition for force transmission, it is difficult to measure in physical tests. It is still a good choice using initial void ratio to correct the induced deviation caused by confining pressure effects in physical models because the mean coordination number is strongly correlated with the void ratio by a unique relationship for each type particle shape as shown in Figure 6.10c.

Chapter 7

Retaining Wall Simulation

7.1   Introduction

It has been shown in Chapter 5 and 6 that Box2D has potent capabilities in capturing granular soil behaviours in simulating biaxial tests (similar to the plane strain compression test and both of them are the most frequently-used approaches in laboratories to measure soil mechanical properties). More practical retaining wall models will be constructed and studied in this part. Large polygonal particles will be modelled as the backfill materials to investigate the effects on wall/backfill interface friction, the earth pressure coefficients in both passive and active conditions.

Fang et al. (1994, 2002) studied mobilised passive earth pressure with various wall movements by physical experiments. It was found that Coulomb and Terzaghi solutions slightly underestimated the critical passive earth pressure coefficient in loose sand backfills, while agree well in medium dense and dense samples. The passive soil thrust will reach the critical state after the ratio of wall movement to initial backfill height exceeds 12%. Compared with the Coulomb's solution, the Terzaghi's solution can better describe the peak passive thrust behaviour in the medium dense and dense samples. It is apparent to observe that the Rankine's solution significantly underestimate the passive pressure in all cases. Besides the horizontal translational wall movement (T mode), rotation about a point above the top (RT mode) and below the base (RB mode) modes in the passive condition were also studied. The critical states in RT and RB modes were observed to reach slightly later than in T mode. The measured critical passive earth pressure coefficient in the RT mode is lower than the solutions give by Coulomb, Terzaghi and Rankine theories, however, there was no ultimate soil thrust observed in the RB mode. In addition, the passive pressure distributions are nonlinear in the RT and RB modes, compared with hydrostatic passive pressure in the T mode. Fang and Ishibashi (1986) also conducted laboratory tests for retaining wall models in the active condition in the modes: translation, rotation about the top and rotation about the heel. The active earth pressure distribution in the case of rotation about the top is highly nonlinear compared with the other two cases, and the active earth pressure coefficients in the cases of rotation about the top and the heel are higher than the case of translation, which agrees well with the Coulomb's solution.

Some researches were also carried out on numerical modelling on retaining wall simulations. Jiang et al. (2014) used disc particles in PFC2D to model retaining walls in both active and passive conditions in three different modes: horizontal translation (T mode), rotation about the base (RB mode) and rotation about the top (RT mode) and proposed a contact model considering inter-particle rolling resistance to be applied in the simulation. The active and passive earth pressure distributions were observed evidently nonlinear in the RB and RT modes. In the active state, as the retaining wall displaces away from the backfill, a sharp drop of the active earth pressure coefficient is found, while in the passive condition, the passive earth pressure coefficient tends to increase to a constant value in the relatively loose backfill or a peak value followed by a strain softening behaviour before reaching a critical value in the relatively dense backfill. It was also reported that the mean particle size increase will raise the passive earth pressure coefficient in both loose and dense backfills. The ratio of wall movement to initial backfill height needs to reach 2% in the active condition, and 20% and 40% for the loose and dense backfills in the passive condition in the case of T mode (20% for the other two modes in the dense backfills). The shear strain field was plotted for each condition and the shear band thicknesses were investigated to be around $(7-16)d_{50}$ and $8d_{50}$ in the active and passive condition respectively. Altunbaş et al. (2019) conducted a 3D simulation on retaining wall models by using EDEM software to analyse the boundary conditions on the failure mechanism and the passive earth pressure. A thicker shear band was observed in the case of frictionless side walls applied, while the shear band was not apparently formed in the case of frictional side walls.

Limited by the computational power, most DEM models on retaining walls used 2D disc or 3D spherical particles as backfill materials, which will be replaced by polygonal particles here. The bottom boundary effects and the relationship between the wall local friction and the wall/backfill interface friction under a constant backfill internal friction will be analysed for both active and passive conditions in this study. In this chapter, Box2D will be applied in modelling retaining walls, and the obtained data along with the failure mechanisms will be compared with theoretical solutions given by Powrie (2018) and limit analysis (simulated via the software LimitState: GEO).

7.2 Model set-up

Rigid vertical retaining walls undergoing pure horizontal translation will be considered in this chapter. Table 7.1 provides the main system and model parameters used in the series of simulations. The system and particle shape parameters are consistent with those set in the biaxial tests. The initial states of the retaining walls and the backfills are shown in Figure 7.1 in which two types of models are considered in this study. In Figure 7.1a, the retaining wall was built directly sitting on the bottom boundary, while for the other type of model in Figure 7.1b, the retaining wall was built above the bottom boundary by a distance of 5-particle sizes to eliminate the bottom boundary effects on the failure wedge and rupture surface developed as the retaining wall moves toward the backfill. This is because, in some cases, the deforming mass will extend the retaining wall base if a half-space continuum is assumed.

Modelling of walls

In Figure 7.1a, the first wall from the left was built as a kinematic body which is one of the three object types in Box2D that has infinite mass and controlled purely by velocity as it does not respond to a force due to its infinite mass. The second wall from the left is a dynamic body which is the same object type as the backfill particles and can respond to either velocity or force. The dynamic wall is moved with the kinematic wall horizontally in the passive condition. The aim of constructing the kinematic wall was to prevent the particles being regarded as "bullets" due to intrinsic system settings. The bullet option can be selected when defining a dynamic body to involve calculation of the potential time of impact (TOI) finding the next collision moment in the continuous collision detection (CCD) algorithm to avoid "tunnelling" happening as introduced in section 3.4, and this is designed for fast moving dynamic bodies however sacrificing the computational efficiency in the meantime.

The right wall and the bottom boundary were defined as static bodies which have infinite mass and do not collide with kinematic or static bodies. The mass of the dynamic wall is extremely large to make sure it will not tilt when interacting with the backfill. In Figure 7.1b, the left wall was defined as the kinematic body as the dynamic wall will fall into the backfill when being pushed by the kinematic wall. To avoid the influences of the right static wall in the passive condition, the initial backfill width to height ratio was set to be 4.0. There was an additional static edge built below the initial kinematic wall to prevent the backfill particles moving outward. The left and bottom boundary and the static wall friction coefficients were chosen as the same value as that of the backfill particles. For simplicity, the models shown in Figure 7.1a and 7.1b will be referred to as condition A and B respectively.

Backfill placement

At the beginning of the simulation, the walls and the bottom boundary were firstly built and then the backfill particles were created and fell onto the bottom boundary under gravity until all the particles came into rest. The retaining wall was set to be frictionless initially to maintain all the backfills to be unique in order to eliminate the packing effects on final data. The particle lying at the highest position will be found, and all the particles above the height which was 1.5 times the average particle diameter below the highest particle were excluded from the simulation in order to make the backfill height even across the entire width. The particle friction coefficient would be changed gradually to 0.4663 from 0.1 which was set during the deposition process for creating backfills of different initial densities and the retaining wall local friction coefficient was also changed to the desired value to analyse the wall local friction effects. The average global and local sample heights were measured by ray-casting method as introduced in section 5.2. Each particle in the horizontal direction was assigned three rays on average to guarantee both accuracy and efficiency. The local void ratio behind the retaining wall was measured within a zone of 4-particle size (diameter of its bounding circle defined beforehand for creating a particle of a specified size) in width, for which the average local backfill height was calculated by using 15 rays displayed as green lines in Figure 7.1. It is efficient to calculate the local void ratio required to be known by this approach to obtain the mobilised lateral earth pressure

coefficients as the wall moved. It is worth mentioning that the lateral earth pressure is the result of the whole sliding wedge of soil adjacent to the wall surface and the sliding wedge weight is partly determined by the local void ratio within it, therefore using the local void ratio adjacent to the wall is an approximation to the local void ratio within the sliding wedge.

Active and passive conditions

After creation of the backfill deposit, the left retaining wall moved towards the backfill in the passive condition or away from the backfill in the active condition. In the passive condition, the process would not terminate until the retaining wall movement reached 25% of the initial backfill width or span, while 0.2% for the active condition as the active critical state will reach earlier than the passive critical state.

Table 7.1: List of main parameters.

Parameters	Values
Box2D default parameters	
Time step size	$1/60\,\text{s}$
Number of velocity iterations per time step	8
Number of position iterations per time step	3
Contact skin thickness	$0.001\,\text{m}$
Particle characteristics	
Density	$2660\,\text{kg/m}^3$
Restitution coefficient	0
Particle bounding circle diameter[1]	$1.0\,\text{m}$
Non-elongated particle aspect ratio	1.0
Test set-up parameters	
Particle friction coefficient[2]	0.1
Gravity acceleration[3]	$0.1\,\text{m/s}^2$
Particle number along the retaining wall width	80
Initial backfill width to height ratio in the passive condition	4.0
Initial backfill width to height ratio in the active condition	1.5
Retaining wall model parameters	
Bottom boundary friction coefficient	0.4663
Particle friction coefficient	0.4663
Kinematic wall absolute translational velocity	$0.006\,\text{m/s}$
Gravity acceleration	$0.1\,\text{m/s}^2$
Retaining wall movement limit[4] in the passive condition	25%
Retaining wall movement limit[4] in the active condition	0.2%

[1] Not for Voronoi-based particles.
[2] By altering the friction coefficients during deposition to obtain packings of different densities.
[3] For particles generated by deposition.
[4] In terms of the initial backfill width.

(a) Wall contacted with the bottom boundary.   (b) Wall raised above a distance of 5-particle size.
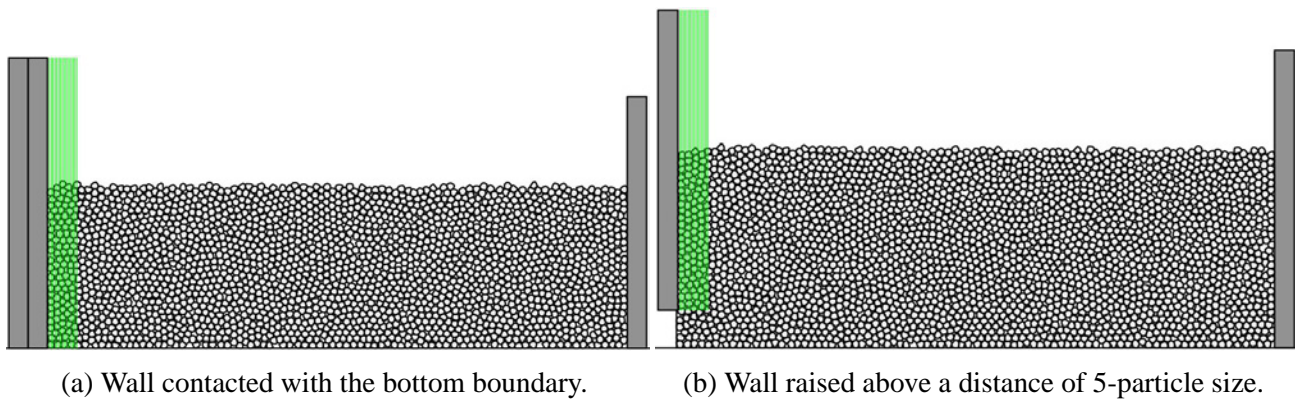
Figure 7.1: Initial retaining wall and backfill set-up.

7.3 Wall friction effects on the lateral earth pressure coefficients

In this section, wall friction effects on the lateral passive earth pressure coefficient will be investigated for backfills made of random dodecagonal polygons in both conditions A and B as shown in Figure 7.1. The first part is establishing the benchmark continuum solutions and the quintessential failure mechanisms for comparisons. Then the backfill packing behaviours, the passive earth pressure coefficient under various wall friction conditions will be analysed, followed by the relationship between local wall friction and wall/backfill interface friction. Graphical interpretation approaches are applied for the modelling in order to better understanding the microscopic backfill restructure events, such as particle accumulated rotations, particle accumulated displacements and inter-particle contact force chains. Backfill initial density effects in the passive condition and wall friction effects in the active condition will also be studied.

7.3.1 Benchmark theoretical solutions

Figure 7.2 and 7.3 illustrate the backfill failure mechanisms under passive and active conditions respectively. The parameters δ and ϕ shown in the figures represent the retaining wall/backfill interface friction angle and the backfill internal friction angle. If the wall is smooth, the lateral force P given by the retaining wall to the backfill is horizontal, while due to the existence of friction between the wall and the backfill, the direction of P is no longer horizontal but inclines with an angle δ clockwise and counterclockwise from the horizontal direction in the passive and the active condition respectively. The shear stress τ generated by the friction is calculated by:

$$\tau = \sigma \tan \delta \tag{7.1}$$

The backfill failure indicates the transition from the plastic equilibrium state into plastic flow and this occurs along the rupture surface (shear line) shown in the figures (Terzaghi, 1943). This rupture surface is constituted with a curved slip line which could be approximately regarded as a part logarithmic or circular line and a part straight line, and these two slip lines constitute the whole shear

pattern. Theoretically, the shear pattern is a plane surface when the retaining wall is smooth and could be simplified as being perfectly plane by Coulomb theory (Coulomb, 1776) when $\delta < \phi/3$. The backfill Rankine zone ACD intersects with the horizontal surface orientated at $45° - \phi/2$ in the passive condition, and $45° + \phi/2$ in the active condition as firstly solved by Rankine (1857). In front of the retaining wall in the passive condition or behind the retaining wall in the active condition there is a wedge-shaped body moving upward or downward respectively associated with the failure of the backfill and this is shown as a sliding wedge $ABCD$ which includes the shearing zone and the Rankine zone. It is mentioned by Terzaghi (1943) that the curved bottom boundary of the shearing zone can be simply assumed to be perfectly plane without excessive error when the backfill is made of cohesionless soils.
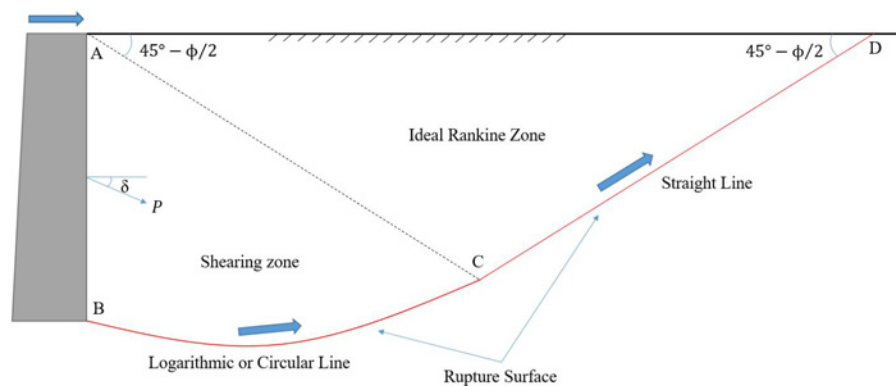
Figure 7.2: Backfill failure mode in the passive condition (Terzaghi, 1943).
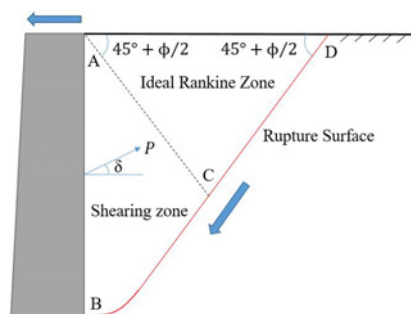
Figure 7.3: Backfill failure mode in the active condition (Terzaghi, 1943).

To investigate the failure mechanisms of retaining walls in the passive condition, a retaining wall model the same as that built in Box2D was established in LimiteState:GEO as shown in Figure 7.4a. The dimensions were kept consistent with that in Figure 7.1b. The backfill was filled with cohesionless dense sand material model of internal friction angle to be $25°$. The interface between the retaining wall and the backfill was modelled by a material without tension existing. The bottom edge of the retaining wall was fixed to prevent from rotation when failure occurs. The backfill was surrounded by fixed boundaries. Figure 7.4b to 7.4d illustrate the failure modes after being pushed by the left retaining wall. It should be noticed that the failure occurs after the retaining wall displaces by an infinitesimal value and the animation is only for visualisation at collapse. The failure surface was

observed to be perfectly plane when the wall is frictionless and intersected with the horizontal sur-
face at $32.5°$ consistent with the value in Figure 7.2. When the wall/backfill interface friction angle
is increased from $0°$ to $25°$, the rupture surface becomes curved however its depth into the bottom
backfill layer below the retaining wall base is rather small, therefore it is considered that the depth of
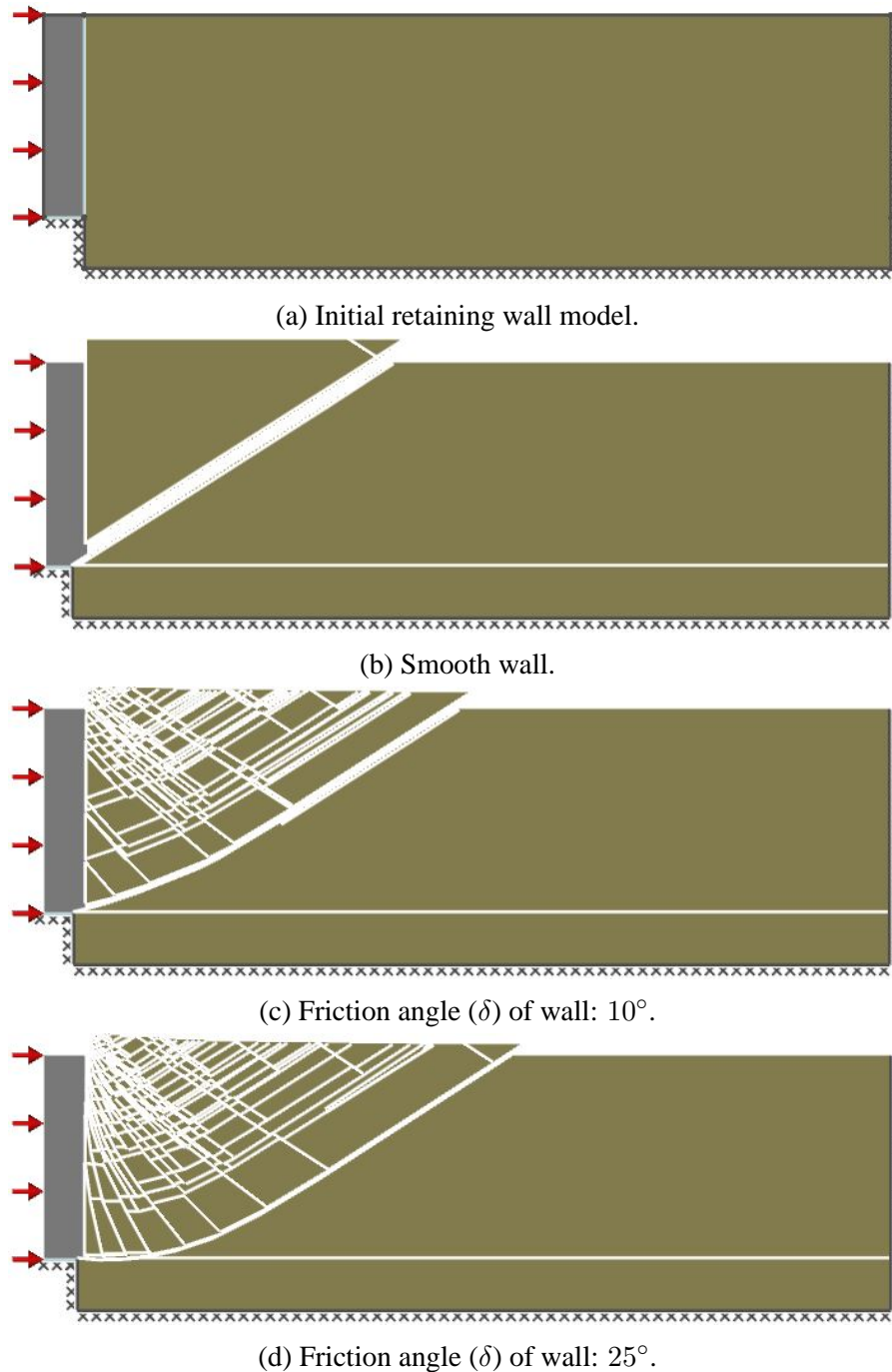the bottom layer set to be 5-particle size will not interfere with the rupture surface.

(a) Initial retaining wall model.

(b) Smooth wall.

(c) Friction angle (δ) of wall: $10°$.

(d) Friction angle (δ) of wall: $25°$.

Figure 7.4: Retaining wall model and failure mechanisms in LimitState:GEO.

The theoretical lateral earth pressure coefficients were calculated following the method provided
by Powrie (2018) which provides better insights in understanding the stress states adjacent to the wall.
Figure 7.5 and 7.6 plot the stress states of the backfills using Mohr-circles in front of the retaining

wall in the passive condition and behind the retaining wall in the active condition respectively. In the passive condition, the major principal stress is horizontal, acting on the vertical plane in zone 1 as the retaining wall moves into the backfill similar to the process of soil compression during which the horizontal stress is increasing and the vertical stress is constant as shown in Figure 7.5b. In zone 2, the backfill will heave after being displaced by the retaining wall and therefore the friction exerted on the backfill is anticlockwise as shown in Figure 7.5a along the interface between the wall and the backfill. The shear stress τ is therefore positive equal to $\sigma \tan \delta$ where δ is the retaining wall/backfill interface friction angle. The Mohr-circle in Figure 7.5c is bounded by the Mohr-Coulomb failure criteria $\tau = \sigma \tan \phi$ and intersected with $\tau = \sigma \tan \delta$. (σ_h, τ_w) indicates the stress state at the wall/backfill interface. The coefficient of earth pressure K is defined as the ratio (σ_h/σ_v) between the horizontal pressure brought by a soil mass on the retaining wall (σ_h) and the normal component of earth pressure of the soil mass (σ_v). The term passive earth pressure indicates the resistance of a soil mass against a force tending to displace it, and the active earth pressure indicates the minimum lateral pressure given by a retaining wall to maintain its adjacent soil mass not to fail. The lateral passive earth pressure
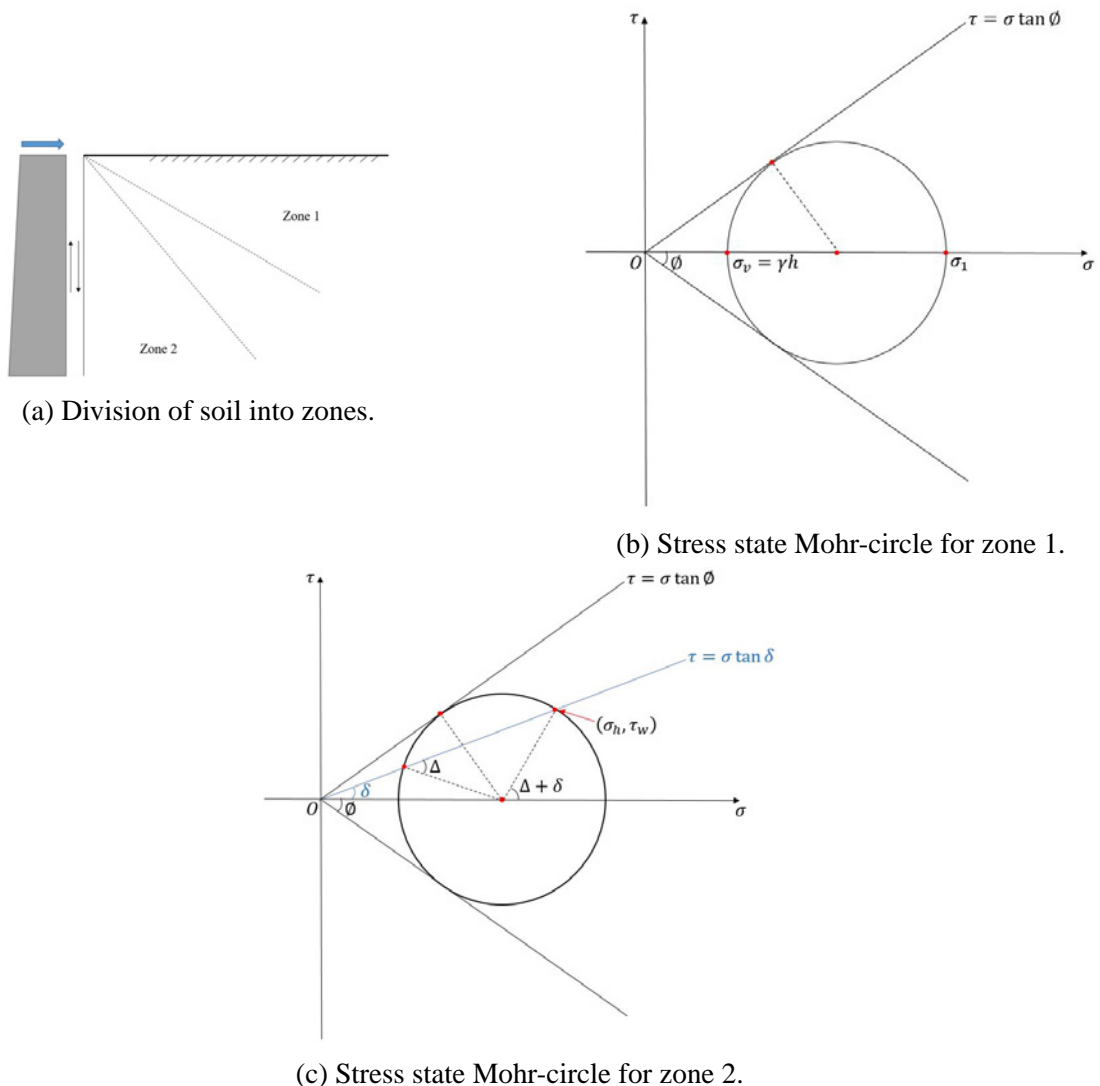

(a) Division of soil into zones.

(b) Stress state Mohr-circle for zone 1.

(c) Stress state Mohr-circle for zone 2.

Figure 7.5: Backfill stress states in the passive condition (Powrie, 2018).

coefficient (K_p) can then be calculated by (Powrie, 2018):

$$K_p = \frac{1 + \sin \phi' \cos (\Delta + \delta)}{1 - \sin \phi'} e^{[(\Delta+\delta) \tan \phi']} \tag{7.2}$$

$$\sin \Delta = \frac{\sin \delta}{\sin \phi'} \tag{7.3}$$

If the retaining wall is smooth ($\delta = 0$), K_p can be simplified as:

$$K_p = \frac{1 + \sin \phi'}{1 - \sin \phi'} \tag{7.4}$$

which is consistent with Rankine's passive earth pressure coefficient (Rankine, 1857).

In the active condition, zone 1 is a conventional active zone where the vertical stress σ_1 is the major principal normal stress acting on the horizontal plane equal to γh in which γ is the soil specific weight and h is the depth from the backfill surface. The Mohr-circle is also bounded by the straight line $\tau = \sigma \tan \phi$. As the backfill is moving downward, the horizontal normal stress σ_h is decreasing and this process is similar to the soil expansion. Zone 2 is contacting with the retaining wall back and settling as the retaining wall moving outward. Therefore, the retaining wall will give the backfill an anticlockwise shear stress τ and hence positive as shown in Figure 7.6a equal to $\sigma \tan \delta$ ($\delta \leq \phi$) represented by straight lines in Figure 7.6c. The stress state on the wall can be solved by their intersection closer to the origin O notated by (σ_h, τ_w) on the graph. The theoretical active earth pressure coefficient (K_a) can be calculated by the equation given by Powrie (2018):

$$K_a = \frac{1 - \sin \phi' \cos (\Delta - \delta)}{1 + \sin \phi'} e^{-[(\Delta-\delta) \tan \phi']} \tag{7.5}$$

If the wall friction angle δ is equal to 0, equation (7.5) can be simplified as:

$$K_a = \frac{1 - \sin \phi'}{1 + \sin \phi'} \tag{7.6}$$

In this study, the lateral earth pressure coefficients K (K_a and/or K_p) are computed by:

$$K = \frac{2P}{\gamma H^2} = \frac{2P(1 + e)}{\rho_s g H^2} \tag{7.7}$$

in which P is the measured lateral contact force at the wall/backfill interface, H is the local backfill height next to the retaining wall, e is the local void ratio adjacent to the wall within the distance of 4-particle size, and ρ_s and g are the particle density and gravitational acceleration respectively. The local friction coefficients of the retaining wall ($\tan \delta_w$) were selected as 0, 0.15 (8.53°) and 0.30 (16.70°), and the inter-particle friction coefficient is kept constant at 0.4663 (25°). Monosized dodecagonal particles and Voronoi-based polygonal particles were both generated as the backfill granular materials in this study to analyse the particle shape and packing effects on the mechanical behaviours of retaining

(a) Division of soil into zones.

(b) Stress state Mohr-circle for zone 1.
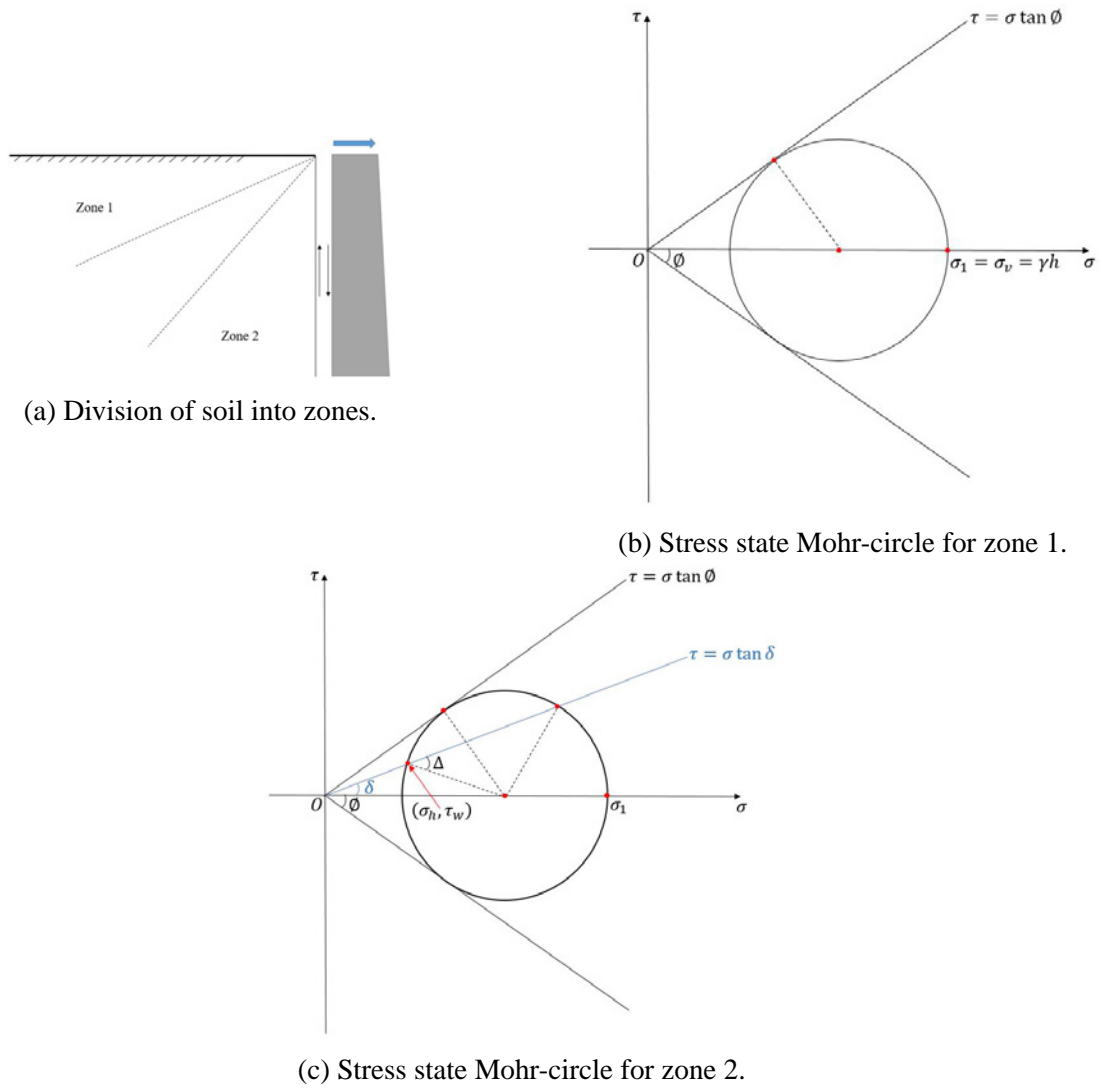

(c) Stress state Mohr-circle for zone 2.

Figure 7.6: Backfill stress states in the active condition (Powrie, 2018).

wall models. Two prior biaxial test simulations using these assemblies were carried out to obtain their critical state friction angles (and hence the continuum K values in equations (7.2) and (7.5) in critical states) and the results are listed in Table 7.2 with their average particle circularities.

Table 7.2: Geometric and global continuum mechanical properties for samples made of two particle shapes.

Particle shape	Average circularity	Angle of shearing resistance (ϕ_{crit})
Monosized dodecagons	0.804	20.6°
Voronoi-based polygons	0.552	26.8°

7.3.2 Backfill deformation in the passive condition

Figure 7.7 shows the global and local void ratios for the models for dodecagonal particles in which the backfills constituted of over 2000 and 2500 random dodecagonal particles in condition A and

condition B respectively for the passive condition. It is clear to see that the local void ratios are generally larger than the global void ratios as the wall moves into the backfills, and this is due to the flat boundary effects at the contact interface decreasing the nearby assembly contact numbers. Besides, the initially densely-packed backfills exhibit dilative behaviours. It is also observed that the wall friction will increase the local and global void ratio in front of the wall in condition A, however this phenomenon reverses in condition B, because of the movements of the particles into the bottom layers in condition B. The local dilatancy is mainly caused by the heave of the local assemblies next to the wall after being pushed, therefore the roughness of the wall will inhibit the dilatancy behaviour and this is also proved by looking at the particle total displacements shown in Figure 7.8 to Figure 7.11 in which the arrows indicate the directions and the accumulated displacements from the start to the corresponding states and their lengths are scaled to fit the graphs. In condition A, the particle vertical displacements are significantly suppressed due to the wall friction and the bottom boundary influences. When the retaining wall starts to move, the top triangular zone next to the retaining wall firstly begin to heave as shown in Figure 7.8a and Figure 7.9a, and more particles are pushed upward at the top compared with the particles at the bottom, additionally, more particles toward the right static wall are involved to move in Figure 7.9b because of the reduced vertical movements. In terms of condition B, the particles at the bottom corner next to the retaining wall are observed to displace along spiral curve trajectories extended into layers of 2- to 3-particle size in depth when being pushed because the bottom particles next to the wall move downwards under gravity in the condition without bottom boundaries. Different from the Coulomb's theory that the sliding wedge is hypothesised as a single mass, a number of gradient sliding wedges are developed as being pushed by the wall. The backfill height increases next to the walls in both conditions were measured as shown in Figure 7.12. The wall back roughness will no doubt inhibit the heave of the assemblies in front of the wall while this effect is more evident in condition A than that in condition B. One of the possible reasons to explain this is that the particles underneath the retaining wall base can help raise the above particles by interactive rotations. Another plausible reason is that the bottom boundary/backfill interface friction angle is smaller than the particle internal friction angle as will be shown in Figure 7.17 later, causing granular soil in condition A being less dilatant than in condition B.

The normal contact forces at the wall/backfill interface were recorded as shown in Figure 7.13. The normal contact forces keep climbing up all the time and at very similar values in both conditions. It is also plausible to see that the wall roughness can increase the produced normal contact forces because from the energy balance perspective, the additional frictional energy consumption at the wall/backfill contact interface should be compensated by the greater external work.

Equation (7.7) can be divided into three parts for calculation of the lateral earth pressure coefficient K: particle properties (ρ_s), packing characteristics (local void ratio e and local backfill height H adjacent to the wall) and contact force (P). In order to analyse the wall/backfill interface friction condition on the resultant local packing characteristics, evolutions of parameter $(1+e)/H^2$ with d/H are plotted in Figure 7.14 for both conditions. This combined parameter is observed to be larger when the wall roughness is greater, and changing more smoothly without the influence of the bottom
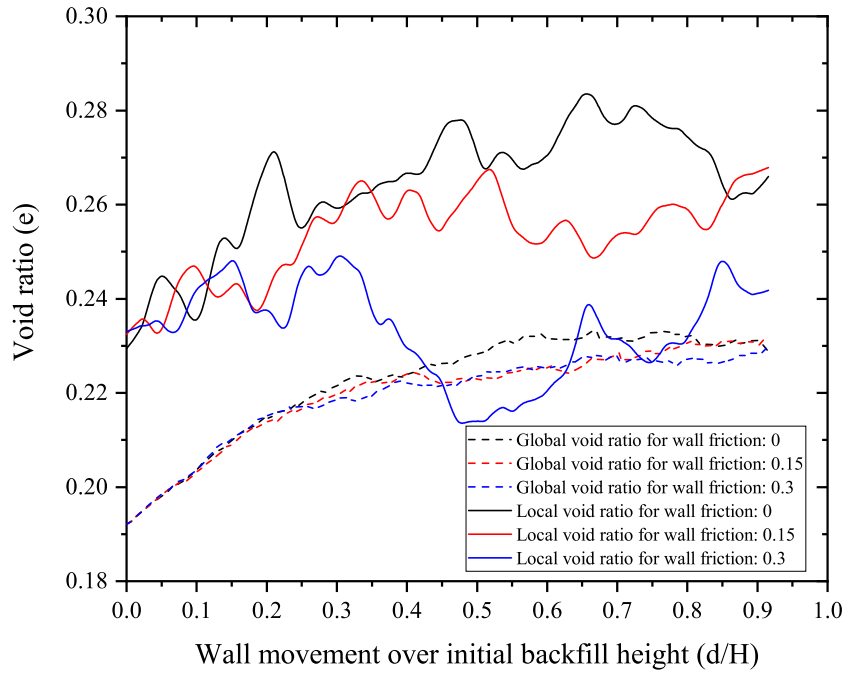
(a) Wall contacted with the bottom boundary.
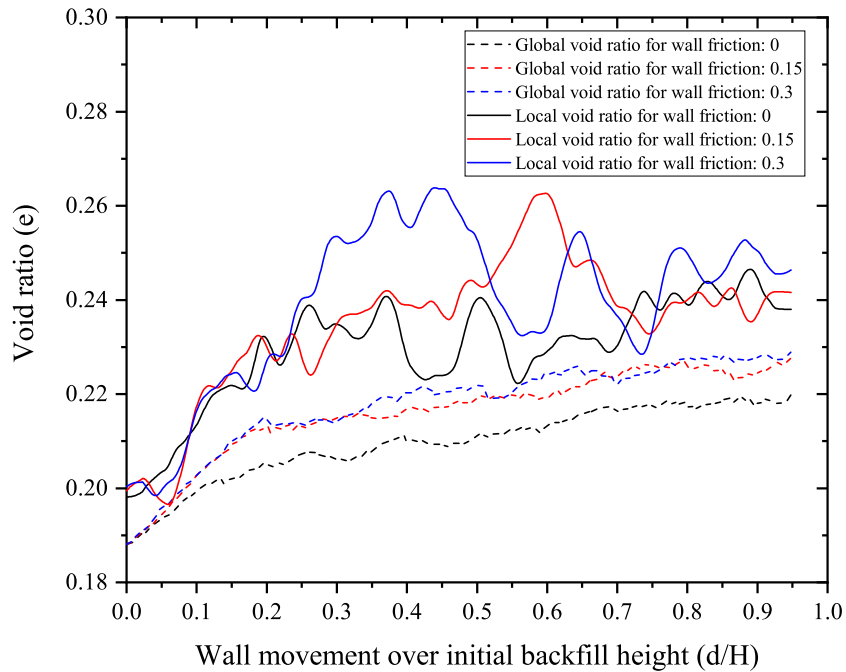
(b) Wall raised above a distance of 5-particle size.

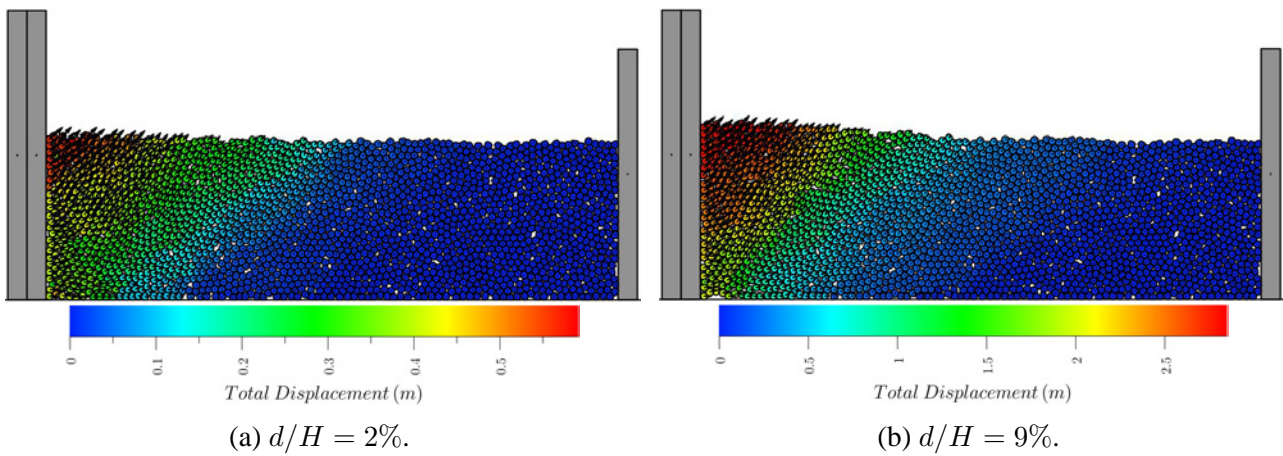Figure 7.7: Void ratio changes in front of the wall.

(a) $d/H = 2\%$.   (b) $d/H = 9\%$.

Figure 7.8: Particle total displacements for the case of smooth wall in condition A.

(a) $d/H = 2\%$.   (b) $d/H = 9\%$.
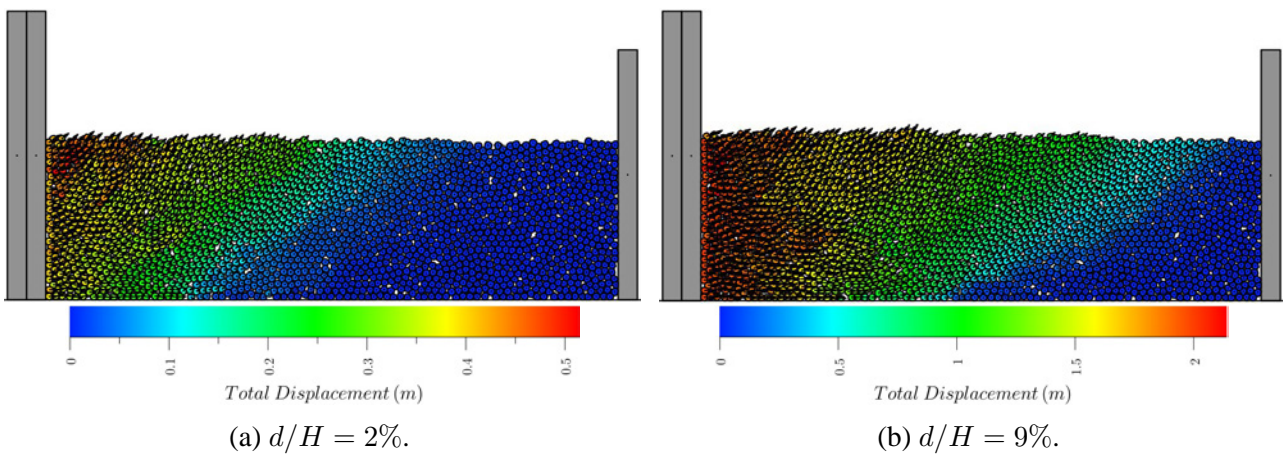
Figure 7.9: Particle total displacements for local wall friction coefficient to be 0.3 in condition A.

(a) $d/H = 2\%$.   (b) $d/H = 9\%$.
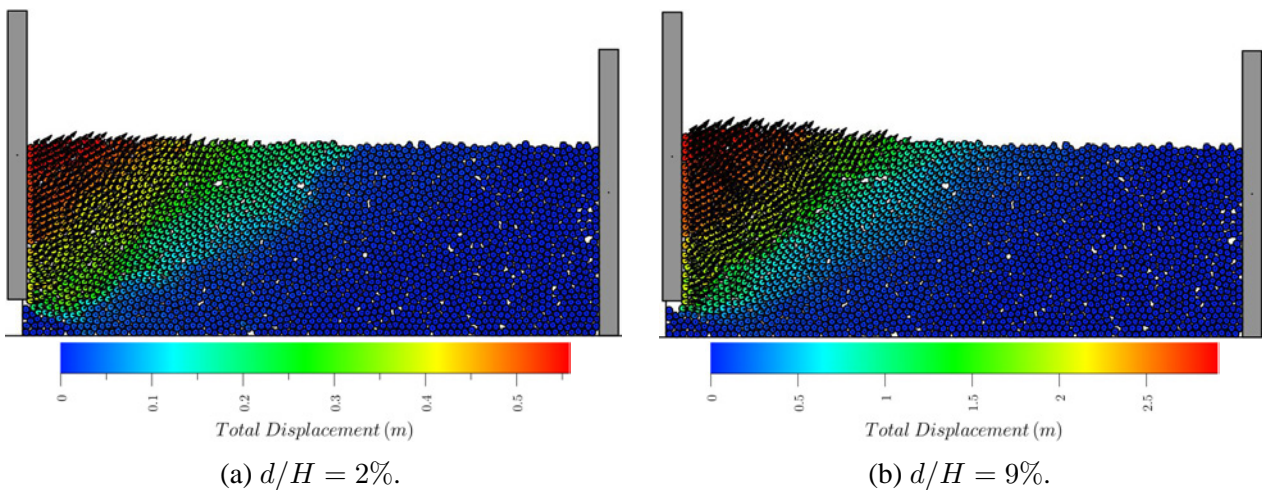
Figure 7.10: Particle total displacements for the case of smooth wall in condition B.

boundary. This parameter is primarily controlled by the backfill height next to the wall in relation
with the local void ratio.

(a) $d/H = 1.87\%$.

(b) $d/H = 9.37\%$.
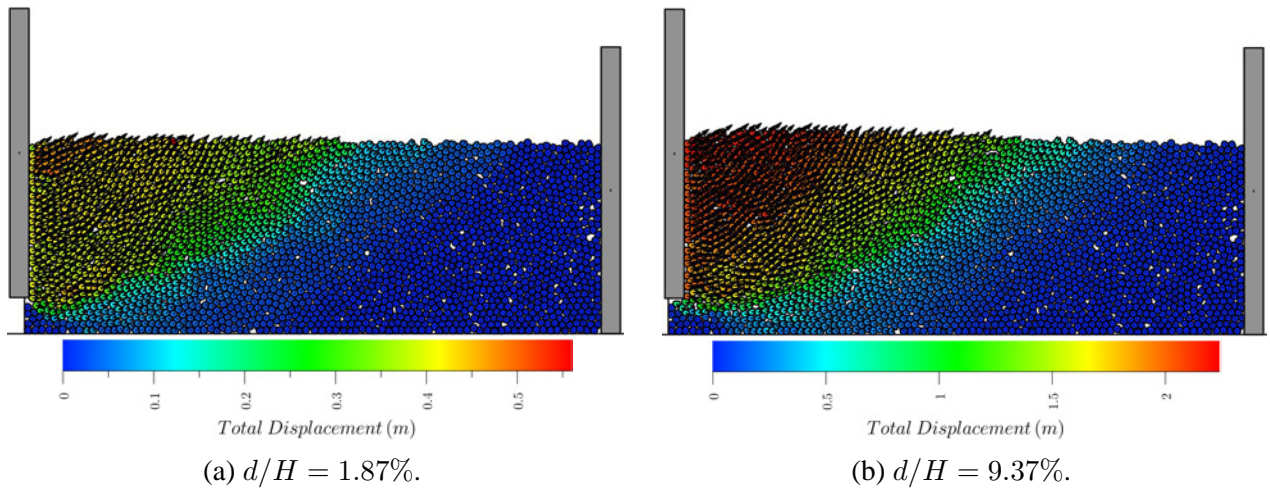
Figure 7.11: Particle total displacements for local wall friction coefficient to be 0.3 in condition B.

(a) Wall contacted with the bottom boundary.

(b) Wall raised above a distance of 5-particle size.
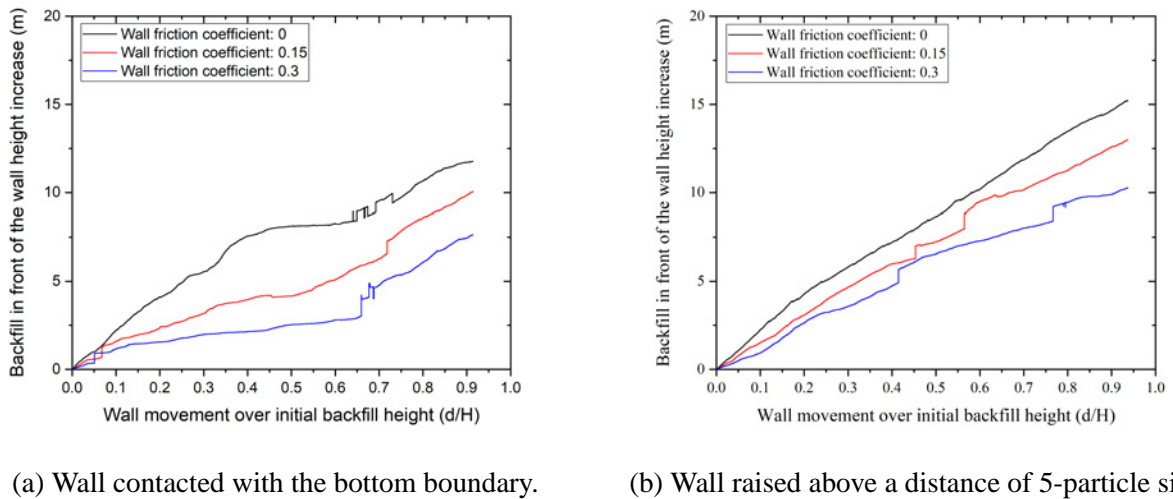
Figure 7.12: Backfills in front of the wall within the distance of 4-particle size.

7.3.3 Wall friction effects on K_p in the passive condition

Based on the results shown above, Figure 7.15 plots the mobilised lateral passive earth pressure coefficient K_p as the retaining wall moves toward the backfill. Although the initial density states are the same in each condition, K_p reaches higher peak values when the wall roughness is greater, and this is different from the observations in the triaxial tests where the peak strength is found to be influenced purely by the initial density state. The K_p values develop to reach peak and critical states roughly at d/H to be 10% and 70% in condition A, while at around 3% and 70% for condition B, respectively. Fang et al. (2002) observed that d/H required before K_p reaching the peak values are 1.5% and 3% for medium dense and dense sand backfills respectively, and 12% for both backfills to reach critical states. According to the data obtained by PFC2D published by Jiang et al. (2014), the peak and critical states occur at approximately 7% and 40% respectively. Two possible reasons for the difference for the d/H values reaching the peak and critical states are the particle shape and the
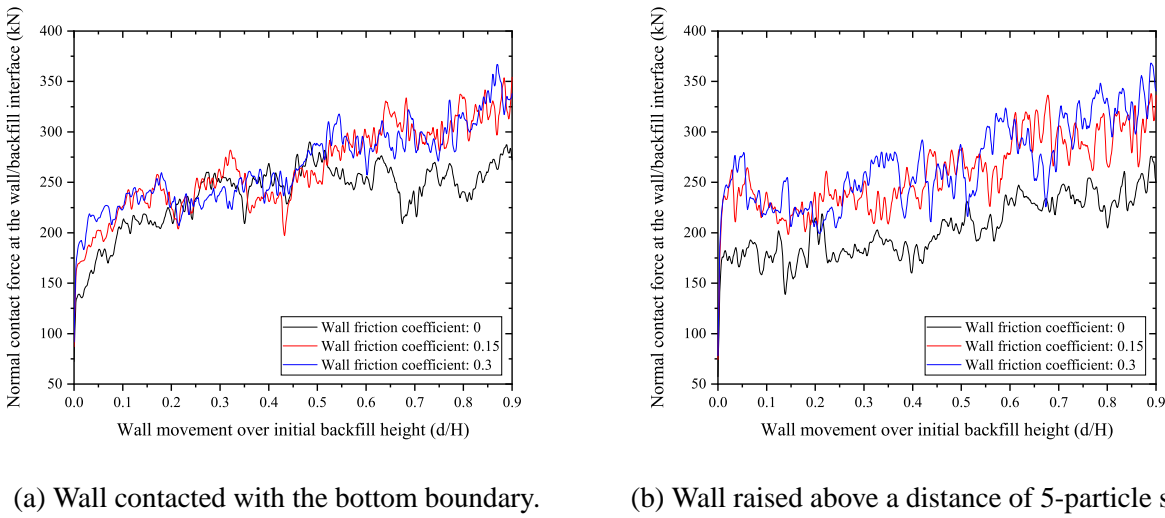
155

(a) Wall contacted with the bottom boundary.   (b) Wall raised above a distance of 5-particle size.

Figure 7.13: Lateral contact forces between wall and backfill.

(a) Wall contacted with the bottom boundary.   (b) Wall raised above a distance of 5-particle size.
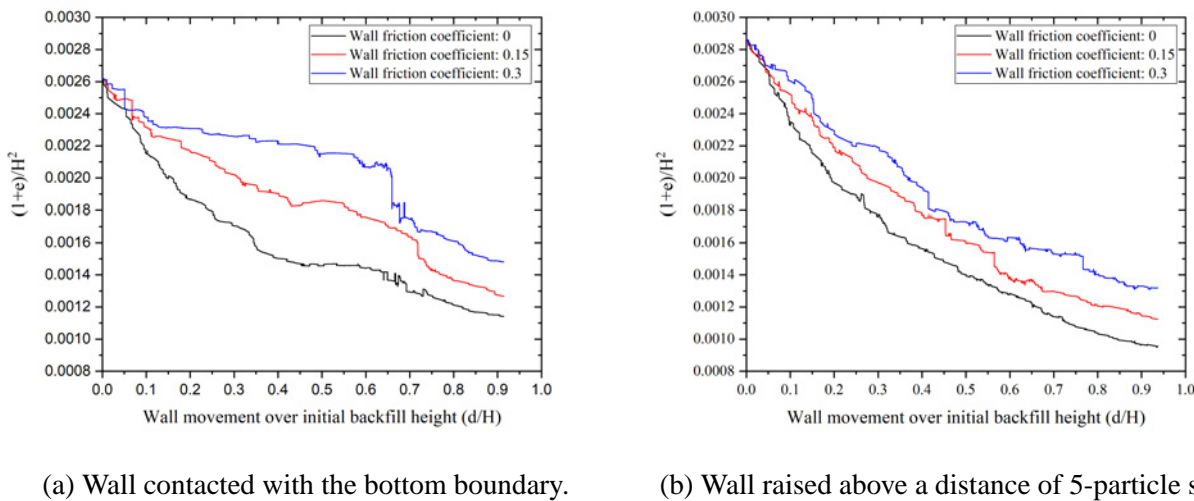
Figure 7.14: $(1 + e)/H^2$ for different wall friction conditions.

relative particle size in the backfill involved in the physical or numerical model. The numerical model
built by Jiang et al. (2014) involved around 100000 disc particles, while only 2500 polygonal particles
were simulated in this study limited by the computational power. Because of the bottom boundary
influences, K_p oscillates more significantly in condition A. The very initial K_p values and the initial
K_p values at d/H to be 0.5% (the retaining wall movement is normally designed to be restricted to
this small value of movement in engineering practice (e.g. Bolton and Powrie (1988))) for different
conditions are summarised in Table 7.3. At the start of wall movement, the K_p values are much lower
than their critical state values. At d/H to be 0.5%, the K_p values are slightly smaller than their critical
values in condition A, while evidently larger their critical values in condition B.

There is no absolute consensus in choosing ϕ_{crit} or ϕ_{peak} in retaining wall design when using the
failure criterion $(\tau/\sigma)_{max} = \tan\phi$. Although ϕ_{peak} is dependent on the backfill initial density states
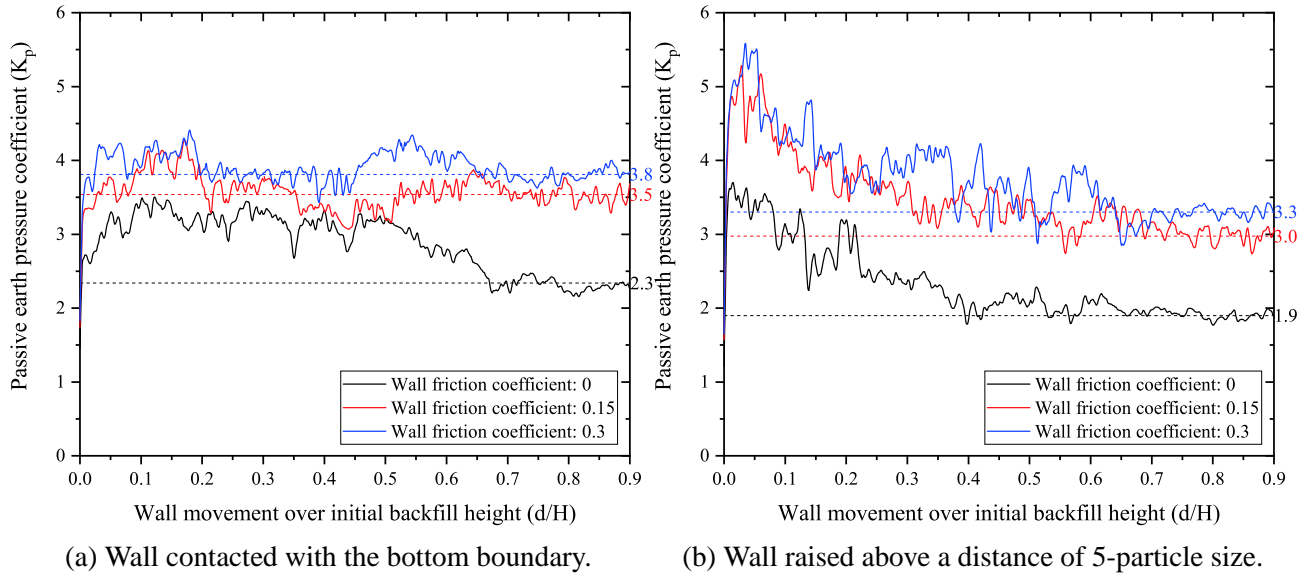and only applicable for relatively dense backfills which display dilatancy and strain softening, it is

156

(a) Wall contacted with the bottom boundary.

(b) Wall raised above a distance of 5-particle size.

Figure 7.15: K_p versus d/H calculated based on the local void ratio.

Table 7.3: Initial stage K_p values.

Local wall friction coefficient ($\tan \delta_w$)	Model set-up	K_p at the start	K_p at $d/H = 0.5\%$
0	condition A	1.18	2.7
	condition B	1.33	3.2
0.15	condition A	1.58	3.2
	condition B	1.39	4.0
0.3	condition A	1.57	3.4
	condition B	1.38	4.2

possible to indicate the low-strain stiffness of backfills of different densities. Besides, as the excessive displacement is often avoided in retaining wall design, the initial state before rupture occurring becomes important to analyse.

7.3.4 Relationship between local wall friction and wall/backfill interface friction

Figure 7.16 plots the wall/backfill interface friction angle (δ) evolution which is obtained by calculating the ratio of shear stress to normal stress at the contact interface. The interface friction angles in condition B are nearly constant during the whole process, while exhibit hardening and softening in condition A. In order to find the relationship between the local retaining wall surface friction angle (δ_w) and the mobilised wall/backfill interface friction angle (δ), 24 additional tests were conducted in which the local wall friction coefficients varied in the range from 0.05 to 0.8 in conditions A and B. The computed contact interface friction angles in critical states are compared with the values based on the Box2D contact model in dealing with two sliding rigid bodies as shown in Figure 7.17. When two rigid bodies are contacting and sliding in Box2D, the computed friction coefficient μ is equal to

(a) Wall contacted with the bottom boundary.　　　　(b) Wall raised above a distance of 5-particle size.
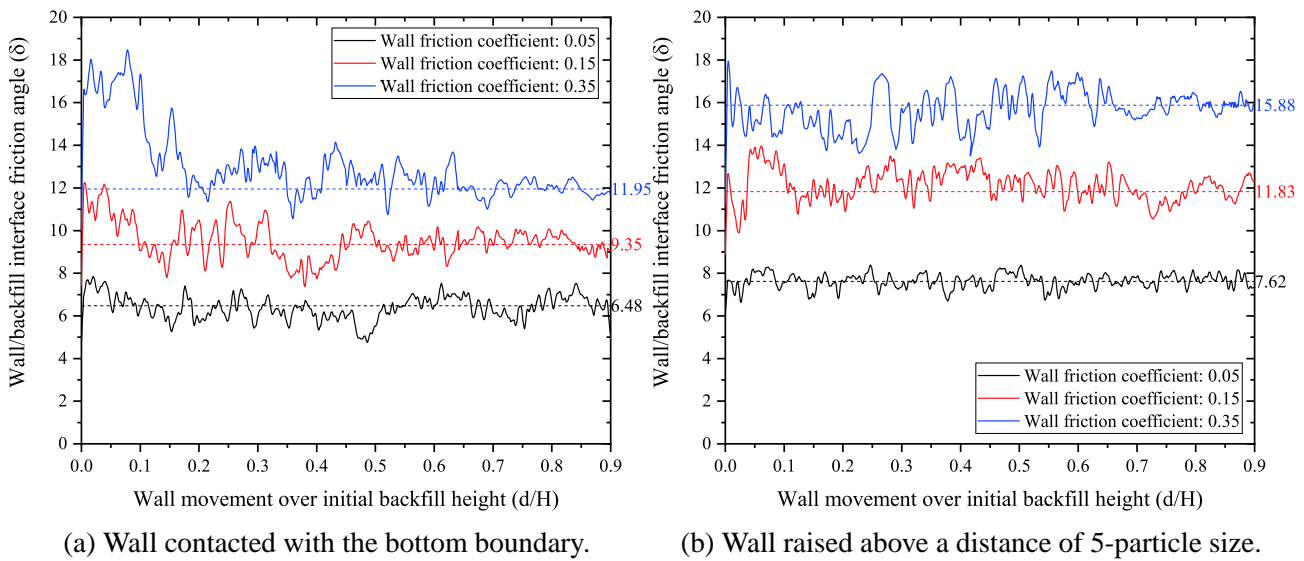
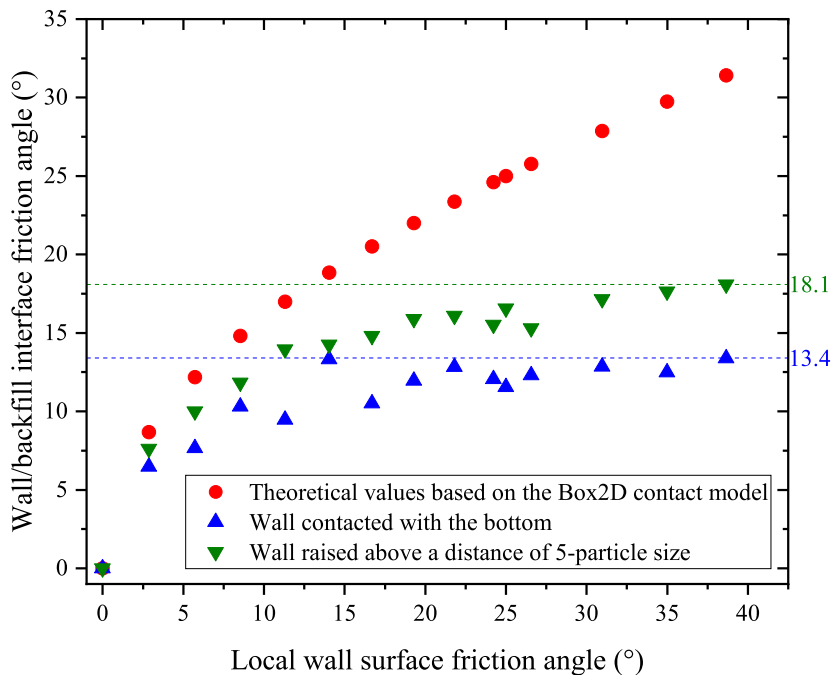Figure 7.16: Measured wall/backfill interface friction coefficients ($\tan \delta$).

Figure 7.17: Wall/backfill interface friction coefficients under different local wall frictions when the particle internal friction coefficient is constant at 0.4663.

the square root of the product of their individual friction coefficient $\sqrt{\mu_1 \mu_2}$, however, when the backfill granular particles are regarded as an integral continuum material, the developed interface friction coefficient is different and smaller than the friction coefficient between the wall and a single particle. It is found that the interface friction angles reach the maximum values roughly at 13.4 and 18.1 in condition A and B respectively after the local wall surface friction angle exceeds the inter-particle friction angle (ϕ). This is because the contacting particles are easier to shear along the flat wall sur-

face and as a result the interface friction cannot reach as high as the particle internal friction. The contact interface friction angles in condition B are found to be consistently slightly larger than those measured in condition A. When the local retaining wall friction angle is larger than the inter-particle friction coefficient, δ is nearly constant at around $0.65\phi_{crit} - 0.88\phi_{crit}$. This is slightly higher than the data reported by Terzaghi (1954) in studying loose to dense clean sand that δ is equal to around $2/3\phi_{crit}$ in front of the wall.

The lateral passive earth pressure coefficients (K_p) are compared with the theoretical values obtained by equation (7.2) and also with the values computed by limit analysis software LimitState:GEO in Figure 7.18. The backfill internal friction angle (ϕ) was set to be $20.6°$ and the bottom boundary/backfill interface friction angle was set to be ϕ and $2/3\phi$ respectively in LimitState:GEO for conditions A and B in order to investigate the bottom/backfill interface friction effects on K_p. The lateral earth pressure coefficients in condition A are evidently higher than the values in condition B at the same wall/backfill interface friction angles, proving that the bottom boundary has a distinct influence on the lateral passive earth pressure coefficient. However, K_p values are nearly equal when the bottom/wall interface friction angle is equal to ϕ for conditions A and B in limit analysis, implying the bottom boundary/particle interaction effects do not influence greatly at the very initial stage of wall movement. In condition A, K_p will decrease as the bottom/backfill interface reduces as shown in Figure 7.18, while keep constant in condition B because of existence of the backfill below the wall base. The bottom differences between limit analysis and equation (7.2) start to become increasingly more significant after the wall/backfill friction coefficient exceeds 0.1. The upper-bound limit analysis results are higher than the theoretical lower-bound solution given by Powrie (2018). Compared with condition A, K_p values in condition B are closer to the theoretical values. One of the possible reasons is that the heave in front of the wall is inhibited in condition A compared with condition B as shown in Figure 7.12, indicating the greater resistance to the wall when being pushed. The results highlight the existing variation in calculating the lateral earth pressure coefficients between Box2D and the continuum methods in which the backfill deformation (i.e. heave in front of the wall) is ignored as the soil is being displaced by the wall. In addition, the key difference between the continuum theories and the discrete approaches is likely to be the presence of soil arching affected by particle size distribution and particle shape that inherently occurs in discrete approaches. The soil arching effects also cause the non-linear distribution of the lateral contact force at the wall/backfill interface. Studies on soil arching effects can be found in Khosravi et al. (2013, 2017) and Li et al. (2017), etc.

For the purpose of making up the modelled particle amount inadequacy due to the computational power, three more simulations of different initial random generators were conducted in the smooth wall condition. Their average values are set out in Figure 7.19. The critical state K_p is 2.09, very close to the theoretical value 2.086. This indicates that the deviation between the DEM and the theoretical results can be reduced by increasing the particles in modelling.
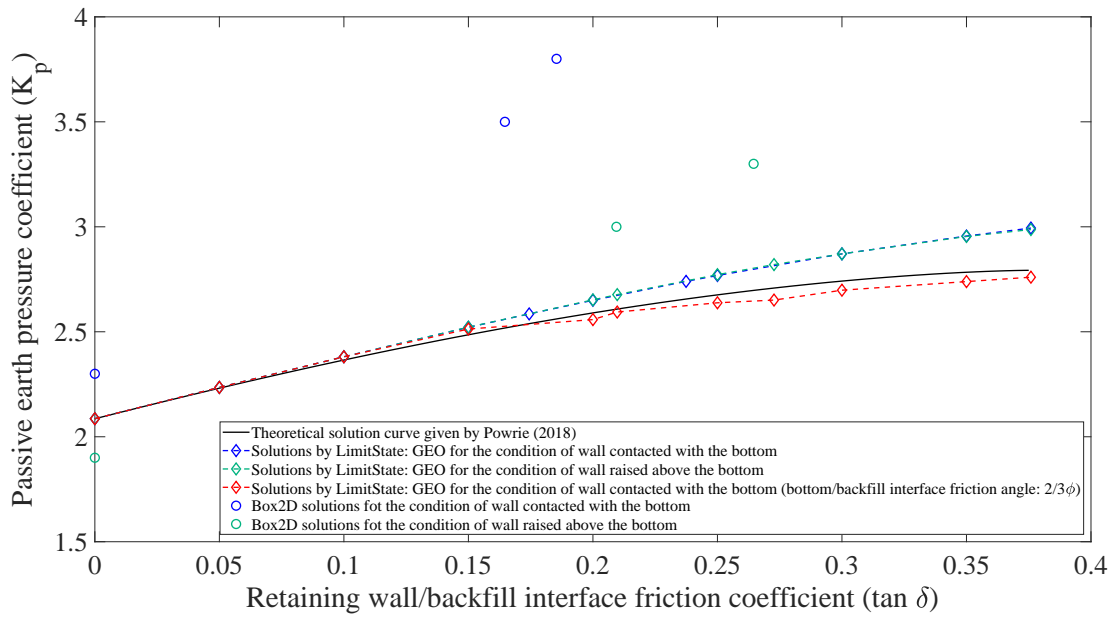
Figure 7.18: Comparison of the simulated critical K_p values for dodecagonal backfills with the theoretical solutions.
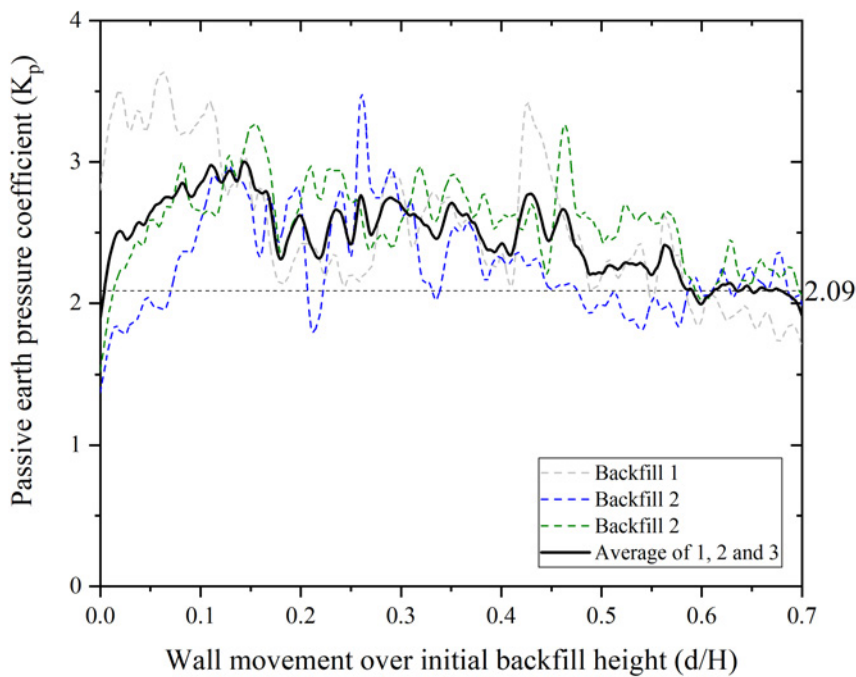

Figure 7.19: Results averaged by three tests on smooth walls.

7.3.5 Graphical interpretations in the passive condition

Figure 7.20 to Figure 7.23 plot the particle total rotations at different stages comparing the different failure mechanisms in the passive condition for smooth and frictional wall/backfill interfaces respectively in conditions A and B. When the wall back is smooth, a nearly plane rupture surface extends from the retaining wall base into the backfill surface intersected with the horizontal direction at around $48°$ in condition A, larger than the theoretical value $34.7°$, while there is a spiral sliding surface developed at the wall base corner followed by a plane sliding surface extended to the backfill surface at $44°$ in condition B. When the wall surface is rough, the ideal Rankine zone as shown in Figure 7.2 is heaved more than the particles adjacent to the wall and this is different with the case of smooth wall in which the local backfill next to the wall heaves higher than other places. The failure mechanism is the same as that shown in Figure 7.2 and the rupture surface intersected with the backfill surface at $38°$ and $35°$ in condition A and B respectively.

(a) $d/H = 2\%$.

(b) $d/H = 9\%$.

(c) $d/H = 46\%$.

(d) $d/H = 91\%$.
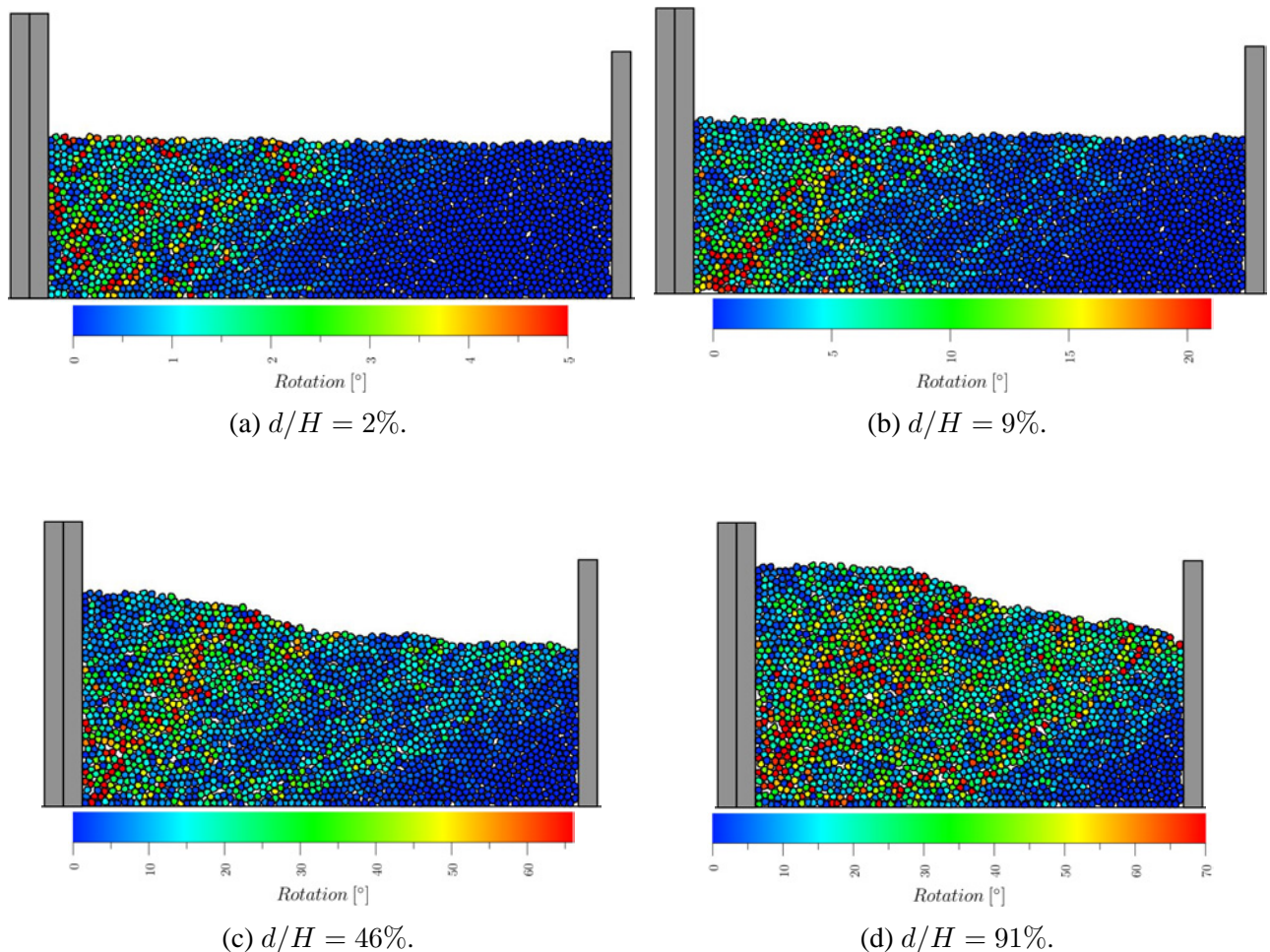
Figure 7.20: Particle total rotations at different stages for the case of smooth wall in condition A.

(a) $d/H = 2\%$.

(b) $d/H = 9\%$.

(c) $d/H = 47\%$.

(d) $d/H = 93\%$.
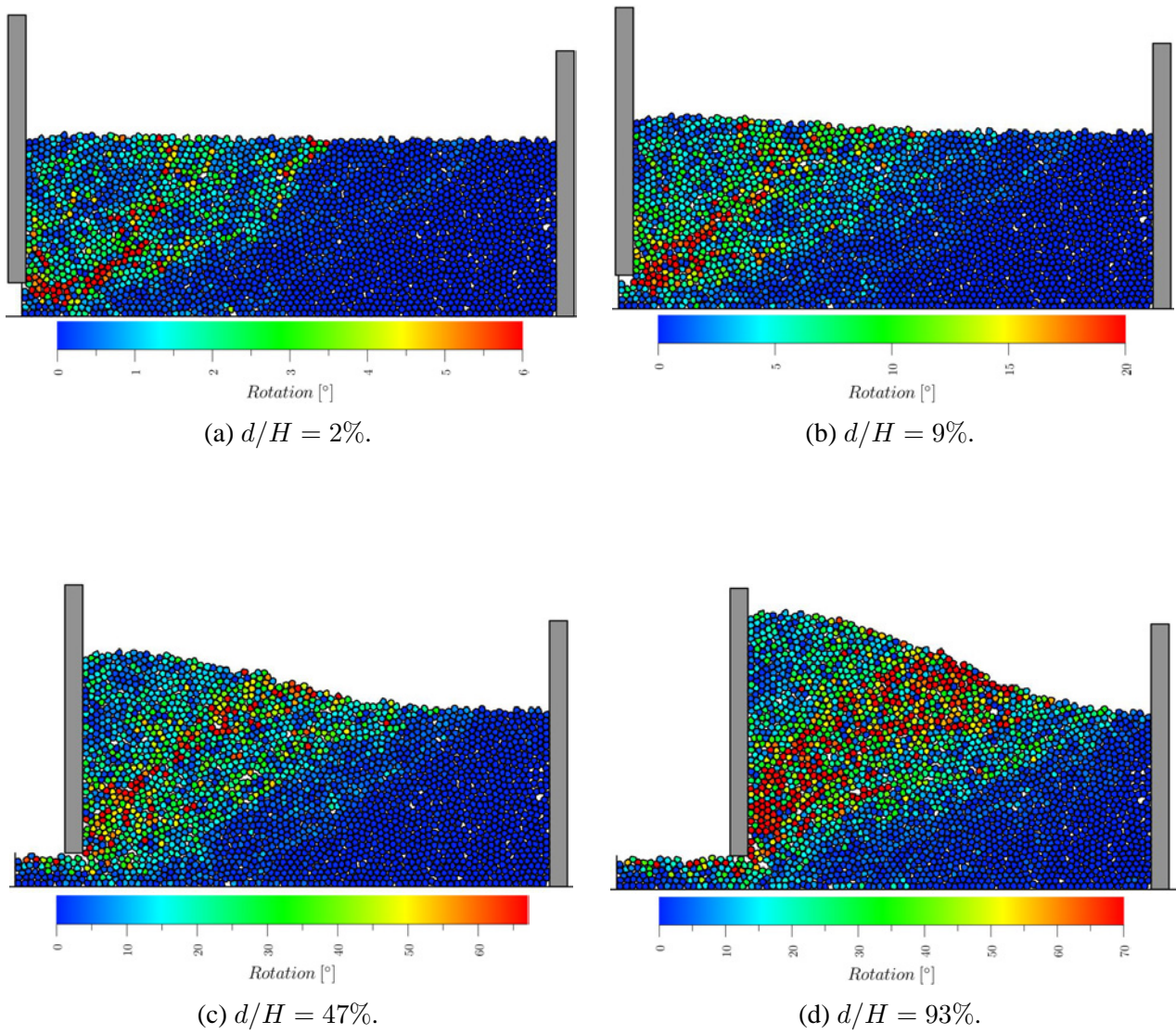
Figure 7.21: Particle total rotations at different stages for the case of smooth wall in condition B.
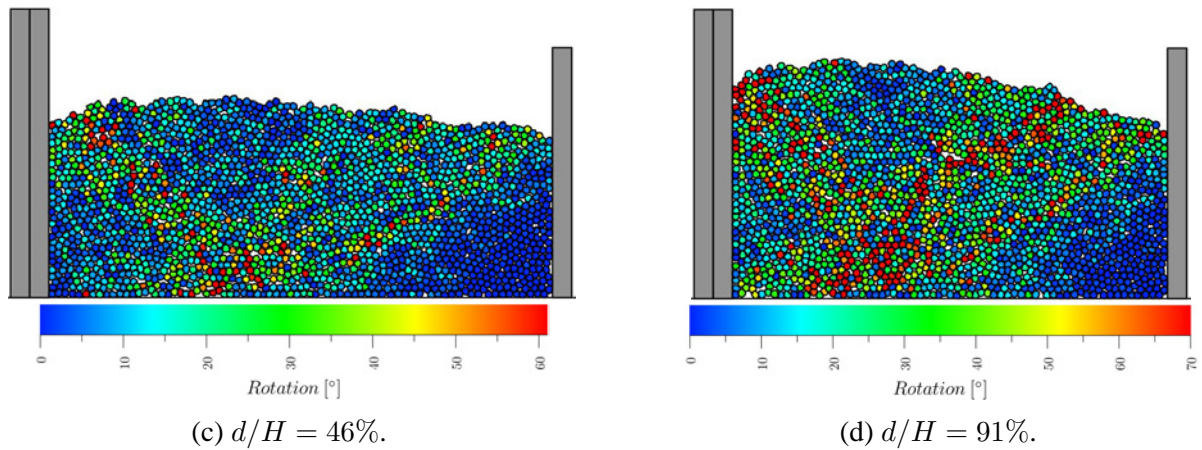

(a) $d/H = 2\%$.

(b) $d/H = 9\%$.

(c) $d/H = 46\%$.

(d) $d/H = 91\%$.
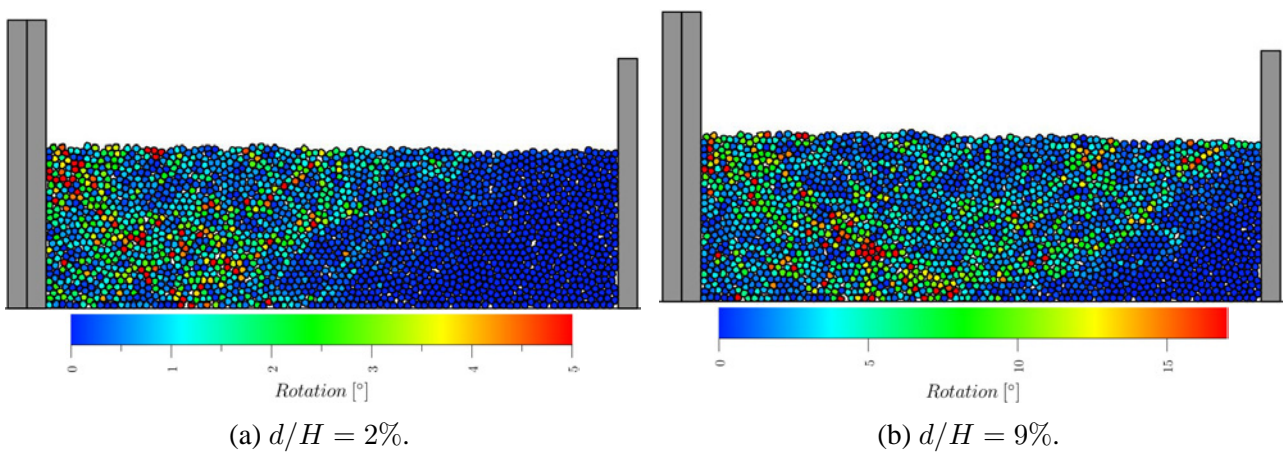
Figure 7.22: Particle total rotations at different stages for local wall friction coefficient to be 0.3 in condition A.
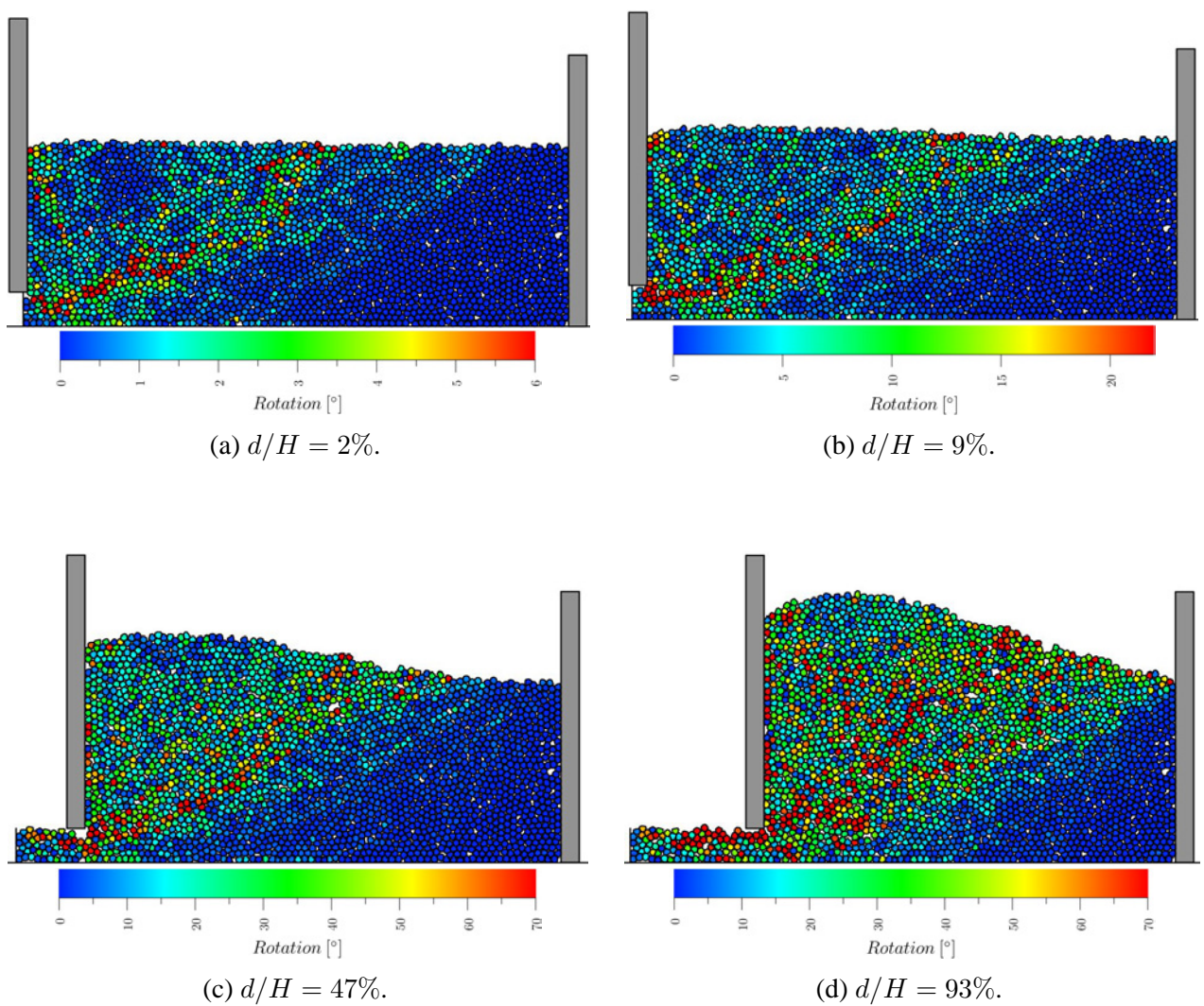

(a) $d/H = 2\%$.

(b) $d/H = 9\%$.

(c) $d/H = 47\%$.

(d) $d/H = 93\%$.

Figure 7.23: Particle total rotations at different stages for local wall friction coefficient to be 0.3 condition B.

Figure 7.24 to 7.27 plot the inter-particle contact normal force chains at peak and critical states for different local wall friction conditions in conditions A and B. The greatest normal force chains are generated at the bottom of the wall and developed into backfills nearly horizontally in condition A and slanted downward in condition B under the combined effects of gravity and lateral thrust.

(a) $d/H = 5\%$.

(b) $d/H = 91\%$.
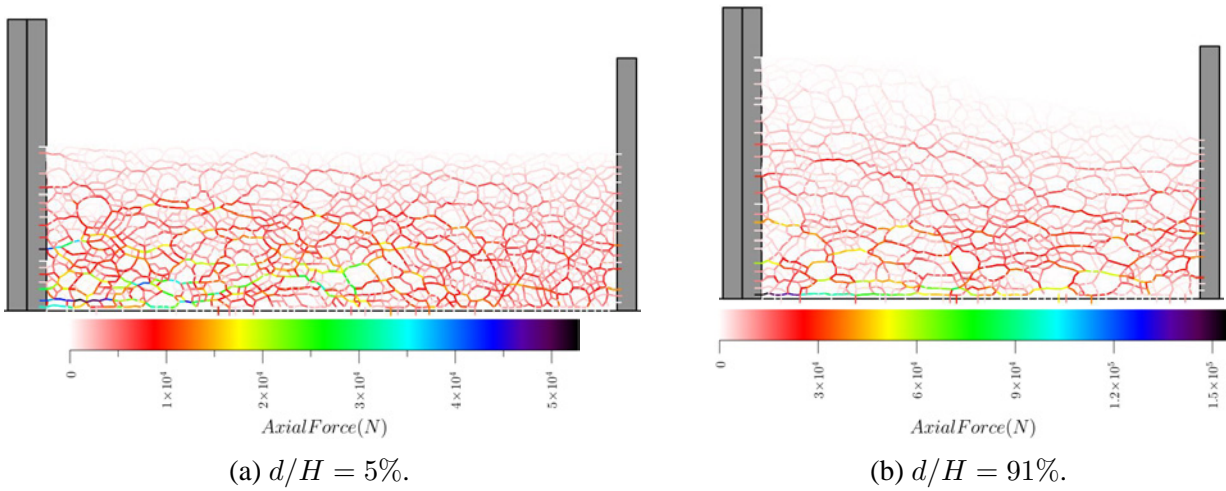
Figure 7.24: Contact normal force chains for the case of smooth wall in condition A.

(a) $d/H = 5\%$.

(b) $d/H = 91\%$.
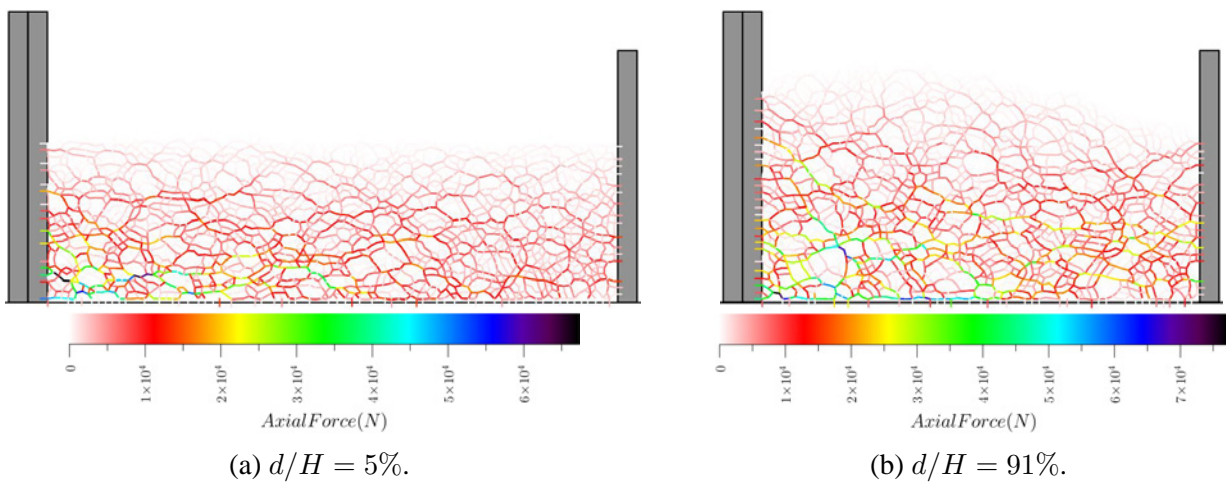
Figure 7.25: Contact normal force chains for local wall friction coefficient to be 0.3 in condition A.

(a) $d/H = 8\%$.

(b) $d/H = 93\%$.
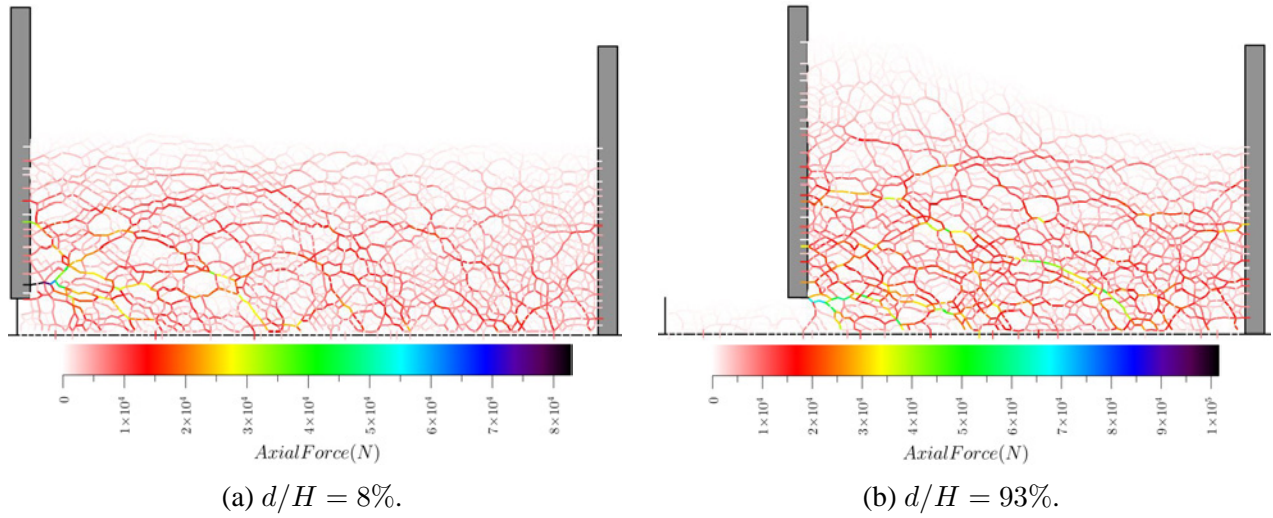
Figure 7.26: Contact normal force chains for the case of smooth wall in condition B.

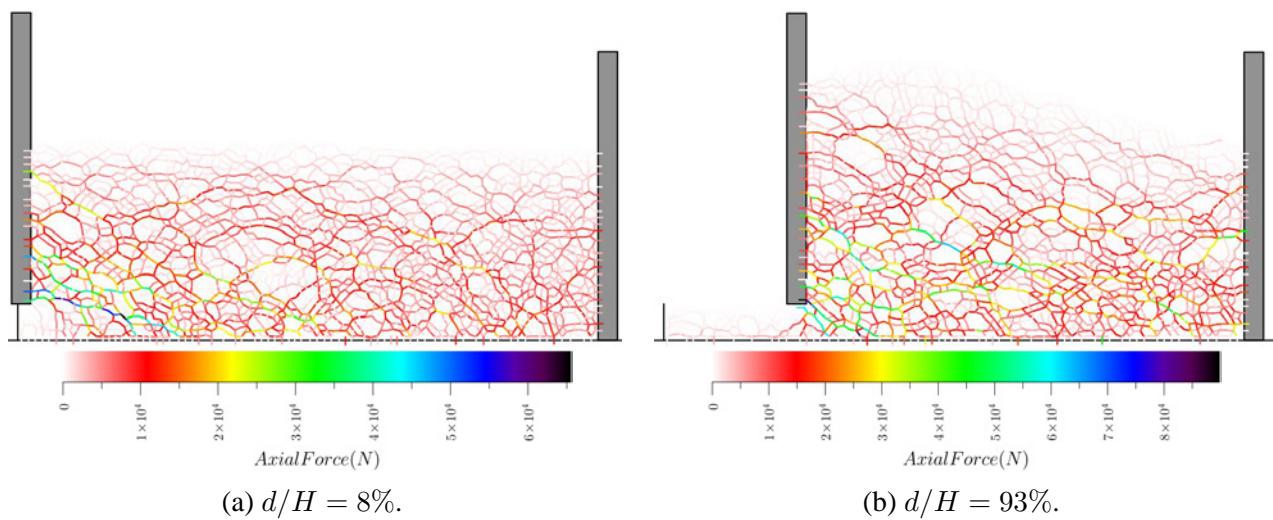(a) $d/H = 8\%$.

(b) $d/H = 93\%$.

Figure 7.27: Contact normal force chains for local wall friction coefficient to be 0.3 in condition B.

7.3.6 Density effects on K_p for in the passive condition

To see the backfill initial density influence on the passive earth pressure coefficient K_p, three additional backfills in condition B were created by setting their initial particle friction coefficient to be 1.0 during the deposition stage and the results are compared with those of initially denser backfills in Figure 7.28. These backfills do not perform strain hardening behaviours in K_p while approach the same critical values as those developed in the initially denser backfills. This proves that the initial backfill density state does not influence the critical passive earth pressure coefficient. By investigating the particle total rotation graphs for the case of smooth wall in Figure 7.29, no distinctive rupture surface is developed in the early stages, therefore the backfills cannot reach the peak strengths as the backfills of initially denser states.
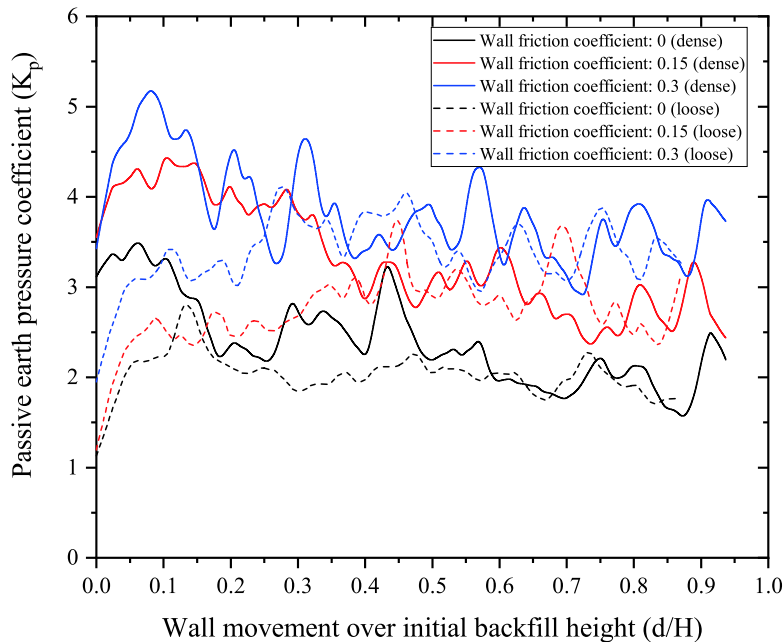

Figure 7.28: Backfills of initial loose densities in the passive condition.
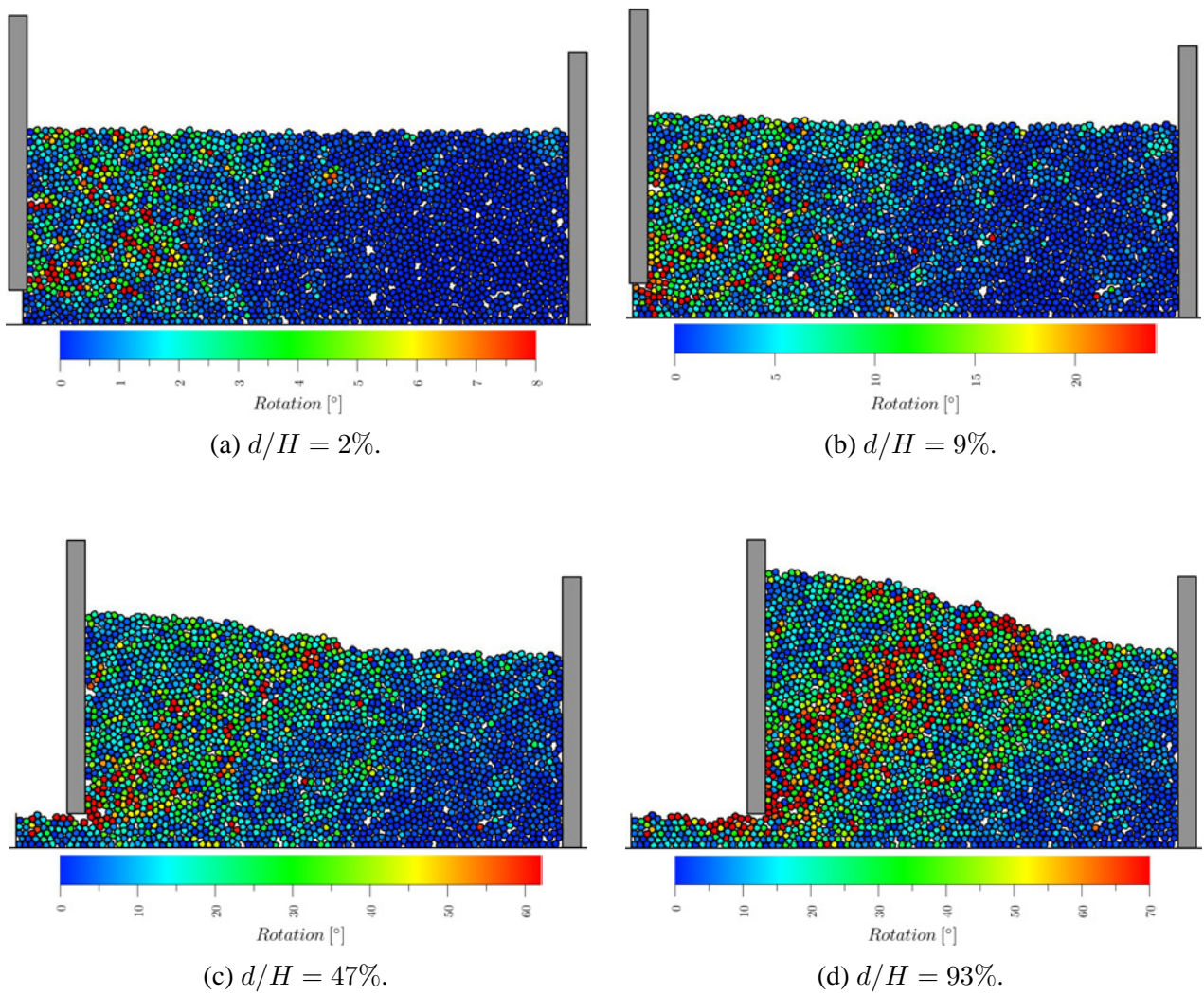
(a) $d/H = 2\%$.

(b) $d/H = 9\%$.

(c) $d/H = 47\%$.

(d) $d/H = 93\%$.

Figure 7.29: Particle total rotations at different stages for the case of smooth wall in condition B.
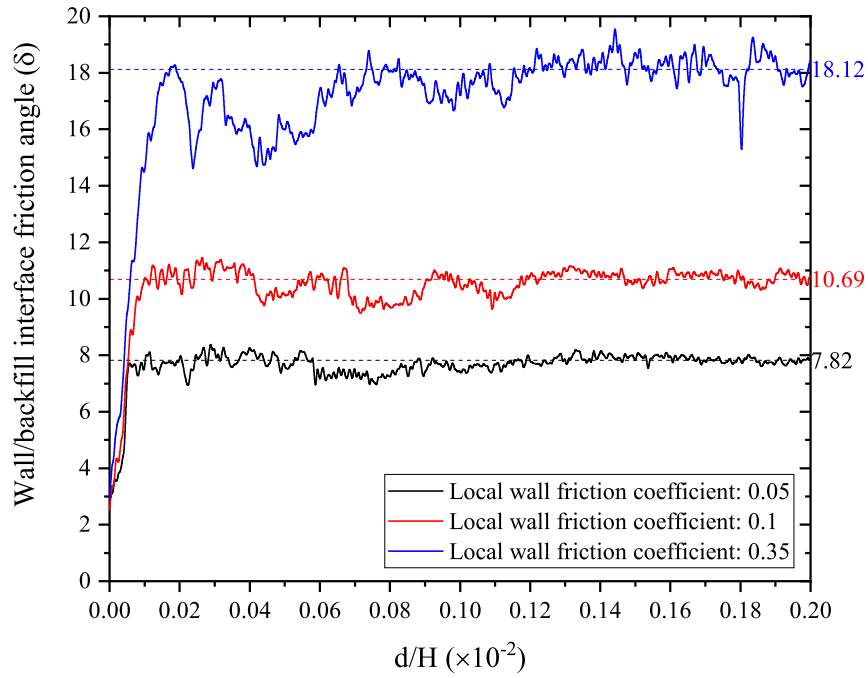
7.3.7   Active condition

The wall surface friction effects on the lateral active earth pressure coefficient K_a will be analysed in this part. The normal contact forces at the wall/backfill interface reduce from high values at the very beginning and then gradually stabilise after d/H reaches around 0.02% as shown in Figure 7.30a. The mobilised wall/backfill interface friction angles δ keep climbing also until d/H to be roughly 0.02% and then gradually keep nearly constant. Figure 7.31 shows the relationship between the wall/backfill interface friction angle and the local wall friction coefficient $\tan\delta_w$ ranging from 0.05 to 0.8. The wall/backfill interface friction angle δ can develop to be equal to ϕ_{crit}, which is double as $0.5\phi_{crit}$ reported by Terzaghi (1954) behind the wall. The critical state active earth pressure coefficients are shown in Figure 7.30c and these values are compared with the theoretical solutions calculated by equation (7.5) and Sokolovskii's solution (Sokolovskii, 1960) in Figure 7.32. The backfills reach critical states when d/H develops to 0.2%, coincident with the observations made by Li et al. (2017) that the required d/H to reach the critical state is dependent on the ratio of the backfill width to its initial height (B/H), and much earlier than that in the passive condition. No strain softening behaviour is observed in the active condition. The K_a values obtained by Box2D are roughly 28.6% lower than the Powrie's solution, and the discrepancies are even over the whole range. The data imply that the theoretical solutions are on the danger side compared with the Box2D results for the active condition and possibly underestimate the retaining wall bearing capacity.
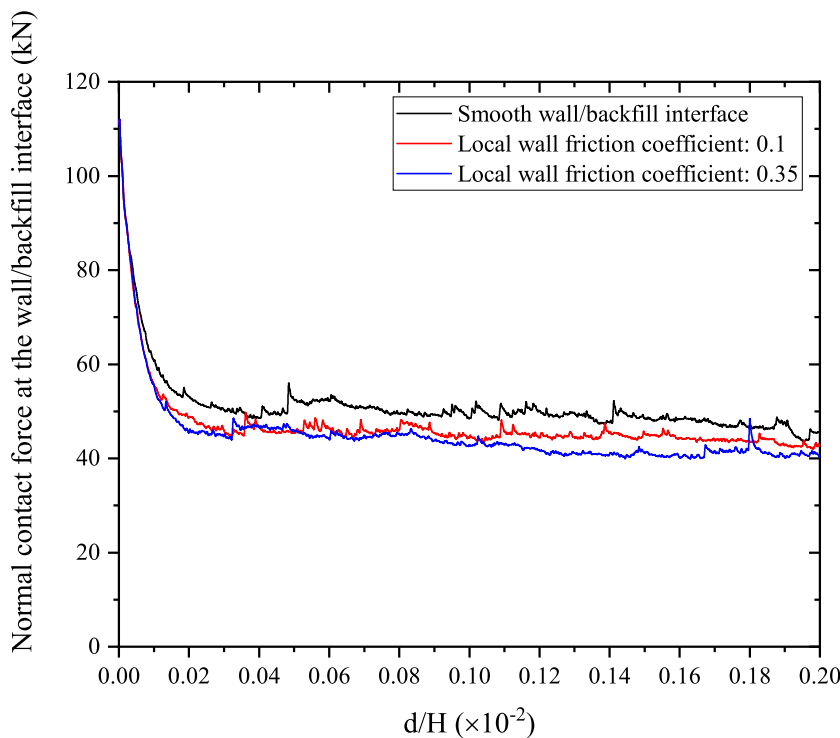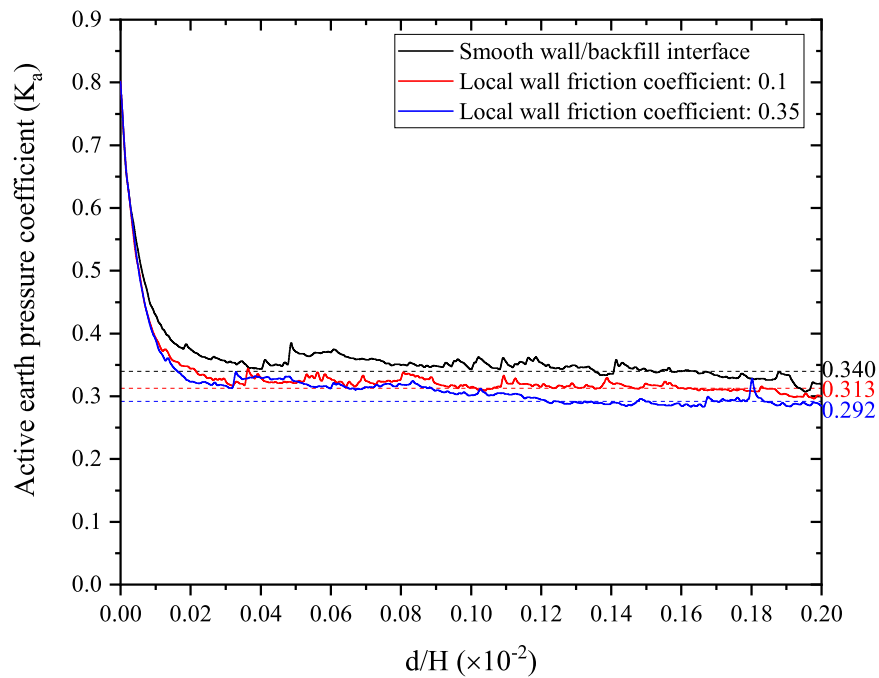

(a) Lateral contact forces between wall and backfill.

Figure 7.33 and 7.34 illustrate the particle total rotations and displacements in the active condition for smooth and frictional walls. The rupture surfaces are found to be intersected with the backfill

(b) Wall/backfill interface friction coefficients ($\tan \delta$).

(c) Active earth pressure coefficient (K_a).

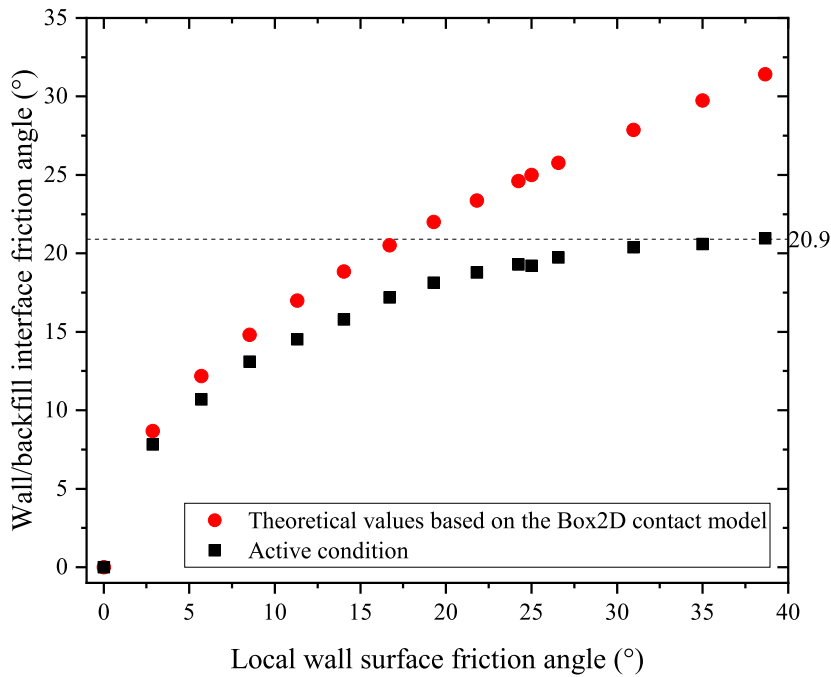Figure 7.30: Backfill behaviours in the active condition.

Figure 7.31: Wall/backfill interface friction coefficients under different local wall frictions when the particle internal friction coefficient is constant at 0.4663
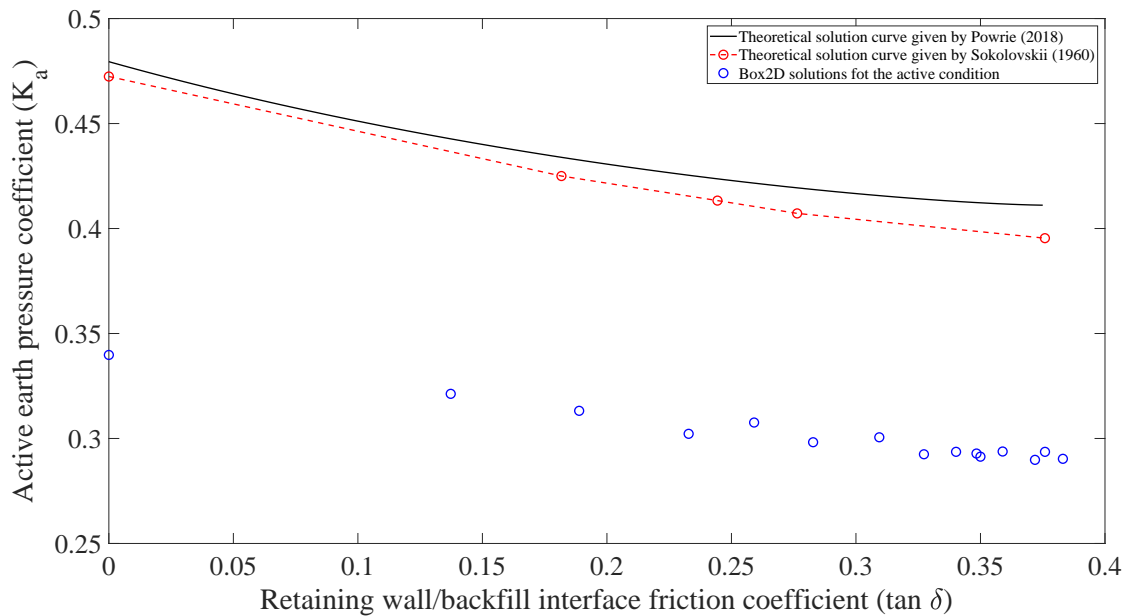

Figure 7.32: Comparison of the simulated K_a values for dodecagonal backfills with the theoretical solutions.

surfaces at an angle of $60°$ in both conditions, which is slightly larger than the theoretical $55.3°$ shown in Figure 7.3. A clear wedge-shaped zone can be observed in the total displacement diagram and the displacements of the particles adjacent to the frictional wall can be found to be significantly

inhibited in Figure 7.34b while replaced by more rotations as shown in Figure 7.33b.
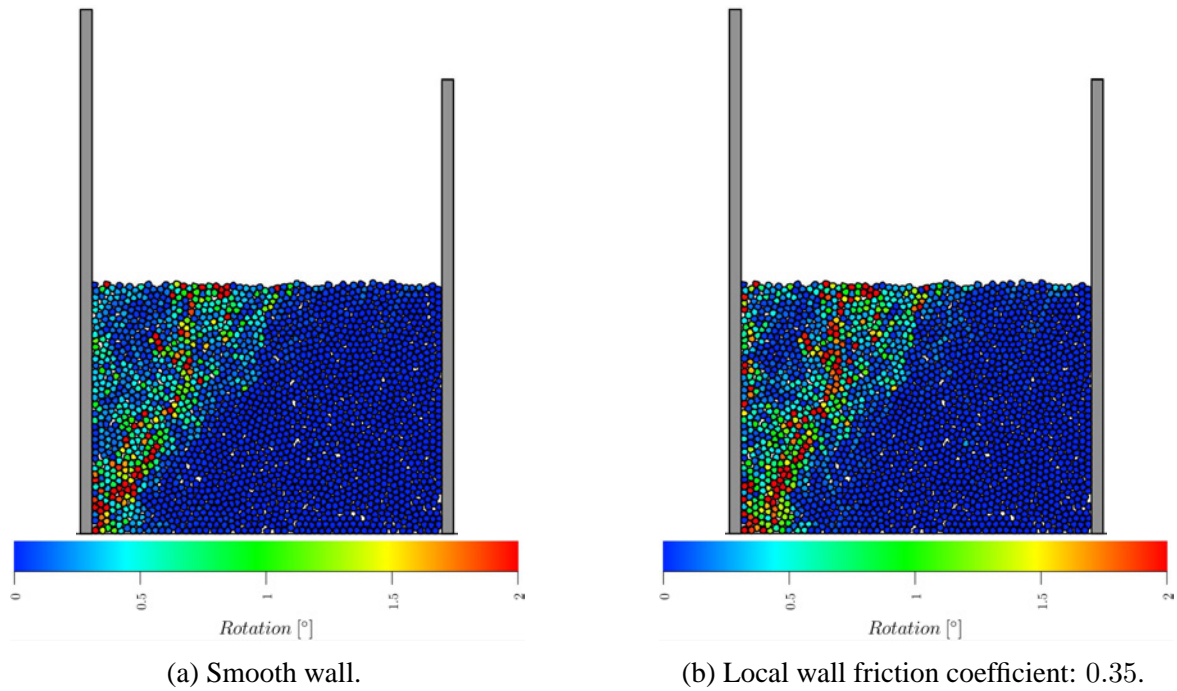

(a) Smooth wall.　　　　　　　　(b) Local wall friction coefficient: 0.35.

Figure 7.33: Particle total rotations for the active condition at d/H to be 0.2%.

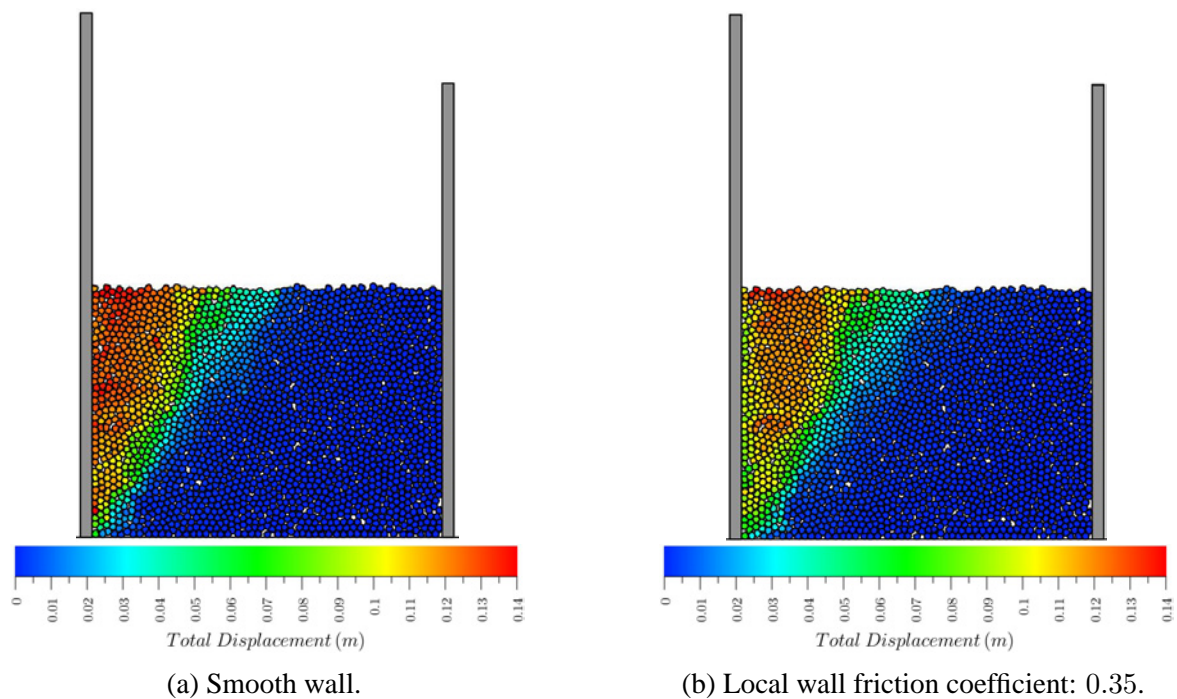(a) Smooth wall.　　　　　　　　(b) Local wall friction coefficient: 0.35.

Figure 7.34: Particle total rotations for the active condition at d/H to be 0.2%.

7.4 Particle size and shape effects on the passive earth pressure coefficient

In this section, particle size and shape effects on the passive earth pressure coefficient will be studied and the backfill packing effects will be also taken into account and compared with the limit analysis solutions using software LimitState:GEO.

7.4.1 Particle size effects

In order to analyse the particle size effects, the initial backfill width is kept constant at $80\,\mathrm{m}$ and the particle size is changed to $2\,\mathrm{m}$ and $0.5\,\mathrm{m}$ in diameter to compare with the case of $1\,\mathrm{m}$, resulting the model scaling ratios along the vertical retaining wall surface to be 10, 20 and 40. The total particle numbers for these two new models are over 620 and 7300 respectively. For the cases of scaling ratios to be 10 and 20, there were three models for each condition built, and the results are based on their averages.

Figure 7.35 shows the particle size effects on the passive earth pressure coefficient for smooth and rough walls (local wall surface friction coefficient to be 0.3). As the particle size decreases, the backfill possesses higher peak K_p and also higher critical state K_p in both conditions. This is consistent with the findings given by Koerner (1970), however contrary to the observations reported by Jiang et al. (2014).
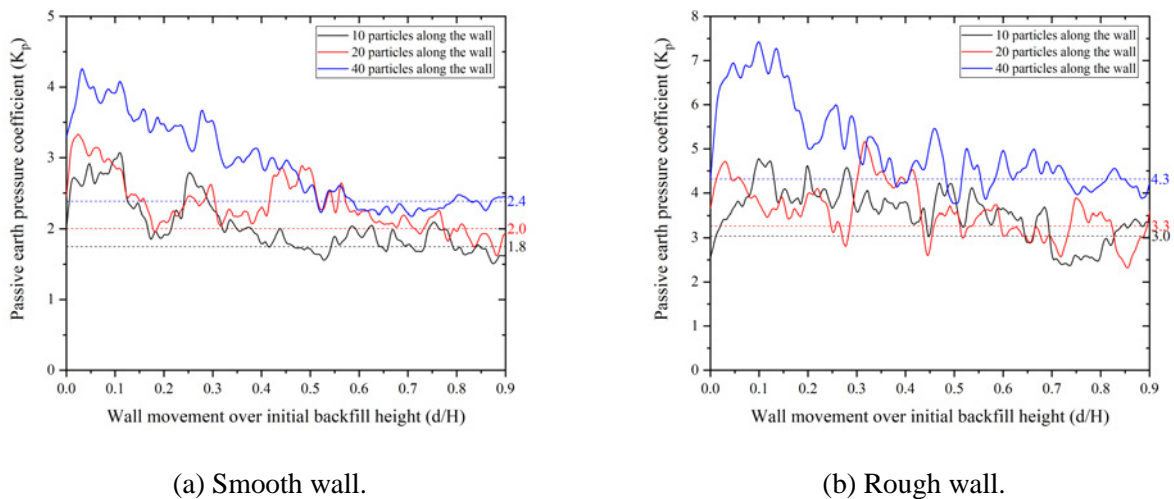

(a) Smooth wall.   (b) Rough wall.

Figure 7.35: Particle size effects on K_p.

Figure 7.36 to 7.39 illustrate the particle accumulative rotations for the backfills made of the biggest and the smallest particles in the cases of smooth and frictional wall surfaces. For the case of particle number along the wall surface to be 40, a single rupture surface is developed from the start and there are more integral rupture surfaces developed as the wall continued displacing the backfill as can be observed in Figure 7.37 and 7.39. However, there is no distinct or integral rupture surfaces

developed in the backfills made of the biggest particles because of the particle number limitation, therefore, the backfills could fail along any chain formed by a number of particles, and the whole local zone near the wall develops to fail as shown in Figure 7.36 and 7.38.
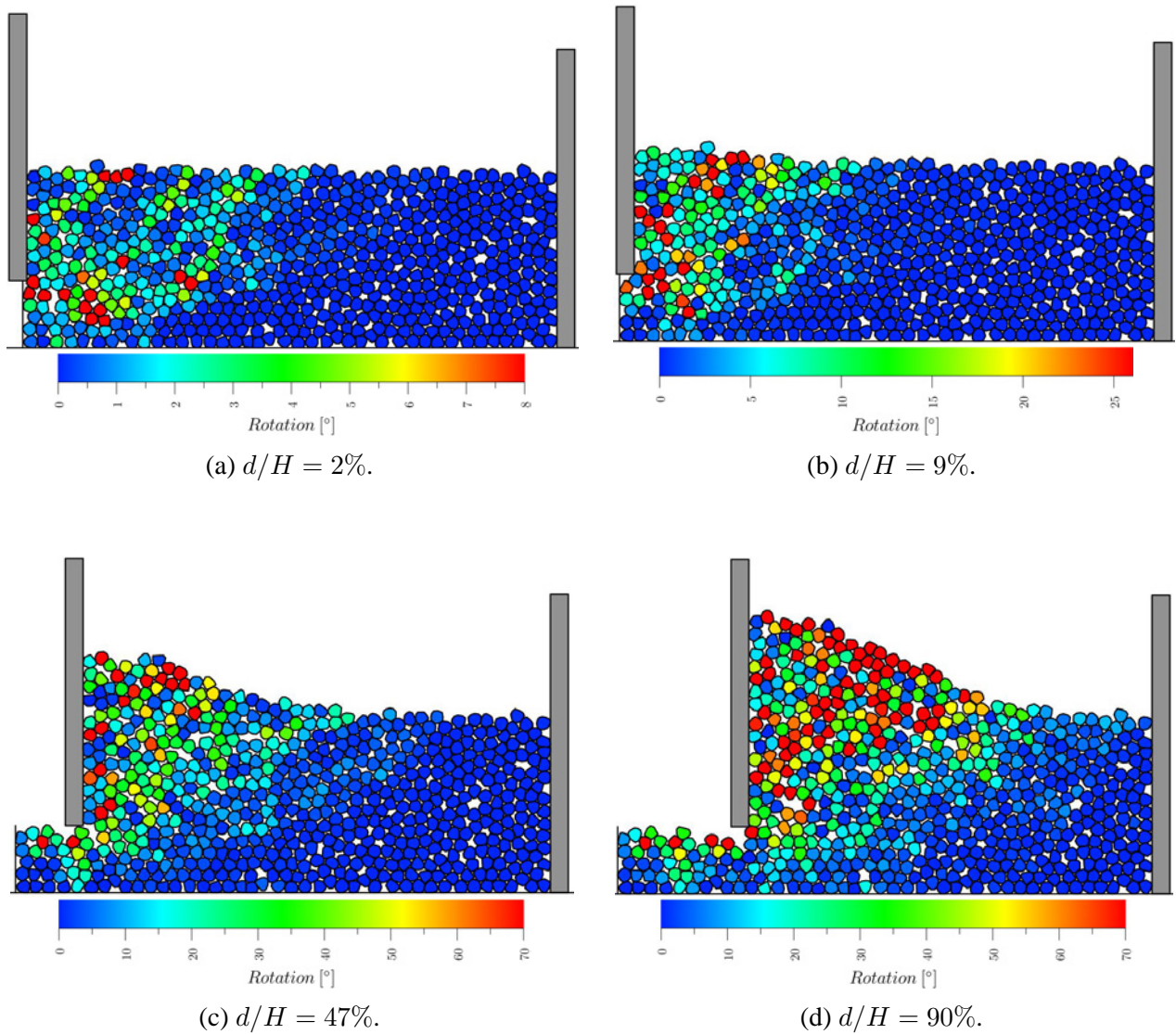

(a) $d/H = 2\%$.

(b) $d/H = 9\%$.

(c) $d/H = 47\%$.

(d) $d/H = 90\%$.

Figure 7.36: Particle total rotations in the case of 10 particles along the smooth wall.

(a) $d/H = 3\%$.

(b) $d/H = 14\%$.

(c) $d/H = 70\%$.

(d) $d/H = 90\%$.
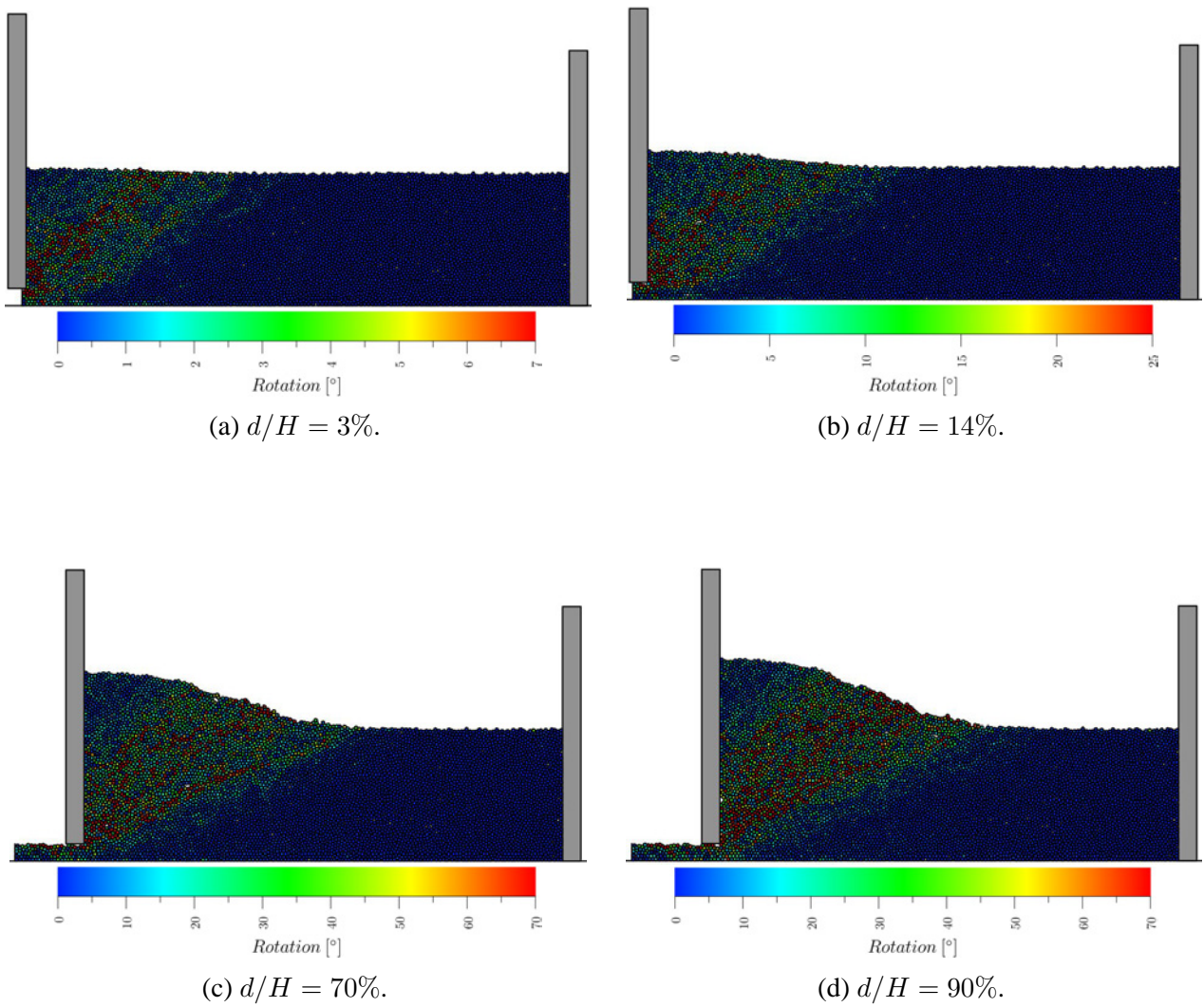
Figure 7.37: Particle total rotations in the case of 40 particles along the smooth wall.

(a) $d/H = 2\%$.

(b) $d/H = 10\%$.

(c) $d/H = 48\%$.

(d) $d/H = 90\%$.
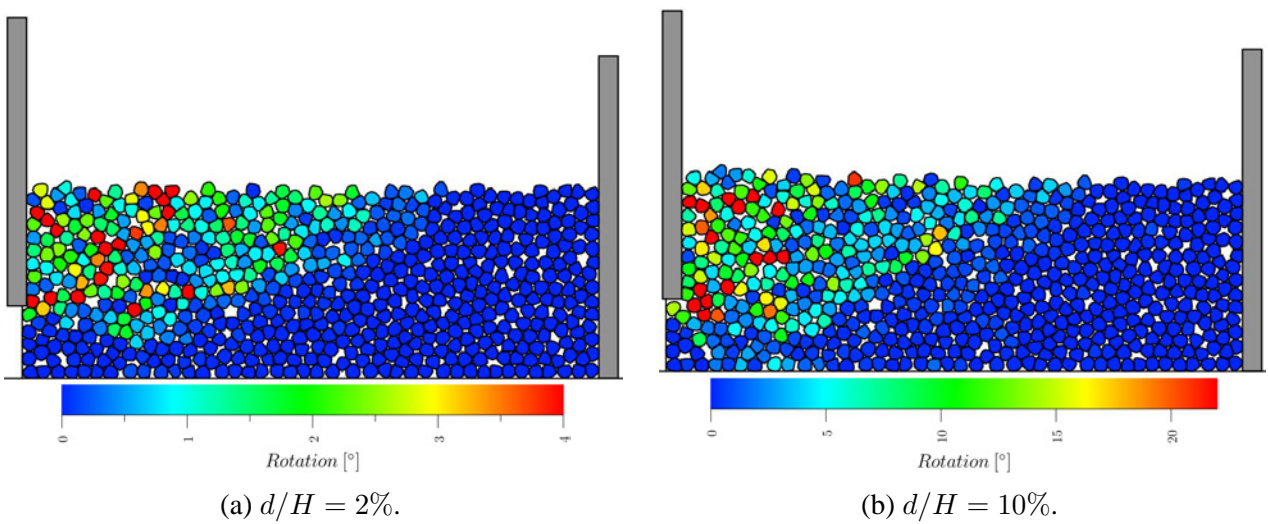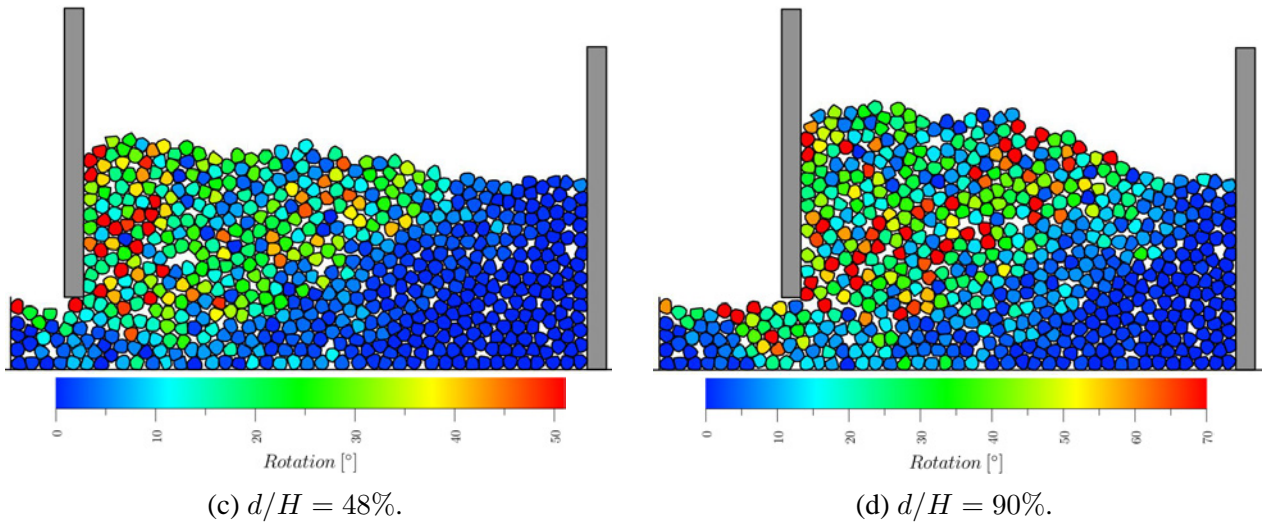
Figure 7.38: Particle total rotations in the case of 10 particles along the rough wall.

(a) $d/H = 3\%$.

(b) $d/H = 14\%$.

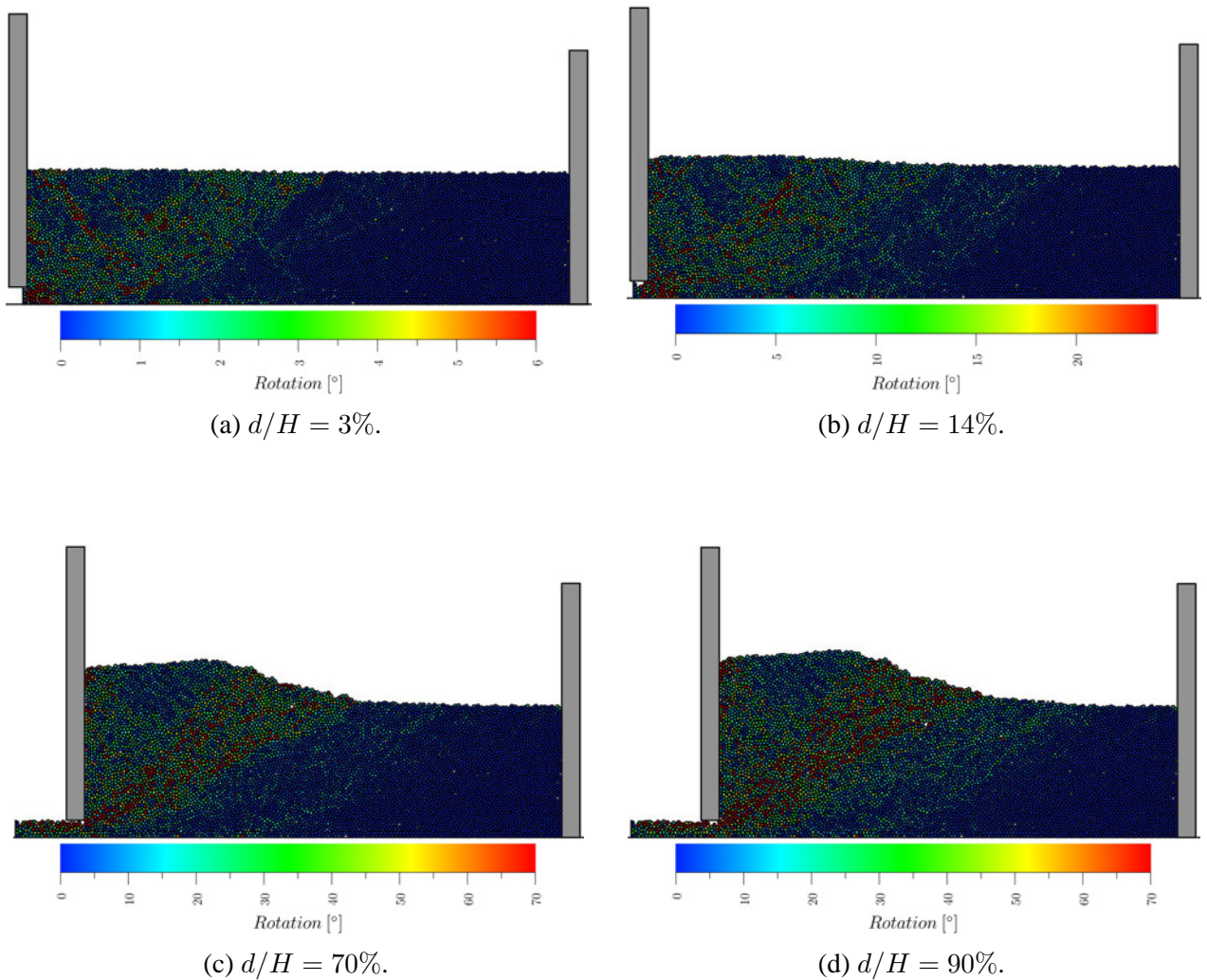

(c) $d/H = 70\%$.

(d) $d/H = 90\%$.

Figure 7.39: Particle total rotations in the case of 40 particles along rough the wall.

7.4.2 Particle shape effects

Figure 7.40 records the relationship between local wall friction angle and wall/backfill interaction friction angle based on 30 models made of Voronoi-based particles. The particle shape properties are listed in Table 7.2 and the K_p results based on 8 models are compared with theoretical solutions in Figure 7.41. The wall/backfill interface friction angle δ stabilises at around $0.66\phi_{crit}$ and $0.74\phi_{crit}$ for condition A and B respectively when δ_w exceeds the inter-particle friction angle ϕ. Although the polygonal particle circularity decrease can slightly increase the wall/backfill interface friction, the ratio of the wall/backfill interface friction angle to the backfill internal friction angle does not increase simultaneously. The K_p values are higher than those for the random dodecagonal backfills because of the larger angularity of Voronoi-based particles. The same as the dodecagonal backfills, the Voronoi-based backfills in condition A exhibit higher K_p values than those in condition B, and as the wall friction increases, the discrepancies between the DEM solutions and the theoretical solutions become larger especially in condition A, indicating the underestimation of the backfill strength when using continuum analysis. Some of the simulation scenarios are captured and displayed in Figure 7.42 to 7.45.
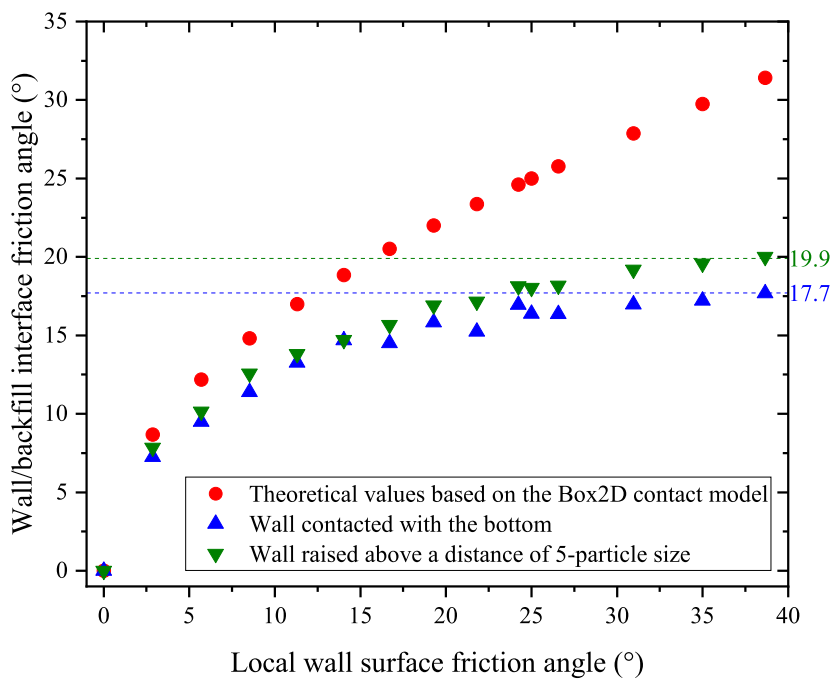
Figure 7.40: Wall/backfill interface friction coefficients under different local wall frictions when the particle internal friction coefficient is constant at 0.4663.
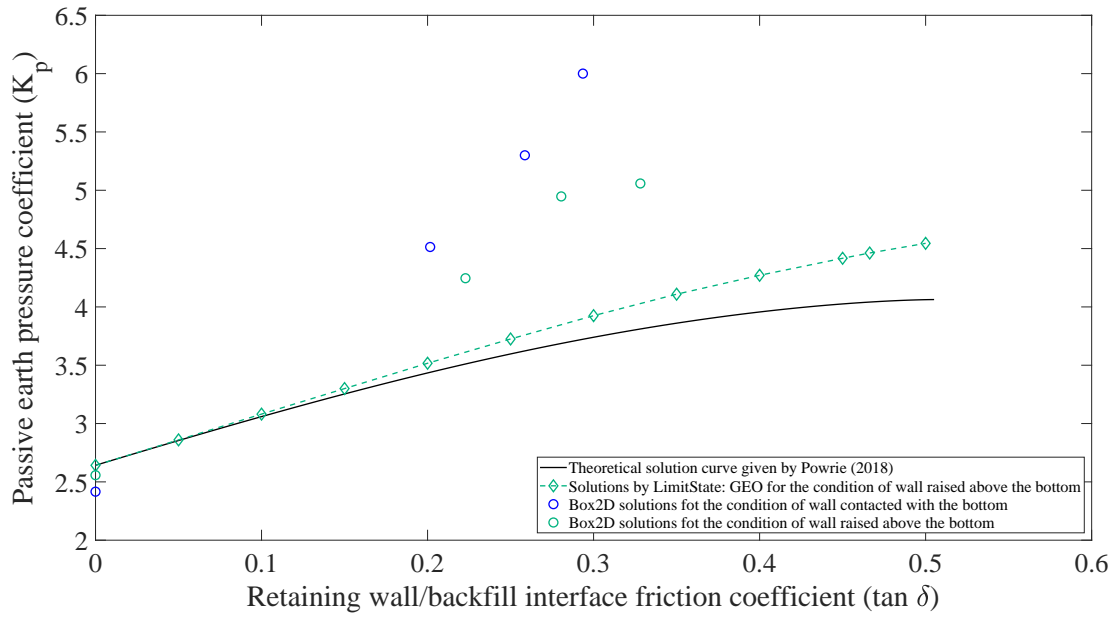
Figure 7.41: Comparison of the simulated critical K_p values for Voronoi-based backfills with the theoretical solutions.

(a) $d/H = 2\%$.

(b) $d/H = 82\%$.
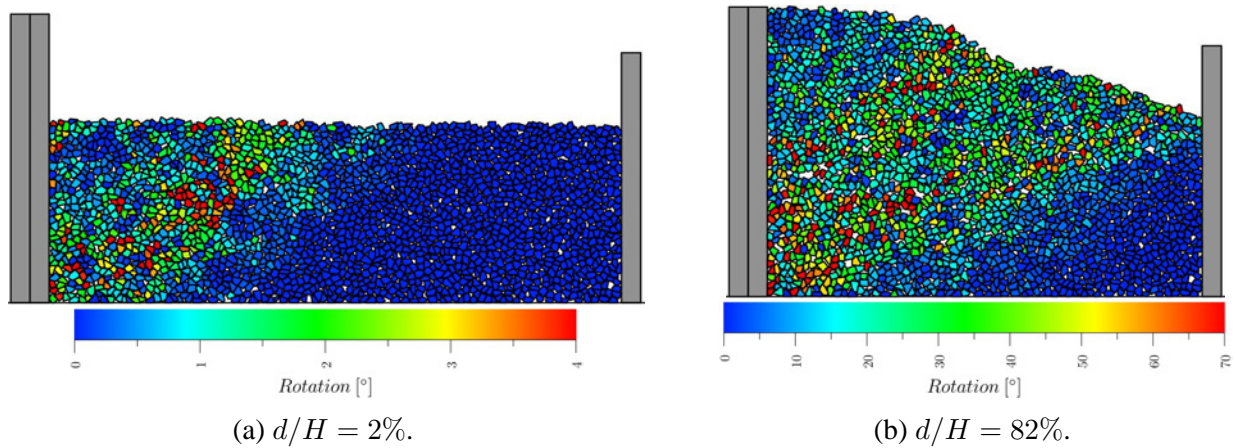
Figure 7.42: Voronoi-based particle total rotations for the case of smooth wall in condition A.

(a) $d/H = 2\%$.

(b) $d/H = 82\%$.

Figure 7.43: Voronoi-based particle total rotations for local wall friction coefficient to be 0.3 in condition A.

(a) $d/H = 2\%$.   (b) $d/H = 82\%$.
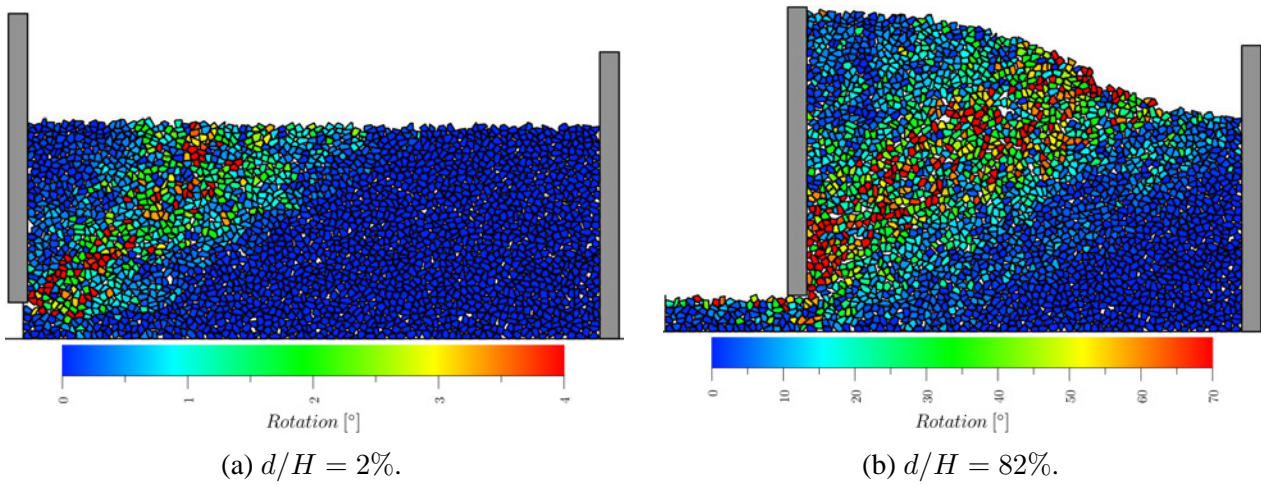
Figure 7.44: Voronoi-based particle total rotations for the case of smooth wall in condition B.

(a) $d/H = 2\%$.   (b) $d/H = 82\%$.

Figure 7.45: Voronoi-based particle total rotations for local wall friction coefficient to be 0.3 in condition B.

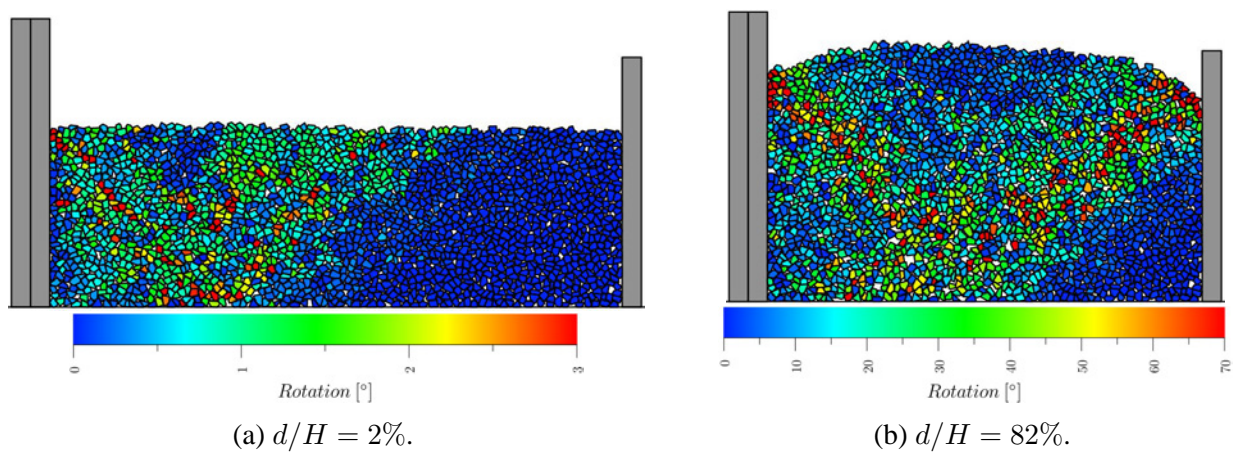### 7.4.3 Backfill packing effects
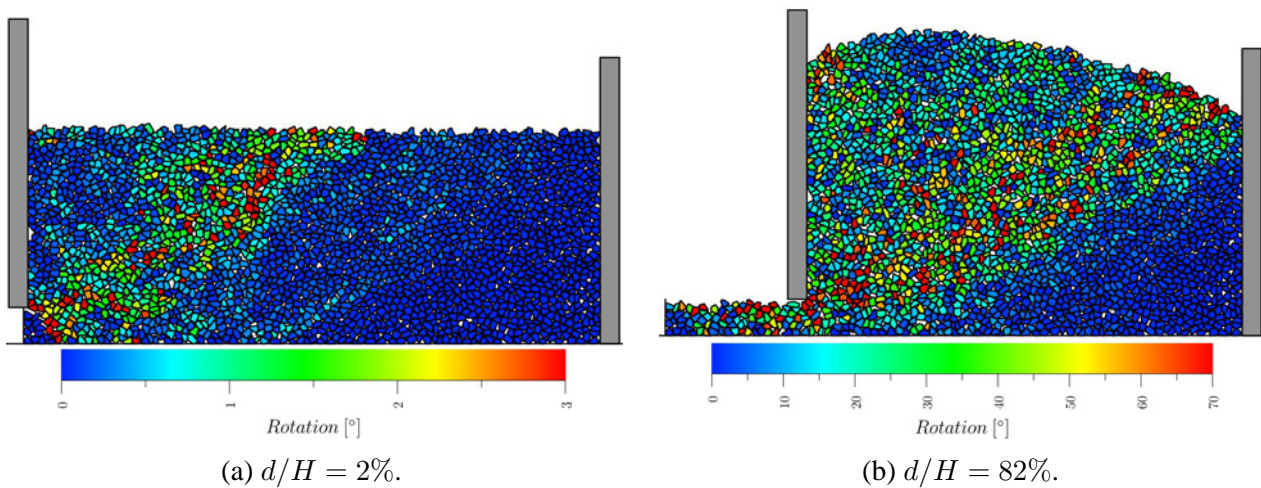
Box2D results

The backfill packing effects on the passive earth pressure coefficient K_p are also considered by building the perfect Voronoi packing in situ as shown in Figure 7.47 to Figure 7.50. The initial backfills are void-free and can be regarded as discretisation of a continuum backfill into meshes, providing the possibility to connect the continuum analysis with the discrete element analysis. Because the initial backfill packings are without void, the backfills develop extremely high peak passive earth pressure coefficients in condition A and even higher in condition B as shown in Figure 7.46. The peak and critical K_p values are compared in Table 7.4. The backfills in condition B can reach higher K_p values compared with condition A, and this is contrary with the previous findings for deposited backfills. One of the possible reasons is that more frictional energy is dissipated in condition B because the bottom boundary/backfill interface friction should be lower than the inter-particle friction as discussed previously. As shown in Figure 7.47 to 7.50, the shifted sliding Rankine zones make up a larger volume in condition B than in condition A, hence more energy will be dissipated in condition B, balanced by larger lateral passive earth pressures. The critical states are reached at d/H around 20% and 30% in condition A and B respectively, much earlier than the poorly-packed backfills made of dodecagon particles.

(a) Wall contacted with the bottom boundary.   (b) Wall raised above a distance of 5-particle size.
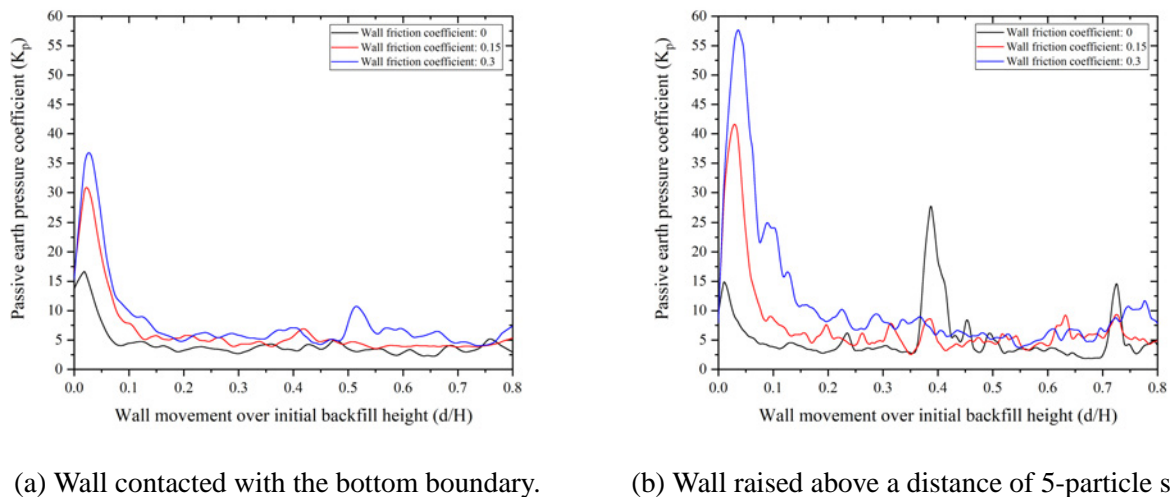
Figure 7.46: K_p versus d/H calculated based on the local void ratio.

Figure 7.47 to 7.50 illustrate how the rupture surface develops from the start of wall movement from the perspective of accumulated particle rotations. Initially, many particles are disturbed by the wall movement and after minute microscale granular skeleton rearrangements, a rupture surface is developed. Therefore, the inter-particle contact normal forces are larger along the potential rupture surface initially, pushing the particles sliding and rotating. Then the sliding wedge and the ideal Rankine zone are formed and contact forces between the particles in the Rankine zone are much weaker than in other zones as shown in Figure 7.51 and 7.52. The rupture surfaces intersect with the

Table 7.4: Peak and critical K_p values.

Local wall friction coefficient $(\tan \delta_w)$	Model set-up	Peak K_p	Critical K_p
0	condition A	16.7	3.4
	condition B	14.9	3.7
0.15	condition A	31.0	4.4
	condition B	41.7	5.4
0.3	condition A	36.9	5.6
	condition B	57.8	6.0

horizonal surface at around $32°$ in both conditions A and B, which are quite close to the theoretical value $33.9°$.

(a) $d/H = 2\%$.

(b) $d/H = 8\%$.

(c) $d/H = 40\%$.

(d) $d/H = 80\%$.
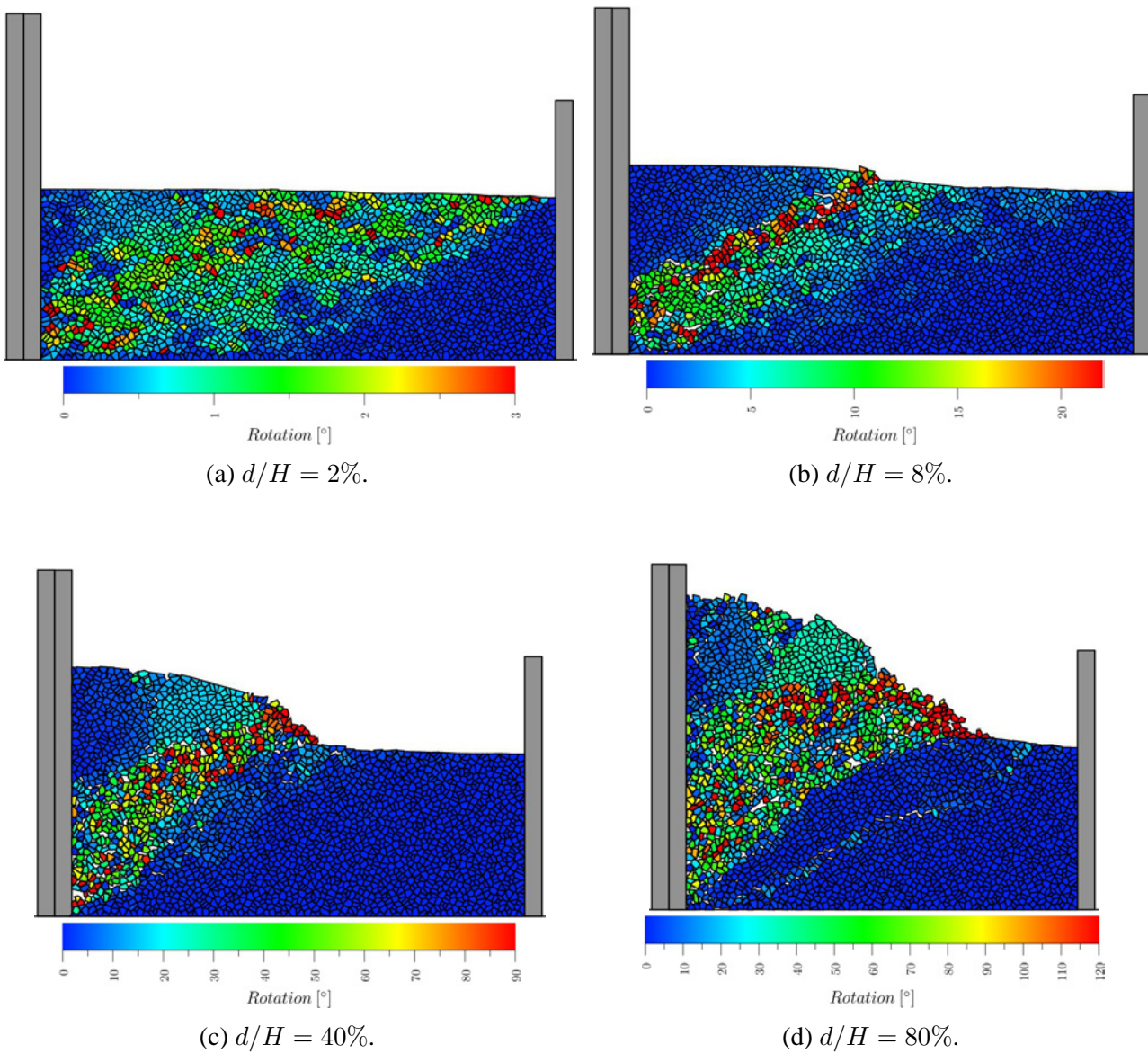
Figure 7.47: Particle total rotations for Voronoi-based in-situ packing in the case of smooth wall in condition A.

(a) $d/H = 2\%$.

(b) $d/H = 8\%$.

(c) $d/H = 40\%$.

(d) $d/H = 80\%$.
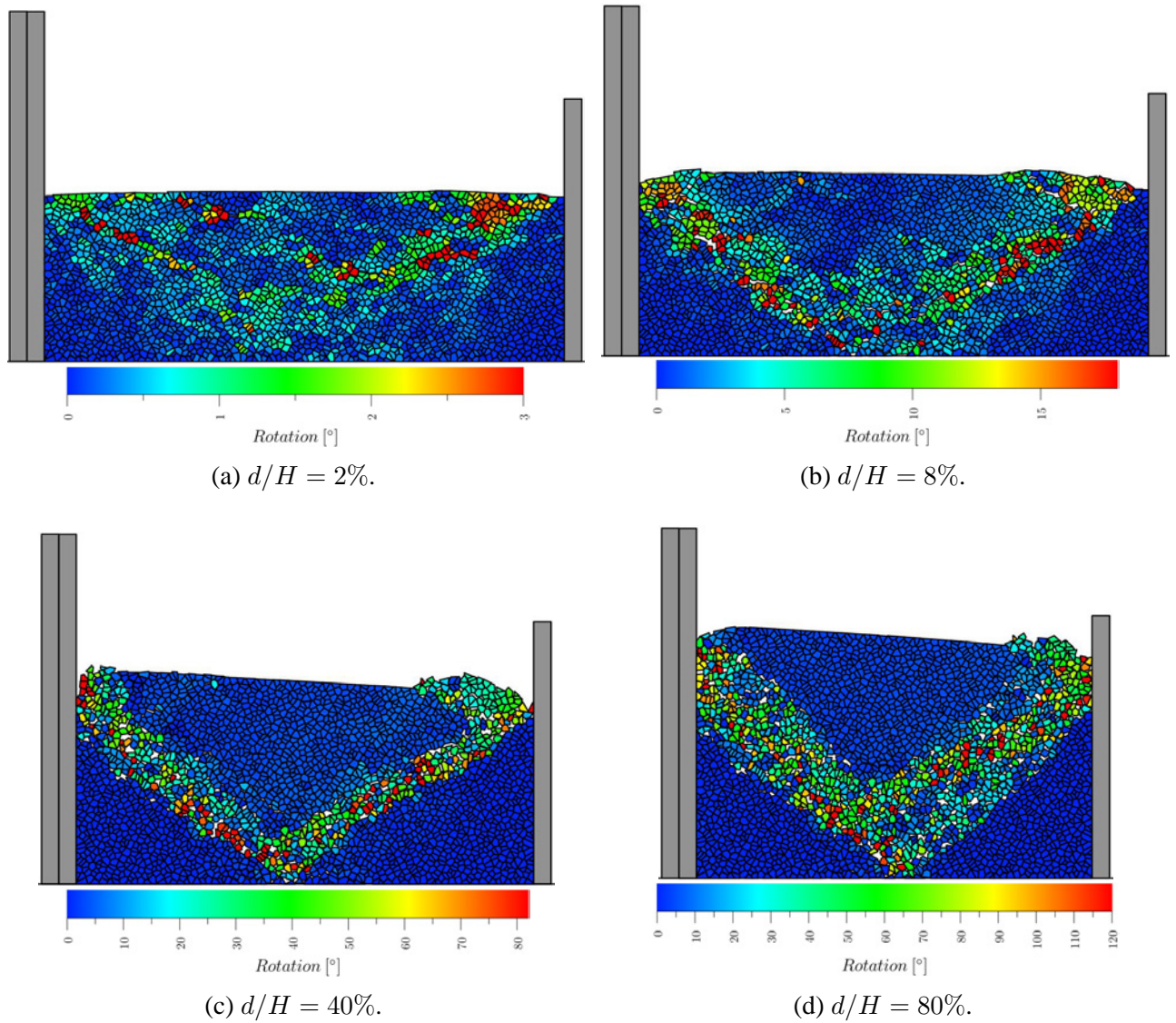
Figure 7.48: Particle total rotations for Voronoi-based in-situ packing for local wall friction coefficient to be 0.3 in condition A.

(a) $d/H = 2\%$.

(b) $d/H = 10\%$.

(c) $d/H = 50\%$.

(d) $d/H = 100\%$.
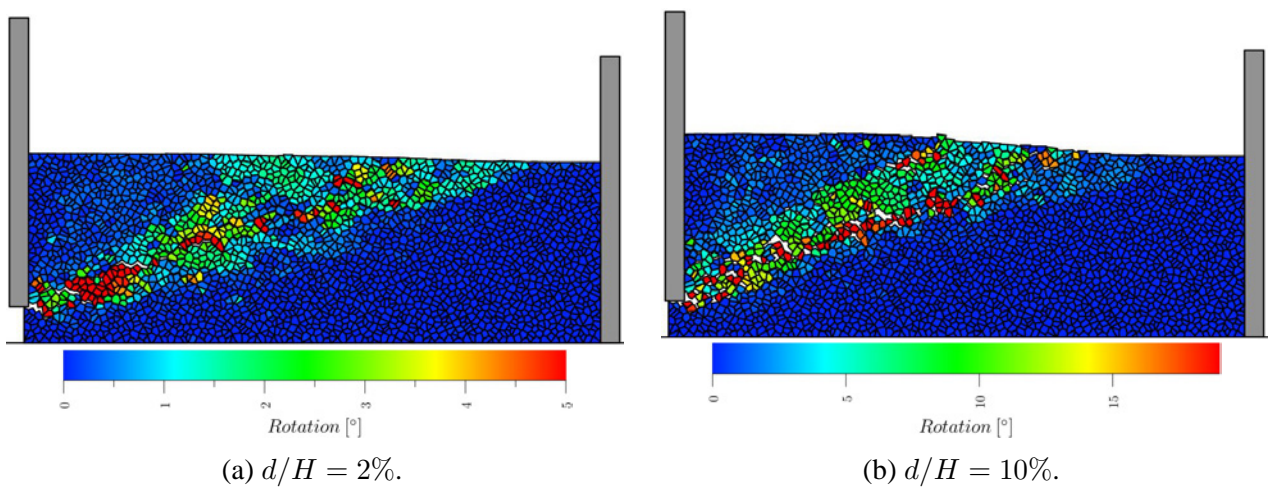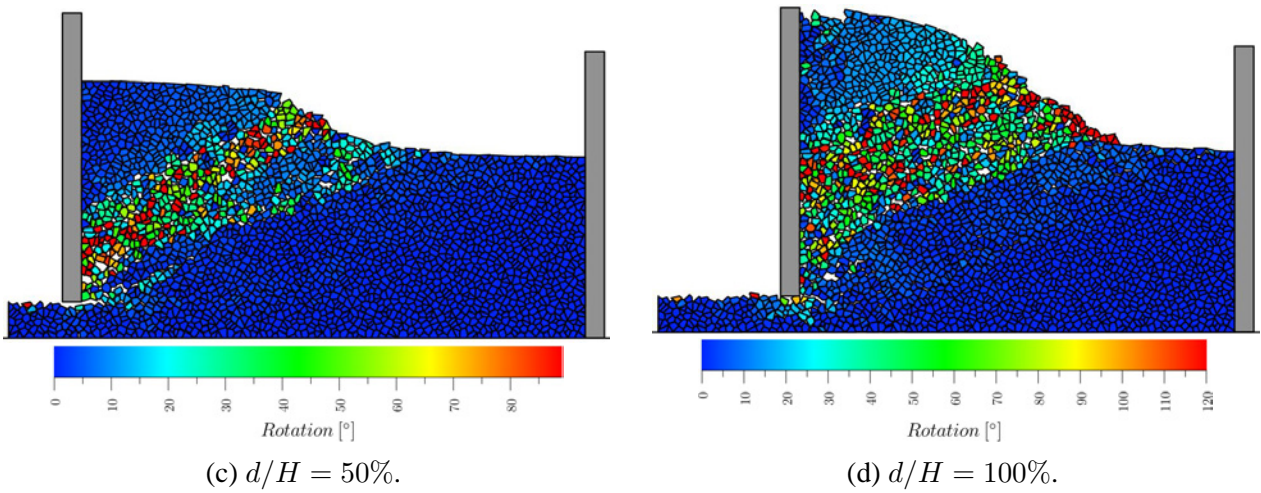
Figure 7.49: Particle total rotations for Voronoi-based in-situ packing in the case of smooth wall in condition B.

(a) $d/H = 2\%$.

(b) $d/H = 10\%$.

(c) $d/H = 50\%$.

(d) $d/H = 100\%$.
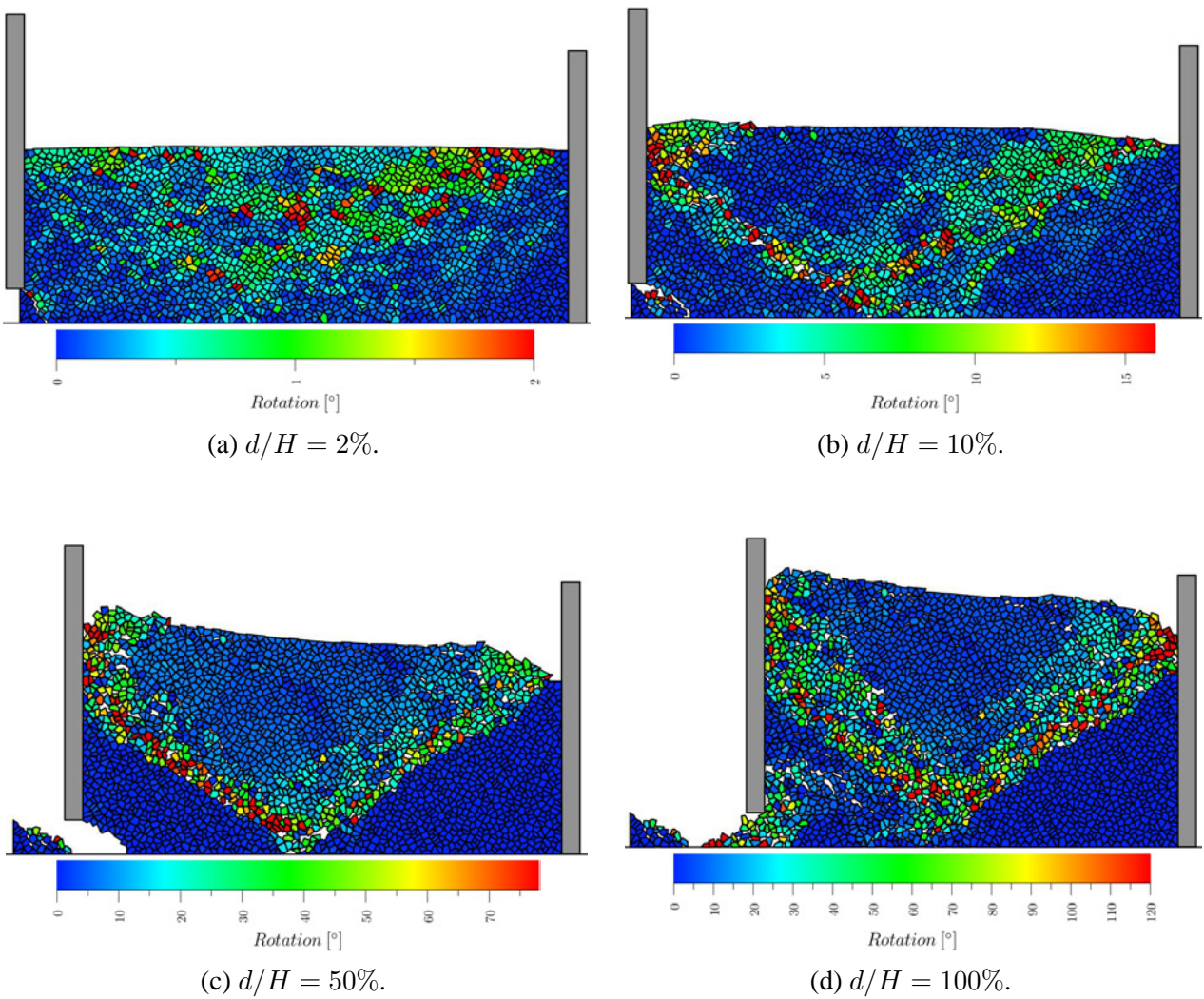
Figure 7.50: Particle total rotations for Voronoi-based in-situ packing for local wall friction coefficient to be 0.3 in condition B.

(a) $d/H = 2\%$.

(b) $d/H = 10\%$.

(c) $d/H = 50\%$.

(d) $d/H = 100\%$.

Figure 7.51: Contact normal force chains for Voronoi-based in-situ packing in the case of smooth wall in condition B.

(a) $d/H = 2\%$.

(b) $d/H = 10\%$.

(c) $d/H = 50\%$.

(d) $d/H = 100\%$.

Figure 7.52: Contact normal force chains for Voronoi-based in-situ packing in the case of smooth wall in condition B.

Comparison with LimitState:GEO
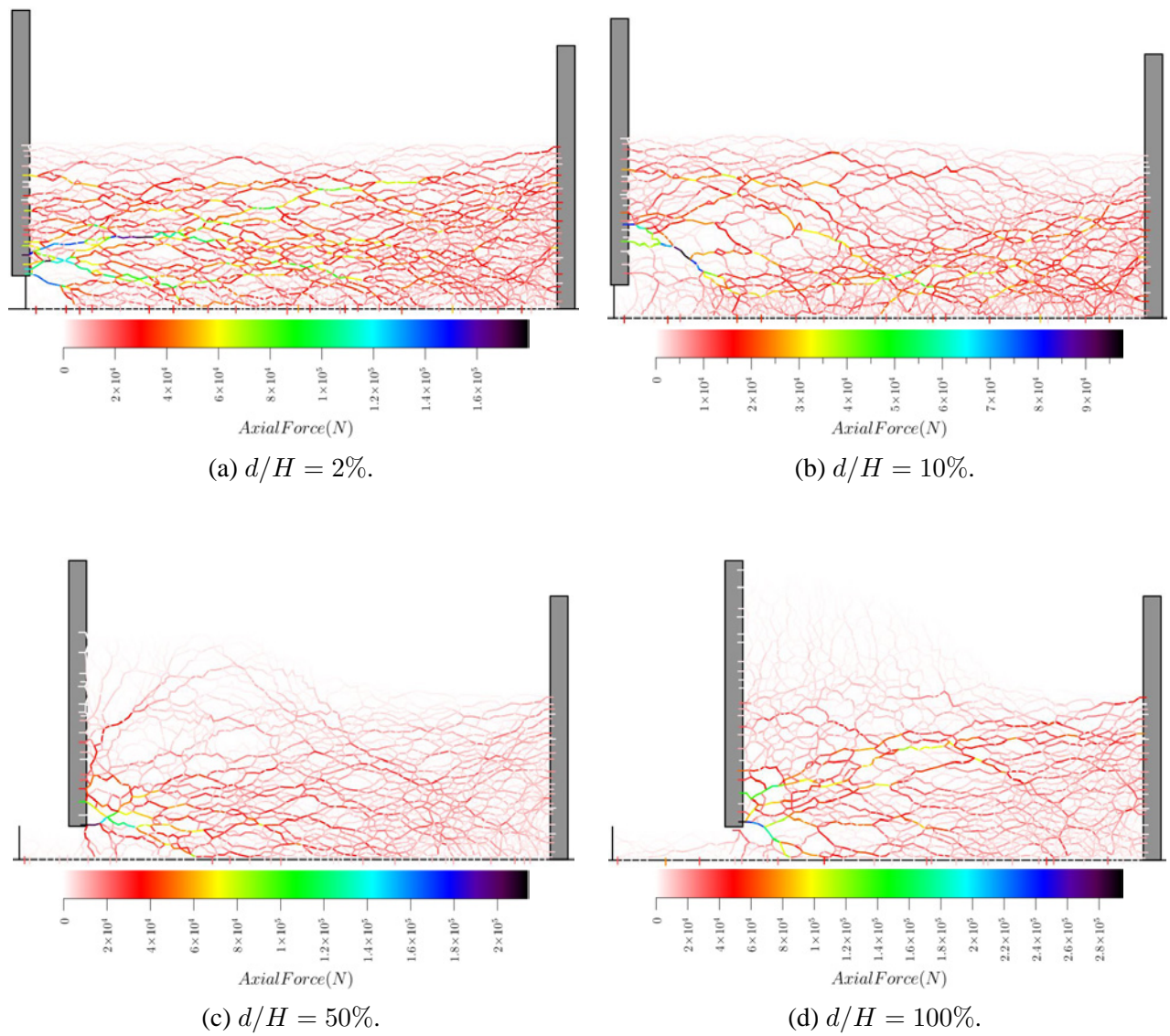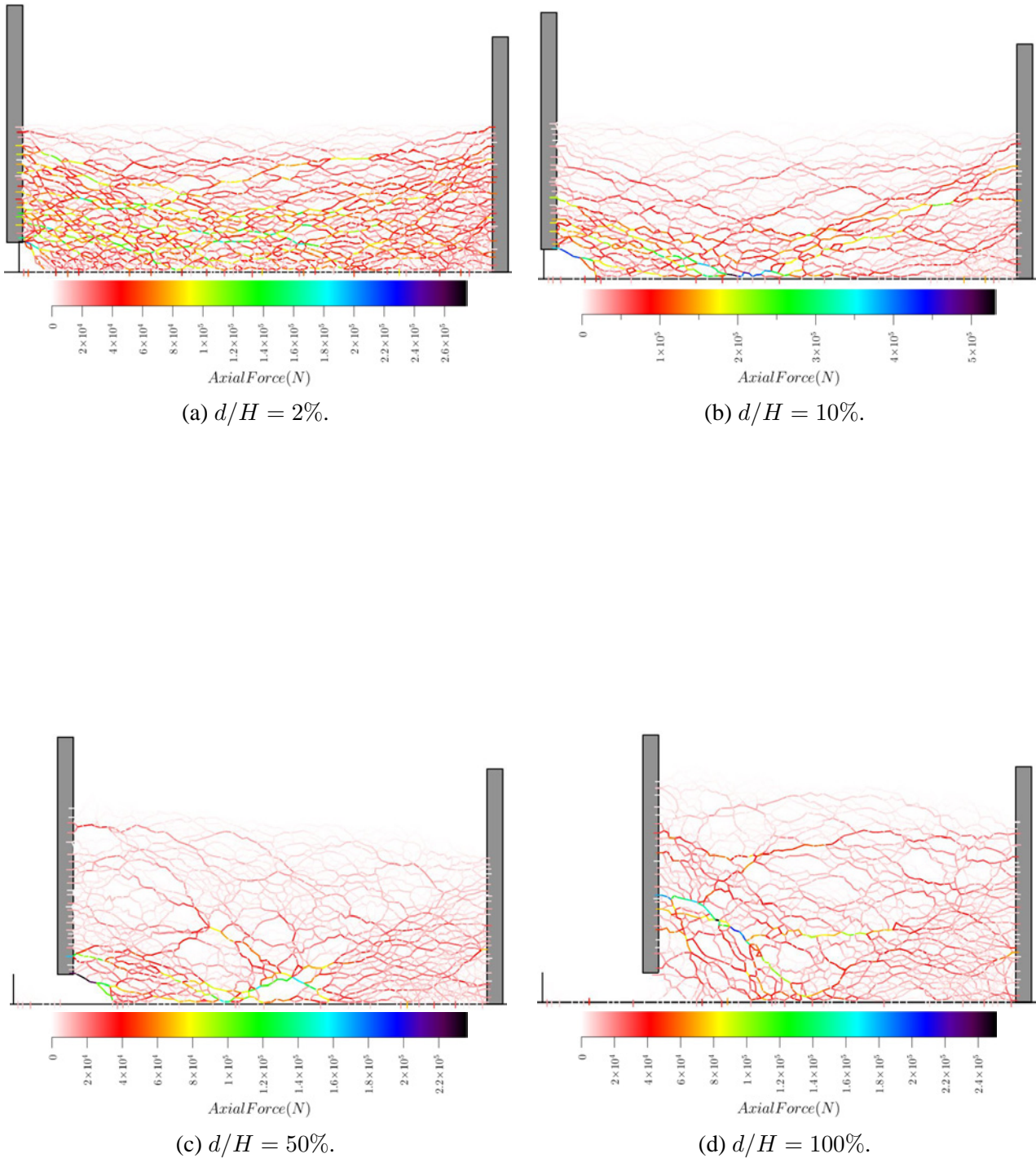
Three discrete particle LimitState:GEO (beta version) models were established to analyse the backfill packing effects on the passive earth pressure coefficient as shown in Figure 7.53 and compared with Box2D on the failure modes as shown from Figure 7.54 to 7.56. The particle contact condition is set to be controlled by Mohr-Coulomb failure criteria without cohesion. The same contact condition is set at the interfaces between the particles and the bottom and right boundaries. The interfaces between the left weightless rigid retaining wall and the contacting particles and the bottom boundary were modelled by a frictionless material and no tension was allowed. Besides the perfect void-free packing A and B as shown in Figure 7.53a and 7.53b, a similar packing C in Figure 7.53c with void modelled by cutting-edge process (introduced in section 5.4) based on the packing B was also built and analysed. This backfill packing generation approach can keep the particle contacts the same as in the perfect packing. Due to the computational power limit, each packing involved 300 particles. According to the rupture surfaces developed, the failure mechanism is highly dependent on the packing characteristic especially the contact condition when the particles involved are limited. The calculated passive earth pressure coefficients in LimitState:GEO for backfill A, B and C are 41.19, 9.04 and 6.04 respectively. To compare with Box2D, three models built by the same packings were established. The critical state K_p for the packings A and B are 3.659, while for packing C it is 2.674. The large discrepancies between LimitState:GEO and Box2D are caused by that LimitState:GEO only computes K_p at the very initial stage without considering further developments of the backfill and models friction as dilation which is not the case in the contact model in Box2D. It can be obviously observed that the initial potential rupture surfaces in Box2D match well with those developed in LimitState:GEO, while as the backfill deforms in Box2D, more rupture surfaces are possible to be developed until reaching the critical state.

(a) Initial model A.

(b) Initial model B.

(c) Initial model C.
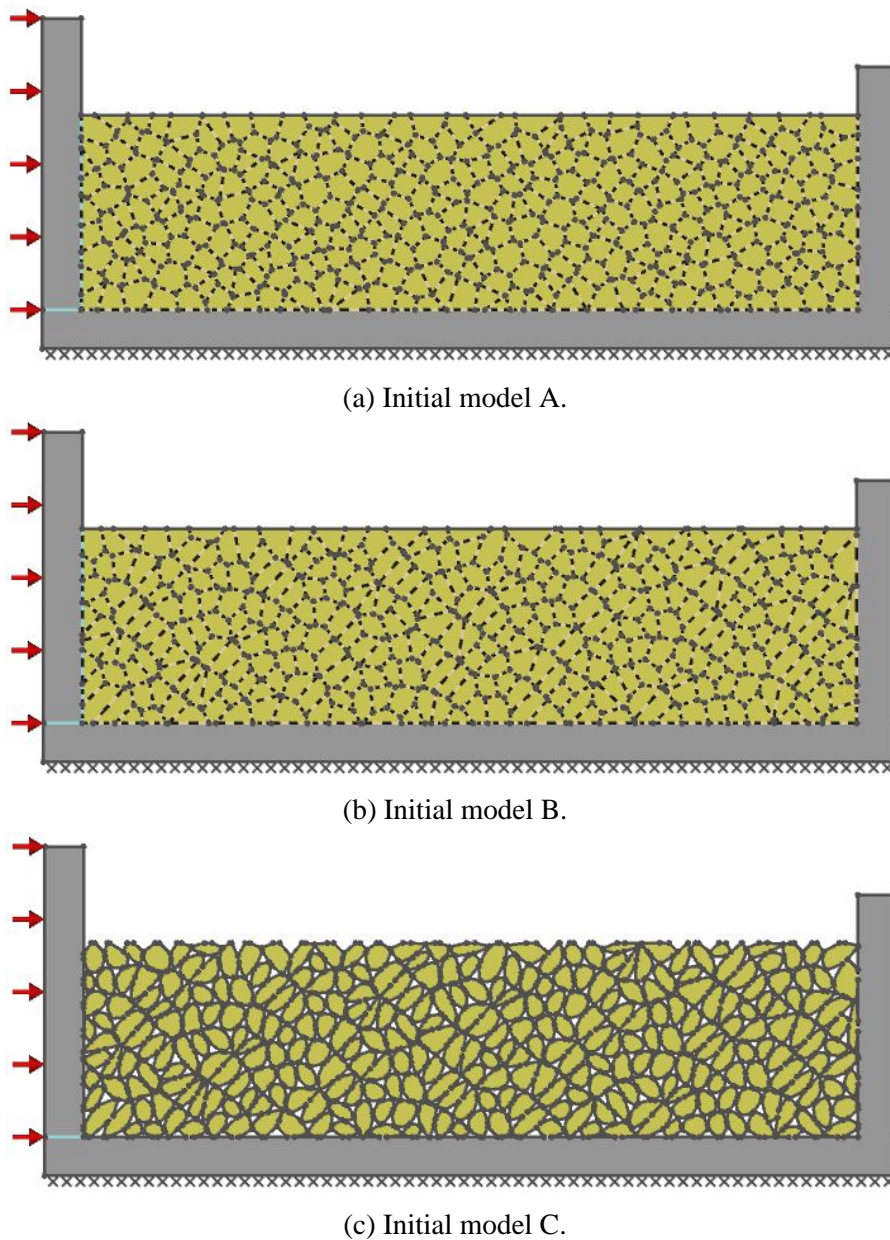
Figure 7.53: In-situ Voronoi-based backfills in LimitState:GEO.
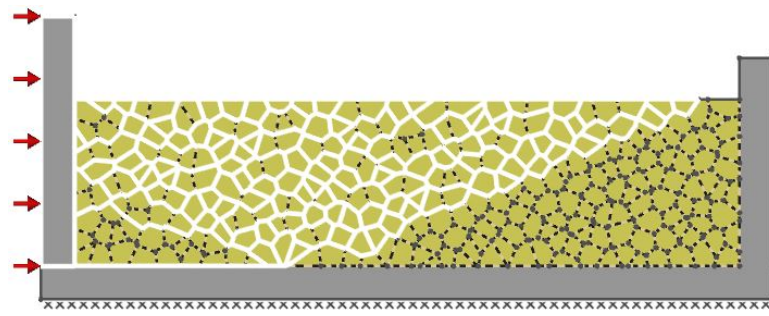
(a) Potential failure mechanism.
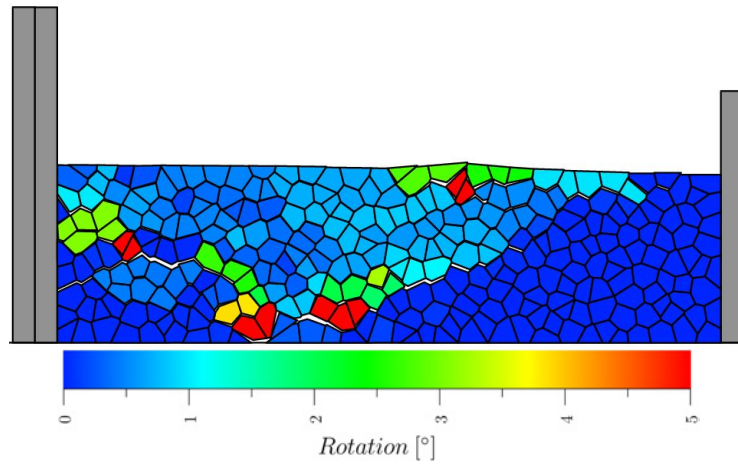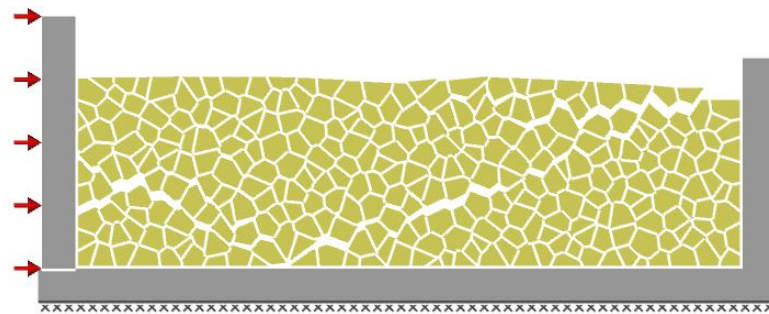
(b) $d/H = 2\%$.

(c) Final failure mechanism.
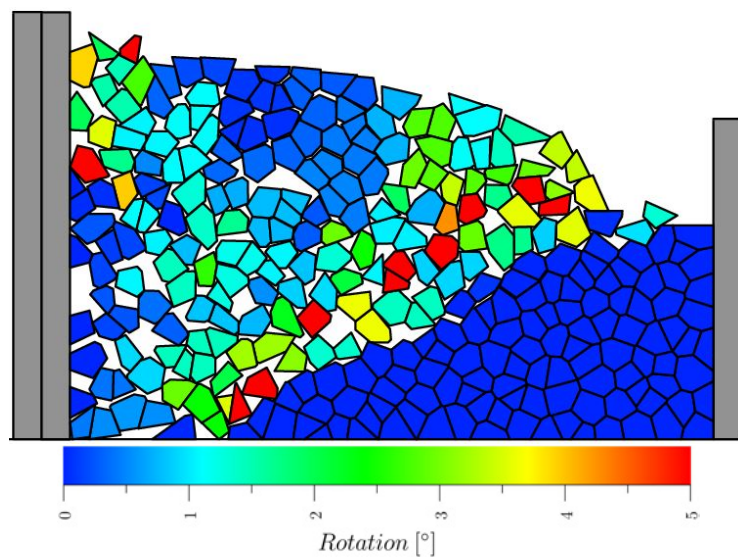
(d) $d/H = 100\%$.

Figure 7.54: Comparison of failure modes between LimitState:GEO and Box2D for model A.
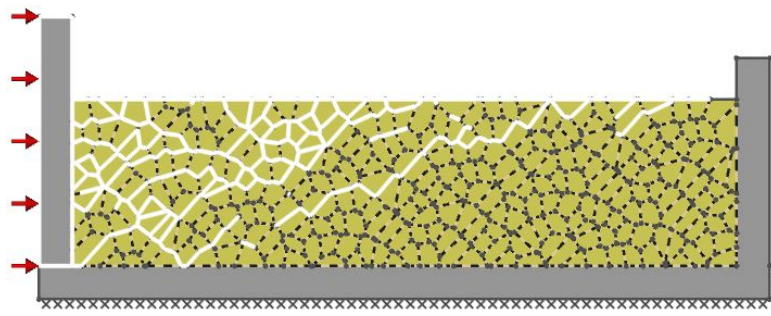
(a) Potential failure mechanism.
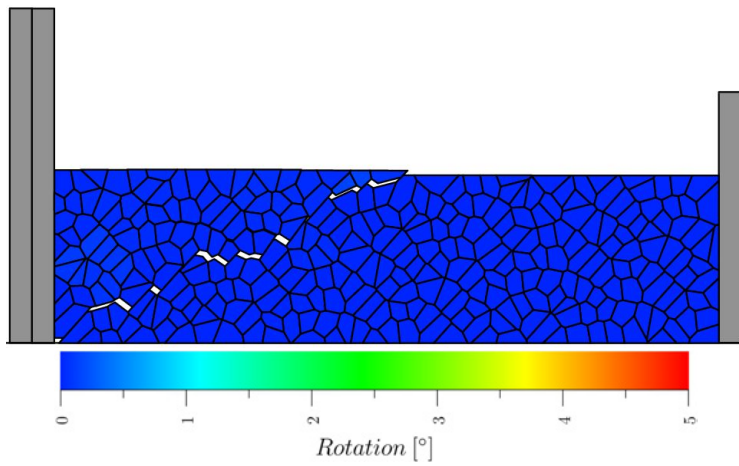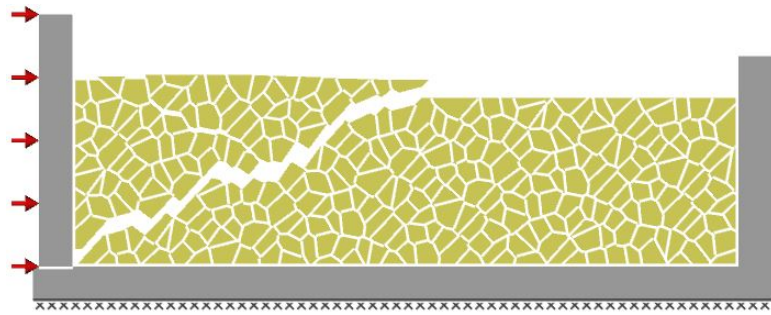
(b) $d/H = 2\%$.

(c) Final failure mechanism.
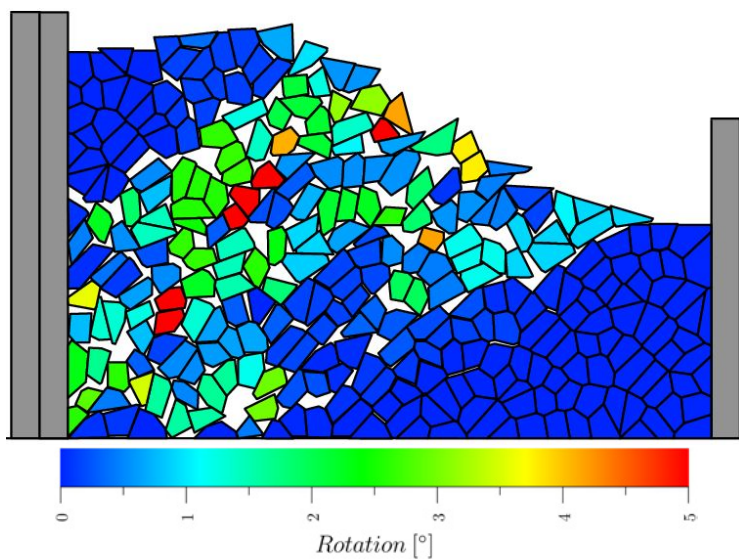
(d) $d/H = 100\%$.

Figure 7.55: Comparison of failure modes between LimitState:GEO and Box2D for model B.
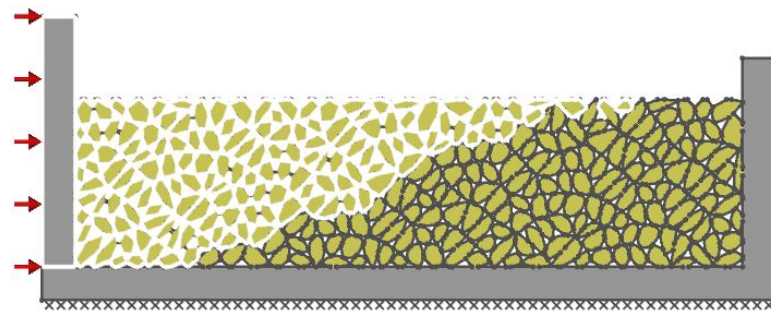
(a) Potential failure mechanism.
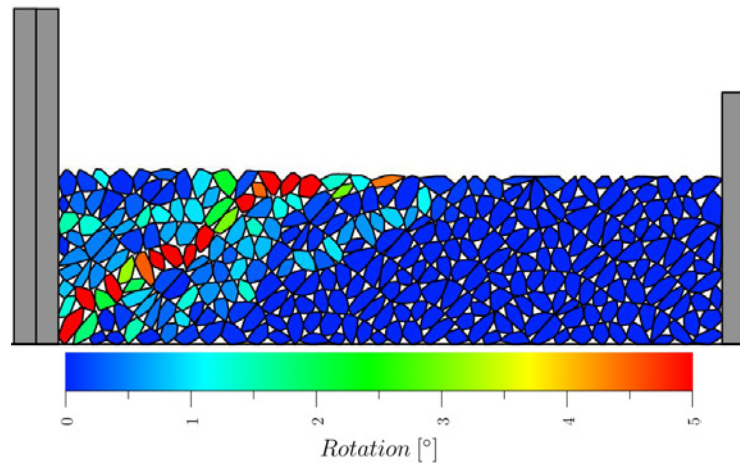
(b) $d/H = 2\%$.
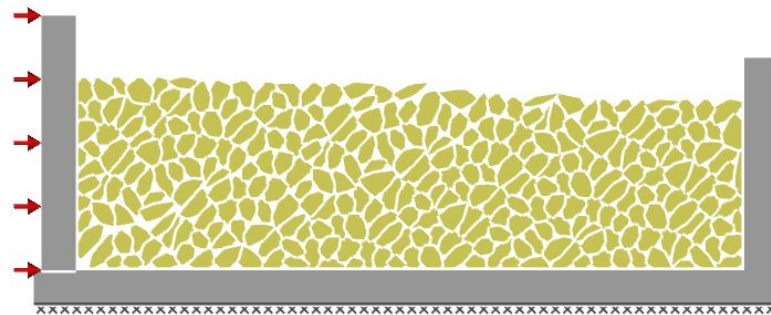
(c) Final failure mechanism.
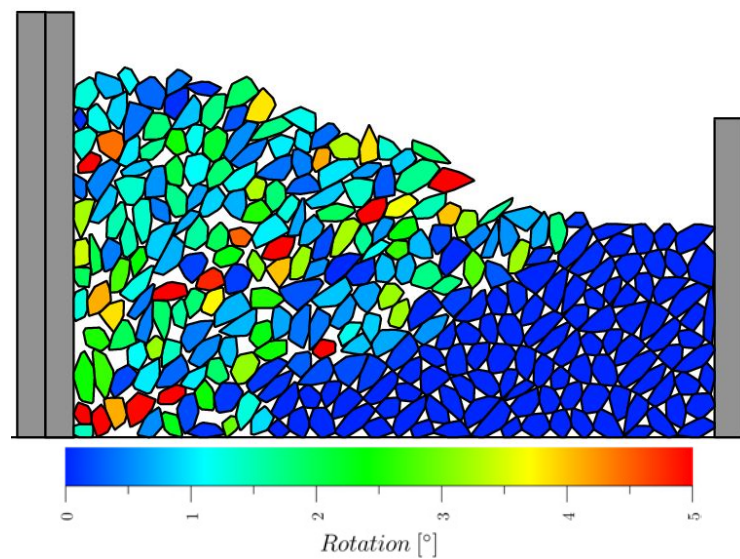
(d) $d/H = 100\%$.

Figure 7.56: Comparison of failure modes between LimitState:GEO and Box2D for model C.

7.5   Summary

In this chapter, retaining wall models were established in Box2D to analyse the local wall friction coefficient effects on the lateral earth pressure coefficients in both passive (K_p) and active (K_a) conditions. Two different conditions: the retaining wall was directly built on the bottom boundary (condition A) and above the bottom boundary by a distance of 5-particle size (condition B), were both considered to analyse the bottom boundary effects in the retaining wall model. The simulation results and the backfill failure mechanisms were compared with the theoretical solutions given by Powrie (2018) and limit analysis using software LimitState:GEO. The primary findings are summarised below.

Local wall friction effects on earth pressure coefficients

1. The local void ratio adjacent to the retaining wall is larger than the global void ratio due to the flat boundary effect. The backfill heave can be inhibited by the wall surface roughness in the passive condition and the backfill height increase in front of the wall is higher in condition B than that in condition A because of the flat boundary effects causing the lower bottom/backfill interface friction in condition A.

2. When the backfill being pushed by the retaining wall, a triangular zone at the top adjacent to the wall firstly starts to move and the displacements propagate further into the backfill in gradient. Evident rupture surfaces and sliding wedges can be distinguished in the particle accumulated rotation plots.

3. The relationship between local wall friction angle δ_w and wall/backfill interface friction angle δ was studied. It was found that δ stabilises at around $0.65\phi_{crit} - 0.88\phi_{crit}$ when δ_w exceeds the inter-particle friction angle ϕ in the passive condition for backfills made of dodecagonal particles, while even higher in the active condition at around $1.0\phi_{crit}$. For backfills made of Voronoi-based particles, δ oscillates around $0.66\phi_{crit}$ and $0.74\phi_{crit}$ in condition A and B respectively. Under the same local wall friction angles, δ in condition B are generally slightly higher than their values in condition A.

4. The critical state passive earth pressure coefficient K_p computed by Box2D is higher than the solution given by Powrie (2018) and limit analysis using software LimitState:GEO. This causes underestimation for the backfill strength and retaining wall bearing capacity in the passive condition using theoretical continuum solutions in geotechnical design, and the discrepancy becomes increasingly more significant as the wall/backfill interface friction increases. The backfills exhibit higher peak K_p values when the wall/backfill interface is more frictional even though their initial packings are the same.

5. For backfills made of deposited dodecagonal and Voronoi-based particles, the critical K_p values in condition A are higher than in condition B. However, the contrary phenomenon occurs for

backfills made of in-situ Voronoi-based packings.

6. The initially loose backfills reach the same critical state K_p values as the initially dense backfills, while no strain hardening behaviour is observed for the relatively loose backfills.

7. The active earth pressure coefficient K_a obtained by Box2D is lower than the Powrie's solution and the Sokolovskii's solution. This indicates that the theoretical solutions underestimate the retaining wall bearing capacity compared with the Box2D solution.

Particle size and shape effects on earth pressure coefficients

1. Based on the obtained data in this study, it is found that as the particle size decreases, the K_p value increases.

2. Backfills made of Voronoi-based particles exhibit higher K_p values than those made of mono-sized dodecagonal particles due to larger angularity effects.

Backfill packing effects on earth pressure coefficients

1. By building in-situ well-packed Voronoi-based backfill packings, it was found that these packings exhibit extremely high peak K_p values and significantly higher critical K_p values than those developed in poorly-packed backfills. The comparison of the critical K_p values for different backfills is shown in Figure 7.57. Therefore, the dry stone structure retaining wall may potentially exhibit higher critical and especially peak bearing capacity.

2. The failure mechanisms of three different in-situ Voronoi packings in Box2D were compared with those in discrete particle LimitState:GEO models, and the failure mechanisms agree perfectly well in all cases. In addition, the strain localisation regions are more distinct in these well-packed backfills than in other poorly-packed backfills.

7.6 Discussion

Bottom boundary effects

From Figure 7.16, Figure 7.31 and Figure 7.40, we know the wall flat surface/backfill interface friction angle δ is lower than the particle internal friction angle ϕ_{crit}. Similarly, the bottom boundary/backfill interface friction angle should also be lower than the particle internal friction angle, therefore the backfill dilation effect should be inhibited in condition A compared with condition B, and this is proved by the local backfill height increase plot in Figure 7.12. In addition, inter-particle rotation is inhibited at the bottom boundary in condition A, also causing dilation behaviour limited. However, the passive coefficient K_p in condition A is higher than that in condition B for backfills made

191
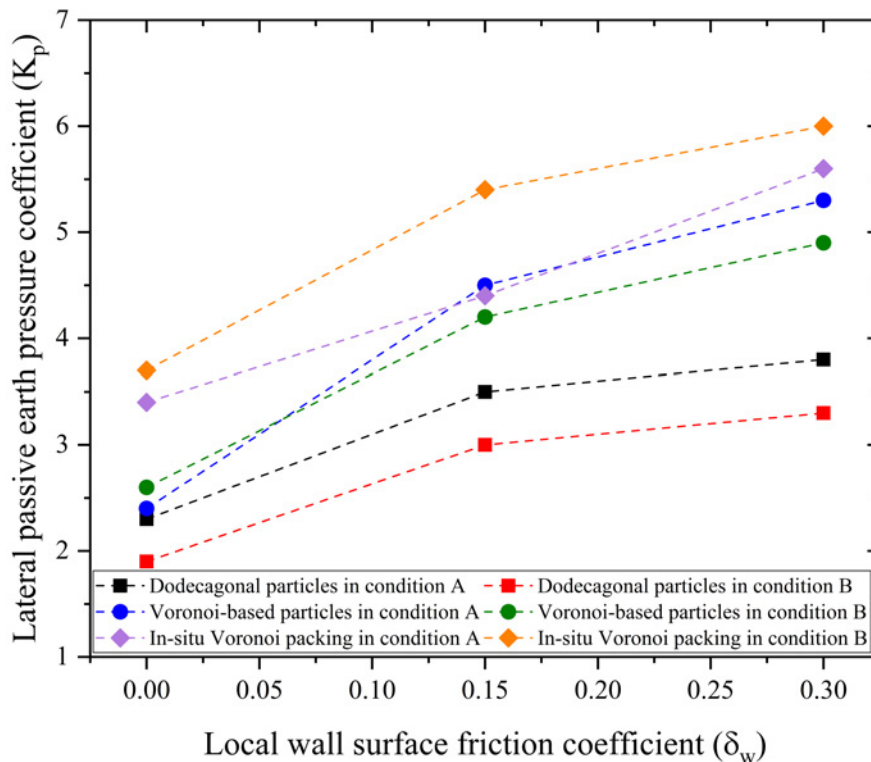
Figure 7.57: K_p values for various backfills under different local wall friction conditions

of monosized dodecagonal particles. One of the possible reasons is that the space for particle translational displacements is restrained compared with condition B, hence higher wall/backfill contact pressures are generated and the excessive energy is released by inter-particle rotations. On the contrary, in terms of backfills made of in-situ Voronoi packings, K_p exhibits higher values in condition B than that in condition A. The excessive energy in condition B caused by higher passive earth pressure is dissipated by the kinematic energy shifting the larger formed Rankine zone. The larger Rankine zone developed in condition B than that in condition A can be observed when comparing Figure 7.47b with Figure 7.49b, and Figure 7.48c with Figure 7.50c.

Choosing ϕ_{peak} or ϕ_{crit} in retaining wall design?

There is no agreement on whether design should be based on critical state strength which is on the safe side but possibly uneconomic or using some proportion of the peak strength. Two issues in design are: (a) avoiding the risk of brittle failure - the post peak falling part of the stress strain curve and this can be addressed by using a suitable fraction of peak strength, and (b) not assuming that peak strength is mobilised simultaneously and determining what proportion can be mobilised at a reasonable strain level. Peak strengths are usually factored, but there is debate about whether critical state strengths should be factored.

Based on the results shown in Figure 7.15, the peak strengths in condition A and B are developed

at d/H around 10% and 3% respectively. However, the retaining wall translational displacement is normally restrained by 0.5% in engineering practice, therefore, it is unable to fully develop to peak strength by this limit according to the observations in this study. At d/H to be 0.5%, the developed K_p in condition A is slightly lower than their critical values, while apparently higher than their corresponding critical values in condition B as summarised in Table 7.3. When replacing ϕ by ϕ_{peak} ($38°$ obtained in Figure 5.8a) in equation (7.2) and selecting δ to be the corresponding critical wall/backfill interface friction angle in Figure 7.17, the theoretical peak K_p values can be calculated and listed in Table 7.5, compared with the measured initial ($d/H = 0.5\%$), peak and ultimate K_p values. The calculated theoretical peak K_p values are consistently higher than the measured peak values. Therefore, using ϕ_{crit} is more conservative and reasonable in geotechnical design, which is also irrespective of the backfill initial density state that is sensitive to disturbance and predominant on ϕ_{peak}. In addition, ϕ_{crit} does not need to be factored according to the data shown in Table 7.5.

Table 7.5: Mobilised K_p values.

Local wall friction coefficient ($\tan\delta_w$)	Model set-up	Initial K_p	Peak K_p	Ultimate K_p	Theoretical peak K_p
0	condition A	2.7	3.5	2.3	4.204
	condition B	3.2	3.7	1.9	4.204
0.15	condition A	3.2	4.2	3.5	5.679
	condition B	4.0	5.3	3.0	6.083
0.3	condition A	3.4	4.4	3.8	5.867
	condition B	4.2	5.5	3.3	6.569

Particle shape and size influences

In this study, polygonal particles were chosen as the backfill materials to replace disc particles which are the most commonly used in discrete element modelling for their simplicity to build and fast simulation speed. Using polygonal particles can better simulate angularity effects which can enhance interlocking effects and rolling resistance between particles, hence give a higher backfill strength. However, the simulation speed is significantly reduced compared with the case of using disc particles. As a result, around 2500 polygonal particles were simulated in the retaining wall model due to limited computational power, and this is far less than 100000 disc particles used in the retaining wall model built by Jiang et al. (2014). Using large or a small number of particles has the drawbacks below:

1. The recorded data oscillate greatly although this can be improved by averaging over several different simulation results as shown in Figure 7.19. This relatively conspicuous data oscillation is also caused by polygonal particle shape effects and the velocity-based contact mode adopted in Box2D in which inter-particle elastic deformation is ignored when collision events occur, and velocity jump is allowed. Further work will be done to simulate more particles by means of higher performance computers (HPC).

2. The low-strain behaviour is influenced more than the critical state behaviour as shown in Figure 7.19. The number of particles involved will also influence the d/H values to reach peak and critical states, since the critical state for the retaining wall model in Box2D is reached much later than in physical models conducted by Fang et al. (2002).

3. It was found that as the particle size decreases, K_p will increase. However, there should be a limit for this increase in K_p and after that K_p will decrease. Due to the limited particle numbers in the retaining wall model, it is difficult to testify this prediction.

4. The measured lateral earth pressures do not turn into distinct critical states as shown in Figure 7.13 due to the particle number limitation.

Chapter 8

Conclusions and Further Work

8.1 Conclusions

8.1.1 Introduction

Many discrete element modelling techniques have been developed until today, among which the distinct element modelling is the most prevalent approach appreciated by many researchers. Due to computational power limitations, new DEM techniques need to be developed and verified in modelling particulate media in geotechnical engineering. For this purpose, the open-source physics engine Box2D was adopted in this study to investigate micro to macro granular soil behaviours. The main contributions of this study include:

1. Develop Voronoi-based polygonal particle and packing generation approach for Box2D to investigate the particle shape and packing effects on granular soil behaviours, facilitating to show that Box2D can accurately model granular soil systems. Graphical interpretation methods were also applied in Box2D as post processing techniques.

2. Quantitatively measure model scaling effects on small-strain stiffness for samples made of random dodecagonal particles, regular hexagonal particles and Voronoi-based particles respectively by building biaxial models, and qualitatively analyse their microscopic mechanisms. This work can provide information on the centrifuge test in which the model scaling effects are often considered to be influential on results.

3. Model large polygonal particles as retaining wall backfills to investigate the wall/backfill interface friction and lateral earth pressure coefficients in both passive and active conditions. The numerical results were compared with theoretical solutions. Well-packed backfills were also modelled and compared with LimitState:GEO models. The failure modes coincide very well.

Three related studies were undertaken and the key conclusions of these studies are summarised below.

8.1.2   Particle shape and packing effects on soil behaviours

1. Taking advantage of the inherent polygon modelling within Box2D, a Voronoi-based random convex polygonal particle generation approach was implemented. This allowed a large range of random polygonal-shaped particles to be studied and a range of in-situ packings to be investigated. Facilitated by this approach, packing effects can be investigated and solutions can be compared with continuum analyses.

2. To control the particle shape distributions in size and circularity, the Inverse Monte-Carlo (IMC) method was introduced. However the algorithm able to more efficiently find the target position to which the seed point should be moved in each time step in order to decrease the discrepancy with the desired distribution is deserved to be further studied.

3. Five particle shapes were studied within a series of biaxial models: polysized discs, monosized non-elongated dodecagons, monosized elongated dodecagons, polysized elongated dodecagons and Voronoi-based polygons. Granular samples were created by deposition process under gravity. It was found that particle shape variation was able to create denser packings than particle size variation.

4. By comparing the void ratios before and after the biaxial confining process, the polysized elongated dodecagons were found to possess the greatest compressibility under isotropic pressure loading. This was attributed to their large size variation and angularity.

5. Monosized elongated dodecagons were found to exhibit the largest increase in contact numbers because of the uniformity in particle size distribution and large angularity.

6. Work hardening, softening, and critical state behaviours were successfully captured within the biaxial test models.

7. It was observed that the critical state strength was independent of particle size and shape variations, but purely dependent on particle average circularity which can enhance the critical soil strength.

8. In critical states, the monosized elongated dodecagon samples possess the highest mean coordination numbers and the average contact number deceases as particle size and shape variate. By calculating critical state contact numbers for particles in different sizes, it was found that the larger the particle, the larger its mean contact number is, indicating the larger particles form the force chains surrounding the smaller particles.

9. The peak strength was found to be significantly influenced by the initial density state as expected.

10. A range of graphical interpretation approaches were applied in Box2D to better investigate the microscopic skeleton evolutions as shearing proceeds. Particle accumulated rotations and displacements, local volumetric strain rates, local void ratios, particle contact numbers and contact normal force chains were plotted to compare the microscale behaviours in various samples. Particle rotation plots were found to be most indicative of shear bands formation since particles rotate much more within shear bands than others. The local volumetric strains and the local void ratios within the shear band failure zones are greater in magnitude than elsewhere, while the particle contact numbers and the contact normal forces are relatively smaller.

11. Two well-packed Voronoi-based in-situ packings with and without void space were built to compare with other two packings created by deposition approach in order to study the potential benefits of engineering well packed stone structures (enhanced dry-stone construction).

12. The peak strengths in the two well-packed in-situ packings were observed to be reached earlier than the other two packings, because the peak strength will be developed upon the initial packing mechanism due to the skeleton rearrangement inhibition in the well-packed samples. It was proved that besides the initial deposit density state, the particle initial contact condition can also influence the peak strength. However, there was no difference observed in critical strength caused by packing effects. The shear bands developed in the well-packed samples oriented at $53°$ from the horizontal, which is very close to the theoretical value of $58.4°$ derived from the Mohr-Coulomb failure criteria, compared with other two samples at $45°$.

8.1.3 Granular soil small-strain stiffness

To study the model scaling effects on small-strain stiffness which are common to be observed in centrifuge tests, the model scaling ratio effects on the small-strain (deviatoric strain below 0.002%) stiffness of cohesionless granular soils in different packings were investigated in this study:

1. It was found that the small-strain stiffness increases as the scaling ratio increases for dodecagonal samples at the same density states due to the boundary effects, however, decreases under the same mean coordination numbers.

2. Scaling ratio effects for regular hexagonal packings are not apparent due to the crystallisation effects. The hexagonal samples exhibit higher small-strain stiffness than the dodecagonal samples under the same mean coordination number condition, while the dodecagonal samples possess higher small-strain stiffness at the same initial density states.

3. For Voronoi-based samples, the same behaviours were observed as in the dodecagonal samples when the initial void ratio is below 0.224, however, the phenomena reversed for looser samples of initial void ratios larger than 0.224. The dodecagonal samples display higher small-strain stiffness than the Voronoi-based samples of similar mean coordination numbers or density states

because of the particle size and shape variation effects easing inter-particle rotations especially at the small-strain stage.

4. The confining pressure effects on the small-strain stiffness were also analysed. The samples exhibited higher stiffness under higher confining pressure and the relationship between the confining pressure and the shear modulus can be better established by the mean coordination number than with the void ratio.

8.1.4   Retaining walls and lateral earth pressure coefficients

To investigate the retaining wall local friction effects on the lateral earth pressure coefficients (K_a and K_p), two types of retaining wall models were established regarding whether or not the wall base contacts the bottom boundary (condition A and B). Backfills made of dodecagonal particles, Voronoi-based particles and in-situ well -packed Voronoi particles were built and compared. The results were compared with theoretical solutions give by Powrie (2018) and limit analysis using software Limit-State:GEO.

1. The relationship between local wall friction angle δ_w and wall/back interface friction angle δ for different packings were studied at constant particle internal friction angle ϕ_{crit}. The maximum wall/backfill interface friction angles that can be developed as the local wall friction increases in the passive condition for the backfills made of dodecagonal particles and Voronoi-based particles were found to be $0.65\phi_{crit} - 0.88\phi_{crit}$ and $0.66\phi_{crit} - 0.74\phi_{crit}$ respectively, when the local wall friction angle exceeds the inter-particle friction angle ϕ. The high interface friction angle is possibly caused by the flat interface making rotations and sliding easier. This corroborates guidance in Eurocode 7 which states that a value no higher than $0.67\phi_{crit}$ should be used for pre-cast concrete or steel sheet piling. Future work is needed for cast in-situ concrete which Eurocode 7 allows $1.00\phi_{crit}$.

2. The friction angle at the wall/backfill interface is generally slightly higher in condition B than that in condition A at the same local wall friction angle in the passive condition. This is attributed to the bottom boundary effect which is an important consideration in modelling.

3. In the active condition, δ can reach $1.0\phi_{crit}$ for backfills made of dodecagonal particles. This only occurs at the cases when δ_w is larger than ϕ.

4. The wall roughness will increase both the peak and critical state passive earth pressure coefficients. The obtained passive earth pressure coefficients by Box2D are higher than the theoretical solutions given by Powrie (2018) and limit analysis via LimitState:GEO, and as the wall friction angle increases, the discrepancies become larger. The active earth pressure coefficients in Box2D are lower than the theoretical values while the discrepancies keep nearly unchanged as the wall roughness increases. The measured mobilised earth pressure coefficients are based on the backfill geometry changes which are not considered in theoretical solutions.

5. The backfills made of in-situ Voronoi packings exhibit higher peak and critical strengths than others formed by deposition. For the smooth wall condition, the critical K_p for the in-situ Voronoi packing and the poorly-packed Voronoi packing are 3.7 and 2.6 respectively.

6. It was found that the measured initial ($d/H = 0.5\%$) K_p values in condition A for the backfills made of dodecagonal particles are slightly lower than the critical K_p values, while the measured initial K_p values in condition B are higher than the critical K_p values. The peak strengths in condition A and B are developed at d/H around 10% and 3% respectively. The calculated peak K_p values based on equation (7.2) are larger than the measured peak values.

Overall, through three specific studies: particle shape and packing effects on soil mechanical behaviours in biaxial simulations, model scaling effects on cohesionless granular soil small-strain stiffness and retaining walls, Box2D shows great capacity in modelling granular cohesionless soils quantitatively and qualitatively.

8.2   Further work

Based on the previous numerical modelling studies by means of physics engine Box2D, it is shown that Box2D is able to be applied in granular soil modelling for both academic research and engineering practice. Below are the recommended works for further studies:

1. In the Bo2D contact model, the cohesion part is not considered. Therefore, the cohesion factor will be added to the Box2D contact model and then a series of parametric studies are to be conducted to investigate macroscopic behaviours of cohesive granular soils. In this way, self-supported unconfined granular samples can next be built and studied.

2. Particle breakage modelling deserves to be achieved in Box2D coupled with the peridynamics approach. Because particle breakages and micro-cracks often occur at the boundaries and strain localisation regions, the interlocking and restructuring phenomena can be better understood by this approach.

3. More complex particle shapes will be applied in modelling by Box2D. For example, by combining multiple polygonal or disc particles together by the welding joint in Box2D, we can further study the particle shape effects and find the relationship between particle shape and size distributions and strength properties.

4. The inter-particle contact conditions on mechanical behaviours will be further studied. By building in-situ Voronoi packings, we can investigate the influences of initial mean coordination numbers and edge-edge contact conditions (edge-edge contact area and the proportion of this contact in all types of contacts) on peak strengths.

5. In addition, the interface friction between a non-flat retaining wall and a backfill will be investigated. Because of the flat wall surface applied in this study, the measured wall/backfill interface friction angle tends to be higher than that at the non-flat wall interface due to the inhibition of rotations and sliding. The local void ratio variation adjacent to the wall across different regions will be analysed. In this study, it was assumed that the local void ratio is within 4-particle-size region adjacent to the wall surface, the variation of the local void ratio within sliding wedge can provide more information on backfill skeleton evolution. The bottom boundary effects on the lateral earth pressure coefficients will continue being studied. Large-scale retaining wall models will be established via high performance computers (HPC) to study the scaling ratio effects.

6. Physical tests on well-packed in-situ packings (dry stone structures) and retaining walls can be carried out to corroborate the simulation results.

References

Agnolin, I. and Roux, J.-N. (2007), 'Internal states of model isotropic granular packings. III. elastic properties', *Physical Review E* **76**(6), 061304.

Alder, B. J. and Wainwright, T. E. (1957), 'Phase transition for a hard sphere system', *The Journal of chemical physics* **27**(5), 1208–1209.

Alder, B. J. and Wainwright, T. E. (1959), 'Studies in molecular dynamics. I. general method', *The Journal of Chemical Physics* **31**(2), 459–466.

Alshibli, K. A. and Sture, S. (2000), 'Shear band formation in plane strain experiments of sand', *Journal of Geotechnical and Geoenvironmental Engineering* **126**(6), 495–503.

Altunbaş, A., Soltanbeigi, B. and Çinicioğlu, Ö. (2019), 'DEM analysis of passive failure state behind a rigid retaining wall: effect of boundary conditions'.

Atkinson, J. (2000), 'Non-linear soil stiffness in routine design', *Géotechnique* **50**(5), 487–508.

Azéma, E., Estrada, N., Preechawuttipong, I., Delenne, J.-Y. and Radjai, F. (2017), Systematic description of the effect of particle shape on the strength properties of granular media, *in* 'EPJ Web of Conferences', Vol. 140, EDP Sciences, p. 06026.

Bagi, K. (1993), 'A quasi-static numerical model for micro-level analysis of granular assemblies', *Mechanics of materials* **16**(1-2), 101–110.

Bagi, K. (2005), 'An algorithm to generate random dense arrangements for discrete element simulations of granular assemblies', *Granular Matter* **7**(1), 31–43.

Baraff, D. (1989), Analytical methods for dynamic simulation of non-penetrating rigid bodies, *in* 'ACM SIGGRAPH Computer Graphics', Vol. 23, ACM, pp. 223–232.

Baraff, D. (1997), 'An introduction to physically based modeling: rigid body simulation II—nonpenetration constraints', *SIGGRAPH course notes* pp. D31–D68.

Bardet, J.-P. (1994), 'Observations on the effects of particle rotations on the failure of idealized granular materials', *Mechanics of materials* **18**(2), 159–182.

Bažant, Z., Gettu, R. and Kazemi, M. (1991), Identification of nonlinear fracture properties from size effect tests and structural analysis based on geometry-dependent R-curves, *in* 'International journal of rock mechanics and mining sciences & geomechanics abstracts', Vol. 28, Elsevier, pp. 43–51.

Belytschko, T., Liu, W. K., Moran, B. and Elkhodary, K. (2013), *Nonlinear finite elements for continua and structures*, John wiley & sons.

Blott, S. J. and Pye, K. (2008), 'Particle shape: a review and new methods of characterization and classification', *Sedimentology* **55**(1), 31–63.

Bolton, M. and Powrie, W. (1988), 'Behaviour of diaphragm walls in clay prior to collapse', *Geotechnique* **38**(2), 167–189.

Bowman, E. T., Soga, K. and Drummond, W. (2001), 'Particle shape characterisation using fourier descriptor analysis', *Geotechnique* **51**(6), 545–554.

Cascante, G. and Santamarina, J. C. (1996), 'Interparticle contact behavior and wave propagation', *Journal of geotechnical engineering* **122**(10), 831–839.

Catto (2013), *Box2D v2. 3.0 User Manual*.

Catto, E. (2010), 'Computing distance', Online slides.

Catto, E. et al. (2006), Fast and simple physics using sequential impulses, *in* 'Game Developers Conference', p. 9.

Chang, C. S., Misra, A. and Sundaram, S. S. (1991), 'Properties of granular packings under low amplitude cyclic loading', *Soil Dynamics and Earthquake Engineering* **10**(4), 201–211.

Cheung, G. and O'Sullivan, C. (2008), 'Effective simulation of flexible lateral boundaries in two-and three-dimensional DEM simulations', *Particuology* **6**(6), 483–500.

Cho, G.-C., Dodds, J. and Santamarina, J. C. (2006), 'Particle shape effects on packing density, stiffness, and strength: natural and crushed sands', *Journal of geotechnical and geoenvironmental engineering* **132**(5), 591–602.

Cicekci, O. C., Turkeri, M. K. and Pekcan, O. (2014), Development of Soil Profile Visualization Software Using Game Engines, *in* 'Geo-Congress 2014: Geo-characterization and Modeling for Sustainability', pp. 3364–3372.

Clough, R. W. (1960), The finite element method in plane stress analysis, *in* 'Proceedings of 2nd ASCE Conference on Electronic Computation, Pittsburgh Pa., Sept. 8 and 9, 1960'.

Coulomb, C. A. (1776), 'Essai sur une application des regles de maximis et minimis a quelques problemes de statique relatifs a l'architecture (essay on maximums and minimums of rules to some static problems relating to architecture)'.

Cui, L. and O'Sullivan, C. (2003), 'Analysis of a triangulation based approach for specimen generation for discrete element simulations', *Granular Matter* **5**(3), 135–145.

Cundall, P. (1974), 'A computer model for rock mass behavior using interactive graphics for the input and output of geometrical data', *A Report Prepared under Contract Number DACW 45-74-C-006, for the Missouri River Division* .

Cundall, P. A. (1971), A computer model for simulating progressive, large-scale movement in blocky rock system, *in* 'Proceedings of the International Symposium on Rock Mechanics, 1971'.

Cundall, P. A. and Strack, O. D. (1979), 'A discrete numerical model for granular assemblies', *geotechnique* **29**(1), 47–65.

Cundall, P. and Strack, O. (1978), 'BALL-A program to model granular media using the distinct element method', *Technical note* .

Cundall, P. and Strack, O. (1983), Modeling of microscopic mechanisms in granular material, *in* 'Studies in Applied mechanics', Vol. 7, Elsevier, pp. 137–149.

Da Cruz, F., Emam, S., Prochnow, M., Roux, J.-N. and Chevoir, F. (2005), 'Rheophysics of dense granular materials: Discrete simulation of plane shear flows', *Physical Review E* **72**(2), 021309.

Dobry, R. and Ng, T.-T. (1992), 'Discrete modelling of stress-strain behaviour of granular media at small and large strains', *Engineering computations* **9**(2), 129–143.

Duran, J. (2012), *Sands, powders, and grains: an introduction to the physics of granular materials*, Springer Science & Business Media.

Edwards, S. (1998), 'The equations of stress in a granular material', *Physica A: Statistical Mechanics and its Applications* **249**(1-4), 226–231.

Ehsan, I. and Bezuijen, A. (2015), Simulation of granular soil behaviour using the bullet physics library, *in* '3rd International Symposium on Geomechanics from Micro to Macro', Vol. 2, Taylor and Francis Group-London, pp. 1565–1570.

Enomoto, T. (2016), 'Effects of grading and particle characteristics on small strain properties of granular materials', *Soils and Foundations* **56**(4), 745–750.

Fang, Y.-S., Chen, T.-J. and Wu, B.-F. (1994), 'Passive earth pressures with various wall movements', *Journal of Geotechnical Engineering* **120**(8), 1307–1323.

Fang, Y.-S., Ho, Y.-C. and Chen, T.-J. (2002), 'Passive earth pressure with critical state concept', *Journal of Geotechnical and Geoenvironmental Engineering* **128**(8), 651–659.

Fang, Y.-S. and Ishibashi, I. (1986), 'Static earth pressures with various wall movements', *Journal of Geotechnical Engineering* **112**(3), 317–333.

Feng, Y., Han, K. and Owen, D. (2003), 'Filling domains with disks: an advancing front approach', *International journal for numerical methods in engineering* **56**(5), 699–713.

Ferellec, J.-F. and McDowell, G. (2008), 'A simple method to create complex particle shapes for DEM', *Geomechanics and Geoengineering: An International Journal* **3**(3), 211–216.

Galindo-Torres, S., Muñoz, J. and Alonso-Marroquin, F. (2010), 'Minkowski-Voronoi diagrams as a method to generate random packings of spheropolygons for the simulation of soils', *physical review E* **82**(5), 056713.

Galindo-Torres, S. and Pedroso, D. (2010), 'Molecular dynamics simulations of complex-shaped particles using Voronoi-based spheropolyhedra', *Physical Review E* **81**(6), 061303.

Giang, P. H. H., Van Impe, P. O., Van Impe, W. F., Menge, P. and Haegeman, W. (2017), 'Small-strain shear modulus of calcareous sand and its dependence on particle characteristics and gradation', *Soil Dynamics and Earthquake Engineering* **100**, 371–379.

Gilbert, E. G., Johnson, D. W. and Keerthi, S. S. (1988), 'A fast procedure for computing the distance between complex objects in three-dimensional space', *IEEE Journal on Robotics and Automation* **4**(2), 193–203.

Gilbert, M., Smith, C., Haslam, I. and Pritchard, T. (2010), Application of discontinuity layout optimization to geotechnical limit analysis problems, *in* 'Proc. 7th Eur. Conf. Num. Meths. Geo. Eng., Trondheim, Norway', pp. 169–174.

Grima, A. P. and Wypych, P. W. (2011), 'Development and validation of calibration methods for discrete element modelling', *Granular Matter* **13**(2), 127–132.

Häggström, O. and Meester, R. (1996), 'Nearest neighbor and hard sphere models in continuum percolation', *Random Structures & Algorithms* **9**(3), 295–315.

Hanley, K. J., Huang, X., O'Sullivan, C. and Kwok, F. C. (2014), 'Temporal variation of contact networks in granular materials', *Granular Matter* **16**(1), 41–54.

Hardin, B. O. and Black, W. L. (1966), 'Sand stiffness under various triaxial stresses', *Journal of Soil Mechanics & Foundations Division* **92**(SM2).

Hardin, B. O. and Black, W. L. (1968), 'Vibration modulus of normally consolidated clay', *Journal of the Soil Mechanics and Foundations Division* **94**(2), 353–369.

Hardin, B. O. and Drnevich, V. P. (1972), 'Shear modulus and damping in soils: measurement and parameter effects', *Journal of Soil Mechanics & Foundations Division* **98**(sm6).

Hardin, B. O. and Richart, F. (1963), 'Elastic wave velocities in granular soils', *Journal of the Soil Mechanics and Foundations Division* **89**(1), 33–65.

He, H. and Zheng, J. (2020), 'Simulations of realistic granular soils in oedometer tests using physics engine', *International Journal for Numerical and Analytical Methods in Geomechanics* .

Head, K. H. et al. (1998), *Manual of soil laboratory testing. Volume 3: effective stress tests.*, number Ed. 2, John Wiley & Sons.

Hicher, P.-Y. (1996), 'Elastic properties of soils', *Journal of geotechnical engineering* **122**(8), 641–648.

Hu, W., Dano, C., Hicher, P.-Y., Le Touzo, J.-Y., Derkx, F. and Merliot, E. (2011), 'Effect of sample size on the behavior of granular materials', *Geotechnical Testing Journal* **34**(3), 186–197.

Izadi, E. and Bezuijen, A. (2018), 'Simulating direct shear tests with the bullet physics library: A validation study', *PLOS one* **13**(4), e0195073.

Jean, M. (1999), 'The non-smooth contact dynamics method', *Computer methods in applied mechanics and engineering* **177**(3-4), 235–257.

Jensen, R. P., Edil, T. B., Bosscher, P. J., Plesha, M. E. and Kahla, N. B. (2001), 'Effect of particle shape on interface behavior of DEM-simulated granular materials', *International Journal of Geomechanics* **1**(1), 1–19.

Jiang, M., He, J., Wang, J., Liu, F. and Zhang, W. (2014), 'Distinct simulation of earth pressure against a rigid retaining wall considering inter-particle rolling resistance in sandy backfill', *Granular Matter* **16**(5), 797–814.

Johnson, K. L. and Johnson, K. L. (1987), *Contact mechanics*, Cambridge university press.

Jung, Y., Jang, E., Chung, C. et al. (2010), 'From micromechanics particle simulation to macroscopic experimental phenomena of cross-anisotropic soil elasticity.', *Proceedings of GeoFlorida 2010: advances in analysis, modeling and design, West Palm Beach, Florida, USA, 20-24 February 2010* pp. 580–590.

Katagiri, J., Matsushima, T. and Yamada, Y. (2014), 'Variations in shear behavior among specimens with different packing patterns', *Granular Matter* **16**(6), 891–901.

Kenny, E. (2004), Stable, Robust, and Versatile Multibody Dynamics Animation, PhD thesis, Department of Computer Science, University of Copenhagen.

Khosravi, M. H., Hamedi Azad, F., Bahaaddini, M. and Pipatpongsa, T. (2017), 'DEM Analysis of Backfilled Walls Subjected to Active Translation Mode', *International Journal of Mining and Geo-Engineering* **51**(2), 191–197.

Khosravi, M., Pipatpongsa, T. and Takemura, J. (2013), 'Experimental analysis of earth pressure against rigid retaining walls under translation mode', *Géotechnique* **63**(12), 1020–1028.

Kocis, L. and Whiten, W. J. (1997), 'Computational investigations of low-discrepancy sequences', *ACM Transactions on Mathematical Software (TOMS)* **23**(2), 266–294.

Koerner, R. M. (1970), 'Effect of particle characteristics on soil strength', *Journal of Soil Mechanics & Foundations Div* .

Kokusho, T. (1980), 'Cyclic triaxial test of dynamic soil properties for wide strain range', *Soils and foundations* **20**(2), 45–60.

Krabbenhoft, K., Huang, J., Da Silva, M. V. and Lyamin, A. (2012), 'Granular contact dynamics with particle elasticity', *Granular Matter* **14**(5), 607–619.

Krabbenhoft, K., Lyamin, A., Huang, J. and da Silva, M. V. (2012), 'Granular contact dynamics using mathematical programming methods', *Computers and Geotechnics* **43**, 165–176.

Li, M.-G., Chen, J.-J. and Wang, J.-H. (2017), 'Arching effect on lateral pressure of confined granular material: numerical and theoretical analysis', *Granular Matter* **19**(2), 20.

Li, Y., Xu, Y. and Thornton, C. (2005), 'A comparison of discrete element simulations and experiments for 'sandpiles' composed of spherical particles', *Powder Technology* **160**(3), 219–228.

Lo Presti, D., Jamiolkowski, M., Pallara, O., Cavallaro, A. and Pedroni, S. (1997), 'Shear modulus and damping of soils', *Geotechnique* **47**(3), 603–617.

Lu, M. and McDowell, G. (2007), 'The importance of modelling ballast particle shape in the discrete element method', *Granular matter* **9**(1-2), 69.

Matsushima, T. (2005), 'Effect of irregular grain shape on quasi-static shear behavior of granular assembly', *Powders and Grains, P&G05* **2**, 1319–1323.

Matsushima, T. and Konagai, K. (2001), 'Grain-shape effect on peak strength of granular materials', *Computer Methods and Advances in Geomechanics, Desai et al. eds., Balkema* **1**, 361–366.

Matsushima, T. and Saomoto, H. (2002), Discrete element modeling for irregularly-shaped sand grains, *in* 'Numerical Methods in Geotechnical Engineering', Paris, pp. 239–246.

Meng, J., Huang, J., Sloan, S. and Sheng, D. (2018), 'Discrete modelling jointed rock slopes using mathematical programming methods', *Computers and Geotechnics* **96**, 189–202.

MiDi, G. (2004), 'On dense granular flows', *The European Physical Journal E* **14**(4), 341–365.

Mindlin, R. D. (1953), 'Elastic spheres in contact under varying oblique forces', *J. Applied Mech.* **20**, 327–344.

Mirghasemi, A., Rothenburg, L. and Matyas, E. (2002), 'Influence of particle shape on engineering properties of assemblies of two-dimensional polygon-shaped particles', *Geotechnique* **52**(3), 209–217.

Mollon, G. and Zhao, J. (2012), 'Fourier–Voronoi-based generation of realistic samples for discrete modelling of granular materials', *Granular matter* **14**(5), 621–638.

Mollon, G. and Zhao, J. (2014), '3d generation of realistic granular samples based on random fields theory and fourier shape descriptors', *Computer Methods in Applied Mechanics and Engineering* **279**, 46–65.

Nguyen, H., O'Sullivan, C. and Otsubo, M. (2018), 'Discrete element method analysis of small-strain stiffness under anisotropic stress states', *Géotechnique Letters* **8**(3), 183–189.

Ning, Z. and Evans, T. (2013), Discrete element method study of shear wave propagation in granular soil, *in* 'Proceedings of the 18th International Conference on Soil Mechanics and Geotechnical Engineering, France, Paris', pp. 1031–1034.

Oda, M. and Kazama, H. (1998), 'Microstructure of shear bands and its relation to the mechanisms of dilatancy and failure of dense granular soils', *Geotechnique* **48**(4), 465–481.

O'Donovan, J., O'Sullivan, C., Marketos, G. and Muir Wood, D. (2015), 'Anisotropic stress and shear wave velocity: DEM studies of a crystalline granular material', *Geotechnique letters* **5**(3), 224–230.

Omar, T. and Sadrekarimi, A. (2014), 'Specimen size effects on behavior of loose sand in triaxial compression tests', *Canadian Geotechnical Journal* **52**(6), 732–746.

O'Sullivan, C. (2011), *Particulate discrete element modelling: a geomechanics perspective*, CRC Press.

Otsubo, M. and O'Sullivan, C. (2018), 'Experimental and DEM assessment of the stress-dependency of surface roughness effects on shear modulus', *Soils and foundations* **58**(3), 602–614.

Otsubo, M., O'Sullivan, C. and Shire, T. (2017), 'Empirical assessment of the critical time increment in explicit particulate discrete element method simulations', *Computers and Geotechnics* **86**, 67–79.

Oztoprak, S. and Bolton, M. (2013), 'Stiffness of sands through a laboratory test database', *Géotechnique* **63**(1), 54–70.

O'Donovan, J., O'Sullivan, C. and Marketos, G. (2012), 'Two-dimensional discrete element modelling of bender element tests on an idealised granular material', *Granular Matter* **14**(6), 733–747.

Pearson, A. and Shepley, P. (2018), Determining shallow foundation stiffness in sand from centrifuge modelling, *in* 'Physical Modelling in Geotechnics, Volume 2', CRC Press, pp. 1303–1308.

Peña, A. A. (2008), Influence of Particle Shape on the Global Mechanical Response of Granular Packings: Micromechanical Investigation of the Critical State in Soil Mechanics, PhD thesis, Institut fúr Geotechnik, Universitat Stuttgärt.

Peña, A., Garcia-Rojo, R. and Herrmann, H. J. (2007), 'Influence of particle shape on sheared dense granular media', *Granular Matter* **9**(3-4), 279–291.

Perez, J. L., Kwok, C., O'Sullivan, C., Huang, X. and Hanley, K. (2016), 'Assessing the quasi-static conditions for shearing in granular media within the critical state soil mechanics framework', *Soils and Foundations* **56**(1), 152–159.

Powrie, W. (2018), *Soil mechanics: concepts and applications*, CRC Press.

Pytlos, M. (2015), New tools for modelling soil-filled masonry arch bridges, PhD thesis, University of Sheffield.

Pytlos, M., Gilbert, M. and Smith, C. (2015), 'Modelling granular soil behaviour using a physics engine', *Géotechnique Letters* **5**(4), 243–249.

Radjai, F. and Richefeu, V. (2009), 'Contact dynamics as a nonsmooth discrete element method', *Mechanics of Materials* **41**(6), 715–728.

Rankine, W. (1857), 'On the Stability of Loose Earth', *Transactions of the Royal Society* **147**.

Repaport, D. (2004), 'The art of molecular dynamics mulation', *Cambridge University Pres, Cambridge* .

Roscoe, K. H. (1970), 'The influence of strains in soil mechanics', *Geotechnique* **20**(2), 129–170.

Sandeep, C. S., Senetakis, K., Cheung, D., Choi, C. E., Wang, Y., Coop, M. and Ng, C. W. W. (2021), 'Experimental study on the coefficient of restitution of grain against block interfaces for natural and engineered materials', *Canadian Geotechnical Journal* **58**(1), 35–48.

Santamarina, J. and Cho, G.-C. (2004), Soil behaviour: The role of particle shape, *in* 'Advances in geotechnical engineering: The Skempton conference: Proceedings of a three day conference on advances in geotechnical engineering, organised by the Institution of Civil Engineers and held at the Royal Geographical Society, London, UK, on 29–31 March 2004', Thomas Telford Publishing, pp. 604–617.

Santos, J. and Correia, A. G. (2000), Shear modulus of soils under cyclic loading at small and medium strain level, *in* 'Proceedings 12th World Conference on Earthquake Engineering, Auckland, New Zealand, paper', number 0530.

Scott, R. (1987), 'Failure', *Géotechnique* **37**(4), 423–466.

Sheng, Y., Lawrence, C., Briscoe, B. and Thornton, C. (2004), 'Numerical studies of uniaxial powder compaction process by 3D DEM', *Engineering Computations* .

Shi, G.-h. (1992), 'Discontinuous deformation analysis: a new numerical model for the statics and dynamics of deformable block structures', *Engineering computations* .

Shin, H. and Santamarina, J. (2013), 'Role of particle angularity on the mechanical behavior of granular mixtures', *Journal of Geotechnical and Geoenvironmental Engineering* **139**(2), 353–355.

Shirley, D. J. and Hampton, L. D. (1978), 'Shear-wave measurements in laboratory sediments', *The Journal of the Acoustical Society of America* **63**(2), 607–613.

Simons, T. A., Weiler, R., Strege, S., Bensmann, S., Schilling, M. and Kwade, A. (2015), 'A ring shear tester as calibration experiment for DEM simulations in agitated mixers–a sensitivity study', *Procedia engineering* **102**, 741–748.

Smith, C. and Gilbert, M. (2007), 'Application of discontinuity layout optimization to plane plasticity problems', *Proceedings of the Royal Society A: Mathematical, Physical and Engineering Sciences* **463**(2086), 2461–2484.

Sokolovskii, V. V. (1960), Statics of soil media, Technical report, Butterworths Scienc. Publ.

Stoyan, D. (1998), Models of random systems of non-intersecting spheres, *in* 'Prague stochastics' 98 (23-28 August 1998)'.

Sulsky, D., Chen, Z. and Schreyer, H. L. (1994), 'A particle method for history-dependent materials', *Computer methods in applied mechanics and engineering* **118**(1-2), 179–196.

Sutmann, G. (2002), 'Classical molecular dynamics', *Quantum simulations of complex many-body systems: from theory to algorithms* **10**, 211–254.

Terzaghi, K. (1943), *Theoretical soil mechanics*, John Wiley & Sons.

Terzaghi, K. (1954), 'Anchored bulkheads', *American Society of Civil Engineers Transactions* .

Thomas, P. A. and Bray, J. D. (1999), 'Capturing nonspherical shape of granular media with disk clusters', *Journal of Geotechnical and Geoenvironmental Engineering* **125**(3), 169–178.

Thornton, C. and Antony, S. (2000), 'Quasi-static shear deformation of a soft particle system', *Powder technology* **109**(1-3), 179–191.

Thornton, C. and Yin, K. (1991), 'Impact of elastic spheres with and without adhesion', *Powder technology* **65**(1-3), 153–166.

Tsuji, Y., Kawaguchi, T. and Tanaka, T. (1993), 'Discrete particle simulation of two-dimensional fluidized bed', *Powder technology* **77**(1), 79–87.

Vardoulakis, I. and Graf, B. (1985), 'Calibration of constitutive models for granular materials using data from biaxial experiments', *Géotechnique* **35**(3), 299–317.

Voronoi, G. (1908), 'Nouvelles applications des paramètres continus à la théorie des formes quadratiques. premier mémoire. sur quelques propriétés des formes quadratiques positives parfaites.', *Journal für die reine und angewandte Mathematik (Crelles Journal)* **1908**(133), 97–102.

Walton, K. (1987), 'The effective elastic moduli of a random packing of spheres', *Journal of the Mechanics and Physics of Solids* **35**(2), 213–226.

Walton, O. R. and Braun, R. L. (1986), 'Viscosity, granular-temperature, and stress calculations for shearing assemblies of inelastic, frictional disks', *Journal of rheology* **30**(5), 949–980.

Wang, J., Gutierrez, M. S. and Dove, J. E. (2007), 'Numerical studies of shear banding in interface shear tests using a new strain calculation method', *International Journal for Numerical and Analytical Methods in Geomechanics* **31**(12), 1349–1366.

Wang, J., Yu, H., Langston, P. and Fraige, F. (2011), 'Particle shape effects in discrete element modelling of cohesive angular particles', *Granular Matter* **13**(1), 1–12.

Wichtmann, T. and Triantafyllidis, T. (2009), 'Influence of the grain-size distribution curve of quartz sand on the small strain shear modulus G_{max}', *Journal of geotechnical and geoenvironmental engineering* **135**(10), 1404–1418.

Wichtmann, T. and Triantafyllidis, T. (2010), 'On the influence of the grain size distribution curve on p-wave velocity, constrained elastic modulus mmax and poisson's ratio of quartz sands', *Soil Dynamics and Earthquake Engineering* **30**(8), 757–766.

Xu, Z., Lu, X., Guan, H. and Ren, A. (2013), 'Physics engine-driven visualization of deactivated elements and its application in bridge collapse simulation', *Automation in Construction* **35**, 471–481.

Yan, Z., Wilkinson, S., Stitt, E. and Marigo, M. (2015), 'Discrete element modelling (DEM) input parameters: understanding their impact on model predictions using statistical analysis', *Computational Particle Mechanics* **2**(3), 283–299.

Yu, P. and Richart Jr, F. (1984), 'Stress ratio effects on shear modulus of dry sands', *Journal of Geotechnical Engineering* **110**(3), 331–345.

Zeghal, M. and Tsigginos, C. (2015), 'A micromechanical analysis of the effect of fabric on low-strain stiffness of granular soils', *Soil Dynamics and Earthquake Engineering* **70**, 153–165.

Zhou, J., Zhang, Y. and Chen, J. (2009), 'Numerical simulation of random packing of spherical particles for powder-based additive manufacturing', *Journal of manufacturing science and engineering* **131**(3), 031004.

Zhu, F. and Zhao, J. (2019), 'Modeling continuous grain crushing in granular media: A hybrid peridynamics and physics engine approach', *Computer Methods in Applied Mechanics and Engineering* **348**, 334–355.